

# **STUDYING THERMOACOUSTIC SYSTEMS IN THE FRAMEWORK OF SYNCHRONIZATION THEORY**

*A THESIS*

*submitted by*

**PAWAR SAMADHAN ANANDA**

*for the award of the degree*

*of*

**DOCTOR OF PHILOSOPHY**



**DEPARTMENT OF AEROSPACE ENGINEERING  
INDIAN INSTITUTE OF TECHNOLOGY MADRAS**

**MAY 2018**

# THESIS CERTIFICATE

This is to certify that the thesis entitled **STUDYING THERMOACOUSTIC SYSTEMS IN THE FRAMEWORK OF SYNCHRONIZATION THEORY**, submitted by **Pawar Samadhan Ananda**, to the Indian Institute of Technology, Madras, for the award of the degree of **Doctor of Philosophy**, is a bona fide record of the research work done by him under our supervision. The contents of this thesis, in full or in parts, have not been submitted to any other Institute or University for the award of any degree or diploma.

**Prof. R. I. Sujith**  
Research Guide  
Professor  
Dept. of Aerospace Engineering  
IIT Madras, 600 036

**Prof. M. V. Panchagnula**  
Research Co-Guide  
Professor  
Dept. of Applied Mechanics  
IIT Madras, 600 036

Place: Chennai

Date: 10<sup>th</sup> May 2018

*To my grandparents,  
and to my brother Niranjan.*

## ACKNOWLEDGEMENTS

First and foremost, I would like to express my sincere gratitude to my supervisors, Prof. R. I. Sujith and Prof. M. V. Panchagnula. Without their endless support and motivation, I would not have completed my Ph.D. programme. The willingness of Prof. Sujith for learning new things, his dedication towards research, his perseverance, and the efforts he puts for his students to make them world leaders have been an immense source of inspiration for me. These things have greatly motivated me to work harder than I imagined possible. In fact, these are the reasons that prompted me to upgrade my master's programme to Ph.D. His selfless and down-to-earth nature have taught me a lot of lessons that I am sure would help me in my academic and non-academic pursuits in the future. His belief in me, that I can do things like any of the extraordinary people, has transformed me, shaped me, and I will be thankful to him for this throughout my life. I have always been amazed by the ability of Prof. M. V. Panchagnula to come up with new and innovative ideas to solve difficult problems. It has helped me tackle the difficulties I encountered during the development of the spray combustor. His friendly nature has always made it easy for me to approach him. I will be always thankful to him for the freedom that he has given me for doing experiments in the Fluid Mechanics lab. I find myself lucky and am thankful to God for having them as research guides.

I would like to express my heartfelt gratitude to the members of my Doctoral Committee, Prof. A. Kumar and Dr. S. Sahu for their support and valuable suggestions and has had a very important role in shaping my research work. I would like to thank the my HODs, Prof. K. Bhaskar, and Prof. P. Sriram for their support and encouragement during my tenure as a research scholar. My sincere gratitude to my teachers, Prof. S. R. Chakravarthy, Dr. A. Sameen, Dr. S. Ghosh, Prof. P. A. Ramakrishna, Dr. N. R. Panchapakesan, Dr. H. S. N. Murthy (Aerospace Engineering), Prof. A. Lakshminarayan (Physics), Prof. C. Sujatha, Dr. A. Sarkar (Mechanical Engineering), and A. K. Tangirala (Chemical Engineering) for their informative lectures, which helped me understand the concepts clearly.

I am thankful to the administration staff, Mrs. Aruna, Mr. Stephen, Mr. Manikan-

dan, Mrs. Nirmala, Mrs. Yamuna, and Mrs. Savitri from Aerospace Department for their endless support for various administrative works over the course of my Ph.D. I would like to acknowledge the great help provided by the staff members in the workshop, Dr. G. Balaganesan, Mr. Shashi Kumar, Mr. Rajesh (Central Workshop); Mr. Kennedy, Mr. Dayalan (Aerospace Engineering); Uday Kumar and V. Bhaskar (Applied Mechanics). Special thanks to Mr. John George for his suggestions on the design of the spray injector and regarding safety in the experimental lab. Many thanks to Mr. Ranganathan (Late.) and Mr. Viju for their excellent fabrication of a number of components of my experimental setup.

I am thankful to Prof. Tim Lieuwen and Dr. Benjamin Emerson for providing their valuable data set on the vitiated combustor used in the present thesis. It was a pleasure to meet them in AIAA conference held in Florida, USA. I had a great learning experience while working with them on a paper. I would like to thank Prof. Jürgen Kurths and Prof. Elena Surovyatkina for hosting me at Potsdam Institute of Climate Impact Research (PIK), Germany for a month-long research visit under the Indo-German project. Special thanks to Prof. Surovyatkina for the generous help she had provided me during my stay at PIK. It was a great experience to meet Dr. Norbert Marwan (PIK) and I am thankful to him for spending time with me on discussing the use of nonlinear dynamics and complex network approaches to study synchronization in thermoacoustic systems. I would also like to thank DAAD-DST for funding me for this visit. I thank Ankit, Roopam, and Ali for their hospitality and for providing savoury Indian food in Germany. I would like to thank Dr. Hiroshi Gotoda for inviting me to write an article for the Journal of the Combustion Society of Japan and for all the interactions we had during the course of submission of the article.

I would like to acknowledge Ministry of Human Resources and Development, India for providing me financial support for my Ph.D. programme. I would also like to express my gratitude to IIT Madras for providing me funds to attend international conferences held in Montreal, Canada (ASME, TurboExpo-2016) and Kissimmee, USA (AIAA SciTech-2018). I am thankful to the Office of Alumni Relations for providing me partial financial support under the IITMAANA Travel Grant program for the ASME conference. I wish to thank the Office of Naval Research Global (ONRG), USA and Gas Turbine Research Establishment (GTRE), DRDO, India for funding our research projects. I would like to especially thank Dr. Ramesh Kolar (ONRG) and, Dr. Ramanu-

jan Chari and Dr. V. Natarajan (RIC, GTRE) for their encouragements and motivations provided during all project review meetings.

I am greatly thankful to my colleagues from both RGD and Fluid Mechanics labs. I am really fortunate to have such people in my life who taught me several aspects and lessons that I find are useful to carry forward in my journey of life. I convey my vote of thanks to Dr. Vineeth Nair for setting up the foundation to start my research. I am also grateful to Dr. E. Gopalakishnan for mentoring me during the initial days in my lab and teaching me how to interact with my guide and labmates. Special thanks to Dr. Vishnu R. Unni for the all the help he has provided during my research at IIT Madras. His motivation, belief in me, and his efforts in driving me to finish things has helped to achieve several deadlines without any difficulty. I want to thank Dr. Koushik Balasubramanian and Dr. Bala Subrahmanyam Pesala for patiently answering questions related to thermoacoustic instability and synchronization.

I am very grateful and honored to collaborate with Dr. Sirshendu, Dr. Vadivukkarasan, Dr. Vishnu (Unni), Akshay, Vishnu (Agni), Krishna, Nitin, Amitesh, Nevin, Vedasri, Suraj and Dr. Nalini on various papers. They have been my source of learning and motivation. Their help in correcting my papers and thesis cannot be expressed by words and I will always be thankful to them for this. Without them, I find myself nowhere near who I am today. I acknowledge Abin, Sreelekha, Tony, R. Manikandan, Praveen, Induja, Subham, Sohail, Dr. Vinu, and Dr. Meenatchidevi for their immense help in correcting my papers and providing their valuable comments on the research. Special thanks to Akshay and Krishna for teaching me several lessons in English. I thank Dr. Gopalakrishnan, S. Manikandan, and Abin for being my chair-neighbors in the lab. Talking with them during breaks used to boost my energy and motivates me to work more. I thank Dileesh, Thilagaraj, and Selva for their help in fabricating some of the parts and drawings of my experimental setups. I thank Syam and Hashir for all the help in purchasing equipments for my experiments. I wish to thank Rama, Sudha, and Jabasteena for helping me with my work whenever needed with lab management. I would like to thank Irfan, Ganesh, Ram, Mrudula, Prabhod, Kushal, Dr. Gireesh (sir), Dr. Rana (sir), Mukund, Diego, Luca from RGD lab, and Nachiketa, Siddharth, Swaminathan, Dr. Pallab, Dr. Vallabha, and Dr. Karthiga Devi from Fluid Mechanics lab for all the help they have provided.

Life outside the lab without having friends would have been empty. It is my pleasure to have friends like Dhivyaraja and Shanmugdas who have constantly supported me emotionally, academically and financially throughout the period of my research. I will always be thankful to them for my entire life. I would like to thank my friends Subhash, Azar, Krishna, Shambhuraj, Mayur, Mahesh, Umesh, Adheesh, Sagar, Rajesh, Mayank, Nagendra, Kiran, and Siddhesh from Aeronautical Society of India. Time spent with them will always remain in my memory and will keep me happy. I would like to express my gratitude towards my school teachers for their motivations and lessons which I still use to move forward in life.

Finally, I would like to thank my parents who encouraged and supported me all the time to pursue my dream of getting a higher education. I dedicate my achievements to all their sacrifices and hard time they have gone through for supporting my education. I will be thankful to my brothers Santosh and Sagar for sacrificing their education for mine and providing financial support to our house from a tender age. Their sacrifice ensured that I wouldn't have to worry and focus on my studies. All the things that I have achieved in life would not have been possible without them. I am thankful to my brothers Chaitanya, Prashant, and Sushant and my lovely sister Pooja for understanding, inspiring and being with me through thick and thin. They are the reason why I work with a smile, and I will be forever grateful to them.

## **ABSTRACT**

**KEYWORDS:** Thermoacoustic instability; Intermittency; Reactive flow instabilities; Nonlinear dynamics; Synchronization; Collective behaviour; Asynchronous quenching.

Thermoacoustic instabilities observed in propulsion as well as power generation systems have remained a challenging field of research for several decades. A complex interaction between hydrodynamic flow field, unsteady combustion, and acoustic field of the confinement can lead to the occurrence of self-sustained, large amplitude oscillations in a combustor, which are commonly referred to as thermoacoustic instabilities. The presence of such instabilities is undesirable for the safe operation of the combustor, and hence, various studies have been conducted either to avoid their occurrence or to reduce their strength once they are established.

The studies on the transition to thermoacoustic instability are getting an immense interest in recent times. Traditionally, the transition to thermoacoustic instability was considered as Hopf bifurcation, wherein the system dynamics exhibit a sudden transition from a state of combustion noise to thermoacoustic instability, due to change in the control parameter. Recently, in several turbulent combustors, it was observed that the onset of thermoacoustic instability is preceded by intermittent oscillations, which consist of bursts of periodic oscillations amidst regions of aperiodic oscillations. Quantitative analysis of the intermittency route to thermoacoustic instability has been performed hitherto using the pressure oscillations alone. In the present study, we perform an experimental investigation on the coupled interaction of the acoustic field of the confinement and the heat release rate fluctuations from the flame in two different configurations of laboratory scale combustors - one with a gas-fired turbulent flame combustor and another with a two-phase flow spray combustor.

In turbulent gas fired combustors, a comparison study is performed for two types of flame holding mechanisms, namely, a bluff body and a swirler. The stability of both combustors is investigated for the increase in mean velocity of the flow that, in turn,

changes the equivalence ratio of the reactive mixture from a value close to stoichiometry to a fuel lean condition. The simultaneous data of acoustic pressure fluctuations and heat release rate fluctuations are acquired for different conditions of flow velocities. We study the coupled interaction of these oscillations during the transition of combustor dynamics from a state of combustion noise to thermoacoustic instability via intermittency. We use a framework of synchronization theory to characterize the coupled behaviour of these processes during the onset of thermoacoustic instability. The synchronization properties of different dynamical states observed in the combustion dynamics are characterized using a synchronization measure called probability of recurrence. We provide a new description to the intermittency route to thermoacoustic instability in the context of synchronization theory. The frequency locking behaviour of the coupled acoustic pressure and heat release rate fluctuations is investigated using different tools such as waterfall diagram, scalogram and cross wavelet transform. The spatiotemporal field of the swirl-stabilized combustor is investigated by simultaneously acquiring high-speed CH\* chemiluminescence images of the flame with acoustic pressure fluctuations in the system. The coupled behaviour of the acoustic field and the local heat release rate fluctuations in the reacting field is executed by calculating the instantaneous phase difference between these oscillations. Our analysis shows that the onset of thermoacoustic instability is a phenomenon associated with mutual synchronization between the acoustic pressure and the heat release rate signals. The spatiotemporal analysis reveals the emergence of order from a disordered reacting field during the onset of thermoacoustic instability. During intermittency, a coexistence of ordered and disordered behaviour is observed at a particular time instant in the reacting field of the combustor, which further resembles a chimera state.

In the spray combustion system, the transition to thermoacoustic instability is investigated for the variation of two control parameters: the location of the flame along the combustor length and a fuel mass flow rate. As these control parameters are gradually varied, we observe the transition of the system behavior (measured in terms of acoustic pressure and heat release rate fluctuations) from combustion noise to thermoacoustic instability occurring through intermittency. Recurrence plots and recurrence quantification analysis are used to characterize the deterministic behaviour of combustion noise and detecting the dynamical transitions in the acoustic pressure signal. The type of intermittency is quantified using tools such as probability distribution and scaling be-

havior of durations of aperiodic oscillations in the intermittency, first return map, and recurrence plot. The synchronization properties of the acoustic field and the global heat release rate fluctuations in the flame are investigated using a measure of cross wavelet transform. We also analyse the collective interaction between multiple flamelets anchored at the flame holder and the acoustic field in the system, during different states of combustor dynamics. We notice an emergence of collective synchronization between these subsystems of the combustor during the onset periodicity in its global dynamics.

Furthermore, we investigate the forced response of a hydrodynamically unstable reacting wake in a highly turbulent bluff body stabilized combustor for different values of density ratios (i.e., the ratio of unburnt gas density ( $\rho_u$ ) to burnt gas density ( $\rho_b$ )) and forcing parameters (i.e., amplitude and frequency). The variation of density ratio from a high to a low value, keeping  $\rho_u/\rho_b > 1$ , alters the dynamical characteristics of the reacting wake from a linearly globally stable (or convectively unstable) to a globally unstable mode. The density ratio across the reacting wake is changed by varying the temperature of reactants incoming to the combustor. The instantaneous CH\* chemiluminescence images of the flame corresponding to different control parameters are acquired. The forced response of the flame is analysed in terms of local fluctuations in heat release rate acquired from the top and the bottom branches of the flame. The symmetry of the forced flame response is characterized by computing the instantaneous phase difference of these local heat release rate fluctuations with the forcing signal. Using this analysis, we show that the globally unstable reacting wakes exhibit more receptivity to forcing as compared to the convectively unstable reacting wakes.

Finally, we propose an open-loop control strategy, based on the framework of forced synchronization theory, to control properties (such as phase, frequency and amplitude) of thermoacoustic instabilities. In an attempt to do a clean experiment, we perform experiments on a horizontal Rijke tube, which is a relatively simple device to study. External acoustic perturbations are used to force the self-sustained limit cycle oscillations in the system, and the forced response of the system is characterized for different values of the forcing parameters such as forcing amplitude and frequency. The instantaneous phase difference, calculated from the Hilbert transform, between the signals of system response and external forcing is used to investigate the phase locking behaviour of these signals. Using this analysis, different states of phase-locking and different routes to forced synchronization of limit cycle oscillations in the system are identified.

The amplitude response of the forced signal is analysed for different conditions of the forcing frequency. We observe that when the forcing frequency is much lower than the natural frequency of the oscillations, the response amplitude of the forced system exhibit a significant decrease (as high as 80% of the amplitude of unforced natural oscillations) due to the phenomenon of asynchronous quenching.

# TABLE OF CONTENTS

<b>ACKNOWLEDGEMENTS</b>	<b>ii</b>
<b>ABSTRACT</b>	<b>vi</b>
<b>LIST OF FIGURES</b>	<b>xxiv</b>
<b>ABBREVIATIONS</b>	<b>xxv</b>
<b>NOTATION</b>	<b>xxvi</b>
<b>1 Introduction</b>	<b>1</b>
1.1 Literature Survey . . . . .	4
1.1.1 Brief History . . . . .	4
1.2 Mechanisms Leading to Thermoacoustic Instability . . . . .	8
1.2.1 Formation of Large-Scale Coherent Structures . . . . .	8
1.2.2 Equivalence Ratio Fluctuations . . . . .	11
1.2.3 Unsteady Spray Dynamics . . . . .	12
1.2.4 Other Mechanisms . . . . .	13
1.3 Classical Linear Stability Analysis . . . . .	13
1.4 Origin of Nonlinearities in Thermoacoustics . . . . .	16
1.4.1 Subcritical Transition and Triggering . . . . .	17
1.4.2 Nonlinear Describing Function . . . . .	19
1.5 Nonlinear Dynamics of Thermoacoustic Systems . . . . .	21
1.5.1 Laminar Thermoacoustic Systems . . . . .	22
1.5.2 Turbulent Thermoacoustic Systems . . . . .	23
1.5.3 Complexities in Combustion Dynamics of Thermoacoustic Systems . . . . .	26
1.5.4 Studying Thermoacoustic Systems Using Synchronization Theory . . . . .	29
1.6 Control and Early Warning of Thermoacoustic Instabilities . . . . .	32

1.6.1	Passive Controls . . . . .	32
1.6.2	Active Controls . . . . .	33
1.6.3	Precursors . . . . .	34
1.7	Objectives and Overview of the Thesis . . . . .	35
<b>2</b>	<b>SYNCHRONIZATION</b>	<b>39</b>
2.1	Basics Concepts . . . . .	39
2.2	Mutual Synchronization . . . . .	43
2.2.1	Periodic and Chaotic Synchronization . . . . .	43
2.3	Other Phenomena of Mutual Synchronization of Coupled Oscillators	45
2.3.1	Amplitude Death and Oscillation Death . . . . .	45
2.3.2	Emergence and Collective Synchronization . . . . .	46
2.4	Forced Synchronization . . . . .	47
2.4.1	Frequency and Phase Entrainment . . . . .	47
2.4.2	Routes to Forced Synchronization . . . . .	50
2.5	Tools to Detect Synchronization . . . . .	52
2.5.1	Instantaneous Phase Calculations . . . . .	52
2.5.2	Synchronization Using Recurrence Theory . . . . .	55
2.5.3	Use of Cross Wavelet Transform . . . . .	57
<b>3</b>	<b>EXPERIMENTAL SETUPS AND MEASUREMENT TECHNIQUES</b>	<b>59</b>
3.1	Turbulent Gas Fired Combustors . . . . .	59
3.2	Two Phase Flow Spray Combustor . . . . .	62
3.3	Vitiated Turbulent Gas Fired Combustors . . . . .	65
3.4	Horizontal Rijke Tube . . . . .	67
<b>4</b>	<b>ONSET OF THERMOACOUSTIC INSTABILITY AS MUTUAL SYNCHRONIZATION OF THE ACOUSTIC FIELD AND TURBULENT REACTING FLOW</b>	<b>70</b>
4.1	Time Domain Analysis of Coupled Acoustic Pressure and Heat Release Rate Fluctuations . . . . .	72
4.2	Frequency Domain Analysis of Coupled Acoustic Pressure and Heat Release Rate Fluctuations . . . . .	74
4.3	Synchronization Behaviour of Coupled Acoustic Pressure and Heat Release Rate Fluctuations . . . . .	76

4.4	Comparison of Phase Synchronization and Generalized Synchronization States . . . . .	79
4.5	Conclusions . . . . .	85
<b>5</b>	<b>INTERMITTENCY, SYNCHRONIZATION AND COLLECTIVE INTERACTION IN A TWO-PHASE FLOW SPRAY COMBUSTOR</b>	<b>86</b>
5.1	Characterization of Transition to Thermoacoustic Instability Using Acoustic Pressure Signal . . . . .	87
5.1.1	Intermittency Route to Thermoacoustic Instability . . . . .	87
5.1.2	Phase Space Reconstruction . . . . .	94
5.1.3	Detection of Chaos . . . . .	95
5.1.4	Determining the Transition to Thermoacoustic Instability Using Recurrence Quantification Analysis . . . . .	97
5.2	Characterizing the Type of Intermittency . . . . .	100
5.2.1	Distribution of the Length of the Turbulent Phase . . . . .	101
5.2.2	Analysis Using First Return Map . . . . .	102
5.2.3	Investigation Based on Recurrence Plot . . . . .	103
5.3	Interim Summary . . . . .	104
5.4	Coupled Behaviour of Acoustic Pressure and Global Heat Release Rate Fluctuations . . . . .	105
5.5	Collective Interaction of Acoustic Field and Multiple Flamelets . . . . .	108
5.5.1	Combustion Noise . . . . .	109
5.5.2	Intermittency . . . . .	110
5.5.3	Thermoacoustic Instability . . . . .	112
5.6	Conclusions . . . . .	113
<b>6</b>	<b>NONLINEAR DYNAMICS AND SYNCHRONIZATION BEHAVIOUR OF A FORCED DENSITY STRATIFIED REACTING WAKE</b>	<b>115</b>
6.1	Comparison of the Dynamics of Unforced and Forced Oscillations of Reacting Wake . . . . .	118
6.2	Symmetry and Asymmetry of Forced Response of Reacting Wake . . . . .	123
6.3	Characterization of Phase-Locking Behavior Between Top and Bottom Branches of the Flame . . . . .	130
6.4	Conclusions . . . . .	135
<b>7</b>	<b>OPEN-LOOP CONTROL OF THERMOACOUSTIC INSTABILITIES USING SYNCHRONIZATION APPROACH</b>	<b>136</b>

7.1	Synchronization Map . . . . .	137
7.2	Effect of Change in Forcing Frequency at Constant Forcing Amplitude	139
7.3	Effect of Change in Forcing Amplitude at Constant Forcing Frequency	144
7.4	Asynchronous Quenching of Response Amplitude . . . . .	148
7.5	Conclusions . . . . .	149
<b>8</b>	<b>CONCLUSIONS AND SCOPE FOR FUTURE WORK</b>	<b>151</b>
<b>A</b>	<b>SYNCHRONIZATION TRANSITION IN A SWIRL STABILIZED COMBUSTOR</b>	<b>156</b>
A.1	Temporal Analysis of Acoustic Pressure and Heat Release Rate Signals	156
A.1.1	Coupled Analysis of Acoustic Pressure and Global Heat Release Rate Fluctuations . . . . .	156
A.1.2	Frequency Domain Analysis of Acoustic Pressure and Heat Release Rate Signals . . . . .	158
A.1.3	Synchronization Analysis of Acoustic Pressure and Heat Release Rate Signals . . . . .	161
A.2	Spatiotemporal Analysis of Coupled Acoustic Field and Reacting Field	166
A.2.1	Analyzing Spatial Synchrony of the Local Heat Release Rate Fluctuations With the Acoustic Pressure Fluctuations . . . . .	166
A.2.2	Comparison of Spatial Fields of Phase Synchronization and Generalized Synchronization States . . . . .	169
A.3	Summary . . . . .	171

## LIST OF FIGURES

1.1	(a) A schematic of the positive feedback loop between the acoustic field of the combustor and the unsteady flame dynamics responsible for driving self-sustained thermoacoustic instabilities. (b) The time series of acoustic pressure ( $p'$ ) and heat release rate ( $\dot{q}'$ ) fluctuations observed during thermoacoustic instability in a bluff body stabilized combustor exhibit an in-phase relation; thus, satisfying the Rayleigh's criterion.	1
1.2	Schematic of the experimental setups used by (a) Higgins, (b) Sondhauss and (c) Rijke. . . . .	5
1.3	Schematic of the two types of Hopf bifurcations. (a) Supercritical Hopf bifurcation and (b) subcritical Hopf bifurcation. The points H and F correspond to Hopf and fold points, respectively. The direction of the control parameter variation is from left to right for the forward path and vice versa for the reverse path. Arrows corresponding to paths A and B show the triggering amplitude necessary for the transition to oscillatory and steady states, respectively, in the bistable zone. . . . .	19
1.4	Schematic showing the difference between the fixed point and the limit cycle attractor. (a) A stable fixed point which attracts all nearby trajectories towards it. (b) A stable limit cycle attractor that all nearby trajectories from outside and inside the attractor. . . . .	21
2.1	Examples of synchronization of two pendulum clocks. (a) The clocks are hung on distinct beams, exhibiting a desynchronized motion with time. (b) The clocks hung on a common beam exhibit synchronization due to the weak coupling exerted through the beam. . . . .	40
2.2	A schematic to explain adjustment of frequencies during synchronization for the two different modes of coupling between the oscillators which are (a) forced coupling, and (b) mutual coupling. . . . .	42
2.3	The difference between the periodic and chaotic oscillators. (a), (c) The time series and (b), (d) the reconstructed phase portraits of periodic and chaotic oscillations, respectively. The equation for the periodic oscillator is a simple harmonic motion: $x(t) = A\sin(\omega t)$ , and that for the chaotic oscillator is a Rössler oscillator: $\dot{x} = -y - z; \dot{y} = x + ay; \dot{z} = b + z(x - c)$ , where $a = 0.25, b = 0.2, c = 10$ are the constants. . .	44

2.4	(a) A synchronization map or Arnold tongue (i.e., V-shaped plot) showing the forced response of a self-sustained (periodic or chaotic) oscillator for different values of the forcing amplitude ( $A_f$ ) and forcing frequency ( $\omega_f$ ) around the natural frequency of the oscillator ( $\omega_n$ ). The shaded region inside the Arnold tongue represents the phase-locking (forced synchronization) behavior of the oscillator. (b) A frequency response curve of the oscillator showing the variation of the frequency difference ( $\omega_f - \omega_n$ ), calculated across the natural frequency of the oscillations, with the forcing frequency ( $\omega_f$ ) for a constant value of the forcing amplitude. When the forcing frequency approaches the natural frequency, natural frequency gets locked with the forcing frequency. This locking of the two frequencies continues for a finite value of detuning around the natural frequency, as shown by the plateau region around the zero frequency difference before both frequencies get separated out at the boundary of the Arnold tongue. The width of the plateau observed in (b) increases with increase in forcing amplitude. . . . .	48
2.5	(a) A schematic of the Arnold tongue showing different regions of synchronization, i.e., locking, suppression and unlocking regions. A transition from the unlocking to the locking region is shown by path A and a transition to suppression region is shown by path B. The region between the dotted and the continuous lines shows the phase trapping behavior of the forced oscillations. (b) The instantaneous phase difference (or relative phase) between the forcing signal and the forced oscillator signal is shown for four different points (1, 2, 3, and 4) located across the right-hand side synchronization boundary of the Arnold tongue. These points correspond to the phase-locking, phase trapping, intermittent phase locking and phase drifting states of the oscillations, respectively. . . . .	50
2.6	The interpretation of the phase of an oscillator is shown through the schematic of a sinusoidal signal and its representation in the 2-D phase portrait. . . . .	52
2.7	The difference between phase coherent and non-phase coherent attractors is shown for Rössler oscillator: $\dot{x} = -y - z; \dot{y} = x + ay; \dot{z} = 0.2 + z(x - 10)$ , where $a = 0.15$ for the phase coherent and $a = 0.25$ for the non-phase coherent attractor. In (a), the projection of the Rössler attractor in 2-D plane show a smeared limit cycle, where the trajectory revolves around a fixed origin. On the other hand, in (b), the projection of the attractor is filled all over the plane, without showing any distinct center of rotation for the trajectory. . . . .	54
3.1	(a) A schematic of the turbulent flame combustor. Experiments were performed with two different flame holding mechanisms (b) bluff body and (c) fixed-vane swirler. . . . .	60

3.2	(a) Schematic of the spray combustion system used to study the transition of the combustor dynamics from a state of combustion noise to thermoacoustic instability. (b) Schematic of the front and the top view of a needle injector. (c) An image of multiple flamelets anchored at the mesh unit. (d) A photograph of the mesh unit along with a measurement scale. . . . .	63
3.3	(a) Schematic of the bluff body stabilized turbulent gas fired combustion system used to study the effect of density ratio and forcing parameters on the characteristics of a reacting wake. Schematic of (b) the test section (second combustor) and (c) the bluff body. The setup figure is reproduced with permission from Emerson and Lieuwen (2015). . .	66
3.4	(a) A schematic of the horizontal Rijke tube used to study forced synchronization behaviour of limit cycle oscillations in the thermoacoustic system. A photograph of the electrical heater used in the present study is shown in the side figure. . . . .	68
4.1	(a)-(d) The time series of the acoustic pressure ( $p'$ - black color) and the heat release rate ( $\dot{q}'$ - red color) signals obtained from experiments at $\bar{u} = 9.4$ m/s, $\bar{u} = 11.9$ m/s, $\bar{u} = 13.2$ m/s and $\bar{u} = 17.2$ m/s, respectively. The magnified views of the corresponding signals are shown in the insets over each figure. (a) A low amplitude aperiodic state, (b) an intermittency, (c) a weakly periodic limit cycle state, and (d) a strongly periodic limit cycle state of oscillations. (e) The variation of root mean square value of the acoustic pressure ( $p'_{rms}$ ) plotted against the mean velocity of the flow ( $\bar{u}$ varies from 9.4 m/s to 18.1 m/s). . . . .	73
4.2	(a) The variation of the power spectral density (PSD) of both $p'$ (black color) and $\dot{q}'$ (red color) for a range of $\bar{u}$ from 9.4 m/s to 17.2 m/s. (b) The magnified view of the PSD for a velocity range of $\bar{u} = 9.4$ m/s to $\bar{u} = 11.1$ m/s. (c) The variation of the dominant frequency ( $f_{Dominant}$ ) of both $p'$ and $\dot{q}'$ obtained for a range of $\bar{u}$ in the system. The magnified view of PSD shown in (b) is highlighted by a blue color in (c). In (b), the separate unlocked frequency bands of $p'$ and $\dot{q}'$ , obtained during initial value of $\bar{u} = 9.4$ m/s, are shown by green arrows; whereas, the frequency corresponding to the first onset of frequency lock-in is shown by a blue arrow. . . . .	75
4.3	The plots of probability of recurrence ( $P(\tau)$ ) of a phase space trajectory at different values of time lags ( $\tau$ ) for $p'$ (green colour) and $\dot{q}'$ (red colour). (a)-(c) represents the plots of $P(\tau)$ corresponding to three states of synchronization viz., desynchronization (aperiodic oscillations), phase synchronization (periodic oscillations) and generalized synchronization (periodic oscillations) obtained at $\bar{u} = 9.4$ m/s, $\bar{u} = 13.2$ m/s and $\bar{u} = 17.2$ m/s, respectively. The parameters used in plotting are embedding dimension = 12, time delay = 2 ms, recurrence threshold = 25% of the maximum size of the attractor. A data set containing 3000 points (shown for 1200 points). . . . .	78

4.4	(a) Plots of time series of $p'$ (green colour) and $\dot{q}'$ (red colour) acquired during the intermittency state at $\bar{u} = 11.6$ m/s. (b), (c) The plots of $P(\tau)$ shown for periodic and aperiodic regions of both $p'$ and $\dot{q}'$ , respectively. The parameters used in plotting (b) and (c) are embedding dimension = 12, time delay = 2 ms, recurrence threshold = 25% of the maximum size of the attractor. A data set containing 3000 points (shown for 1200 points). . . . .	78
4.5	(a), (b) The temporal variation of the relative phase ( $\Delta\phi_{p',\dot{q}'}$ ) between $p'$ and $\dot{q}'$ calculated using the analytic signal approach based on the Hilbert transform (refer Section 2.5.1 in Chapter 2). (a) The phase synchronization ( $\bar{u} = 13.2$ m/s) and (b) the generalized synchronization ( $\bar{u} = 17.2$ m/s) state of oscillations. (c) The plot depicting the variation of mean value of relative phase ( $\langle\Delta\phi_{p',\dot{q}'}\rangle$ ) with mean velocities of the flow observed during the transition from PS to GS states. . . . .	80
4.6	(a) A portion of the time series of $p'$ (black color) and $\dot{q}'$ (red color) obtained from experiments during the GS state ( $\bar{u} = 17.2$ m/s). (b) A portion of the signal obtained from an assumed functional form for both acoustic pressure ( $p'$ - black color) and heat release rate ( $\dot{q}'$ - red color) oscillations. (c), (d) are the temporal variation of the relative phases obtained from Hilbert transform for the signals shown in (a), (b) respectively. . . . .	82
4.7	(a) The portion of acoustic pressure and (b) heat release rate oscillations depicting the computation procedure for the amplitude difference and the kicking times, respectively. (c), (e) The temporal variation of the amplitude difference (normalized by signal global maxima) between consecutive peaks of the acoustic pressure oscillations obtained for PS and GS states, respectively. (d), (f) The temporal variation of the time difference (normalized by signal period $T = 1/f_{Dominant}$ ) between the consecutive peaks of the heat release rate oscillations, referred to as kicking times, obtained for PS and GS states, respectively. PS state corresponds to $\bar{u} = 13.2$ m/s and GS state corresponds to $\bar{u} = 17.2$ m/s. (g) A variation of the cross-correlation coefficient ( $r$ ) between $p'$ and $\dot{q}'$ with different values of mean velocity of the flow ( $\bar{u}$ ). . . . .	83
5.1	Time series data of the acoustic pressure fluctuations acquired at different locations of flame in the combustor. (a) combustion noise state ( $x_f = 520$ mm), (b)-(o) intermittency state ( $x_f = 540$ mm to $x_f = 670$ mm) and (p) limit cycle state ( $x_f = 680$ mm). These plots show the intermittency route to limit cycle oscillations in a spray combustion system. (q) A magnified portion of intermittency signal obtained at $x_f = 550$ mm shows the low amplitude aperiodic oscillations and the burst of high amplitude periodic oscillations present in the signal. The value of air and fuel flow rates are fixed at $\dot{m}_a = 100$ slpm and $\dot{m}_f = 8$ mlpm, respectively. . . . .	88

5.2	The amplitude spectrum of the acoustic pressure signals acquired during the state of (a) combustion noise ( $x_f = 520$ mm), (b) intermittency ( $x_f = 590$ mm), and (c) limit cycle ( $x_f = 680$ mm) oscillations in the combustor. . . . .	89
5.3	(a)-(e) The time series of acoustic pressure representing the effect of increasing fuel flow rate ( $\dot{m}_f$ ) on the occurrence of intermittency and eventually the onset of thermoacoustic instability when the control parameter, the location of flame in the duct ( $x_f$ ), is varied in the system. The value of air flow rate is fixed at $\dot{m}_a = 120$ slpm during all experiments. . . . .	90
5.4	The variation of (a) a global maximum ( $p'_{max}$ ) and (b) a root mean square ( $p'_{rms}$ ) value of the acoustic pressure signal versus the location of flame ( $x_f$ ) inside the combustor. The plots are divided into three distinct regions of system dynamics as (I) low amplitude aperiodic oscillations, (II) intermittency, and (III) limit cycle oscillations. The value of air and fuel flow rates are fixed at $\dot{m}_a = 100$ slpm and $\dot{m}_f = 8$ mlpm, respectively. . . . .	91
5.5	The effect of increase in the value of fuel flow rate $\dot{m}_f$ from 9 to 14 mlpm for a constant value of $\dot{m}_a = 120$ slpm, on the variation of (a) $p'_{max}$ and (b) $p'_{rms}$ of the acoustic pressure signal for different values of $x_f$ in the system. . . . .	92
5.6	Reconstructed phase portrait of a portion of the pressure time series (0.5 s) obtained during three different dynamical states system dynamics such as (a) combustion noise ( $x_f = 520$ mm, $\tau_{opt} = 3$ , $E = 11$ ), (b) intermittency ( $x_f = 590$ mm, $\tau_{opt} = 10$ , $E = 9$ ), and (c) thermoacoustic instability ( $x_f = 680$ mm $\tau_{opt} = 10$ , $E = 9$ ). . . . .	94
5.7	(a), (b) The acoustic pressure signals measured at $x_f = 520$ mm and that obtained from a random shuffling of its data points, respectively. The recurrence plots corresponding to these signals are shown in (c), (d). The parameters that are fixed, number of data points in a signal $N = 1000$ , optimum delay $\tau_{opt} = 3$ , embedding dimension $E = 10$ , and recurrence threshold $\epsilon = 30\%$ of the mean diameter of the attractor. . . . .	96
5.8	(a)-(c) The acoustic pressure signals obtained at $x_f = 520$ mm (combustion noise), $x_f = 560$ mm (intermittency) and $x_f = 680$ mm (thermoacoustic instability), respectively. (d)-(i) The variations of $\%DET$ and $L_{max}$ for a non-overlapping time window of 1000 data points. The parameters that are fixed, number of data points in a signal $N = 300000$ , optimum delay $\tau_{opt} = 10$ , embedding dimension $E = 10$ , and recurrence threshold $\epsilon = 25\%$ of the mean diameter of the attractor. . . . .	98
5.9	(a), (b) The variation of average values of the percentage of determinism ( $\%DET$ ) and the length of the maximum diagonal structures ( $L_{max}$ ) with the location of flame in the combustor. The parameters fixed during the analysis are $\tau_{opt} = 10$ , $E = 10$ , $\epsilon = 25\%$ of the mean diameter of the attractor. . . . .	99

5.10	The intermittency signal consists of epochs of low amplitude aperiodic oscillations, referred to as turbulent phases, in between consecutive bursts of high amplitude periodic oscillations, referred to as laminar phases. A pressure threshold demarks the high amplitude periodic oscillations from low amplitude aperiodic oscillations. . . . .	100
5.11	(a) The distribution of the length of the turbulent phases obtained at $x_f = 540$ mm shows an exponential tail. (b) A log-log plot of the average value of the length of the turbulent phase ( $\langle L_T \rangle$ ) versus the normalized flame location ( $X_f$ ) shows a scaling law behaviour of type-II intermittency. . . . .	101
5.12	(a) First return a map of the intermittency signal shows a scatter of points along the diagonal line. (b), (c) The time evolution of these points indicates a spiraling behaviour of the trajectory, which confirms the possibility of type-II intermittency in the system dynamics. . . .	102
5.13	(a) A portion of the signal displaying intermittency. (b)-(d) Recurrence plots (RP) obtained from different regions of the intermittency signal. (c) RP shows a kite-like structure of type-II intermittency. Data points ( $N$ ) = 7500, $\tau_{opt} = 3$ , $E = 10$ , $\epsilon = 20\%$ of the mean diameter of the attractor. . . . .	104
5.14	Time series of the simultaneously acquired acoustic pressure and the heat release rate fluctuations during different states of the combustion dynamics as (a) combustion noise ( $x_f = 500$ mm), (b) intermittency ( $x_f = 530$ mm) and (c) thermoacoustic instability ( $x_f = 640$ mm). Insets in the plots show zoomed in view of the signal observed during a particular state of oscillation. . . . .	106
5.15	The cross wavelet transforms of both acoustic pressure and heat release rate fluctuations obtained from a continuous wavelet transform of the complex Morlet wavelet during different states of the combustion dynamics as (a) combustion noise ( $x_f = 500$ mm), (b) intermittency ( $x_f = 530$ mm) and (c) thermoacoustic instability ( $x_f = 640$ mm). . . . .	107
5.16	(a) A portion of the acoustic pressure signal acquired during combustion noise state ( $x_f = 540$ mm), wherein the dynamics of the signal show low amplitude aperiodic oscillations. (b) The simultaneously acquired instantaneous images of the flame corresponding to dotted points marked in (a). . . . .	109
5.17	(a) A portion of the acoustic pressure signal showing the transition from low amplitude aperiodic to high amplitude periodic oscillations of the burst observed during the state of intermittency ( $x_f = 570$ mm). (b) The different regions of the signals are classified as (I) low amplitude aperiodicity, (II) growth in the amplitude of the burst, and (III) constant amplitude oscillations of the burst. (c) The simultaneously acquired instantaneous images of the flame corresponding to dotted points marked in (b). . . . .	111

5.18	(a) A portion of the acoustic pressure signal acquired during the state of thermoacoustic instability ( $x_f = 720$ mm), wherein the system dynamics exhibits self-sustained periodic oscillations. (b) The simultaneously acquired instantaneous images of the flame corresponding to dotted points marked in (a). . . . .	113
6.1	The instantaneous CH* chemiluminescence images of the flame shown for different time instances of the oscillation cycle captured during (a)-(d) unforced ( $A_f = 0$ ) and (e)-(h) forced ( $A_f = 0.02$ ) states. (i), (j) and (k), (l) The time series of the local heat release rate fluctuations acquired from top (shown by red line in a) and bottom (shown by yellow line in a) branches of the flame correspond to $A_f = 0$ and $A_f = 0.02$ , respectively. The parameters that are fixed: $x/D = 3$ , $\rho_u/\rho_b = 2$ , $U_{lip} = 40$ m/s, and $f_n/f_f \approx 1$ . The flow direction is from right to left. . . . .	119
6.2	The reconstructed phase portraits of the local heat release rate fluctuations obtained from the top ( $I_T$ ) and bottom ( $I_B$ ) halves of the flame for the conditions of (a), (b) unforced ( $A_f = 0$ ) and (c), (d) forced at amplitude $A_f = 0.02$ . The parameters chosen for the reconstruction of the phase space are: $\tau_{opt} = 0.6$ ms and $E = 6$ . The conditions that are fixed: $x/D = 3$ , $U_{lip} = 40$ m/s, $f_n/f_f \approx 1$ and $\rho_u/\rho_b = 2$ . . . . .	120
6.3	The recurrence plots of the local heat release rate fluctuations obtained from the top ( $I_T$ ) and bottom ( $I_B$ ) portions of the flame for (a), (b) the absence of forcing and (c), (d) the presence of forcing at $A_f = 0.02$ . The variation of recurrence quantification measures such as (e) %RR and (f) %DET are plotted for different values of the forcing amplitude. The conditions that are fixed: $x/D = 3$ , $U_{lip} = 40$ m/s, $f_n/f_f \approx 1$ , and $\rho_u/\rho_b = 2$ . Recurrence parameters used for plotting are: time delay ( $\tau_{opt}$ ) = 0.6 ms, embedding dimension ( $E$ ) = 6, recurrence threshold ( $\epsilon$ ) = 20% of the maximum size of the attractor and the number of data points equal to 1000. . . . .	121
6.4	The reconstructed phase portraits of the local heat release rate fluctuations obtained from the top and bottom sides of the flame are shown for the conditions of two frequency ratios $f_n/f_f < 1$ and $f_n/f_f > 1$ , and four density ratios (a) $\rho_u/\rho_b = 1.7$ , (b) $\rho_u/\rho_b = 1.9$ , (c) $\rho_u/\rho_b = 2$ , and (d) $\rho_u/\rho_b = 2.4$ . The flow velocity conditions, for $\rho_u/\rho_b = 1.7$ ( $U_{lip} = 35$ m/s and 44 m/s), for $\rho_u/\rho_b = 1.9$ ( $U_{lip} = 35$ m/s and 46 m/s) for $\rho_u/\rho_b = 2$ ( $U_{lip} = 34$ m/s and 46 m/s), and for $\rho_u/\rho_b = 2.4$ ( $U_{lip} = 34$ m/s and 45 m/s), are chosen such that the conditions of frequency ratios are $f_n/f_f < 1$ and $f_n/f_f > 1$ , respectively. The parameters chosen for the reconstruction of the phase space are optimum time delay $\tau = 0.6$ ms and embedding dimension $d = 6$ . The conditions that are fixed: $x/D = 3$ and $A_f = 0.02$ . . . . .	124

6.5	(I) Time-frequency plot obtained from wavelet transform, (II) amplitude spectrum obtained from Fourier transform, and (III) analytic plane representation of the signal. These plots demonstrate the different properties of local heat release rate fluctuations obtained from the bottom half of the flame (I) for different conditions (a) unforced ( $A_f = 0$ ), (b) forced at high amplitude ( $A_f = 0.02$ ), and (c) filtered signal corresponding to the forced state. The conditions that are fixed $x/D = 3$ , $U_{lip} = 35$ m/s, $f_n/f_f < 1$ and $\rho_u/\rho_b = 1.7$ . The forcing frequency ( $f_f$ ) is fixed at 515 Hz. The frequency range chosen for bandpass filtering of the heat release rate signals is $0.5f_f < f_f < 1.5f_f$ . . . . .	125
6.6	The temporal variation of the relative phase of local heat release rate fluctuations obtained from the top and bottom branches of the flame with the external forcing for a low density case. The test conditions correspond to three values of the forcing frequency such that (a), (b) $f_n/f_f < 1$ ( $U_{lip} = 35$ m/s), (c), (d) $f_n/f_f \approx 1$ ( $U_{lip} = 41$ m/s), and (e), (f) $f_n/f_f > 1$ ( $U_{lip} = 46$ m/s). The parameters that are maintained constant are $x/D = 3$ , $\rho_u/\rho_b = 1.9$ and $A_f = 0.02$ . . . . .	127
6.7	The temporal variation of the relative phase of the local heat release rate fluctuations obtained from top and bottom branches of the flame with the external forcing for a high density case. The test conditions correspond to three values of the forcing frequency such that (a), (b) $f_n/f_f < 1$ ( $U_{lip} = 24$ m/s), (c), (d) $f_n/f_f \approx 1$ ( $U_{lip} = 41$ m/s), and (e), (f) $f_n/f_f > 1$ ( $U_{lip} = 44$ m/s). The parameters that are maintained constant are $x/D = 3$ , $\rho_u/\rho_b = 3.2$ and $A_f = 0.02$ . . . . .	129
6.8	(a)-(c) The distribution and the temporal variation (in insets) of the instantaneous phase difference between the signals of heat release rate fluctuations obtained from top and bottom branches of the flame for three different conditions of density ratios as $\rho_u/\rho_b = 1.9, 2.5$ and $3.2$ , respectively. (d) The plot showing the variation of mean relative phase angle between the top and bottom branches of a reacting wake with different values of the density ratio i.e., $\rho_u/\rho_b = 1.9, 2, 2.2, 2.4, 2.5$ and $3.2$ . The parameters that are fixed $U_{lip} = 41$ m/s, $f_n/f_f \approx 1$ , $A_f = 0.02$ , and $x/D = 3$ . During $f_n/f_f \approx 1$ , the flame dynamics is such that both branches of the flame are perfectly phase locked state with each other (see insets of a-c). . . . .	131
6.9	The plots of relative phase between the local heat release rate fluctuations obtained from the top and bottom branches of the flame at three different locations along the flame length as $x/D = 3, 5$ , and $7$ , for two different values of the density ratios (a)-(c) $\rho_u/\rho_b = 1.9$ and (d)-(f) $\rho_u/\rho_b = 3.2$ . The parameters that are fixed $U_{lip} = 41$ m/s, $f_n/f_f \approx 1$ and $A_f = 0.02$ . . . . .	133
6.10	The variation of recurrence quantities $\%RR$ and $\%DET$ for (a), (b) top and (c), (d) bottom sides of the flame with different values of forcing amplitudes obtained at various locations along the flame length. The flame distances are $x/D = 3, 4, 5, 6$ and $7$ , and the forcing amplitude values are $A_f = 0, 0.005, 0.01, 0.015$ , and $0.02$ . The conditions that are fixed $\rho_u/\rho_b = 2$ , $U_{lip} = 40$ m/s, and $f_n/f_f \approx 1$ . . . . .	134

- 7.1 A map of 1:1 forced synchronization of the periodically forced limit cycle oscillations in a horizontal Rijke tube, where the forcing amplitude ( $A_f$ ) is plotted against the forcing frequency ( $f_f$ ). Regions of phase locking, phase trapping and phase drifting are indicated as I, II and III, respectively. The synchronization region indicated by phase locking forms the Arnold tongue. The linear fit is applied to the experimental data points shown at the boundaries between regions I and II (●) and between regions II and III (■). The regime where phase trapping is not observed is indicated with a dashed circle near  $f_n$ . . . . . 138
- 7.2 (a) Variation of the spectral amplitudes of the self-excited mode or natural oscillations ( $A_n/A_0$ , in open circles) and that of the forcing mode ( $A_f/A_0$ , in filled circles) when the forcing frequency is varied across the natural frequency ( $f_n$ ) of the system at a constant value of the forcing amplitude ( $A_f = 5$  mV). A region of frequency locking is highlighted. (b) A frequency response plot shows the variation of normalized frequency difference ( $(f_f - f_n)/f_{n0}$ ) with the normalized forcing frequency ( $f_f/f_{n0}$ ), where  $f_n$  is the frequency corresponding to the natural oscillations in the presence of forcing. (c) Response characteristics of the acoustic pressure signal shown in terms of the variation of root mean square amplitude  $P_{rms}$  with the normalized forcing frequency ( $f_f$ ). . . . . 140
- 7.3 The effect of change in the forcing frequency ( $f_f$ ) on the response dynamics of the acoustic pressure signal when  $f_f < f_n$  and the forcing amplitude ( $A_f$ ) is constant. The forced response of the system dynamics is characterized in terms of first return map (I), time series (inset of I), amplitude spectrum (II), and instantaneous phase difference (inset of II). The forcing frequencies ( $f_f$ ) corresponding to (a)-(d) are 90 Hz (phase drifting), 161.1 Hz (intermittent phase locking), 164.3 Hz (phase trapping), and 164.7 Hz (phase locking), respectively. The frequency corresponding to natural oscillations is indicated by a dotted line in II. The frequency corresponding to external forcing is marked by a dot in I. . . . . 143
- 7.4 The plots showing frequency spectra of the response signal, and temporal variation of the relative phase between the response dynamics and the forcing signal (insets) at different values of  $A_f = 3$  mV (a), 12 mV (b), 18 mV (c), and 24 mV (d), when  $f_f$  is maintained constant at 155 Hz which is sufficiently away from  $f_n$  (168.8 Hz). The dots in the frequency spectra correspond to the location of forcing frequencies ( $f_f$ ). . . . . 145
- 7.5 The plots showing frequency spectra of the response signal, and instantaneous relative phase variation between the response and the forcing signal (insets), obtained for different values of  $A_f$  as (a) 0.4 mV, (b) 0.8 mV, (c) 1.2 mV, and (d) 1.7 mV, when  $f_f$  (168 Hz) is very close to  $f_n$  (168.8 Hz). . . . . 146

7.6	The variation of response amplitude ( $P_{rms}$ ) of the acoustic pressure signals with the variation of $A_f$ for different $f_f$ as (a) 100 Hz, (b) 155 Hz, (c) 175 Hz, and (d) 200 Hz. Suppression of response amplitude is observed for all forcing frequency except when $f_f$ is sufficiently higher than $f_n$ (d). On the right hand side of the vertical dashed line shown in (a)-(d), the instantaneous phases of the response signal are perfectly locked with the forcing signal; thus, it indicate the phase locking region.	147
7.7	Suppression in response amplitude for different forcing frequency. Suppression is normalized with $rms$ value of the unforced amplitude ( $P_0$ ) and $P_{min}$ represents the minimum amplitude ( $P_{max}$ ) obtained forcing the signal with different forcing amplitude and keeping $f_f$ constant.	148
A.1	(a)-(d) The time trace of acoustic pressure ( $p'$ ) and heat release rate ( $\dot{q}'$ ) fluctuations obtained during the different states of combustion dynamics such as combustion noise ( $\bar{u} = 7.8$ m/s), intermittency ( $\bar{u} = 9.6$ m/s), weakly correlated periodic oscillations ( $\bar{u} = 10.4$ m/s), and strongly correlated periodic oscillations ( $\bar{u} = 11.4$ m/s), respectively. . . . .	157
A.2	(a)-(d) The scalograms (I, III) and amplitude spectrums (II, IV) of the acoustic pressure ( $p'$ ) and the heat release rate ( $\dot{q}'$ ) signals corresponding to the states of combustion noise ( $\bar{u} = 7.8$ m/s), intermittency ( $\bar{u} = 9.6$ m/s), weakly correlated periodic oscillations ( $\bar{u} = 10.4$ m/s), and strongly correlated periodic oscillations (thermoacoustic instability) ( $\bar{u} = 11.4$ m/s), respectively. . . . .	159
A.3	(a) The waterfall diagram representing the variation of power spectral density of the acoustic pressure ( $p'$ -red color) and the heat release rate ( $\dot{q}'$ -black color) signals for different values of $\bar{u}$ , while the system dynamics transition from combustion noise to thermoacoustic instability. (b) The variation in the dominant frequencies of both $p'$ and $\dot{q}'$ signals corresponding to the velocity range shown in (a). In (a), the regions A, B, C and D correspond to the frequency bands of the natural acoustic mode of the duct ( $f_a$ ), hydrodynamic mode of the reacting flow ( $f_h$ ), partial lock-in mode ( $f_l$ ), and perfect lock-in or synchronization mode ( $f_s$ ) of the coupled dynamics of acoustic and heat release rate fluctuations, respectively. . . . .	160
A.4	(a)-(d) The cross wavelet transforms of the acoustic pressure ( $p'$ ) and the heat release rate ( $\dot{q}'$ ) signals obtained for different states of the combustor dynamics such as combustion noise ( $\bar{u} = 7.8$ m/s), intermittency ( $\bar{u} = 9$ m/s), weakly correlated periodic oscillations ( $\bar{u} = 10.8$ m/s), and strongly correlated periodic oscillations ( $\bar{u} = 11$ m/s), respectively. . . . .	162
A.5	(a)-(d) The sequence of plots between the acoustic pressure ( $p'$ ) and the heat release rate ( $\dot{q}'$ ) oscillations representing the evolution of the phase space trajectories corresponding to the signals shown in Fig. A.1 for different states of the combustor dynamics. The flow velocities corresponding to (a)-(d) are $\bar{u} = 7.8, 9.6, 10.4,$ and $11.4$ m/s, respectively.	164

- A.6 (a), (b) The recurrence plots of the acoustic pressure ( $p'$ ) and heat release rate ( $\dot{q}'$ ) signals acquired during the weakly correlated and the strongly correlated periodic oscillations at  $\bar{u} = 10.4$  m/s and  $\bar{u} = 11.4$  m/s, respectively. (c), (d) The plots of the probability of recurrence ( $P(\tau)$ ) with respect to delay time ( $\tau$ ) for both  $p'$  and  $\dot{q}'$  signals obtained during the states shown in (a), (b), respectively, representing the states of phase synchronization and generalized synchronization. The parameters being used in plotting the recurrence plots are: embedding dimension = 6, time delay = 2.1 ms, recurrence threshold = 20% of maximum size of the attractor, and data length = 3000 points. . . . . 165
- A.7 (a)-(d) Typical phasor plots depicting the instantaneous phase difference (by arrows) between the acoustic pressure and the local heat release rate fluctuations. A pattern of phasors for a time instant (arbitrarily chosen) is shown for each of the dynamical states such as (a) combustion noise ( $\bar{u} = 8.2$  m/s), (b) intermittency ( $\bar{u} = 8.8$  m/s), (c) weakly correlated periodic oscillations ( $\bar{u} = 10.8$  m/s) and (d) strongly correlated periodic oscillations ( $\bar{u} = 11.4$  m/s), similar to that described previously in Fig. A.1. . . . . 167
- A.8 Time-averaged Kuramoto order parameter ( $R$ ) is plotted against the mean velocity of the flow ( $\bar{u}$ ). Different dynamical states are indicated in the plot as (a) combustion noise ( $\bar{u} = 8.2$  m/s), (b) intermittency ( $\bar{u} = 8.8$  m/s), (c) weakly correlated periodic oscillations ( $\bar{u} = 10.8$  m/s) and (d) strongly correlated periodic oscillations ( $\bar{u} = 11.4$  m/s). For each state we show a typical CH\* intensity field at the time instant for which the phasor field is shown in Fig. A.7. . . . . 168
- A.9 (a)-(e) The instantaneous field of local  $p'(t)\dot{q}'(x, y, t)$  during the states of (I) phase synchronization (PS) and (II) generalized synchronization (GS) along with the corresponding CH\* chemiluminescence images of the flame. The simultaneous time traces of the pressure oscillations and the global heat release rate oscillations are presented in (f) and (g) for the states of PS and GS, respectively. . . . . 170

## ABBREVIATIONS

<b>PS</b>	Phase Synchronization
<b>GS</b>	Generalized Synchronization
<b>IPS</b>	Intermittent Phase Synchronization
<b>XWT</b>	Cross Wavelet Transform
<b>CWT</b>	Continuous Wavelet Transform
<b>RP</b>	Recurrence Plot
<b>RQA</b>	Recurrence Quantification Analysis
<b>DET</b>	Determinism
<b>RR</b>	Recurrence Rate
<b>LPG</b>	Liquefied Petroleum Gas
<b>FTF</b>	Flame Transfer Function
<b>FDF</b>	Flame Describing Function
<b>slpm</b>	Standard Litres Per Minute
<b>mlpm</b>	Milliliters Per Minute
<b>P.V.</b>	Cauchy Principle Value
<b>pdf</b>	Probability Density Function
<b>rms</b>	Root Mean Square
<b>max</b>	Maximum

# NOTATION

## Upper-case Roman

$A$	Instantaneous amplitude
$A$	Forcing amplitude
$A_f$	Forcing amplitude, $mV$
$A_0$	Spectral amplitude of natural frequency in the unforced state
$D$	Inner diameter of burner, $mm$
$E$	Embedding dimension obtained from false nearest neighbor
$F$	Forcing signal
$\mathcal{F}$	Flame describing function
$\mathcal{G}$	Gain
$I$	Local heat release rate signal
$I_B$	Local heat release rate fluctuations corresponding to bottom flame branch
$I_T$	Local heat release rate fluctuations corresponding to top flame branch
$\mathcal{L}$	Linear operator
$L_{max}$	Length of maximum diagonal structure
$L_T$	Length of turbulent phase
$N$	Total number of points in the signal
$N_1$	Total number of reconstructed vectors
$P(\tau)$	Probability of recurrence
$R$	Kuramoto order parameter
$\mathcal{R}$	Rayleigh index
$Re$	Reynolds number
$R_{i,j}$	Recurrence matrix
$T$	Time period of the signal
$T_b$	Temperature of burned products, $K$
$T_u$	Temperature of unburned reactants, $K$
$U_{tip}$	Mean velocity at the bluff body, $m/s$
$W$	Continuous wavelet transform
$W^{xy}$	Cross wavelet transform, XWT, of signals $x$ and $y$
$X$	State vector
$X_f$	Normalized flame location
$X_n$	Vector consists of local maximum in the time series

## Lower-case Roman

$a, b$	Arbitrary constants
$c$	Speed of sound, $m/s$
$f_a$	Frequency of acoustic mode of the combustor, $Hz$
$f_{Dominant}$	Dominant frequency, $Hz$
$f_f$	Forcing frequency, $Hz$

$f_h$	Frequency of hydrodynamic oscillations, $Hz$
$f_l$	Frequency of partial lock-in mode, $Hz$
$f_{n0}$	Natural frequency in absence of forcing, $Hz$
$f_n$	Natural frequency in presence of forcing, $Hz$
$f_s$	Frequency of synchronization mode, $Hz$
$\dot{m}_a$	Mass flow rate of air, $slpm$
$\dot{m}_f$	Mass flow rate of fuel, $slpm$
$p'$	Acoustic pressure, $V$
$\bar{p}$	Mean acoustic pressure
$\dot{q}'$	Heat release rate, $V$
$\bar{q}$	Mean heat release rate
$r$	Pearson's correlation coefficient
$s$	Scale parameter
$t$	Time, $s$
$u$	Translation parameter
$\bar{u}$	Mean velocity of the flow, $m/s$
$u'$	Acoustic velocity
$\vec{x}$	Reconstructed vector using Takens's delay embedding theorem
$x/D$	Location along the flame length from the trailing edge of the bluff body
$x_{f0}$	Critical location of flame in the combustor
$x_f$	Location of flame in the combustor
$x_H$	Hilbert transform of signal $x$
$x, y, z$	Arbitrary signals

## Greek

$\Delta$	Difference
$\epsilon$	Distance threshold of recurrence
$\eta$	Dimensionless time
$\Lambda$	Nonlinear damping
$\mu$	Dynamic viscosity, $Ns/m^2$
$\omega_0$	Dimensionless frequency
$\omega$	Angular frequency, $Hz$
$\Omega$	Frequency detuning, $Hz$
$\phi$	Instantaneous phase
$\varphi$	Equivalence ratio
$\phi_0$	Initial phase
$\Psi_0$	Mother wavelet function
$\rho_u$	Density of unburned reactants, $Kg/m^3$
$\rho_b$	Density of burned products, $Kg/m^3$
$\tau$	Delay time
$\tau_{opt}$	Time delay obtained from average mutual information
$\Theta$	Heaviside step function
$\theta_j$	Instantaneous phase of $j^{th}$ spatial oscillator
$\zeta$	Analytic signal

## Operators

$\ \cdot\ $	Euclidean norm
*	Complex conjugate

# CHAPTER 1

## Introduction

Thermoacoustic instabilities have been a topic of immense research for the combustion community for several decades. Initially, such instabilities were observed in liquid and solid rocket motors in the mid of the twentieth century, and henceforth were reported in other propulsion engines (such as ramjet and afterburner), land-based gas turbine engines, boilers, industrial furnaces etc. (Culick and Kuentzmann, 2006). These are self-sustained, large amplitude periodic oscillations in the acoustic field generated mainly due to the complex interaction between unsteady heat release rate from the flame and natural acoustic modes of the combustor (Zinn and Lieuwen, 2005).

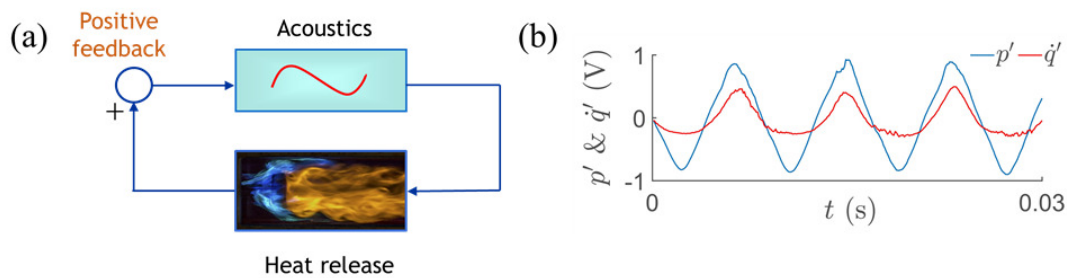


Figure 1.1: (a) A schematic of the positive feedback loop between the acoustic field of the combustor and the unsteady flame dynamics responsible for driving self-sustained thermoacoustic instabilities. (b) The time series of acoustic pressure ( $p'$ ) and heat release rate ( $q'$ ) fluctuations observed during thermoacoustic instability in a bluff body stabilized combustor exhibit an in-phase relation; thus, satisfying the Rayleigh's criterion.

The fluctuations in the acoustic field lead to fluctuations in the heat release rate either by modulating the flame surface area, changing the fuel-air mixing ratio, varying the chemical kinetics or by affecting the underlying hydrodynamic flow field of the combustor (Ducruix *et al.*, 2003). This oscillatory heat release, in turn, adds energy to acoustic field of the system; thus, completing a feedback loop (Fig. 1.1a). According to Lord Rayleigh (Rayleigh, 1878), when the fluctuations in the heat release rate happen in phase with the acoustic pressure oscillations (Fig. 1.1b), a positive feedback is developed between the coupled processes of the combustor. Furthermore, when the net driving of the acoustic oscillations overcomes the overall damping in the system,

the fluctuations in the system dynamics get amplified exponentially and saturates to the high amplitude limit cycle oscillations when the driving matches with the damping in the system (Zinn and Lieuwen, 2005).

The intense growth in pressure amplitude may have serious damage to mechanical components of the combustor such as liners, fuel injectors, turbine blades, etc., due to increased vibrations, or may degrade their performance (Culick and Kuentzmann, 2006). These large amplitude acoustic oscillations can also affect the functioning of electronics and control systems, or lead to performance loss due to oscillations in thrust. The presence of these instabilities has led to the operational failure of a space mission, and immediate shutdown of gas turbine power plants, costing revenue losses amounting to billions of dollars annually. Various control strategies have been developed over the years to either reduce the strength of such instabilities or to forewarn their occurrences. In spite of decades of scientific research, the study of this phenomenon still draws considerable interest due to unresolved complexities and the practical importance associated with it (Sujith *et al.*, 2016). Therefore, an understanding of the transition to such instabilities is critical for implementing measures that would either avoid or mitigate these instabilities.

Traditionally, the transition to thermoacoustic instability was characterized as Hopf bifurcation, wherein the dynamics of a system undergo an abrupt change from a state of combustion noise to thermoacoustic instability (Lieuwen, 2002). Most of the previous studies were, therefore, focused on understanding the behavior of flame-acoustic interactions during these two states of combustion dynamics alone, and less attention was paid to the transition of dynamics from one state to another due to the change in control parameters. Against this backdrop, Nair *et al.* (2014) showed that the transition to thermoacoustic instability from the state of combustion noise happens via intermittency when the equivalence ratio is reduced from a value near stoichiometry to a fuel lean condition.

It is well-known that the onset of thermoacoustic instability is a coupled response of the acoustic field and the unsteady heat release rate fluctuations in the system. Therefore, understanding the spatiotemporal field of the combustor is necessary for revealing the physics behind the occurrence of different dynamical states in the combustor. During the onset of thermoacoustic instability, the periodic formation of large-scale vortices

at the frequency of acoustic oscillations are observed in the reacting flow field of the combustor (Poinsot *et al.*, 1987). Chakravarthy *et al.* (2007) reported that during the onset of thermoacoustic instability, the acoustic mode of the combustor locks-in with the hydrodynamic mode of the flow. Further, Mondal *et al.* (2017b) showed the coexistence of synchronized periodic and desynchronized aperiodic oscillations at the same instant in the reacting flow field during intermittency, which resembles a chimera state.

It is to note that, in these studies, the unburned reactants are non-preheated, whereas, in practical combustors, the reactants entering into the combustor are preheated to higher temperatures. The hydrodynamic stability of the reacting wake in such combustors primarily depends on the temperature ratio (or density ratio) of the unburnt reactants and the burnt products in the combustor. Emerson *et al.* (2012a) experimentally showed that the stability of such wake transitions from a globally stable mode to a globally unstable mode when the density ratio is varied from a high value to a low value, keeping the density ratio  $> 1$ . Therefore, the interaction of acoustic field of the combustor with the reacting flow field is different for different conditions of preheating.

Despite achieving some success in characterizing transitions in thermoacoustic systems (Juniper and Sujith, 2018), most of these studies were focused on analyzing the characteristics of acoustic pressure signal alone. Since the onset of thermoacoustic instability is known to be a coupled response of the acoustic fluctuations and the unsteady heat release rate fluctuations, a simultaneous examination of these subsystems is necessary for providing a clear explanation for the transition to thermoacoustic instability. A recent observation of Nair *et al.* (2014) showed the existence of intermittency, where bursts of periodic oscillations occur in between the epochs of aperiodic oscillations, prior to thermoacoustic instability. The existence of intermittency helped them to provide various preventive measures that can forewarn the impending thermoacoustic instabilities. In spite of intermittency being an important state, none of the studies quantitatively analyzed the relationship between acoustic pressure and heat release rate fluctuations during the transition from combustion noise to thermoacoustic instabilities via intermittency. Furthermore, locking of frequencies of these fluctuations at the onset of thermoacoustic instability naturally motivates us to adopt the framework of synchronization theory. Synchronization theory mainly deals with the phenomenon of adjustment of time and frequency scales of two independently oscillating objects to a common value as a result of coupling between them. Therefore, the adoption of this

framework in thermoacoustics would give more physical insights on the occurrence of different dynamical states in the combustion dynamics, as these states are a result of the interaction between multiple subsystems such as flow, sound, and flame of the combustor. Although these recent studies in gaseous combustion systems advanced the knowledge of the transition to thermoacoustic instability, the presence of such studies in spray combustion systems is a few in number. Since most combustion systems in practice utilize liquid fuels as a source of energy, it is important to understand the phenomenon of onset of thermoacoustic instabilities in such systems.

Furthermore, in practical combustors, since the reactants are preheated, the stability of the reacting flow field (or flame) in a combustor is different for different levels of preheating. In such systems, the interaction of the reacting flow field with the acoustic field of the combustor can alternately be studied through the characterization of the response of the flame to the external acoustic forcing (Emerson and Lieuwen, 2015). Hitherto, the forced response of such reacting flow fields was mostly studied using the measures from linear theory, e.g. coherence, cross-correlation coefficient, Fourier phase, etc. Since the response of reacting field to the external forcing is a nonlinear phenomenon, additional insights can be gained through the use of tools from recurrence analysis and synchronization theory.

Various measures have been discovered either to control, mitigate or forewarn thermoacoustic instabilities in the past. A framework of open-loop control based on a forced synchronization theory provides a simple way to control the properties such as phase, frequency, and amplitude of such instabilities. Although a few of the recent studies have characterized the response of limit cycle oscillations to the external acoustic forcing, a detailed characterization of this technique to reduce the strength of thermoacoustic instabilities is yet to be explored.

## **1.1 Literature Survey**

### **1.1.1 Brief History**

The sound produced by a flame, when it is confined in a duct, has fascinated various researchers over the last three centuries. In 1777, Higgins (Higgins, 1802) reported

the first observation of such sound produced by the flame. He observed that when a hydrogen diffusion flame is placed in an open-ended glass duct, acoustic oscillations are excited by the flame (Fig. 1.2a). He referred to the behaviour of such flames as 'singing flames'. (In recent times, such a phenomenon of the production of sound by the flame is referred to as thermoacoustic instability and corresponding combustion systems are referred to as thermoacoustic systems). He further noticed that the intensity of the sound depends on the size of the fuel supply tube, flow rates of the fuel, size as well as boundary conditions of the resonating tube, and the position of the flame inside the resonator. Subsequently, in 1850, Sondhauss (Sondhauss, 1850) used a tube whose one end is open and another end is closed by a hot glass bulb. In this tube, he noted the production of sound due to the existence of temperature gradient in the tube (Fig. 1.2b). He further proposed a relationship between the frequency of the oscillations and dimensions of the tube.

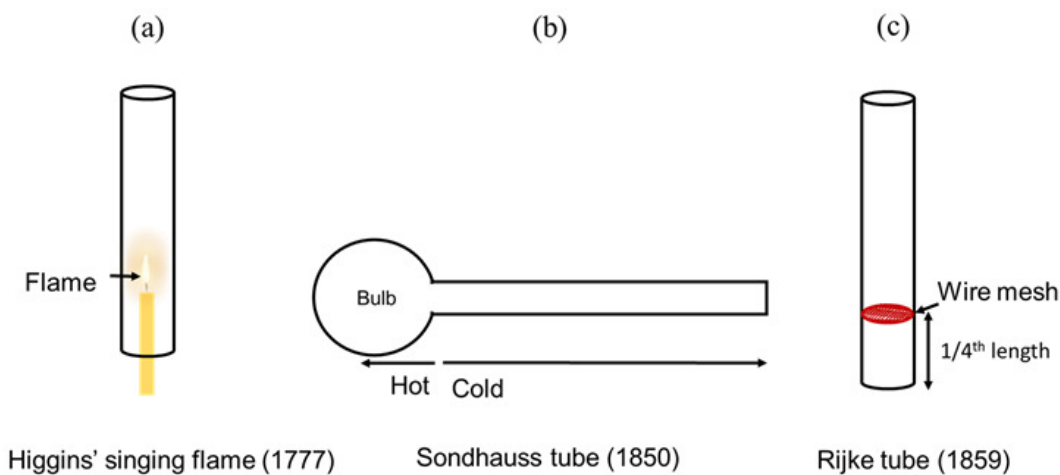


Figure 1.2: Schematic of the experimental setups used by (a) Higgins, (b) Sondhauss and (c) Rijke.

Rijke, in 1859, simplified these experiments (Rijke, 1859). He used a glass tube open at both ends and placed a fine metallic gauze in the lower portion of the tube (Fig. 1.2c). The gauze was heated by an external flame until it becomes red hot and, upon removal of the flame, an audible sound was perceived for a few seconds in the tube. In order to get a continuous production of sound, the gauze was heated by an electrical heating source. He found that when the heater location was at a quarter length of the resonating tube, the strength of the sound was maximum. According to Rijke, a convecting air current set in by the heated gauze in the upward direction is the reason for the driving of acoustic oscillations in the tube. Further, Rayleigh, in 1878, put forth

a general criterion for explaining the sound produced by a heating element in the duct. The Rayleigh's criterion (Rayleigh, 1878) in his own words is stated as follows:

*"If heat be communicated to, and abstracted from, a mass of air vibrating (for example) in a cylinder bounded by a piston, the effect produced will depend upon the phase of the vibration at which the transfer of heat takes place. If heat be given to the air at the moment of greatest condensation, or be taken from it at the moment of greatest rarefaction, the vibration is encouraged. On the other hand, if heat be given at the moment of greatest rarefaction, or abstracted at the moment of greatest condensation, the vibration is discouraged."*

Thus, Rayleigh's criterion provides an explanation for the production and the persistence of sound by the heating source. Until now, this criterion has been considered as a necessary condition for the detection of thermoacoustic instability by various researchers. However, this criterion is insufficient to explain the physical mechanisms that cause the production of sound in a thermoacoustic system. Putnam and Dennis (1956), and Chu (1965) formulated Rayleigh's explanation in a mathematical form, which is given by the following equation:

$$R = \int_0^T p'(t)\dot{q}'(t)dt > \text{acoustic damping} \quad (1.1)$$

where  $R$  is the Rayleigh index,  $p'$  is the acoustic pressure fluctuations at the flame,  $\dot{q}'$  is the heat release rate fluctuations in the flame,  $t$  is the time variables, and  $T$  is the time period of the oscillations. In the above equation, the left hand side refers to the acoustic driving and right hand side refers to the acoustic damping. According to Zinn and Lieuwen (2005), damping in the system could arise from various sources such as the viscous dissipation at the boundary layers, heat loss from the combustor walls, and acoustic energy loss due to convection and radiation through the exhaust of the combustor. In order to satisfy Rayleigh's criterion, a proper phase relation ( $\phi_{p'\dot{q}'}$ ) between  $p'$  and  $\dot{q}'$  should be established, and the phase angle between these processes should satisfy the condition  $0^\circ < \phi_{p'\dot{q}'} < 90^\circ$ . Therefore, when the condition for the Rayleigh's criterion is satisfied, acoustic oscillations in the combustor grow during the initial period of the oscillations and saturate afterwards to constant amplitude limit cycle oscillations when the nonlinear damping in the system balances the acoustic driving.

Although some basic knowledge about the occurrence of thermoacoustic instabilities was attained till the 18<sup>th</sup> century, serious studies on the phenomenon started only in the early 20<sup>th</sup> century during the development of high-performance propulsive engines and power generating units. The occurrence of thermoacoustic instability was reported for the first time in liquid rocket motors in early 1940's and then subsequently observed in solid rocket motors (Culick and Kuentzmann, 2006). Thermoacoustic instability then received a widespread attention in 1960's during the development of F1 engine used for the Apollo Lunar mission (Oefelein and Yang, 1993; Fisher and Rahman, 2009). In liquid rocket motors, the interaction of the oscillatory chamber pressure with the fuel and oxidizer manifolds lead to an oscillatory mixture fraction that, in turn, resulted in the occurrence of oscillatory heat release rate in the system. The coupling of this fluctuating heat release rate with the acoustic field of the combustor leads to the onset of thermoacoustic instability. The problem of thermoacoustic instability in such systems was avoided by incorporating axial baffles on the face of the fuel injectors. In the case of solid rocket motors, the unsteady burn rate of the propellant causes unsteady mass addition in the chamber (Blomshield, 2007). The unsteadiness in the burning rate could arise due to the fluctuations in pressure or temperature in the chamber, causing corresponding fluctuations in the local burning rate of the propellant due to the increased mass flux. This further increases the pressure oscillations. Thus, a feedback cycle between pressure and burning rate continues, leading to an intense growth in the mean pressure as well as the acoustic pressure oscillations in the system.

Later on, these instabilities became a serious concern for the development of afterburners or thrust augmenters of the aircraft engines in the 1980's (Culick and Kuentzmann, 2006). In such devices, high-frequency oscillations, known as screech, were noticed due to the interaction of vortex shedding mechanism with the acoustic field in the combustor Rogers and Marble (1956). In these systems, thermoacoustic instabilities were suppressed by installing passive devices, for example, acoustic liners on the combustor walls. Similar instabilities were also noticed in liquid-fueled ramjet engines (Hegde *et al.*, 1987). The thermoacoustic instabilities in gas turbine engines received attention in recent years due to the implementation of stringent NOx emission regulations on the operation of these engines (Correa, 1993). Burning of fuel in rich or near stoichiometric condition results in high flame temperatures in the combustor. At such high-temperature conditions, the emission of NOx gases from the exhaust nozzle

is high, resulting in increased air pollution and in some cases, even acid rain and depletion of the ozone layer Correa (1993). In order to reduce the flame temperatures, one of the solutions is to operate combustors under lean premixed conditions Correa (1993). However, as the flames become more susceptible to the perturbations of acoustic oscillations at fuel lean conditions, low-frequency thermoacoustic instabilities can easily occur in such systems. In order to attenuate these oscillations, active control strategies were invented, as the passive control techniques are inefficient in controlling low-frequency oscillations (Culick and Kuentzmann, 2006).

Until now, various mechanisms have been identified over the years of research that play a major role in driving thermoacoustic instabilities. However, these mechanisms were found mostly to be system specific. Since the occurrence of thermoacoustic instability is a result of interactions between multiple subsystems such as acoustics, combustion and the hydrodynamic field existing in the combustor, the investigation of the role of these individual subsystems in driving such instabilities is important. In the next section, a brief review of a few dominant mechanisms that have been identified to contribute in the generation of thermoacoustic instability, in particular to gas turbine combustors, is discussed.

## **1.2 Mechanisms Leading to Thermoacoustic Instability**

### **1.2.1 Formation of Large-Scale Coherent Structures**

The dynamics of the underlying hydrodynamic flow field controls the structure of the flame in many combustion systems (Renard *et al.*, 2000). In the case of laminar combustors, as the flow velocities are very low and the hydrodynamic field is stable, the structure of the flame exhibits a definite shape. Conversely, for turbulent combustors, as the flow velocities are high and the hydrodynamic field exhibits irregular rotational motions, the flame shape is more wrinkled and distorted without exhibiting any definite pattern. In such combustors, flame holding mechanisms such as bluff-body, swirler, dump plane, etc. are used to stabilize the flame in the high-speed flow environment. Flames are stabilized in the recirculation zones of such devices (Schadow *et al.*, 1992). For instance, when a high Reynolds number flow is established over a bluff body, two shear

layers (consisting of high-speed, cold reactants on one side and low-speed, hot combustion products on the other side) are formed outside the recirculation zone (Schadow and Gutmark, 1992). These shear layers are hydrodynamically unstable, causing the formation of large-scale vortical structures in the system. The shed vortices from the bluff body are then convected downstream with the mean flow. These convecting vortices interact with their neighboring vortices or impinge on obstacles such as bluff-body or combustor walls in their path. This, in turn, causes breaking of these vortices into fine-scale structures, resulting in a sudden heat release due to the enhanced turbulence mixing in the combustor (Schadow and Gutmark, 1992). The presence of vortices also warps the flame surface area, resulting in fluctuating heat release rate in the system (Renard *et al.*, 2000). The modulated heat release rate adds energy to the acoustic field, which may, in turn, excite the hydrodynamically unstable shear layers to shed another vortex. This shed vortex again affects the heat release rate, and thus, a feedback loop is developed. When the instantaneous phases of these coupled processes demonstrate an in-phase relation, the pressure oscillations in the system may attain a high amplitude, self-sustained oscillatory state known as thermoacoustic instability.

During the stable operation of the combustor, vortex shedding is observed to be incoherent, causing low-frequency aperiodic oscillations of the flame surface. On the contrary, during the onset of thermoacoustic instability (or unstable operation), a periodic emergence of large-scale vortical structures at the acoustic frequency is observed in the system. Various studies have characterized the importance of large-scale structures in the generation of thermoacoustic instabilities (Rogers and Marble, 1956; Smith and Zukoski, 1985; Sterling and Zukoski, 1987; Poinso *et al.*, 1987; Schadow and Gutmark, 1992; Ken *et al.*, 1991a; Najm and Ghoniem, 1994; Ghoniem *et al.*, 2005; Altay *et al.*, 2009; Sampath and Chakravarthy, 2016; Unni and Sujith, 2017). In the process of formation of vortices in the combustor, the instability of the shear layer plays an important role. Schadow and Gutmark (1992) showed the existence of three types of instability frequencies in the shear layer formed at the dump plane, i.e., initial vortex shedding frequency, vortex merging frequency, and preferred mode frequency. When the acoustic mode frequency matches with the preferred mode frequency, the emergence of large-scale coherent structures is observed in the combustor. Chakravarthy *et al.* (2007) reported that during the onset of thermoacoustic instability, the frequency corresponding to the natural acoustic mode of the combustor shifts to the unsteady hy-

drodynamic mode of the reacting flow.

Nair *et al.* (2014) showed the existence of intermittency prior to thermoacoustic instability in turbulent combustors. During intermittency, the system dynamics fluctuates alternately between epochs of bursts of periodic oscillations and epochs of aperiodic oscillations. Unni and Sujith (2017) characterized the flame behaviour at the dump plane observed during intermittency using Mie scattering images of the flow. They observed that during the periodic segments of intermittency, ring vortices are periodically shed from the dump plane and convected downstream along the outer shear layer. This causes periodic fluctuations in the flame surface area, and when the shed vortex impinges on the obstacles (the bluff body and the sidewalls), it correspondingly leads to the periodic heat release in the system. On the other hand, during aperiodic epochs of the oscillations, this periodic shedding of vortices ceases, and the tip of the flame exhibits oscillations in an aperiodic manner. The theoretical models of Matveev and Culick (2003), and Seshadri *et al.* (2016) showed that the acoustic feedback generated due to the instantaneous release of heat at the bluff body affects the time instant at which vortices shed from the dump plane. The variation in the vortex shedding time is a responsible factor for the occurrence of different dynamical states such as stable operation, intermittency and thermoacoustic instability in the combustor.

Furthermore, Erickson and Soteriou (2011), and Emerson *et al.* (2012a) studied the effect of preheating of unburnt reactants on the dynamics of reacting wake in the combustor. They experimentally showed that depending on the value of the density ratio across the flame, the dynamics of the reacting wake transitions from a convectively unstable (for high-density ratio = 3.2) to globally unstable (for low-density ratio = 1.7) mode. The dynamics of the convectively unstable flows are aperiodic; whereas, because the globally unstable flows are inherently self-sustained, they exhibit nearly periodic oscillations in their dynamics. Furthermore, the transition from globally unstable mode to convectively unstable mode may not be sudden but can happen gradually through the occurrence of intermittency, where dynamics of both the modes observed to occur alternately (Suresha *et al.*, 2016). Therefore, the response of the flame to the density stratified hydrodynamic flow field is completely different for different conditions of preheating, causing the difference in the nature of the interaction of such heat release rate fluctuations with the acoustic field in the combustor.

## 1.2.2 Equivalence Ratio Fluctuations

Another factor that has been found to play a major role in the initiation of thermoacoustic instability is the equivalence ratio fluctuations (Lieuwen *et al.*, 1998). The value of the equivalence ratio is directly dependent on the flow rates of the fuel and air reacting in the combustor. The fluctuations in these quantities can directly give rise to fluctuations in the equivalence ratio, which may happen in two different ways: (i) the improper mixing of the fuel and air flow rates due to the space and time constraints of the practical combustors, and (ii) the fluctuations in the injection mass flow rates of the unchoked fuel and air manifolds, resulting from the interaction of the fluctuating chamber pressure with the injection pressure of these manifolds. The fluctuations in equivalence ratio lead to fluctuations in both the reaction rate and the flame speed that, in turn, fluctuates the heat release rate (Lieuwen *et al.*, 1998). When this oscillatory heat release rate happens to be in-phase with the acoustic fluctuations in the combustor, the onset of thermoacoustic instability can occur.

Lieuwen *et al.* (1998) performed a detailed investigation of the role of equivalence ratio fluctuations on the generation of thermoacoustic instabilities in a lean premixed combustor. By using a time lag model developed by (Crocco and Cheng, 1956), they showed that the fuel time lag induced by the location of the injector inside the combustor is a critical parameter in driving thermoacoustic instabilities. If the pressure fluctuations at the fuel injector are in-phase with that at the flame location, depending on the boundary condition, the velocity fluctuations at the fuel inlet will lead or lag the pressure fluctuations by 90 degrees. For low Mach number flows, the fluctuations in the acoustic velocity could be assumed to be in-phase with the fluctuating mass flow rates. Further, the convection of the reaction mixture from the inlet, and their burning at the flame location involves a finite amount of delay. If this delay is such that the heat release rate fluctuations happen in-phase with the acoustic pressure fluctuations, thermoacoustic instabilities can be established in the combustor.

Thermoacoustic instabilities in spray combustors are generally classified as injection-coupled instabilities, where the pressure oscillations in the combustor affect the injection pressure difference across the spray nozzle, thereby, modulating the fuel flow rate entering the combustor (Bazarov and Yang, 1998). The modulation of fuel flow rate can

fluctuate the equivalence ratio of combustion that, in turn, modulates the heat release rate in the system (Young, 1995). Henceforth, various studies have characterized the response of the flame to the equivalence ratio fluctuations in different systems (Peracchio and Proscia, 1998; Lee *et al.*, 2000; Cho and Lieuwen, 2005; Shreekrishna *et al.*, 2010; Hermeth *et al.*, 2013).

### 1.2.3 Unsteady Spray Dynamics

Spray combustors are susceptible to thermoacoustic instability because of the inherent unsteady processes involved in the combustion of such two-phase mixtures. The possible sources contributing to unsteadiness in the spray combustion are the methods of fuel injection, atomization and evaporation of droplets, mixing of fuel vapors with air, and finally, the burning of this mixture in the hot environment of the combustor (Culick and Yang, 1995). Factors affecting the onset of thermoacoustic instability can be understood by simplifying the studies of spray-acoustic interaction. For instance, most of the studies in spray-acoustic interaction have been performed on single droplets. The presence of acoustic oscillations is simulated by imposing the external perturbations on the liquid droplets (Sujith *et al.*, 2000). The presence of acoustic field modifies the spray characteristics such as droplet diameter, velocity, evaporation and burning rates. Further, the response of droplets to the acoustic field depends highly on their spatial location inside the spray (Chishty, 2005).

The experimental studies (Kumagai and Isoda, 1955; Tanabe *et al.*, 2000; Saito *et al.*, 1996; Okai *et al.*, 2000; Dattarajan *et al.*, 2006) on the effect of acoustic oscillations on a single pendant drop showed that the increase in amplitude of acoustic forcing increases the rate of evaporation and burning of the droplet. Furthermore, for a moving droplet, the application of axial acoustic perturbations reduces its terminal velocity (Sujith *et al.*, 1997, 2000). The modeling studies by Duvvur *et al.* (1996) and Lei and Turan (2009) revealed that the vaporization of droplet acts as a main driving force in the generation of thermoacoustic instabilities. Whereas, the study by Anderson *et al.* (1998) indicated that the mean size of the droplets, the spatial distribution of droplets of variable sizes in the combustor and periodicity in atomization of the spray also have important effects on the onset of thermoacoustic instability. Besides, the position of spray in the combustor affects the intensity of acoustic oscillations generated in

the system (Carvalho *et al.*, 1989; Dubey *et al.*, 1998). The presence of high amplitude acoustic oscillations reduces the length of the spray either by decreasing the droplets size (through increased evaporation rate) or by increasing the mean drag on the droplets (Sujith, 2005).

#### **1.2.4 Other Mechanisms**

In addition to the mechanisms mentioned above, there are several other factors that have been identified to contribute to the occurrence of thermoacoustic instabilities. Some of them are briefly summarized in this section. The geometry of the combustor, size of the fuel and air supply manifolds, acoustic boundary conditions of the inlet and exhaust sections, and shape of the flame holder can have an influence on the occurrence of a thermoacoustic instability in the system (Candel, 2002). Interaction of flame surfaces with the combustor walls (Durox *et al.*, 2002), fluctuations of velocity at the flame stabilization point Gutmark *et al.* (1989), and unsteady stretch and strain rates of the flame (Sun and Law, 2000) can also affect the unsteady heat release in the system. Unsteady combustion sometimes generates 'hot spots' or 'entropy waves' in the combustor. The movements of such entropy waves with the convecting flows in the downstream direction can generate acoustic waves in the combustor (Lieuwen, 2003a; Morgans and Duran, 2016).

### **1.3 Classical Linear Stability Analysis**

Traditionally, the stability analysis of thermoacoustic systems has been performed using a linear theory. During the onset of thermoacoustic instability, the amplitude of pressure oscillations grows from a steady state to a state of large amplitude periodic oscillations. In such a situation, the initial region of growth in the amplitude of the oscillations was considered linear where the effects of nonlinearity are assumed to be negligible. In the linear stability analysis, the governing equations of a system, obtained in the form of ordinary differential equations, are linearized around a steady state. In thermoacoustics, the governing equations are mostly partial differential equations, which are converted into ordinary differential equations using suitable methods such as modal expansion (McManus *et al.*, 1993) or spatial discretization (Schmid and Henningson, 2001).

The linearized ordinary differential equations are represented in the form  $dX/dt = \mathcal{L}X$ . Here,  $X$  is a vector of state variables, for example, acoustic pressure, acoustic velocity, temperature, etc.  $\mathcal{L}$  is a linear operator, which is a function of system parameters. The eigenvalues of this operator, which are mostly complex, determine the stability of the system. Here, the real part of an eigenvalue indicates the growth rate and the imaginary part indicates the frequency of the oscillations. Therefore, if the real parts of all eigenvalues of  $\mathcal{L}$  are negative, then the system is considered to be a linearly stable. On the other hand, if the real part of at least one of the eigenvalues is positive, the system becomes linearly unstable and the oscillations in the system grow from a steady state value. Thus, the linear stability analysis can be used to detect unstable frequency modes of the combustor and also to define the linear stability margin for the system components.

In one of the approaches of linear stability analysis to thermoacoustic systems, Crocco and Cheng (1956) proposed a linear relation between the acoustic velocity and the heat release rate fluctuations in the system, which is also known as  $n - \tau$  model (where  $n$  is the coupling strength and  $\tau$  is the delay) for the flame. In this relation, heat release rate fluctuations are expressed in terms of acoustic velocity fluctuations observed at the flame location delayed by time  $\tau$ . In mathematical terms, it is written as  $\dot{q}' \propto u'(x_f, t - \tau)$ . This relation highlights the importance of time delay in the generation of thermoacoustic instabilities in a combustor. This model has been widely used in the industry as well as academia to predict the instability frequencies and growth rates of thermoacoustic systems (McManus *et al.*, 1993; Bloxsidge *et al.*, 1988; Macquisten, 1995; Dowling, 1997).

Furthermore, the linear stability of the combustor can be determined through the forced response of the flame, where the flame is forced by the external velocity perturbations during a stable operation of the combustor. Here, the response of the flame to the acoustic perturbations is estimated through a flame transfer function (FTF) at a given condition of the forcing frequency ( $\omega$ ). FTF measures the linear response of the heat release rate fluctuations ( $\dot{q}'$ ) to the external velocity perturbations ( $u'$ ) at different values of forcing frequencies. FTF is a complex quantity and can be calculated using the following equation

$$FTF(\omega) = \frac{\dot{q}'(\omega)/\bar{q}}{u'(\omega)/\bar{u}} \quad (1.2)$$

where  $\bar{q}$  is the mean heat release rate fluctuations and  $\bar{u}$  is the mean velocity of the flow. With the help of this approach, the interaction between the flame dynamics and the acoustic field can be understood to some extent. The response of this interaction is incorporated in the linear acoustic models of the system. Methods from control theory are then used to detect the stability of the system using such low order models. The system is linearly unstable for the frequencies corresponding to positive growth rates.

Numerous studies have been conducted to evaluate the FTF from theoretical models (Bloxsidge *et al.*, 1988; Fleifil *et al.*, 1996; Boyer and Quinard, 1990; Schuller *et al.*, 2002; Candel, 2002; Lieuwen, 2005a) and also from experiments with a simple configuration of laminar flames (Baillot *et al.*, 1992; Ducruix *et al.*, 2000; Durox *et al.*, 2005) to more complex turbulent flame combustors (Külsheimer and Büchner, 2002; Balachandran *et al.*, 2005).

Sometimes, in a linearly stable regime of operation, the decaying eigenmode mode of the system can exhibit a transient growth in the resultant amplitude of the oscillations before displaying a monotonic decay with time. Such behaviour of linear systems is referred to as non-normality (Balasubramanian and Sujith, 2008a). In mathematical terms, for non-normal systems, the linear operator  $\mathcal{L}$  does not commute with its adjoint,  $\mathcal{L}^\dagger$  i.e.,  $\mathcal{L}\mathcal{L}^\dagger \neq \mathcal{L}^\dagger\mathcal{L}$  (Schmid and Henningson, 2001). The eigenvectors of the non-normal system are non-orthogonal to each other. If the transient growth in amplitude achieved by the non-normal system is such that the nonlinearity in the system overtakes the linear part of the oscillations, the dynamics of the system can be triggered to another stable state (for example, limit cycle). Balasubramanian and Sujith (2008b) discovered the non-normal nature of the thermoacoustic system in a model of electrically heated horizontal Rijke tube. Subsequently, several other theoretical studies showed the existence of non-normality in different models of thermoacoustic systems such as a ducted diffusion flame (Balasubramanian and Sujith, 2008a), kicked oscillator model of vortex shedding (Tulsyan *et al.*, 2009), ducted premixed flame (Subramanian, 2011), solid rocket motors (Mariappan and Sujith, 2010), Rijke tube (Mangesius and Polifke, 2011; Selimefendigil *et al.*, 2011), ducted flame with choked nozzle (Wieczorek *et al.*, 2011). Furthermore, Juniper (2011) and, Waugh *et al.* (2011) investigated the role of non-normality in inducing triggering in thermoacoustic systems. Kulkarni *et al.* (2011) showed that active controllers designed on classical linear stability analysis can fail in the case of the non-normal system.

Most of the research in last 50 years was concentrated on applying tools based on linear stability analysis to thermoacoustic systems. Although some success has been gained in predicting the unstable frequency of the system using a classical linear theory, the use of this analysis cannot predict the occurrence of asymptotic ( $n \rightarrow \infty$ ) nonlinear states (such as limit cycle, period-2, quasiperiodicity, intermittency or chaos) of thermoacoustic systems. Furthermore, the models based on this theory cannot predict the amplitude of limit cycle oscillations, which is a major concern of the field engineers. Therefore, the investigation of sources of nonlinearities in thermoacoustic systems and methods to characterize nonlinear behaviour of thermoacoustic systems need to be studied further. A brief summary of such studies is provided in Sections 4 and 5.

## 1.4 Origin of Nonlinearities in Thermoacoustics

Thermoacoustic systems are nonlinear. The nonlinear behavior of such systems is evident from the existence of limit cycle oscillations during the onset of thermoacoustic instability in the system (Culick, 1994). When driving in the system overcomes damping, oscillations in the system grow almost exponentially and saturate at constant amplitude periodic oscillations when nonlinearities in the system dominate, resulting in the balance of acoustic driving and damping processes in the combustor. Therefore, understanding the nonlinear nature of the system behaviour is important in order to predict the amplitude of limit cycle oscillations.

In thermoacoustic systems, the sources of nonlinearities can arise from different processes of the combustor. Further, the origin of the nonlinearity was found to be specific to the type of the thermoacoustic system. In solid and liquid rocket motors, as the order of magnitude of acoustic fluctuations is almost similar to the magnitude of mean pressure in the system (i.e.,  $p'/\bar{p} \sim 20 - 50\%$ ), the source of nonlinearity was primarily considered to arise from acoustic field in the combustor. Culick (1970) modelled the presence of such nonlinearity in the acoustic field in the form of nonlinear gas dynamic equations, and observed a nonlinear growth and saturation of acoustic pressure oscillations in the system. On the other hand, in premixed gas turbine combustors, the magnitude of acoustic pressure oscillations is much smaller than the mean pressure in

the system (i.e.,  $p'/\bar{p} \sim 1 - 5\%$ ) and the mean velocity of the flow is much smaller than the speed of sound (Dowling, 1997; Lieuwen, 2002). Therefore, in such systems, the nonlinear effects originating from the acoustic field (or gas dynamics) are significantly low and these effects are considered to be linear in the models. The modeling study by Sterling (1993) suggested that nonlinearities in the combustor mainly arise from combustion processes. Furthermore, Dowling (1997) showed that the nonlinearities in the combustion system are dominated by the coupled interaction between the acoustic field and the unsteady flame dynamics.

Other studies, wherein the effect of external acoustic forcing is used to characterize the response of the flame dynamics, have shown that for a low value of the perturbation amplitude, the heat release rate fluctuations are linear and the interaction becomes nonlinear only when the forcing amplitude becomes high (Bellows *et al.*, 2006). The nonlinear effects of such heat release rate fluctuations become significant when the magnitude of acoustic velocity fluctuations is of the order of mean velocity of the flow (i.e.,  $u' \sim \bar{u}$ ). Balachandran *et al.* (2005) experimentally showed that this velocity ratio ( $u'/\bar{u}$ ) is around 15% for the nonlinearities in the heat release rate to dominate. Several other sources of nonlinearities such as flow-flame interaction (Dowling, 1997; Poinso and Candel, 1988; Emerson and Lieuwen, 2015), equivalence ratio fluctuations (Peracchio and Proscia, 1998; Shreekrishna *et al.*, 2010), flame front kinematics (Baillot *et al.*, 1992; Lieuwen, 2003a), burning rate (McIntosh, 1999), flame speed and stretch rate (Kelley and Law, 2009) have been found in the past. The existence of nonlinearities in the system leads to different kinds of unexpected behaviours of the system dynamics. Some typical examples of such behaviours are discussed in the following Section.

### 1.4.1 Subcritical Transition and Triggering

The transition of a thermoacoustic system from a linearly stable to a linearly unstable state happens via bifurcation (Strogatz, 1994). When the system dynamics change from a steady state to an oscillatory state, the bifurcation associated this transition is referred to as Hopf bifurcation (Lieuwen, 2002). This kind of bifurcation is mainly classified into two types: supercritical Hopf and subcritical Hopf (Strogatz, 1994). The existence of these types of Hopf bifurcations for different choices of the control parameters was reported in thermoacoustic systems studied by Lieuwen (2002), Nair *et al.* (2014), and

Etikyala and Sujith (2017).

In the case of supercritical bifurcation, the transition from one stable state to another stable state happens at Hopf point, wherein a low amplitude oscillatory state emerges from the steady state (see Fig. 1.3a). The amplitude of this oscillatory state continuously increases with an increase in the control parameter, beyond the Hopf point. As the control parameter is changed in the reverse direction, the system behaviour retraces this path without exhibiting any hysteresis in the parameter space. On the other hand, in a subcritical Hopf bifurcation, the system dynamics exhibit a sudden change from a steady state to large amplitude oscillatory state at the Hopf point, during the variation of control parameter in the forward direction (see Fig. 1.3b). As the control parameter is changed in the reverse direction, the system behaviour retraces the path until a fold point for transitioning to the steady state (Fig. 1.3b). Thus, a subcritical bifurcation is associated with a hysteresis (bistable) zone, wherein two stable states, i.e., steady state and oscillatory state coexist in the same parameter space (shown by shaded region in Fig. 1.3b). The transition of the system behaviour to either of these states completely depends on the value of the initial condition. If the value of the initial perturbation amplitude is greater than that required to cross the unstable branch (shown by arrow A in Fig. 1.3b) existing in the bistable region, the system dynamics can directly reach the oscillatory (stable limit cycle) state even though the system is already at the steady state. The phenomenon of such a direct transition of the system dynamics from a non-oscillatory state to an oscillatory state for a finite amplitude of perturbations is called triggering.

The investigation of triggering phenomenon in thermoacoustic systems was started in the late 60s. During initial investigations, Crocco (1969) studied the occurrence of this phenomenon in solid and liquid rocket motors. In such systems, a pulse of acoustic wave is created through the explosion of a bomb and the response of the system to this pulse is measured (Blomshield *et al.*, 1997). If the amplitude of the pulse is greater than a threshold, instability will be triggered in the system. If the amplitude of the pulse is smaller than the threshold required to trigger the instability, the system will regain its steady state after the removal of the effect of the pulse in the system. Such studies have also been conducted in gas turbine engines Wicker *et al.* (1996); Lieuwen (2002). Detailed theoretical as well as experimental investigations on triggering phenomenon have been conducted on a Rijke tube for the variation of different parameters such as

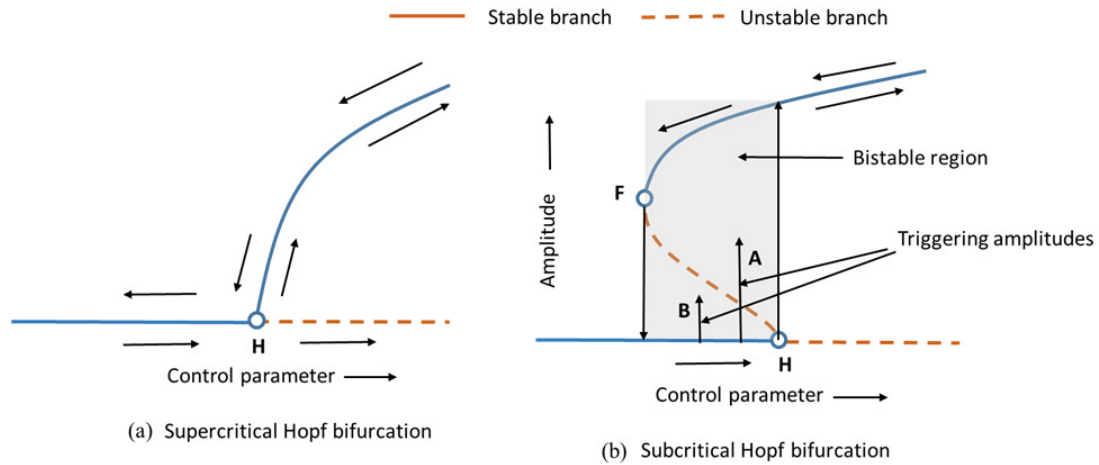


Figure 1.3: Schematic of the two types of Hopf bifurcations. (a) Supercritical Hopf bifurcation and (b) subcritical Hopf bifurcation. The points H and F correspond to Hopf and fold points, respectively. The direction of the control parameter variation is from left to right for the forward path and vice versa for the reverse path. Arrows corresponding to paths A and B show the triggering amplitude necessary for the transition to oscillatory and steady states, respectively, in the bistable zone.

heater power and mass flow rate of air (Matveev and Culick, 2003; Balasubramanian and Sujith, 2008b; Mariappan and Sujith, 2011; Juniper, 2011; Waugh *et al.*, 2011; Subramanian *et al.*, 2013; Gopalakrishnan and Sujith, 2014; Li *et al.*, 2018). The presence of background noise can also lead to the triggering of thermoacoustic instabilities (Lieuwen and Banaszuk, 2005). Waugh *et al.* (2011) investigated the effect of different types of noise such as pink, white and blue noise on the triggering behaviour of the Rijke tube. On the other hand, Gopalakrishnan and Sujith (2015); Gopalakrishnan *et al.* (2016b) studied the effect of noise intensity on the hysteresis characteristic of the Rijke tube for different mass flow rates, and found a decrease the region of hysteresis with the increase of noise intensity in the system. Jegadeesan and Sujith (2013) examined the possibility of the triggering behaviour for a ducted non-premixed flame combustor.

## 1.4.2 Nonlinear Describing Function

In modern gas turbine engines, the prediction of the nonlinear behaviour of the system dynamics is important during early development stages of the combustor. Linear flame transfer functions are not capable of predicting the amplitude of limit cycle oscillations as well as other nonlinear effects such as triggering and mode switching behaviours observed in the practical combustion systems. Subsequently, a practical approach called

flame describing function is widely used to detect nonlinearities of the forced flame response in thermoacoustic systems (Dowling, 1997; Stow and Dowling, 2004; Noiray *et al.*, 2008). The origin of this transfer function is from nonlinear control theory (Van-der Velde, 1968). Using this technique, the response of the flame is measured in terms of a transfer function for different conditions of the forcing amplitude ( $u'$ ) and the forcing frequency ( $\omega$ ), which can be written in the following form,

$$\mathcal{F}(\omega, |u'|) = \frac{\dot{q}'(\omega)/\bar{q}}{u'(\omega)/\bar{u}} = G(\omega, |u'|)e^{i\phi(\omega, |u'|)} \quad (1.3)$$

where  $\mathcal{F}$  is the flame transfer function measured in the frequency domain,  $G$  is the gain and  $\phi$  is the phase of the flame response.  $\dot{q}'(\omega)/\bar{q}$  is the normalized heat release rate fluctuations in the flame and  $u'(\omega)/\bar{u}$  is the normalized velocity perturbations imposed on the flame. In this analysis, the assumption of quasi-linearity is made, wherein it is assumed that the flame responds only to the forcing frequency and the response of the flame at higher harmonics is discarded. This implies that the acoustic field is harmonic in time, which might not be the case in practical systems where non-harmonic responses such as quasiperiodicity and chaos are observed in the self-excited state.

The use of flame describing function is able to predict both linear (i.e., growth rate and frequency) as well as nonlinear (i.e., amplitude and frequency of limit cycle, triggering, frequency shifting) effects of the flame response. This approach was initially applied to thermoacoustics by Dowling (1997) in her theoretical work. Subsequently, Noiray *et al.* (2008) performed detailed analysis in terms of both experiments and theory to predict properties of thermoacoustic instability with a fairly good accuracy. Afterward, the several studies have been performed to investigate the flame describing function for different types of systems ranging from lab scale model to more practical systems (Han *et al.* (2015) and references therein).

Thus, the studies on linear and nonlinear stability analysis of thermoacoustic systems have shown the importance of nonlinearity in driving and maintaining thermoacoustic instabilities in such systems. Most of the recent studies are focused on using the methods from dynamical systems theory and complex systems theory to reveal the various hidden nonlinear features exhibited by thermoacoustic systems. A brief summary of such studies is presented in the following Section 5.

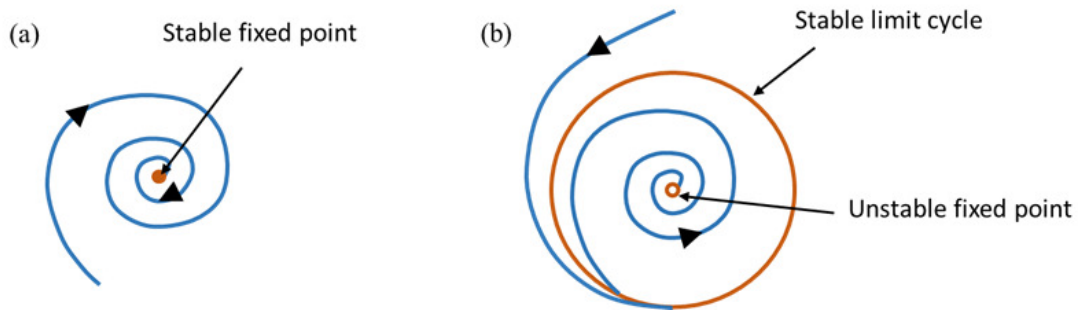


Figure 1.4: Schematic showing the difference between the fixed point and the limit cycle attractor. (a) A stable fixed point which attracts all nearby trajectories towards it. (b) A stable limit cycle attractor that all nearby trajectories from outside and inside the attractor.

## 1.5 Nonlinear Dynamics of Thermoacoustic Systems

The time evolution of the system dynamics can be effectively represented through the use of tools from dynamical systems theory. In order to accurately predict the state of the system, the number of independent variables that directly play a role in deciding the dynamical state of the system needs to be known. The temporal evolution of such dynamical variables of a system can be represented in the form  $\dot{X} = \Phi(X)$ , where  $X$  is a vector of state variables,  $\Phi$  is a function that relates state variables and dot represents the time derivative. A path traced by the points obtained from the solution of this equation is called trajectory. The evolution of this trajectory in the higher dimension space (equal to or greater than 2) is represented in a plot known as phase portrait (Hilborn, 2000). The trajectories of such phase portraits get attracted or repelled from a particular basin of attraction (Fig. 1.4), whose stability is decided by the eigenvalues obtained from the solution of the dynamical equations of the system. The presence of an attractor limits the motion of the trajectory in a finite dimensional phase space. The name of a few attractors that are common in the dynamical systems literature are fixed point, limit cycle (or period- $k$  attractor), quasiperiodic (torus attractor), and chaos (strange attractor). Various methods such as phase space reconstruction, recurrence plots and Poincaré section (return maps), and the measures based on these methods such as Lyapunov exponents, correlation dimension, entropy and recurrence quantification analysis have been used successfully in various field of science and technology to detect the hidden complexities of the one-dimensional time series obtained from the system (Kantz and Schreiber, 2004; Hilborn, 2000; Nayfeh and Balachandran, 2008).

Although the approach of dynamical systems theory to thermoacoustics applied first in the 1960's, it received more attention and a good success only in the last decade. In this section, the recent advances in the use of tools from dynamical systems theory in revealing various features of combustion dynamics are discussed for two types of thermoacoustic systems, i.e., laminar and turbulent combustors. In laminar combustors, the flow velocities are very small so that the flame surfaces exhibit a definite geometry such as V-flame, M-flame, conical flames, etc. In contrast, turbulent combustors consist of high mean flow velocities that cause the flame surfaces to have more wrinkles and distortions; for instance, bluff-body and swirl stabilized flames. As explained earlier, nonlinearities play a significant role in the genesis of thermoacoustic instabilities (Culick, 1976; Lieuwen, 2003a). The nonlinear behaviour of a thermoacoustic system is evident from the occurrence of limit cycle oscillations (Culick, 1994). Using dynamical systems theory, the diverse dynamical behaviours exhibited by thermoacoustic systems was brought to light (Sterling, 1993; Jahnke and Culick, 1994; Datta *et al.*, 2009; Gotoda *et al.*, 2011; Kabiraj and Sujith, 2012; Kabiraj *et al.*, 2012a; Nair *et al.*, 2014). In the parlance of dynamical systems theory, the transition of combustion systems from stable to unstable operation is the result of a bifurcation (Lieuwen, 2002; Ananthkrishnan *et al.*, 2005; Subramanian *et al.*, 2010).

### **1.5.1 Laminar Thermoacoustic Systems**

In laminar combustion systems, the transition to thermoacoustic instability is observed to happen mainly through Hopf bifurcation, wherein the system dynamics change from a steady state to limit cycle oscillations (Subramanian *et al.*, 2010). With the further change in the control parameter, such systems are found to undergo secondary bifurcations leading to the existence of different types of nonlinear behaviours such as quasiperiodicity (simultaneous existence of two incommensurate frequencies) or chaos (simultaneous existence of multiple frequencies) in their combustion dynamics. Jahnke and Culick (1994) were the first to observe the bifurcation of limit cycle oscillations to a quasiperiodic state through the birth of a torus in the model of a solid rocket motor. The period doubling route to chaos was observed by Sterling (1993), Lei and Turan (2009), Datta *et al.* (2009), and Subramanian *et al.* (2010) in their modeling studies, by incorporating different models for combustion.

Kabiraj & co-workers 2012*c*; 2012*b*; 2012*a*; 2012 performed a detailed experimental study of a thermoacoustic system consisting of a ducted laminar flame combustor and characterized the acoustic response of the combustor against the variation of the location of the flame inside the duct. They witnessed the presence of different dynamical states such as period- $k$ , quasiperiodic, frequency locked, intermittency, and chaotic oscillations, in addition to limit cycle oscillations in the system dynamics. They also reported experimental observation of different routes to chaos such as the Ruelle-Takens route and the frequency locking quasi-periodic route in their system. Furthermore, Kashinath *et al.* (2014) reported the possibility of period-1, period-2, quasi-periodic and chaotic oscillations, and also the existence of the period-doubling route and the Ruelle-Takens-Newhouse route in their numerical simulation of a premixed flame system, for different choices of control parameters. Vishnu *et al.* (2015) characterized the change in the behaviour of V-flame during the transition of system dynamics from a stable state to chaotic oscillations through the occurrence of frequency-locked, quasiperiodicity, and period-3 oscillations in their experiments.

## 1.5.2 Turbulent Thermoacoustic Systems

Unlike laminar combustors, turbulent combustion systems exhibit different dynamical behaviors in the system dynamics. In most practical turbulent combustion systems, the periodic formation of large-scale vortical structures is observed in the reacting field of the combustor during the onset of thermoacoustic instability (Keller *et al.*, 1982; Poinso *et al.*, 1987). The breakdown of these coherent structures results in the fine scale mixing of cold unburnt reactants with the hot reacting products, leading to an instantaneous release of heat in the system (Schadow and Gutmark, 1992). This unsteady heat release rate adds energy to the acoustic field, which in turn, affects the vortex formation process and thus establishes a feedback loop. Such a coupled interaction between the duct acoustics and the hydrodynamic field of the reacting mixture has been studied by various researchers in the past in experimental (Poinso *et al.*, 1987; Keller *et al.*, 1982; Smith and Zukoski, 1985; Ken *et al.*, 1991*a*; Altay *et al.*, 2009) and numerical (Menon and Jou, 1991; You *et al.*, 2005; Schmitt *et al.*, 2007; Gicquel *et al.*, 2012) studies; however, the focus of these studies was mostly on the states of the stable and the unstable operation of the combustor.

Traditionally, the passage to thermoacoustic instability in turbulent flow combustors have been reported to occur through Hopf bifurcation, wherein the system dynamics transition from a stable to an unstable operation due to change in the control parameter (Lieuwen, 2002). Here, the stable operation, which is manifested as low amplitude aperiodic oscillations, is referred to as combustion noise. The unstable operation, characterized by high amplitude periodic (limit cycle) oscillations, is known as thermoacoustic instability (Lieuwen, 2002). Recently, Gotoda *et al.* (2011) reported that the transition to thermoacoustic instability happens from stochastic fluctuations through a state of low-dimensional chaotic oscillations, when the equivalence ratio is increased. Nair *et al.* (2014), however, observed the presence of a state called intermittency prior to the onset of limit cycle oscillations in their system. Intermittency is a dynamical state consisting of an apparently irregular appearances of bursts of large amplitude periodic oscillations amongst the regions of aperiodic oscillations<sup>1</sup>. Thenceforth, numerous experimental studies (Gotoda *et al.*, 2014; Murugesan and Sujith, 2015; Domen *et al.*, 2015; Sampath and Chakravarthy, 2016; Wilhite *et al.*, 2016; Unni *et al.*, 2016; Kheirkhah *et al.*, 2017; Unni and Sujith, 2017; Murugesan and Sujith, 2018; Ebi *et al.*, 2017) and numerical studies (Nair and Sujith, 2015; Seshadri *et al.*, 2016; Seshadri and Sujith, 2016) have reported the presence of such intermittent oscillations prior to the onset of limit cycle oscillations in a variety of combustion systems.

The presence of intermittency is common in a variety of physical systems such as turbulent flows, Rayleigh-Bénard convection, plasmas, lasers, electronic circuits, etc. Intermittency, in dynamical systems theory, is described as an irregular alternation of the system behaviour from periodic to chaotic oscillations (Hilborn, 2000). Traditionally, there are three basic types of intermittency (i.e. type-I, type-II and type-III) which can cause the transition of system behaviour from periodic to chaotic state (Pomeau and Manneville, 1980). In addition to these, various other types of intermittencies such as on-off, type-V, type-X, eyelet, crisis-induced, etc. exist in the literature of dynamical systems theory (Elaskar and Del Río, 2017). The type of intermittency is based on the specific kind of bifurcation a system has to undergo while transitioning from one type of dynamics to another through intermittency. Type-I intermittency is associated with saddle-node bifurcation, type-II intermittency with subcritical-Hopf bifurcation, and

---

<sup>1</sup>Kabiraj and Sujith (2012) were the first to discover intermittency in a ducted laminar flame combustor. They reported the presence of high amplitude bursts of chaotic oscillations amidst regions of low amplitude periodic oscillations prior to a flame blowout.

type-III intermittency with period-doubling bifurcation. In a saddle-node bifurcation, two fixed points (i.e., one is stable and another is unstable) are created at a particular value of the control parameter. With the change in the control parameter, these fixed points move closer to each other and merge at a critical value, after which they vanish due to the further increase in the control parameter. Thus, the system does not exhibit any fixed point after the bifurcation. Such creation and disappearance of fixed points due to the variation of the control parameter are associated with a saddle-node bifurcation. During Hopf bifurcation, the behaviour of the system transitions from a steady state to a periodic state (self-sustained limit cycle) at the bifurcation point. The emergence of stable or unstable periodic orbit from the focus (or node) decides whether the bifurcation type is supercritical Hopf or subcritical Hopf, respectively. In a period-doubling bifurcation, a periodic behaviour of the system changes to a new stable state whose period is twice the period of the original dynamics. A further change in the control parameter causes the period-two behaviour to bifurcate to a period-four state, i.e., the period of the new dynamical state is four times higher than that of the original state. This behaviour of doubling the period of the dynamical system after every bifurcation is also referred to as a period-doubling cascade.

Characterization of the type of intermittency is based on a few statistical methods such as i) probability distribution of the duration between two consecutive bursts, and statistical variation of the mean of this duration with control parameter, ii) first return map and iii) recurrence plot analysis (Pomeau and Manneville, 1980; Schuster and Just, 2006; Klimaszewska and Żebrowski, 2009). Establishing the type of intermittency from experiments is necessary for improving the understanding of the phenomena and also validating the models that predict the onset of thermoacoustic instability. In thermoacoustics, Kabiraj and Sujith (2012) observed type-II intermittency in the gaseous laminar premixed combustor, whereas Nair *et al.* (2013) mentioned the existence of type-II or type-III intermittency in the gaseous flame bluff body stabilized turbulent combustor. Furthermore, Unni and Sujith (2017) compared the intermittent oscillations observed in this combustor prior to thermoacoustic instability and flame blowout, and confirmed the presence of type-II intermittency in both the cases.

According to Nair *et al.* (2014), “*The intermittent oscillations can arise if the acoustic subsystem is modulated by the hydrodynamics over slower time scales (turbulent velocity fluctuations typically have increased energy content at lower frequencies), es-*

*entially shifting the dynamics of the acoustic subsystem back and forth across the Hopf point. These back-and-forth fluctuations thus transition the dynamics from a chaotic turbulent state towards a periodic state and back, forming a homoclinic orbit in phase space.”* Thus, the presence of turbulence plays an important role in the existence of intermittency in the system dynamics; otherwise, if the effects of turbulence are discounted from the modeling, one would observe a sudden transition of the system behavior from a fixed point to a limit cycle through a Hopf bifurcation. Nair and Sujith (2015) have proposed a simple phenomenological model that captures the occurrence of intermittency prior to the onset of thermoacoustic instability, for a bluff body stabilized combustor. In order to do this, they modified a kicked oscillator model developed by Matveev and Culick (2003) for a dump combustor. In order to do so, they added a stochastic noise term to the equation of the mean convection velocity of the vortex to mimic the effects of turbulence on the convection of the vortex. In contrast, Seshadri *et al.* (2016) used a deterministic approach to capture different dynamical states such as chaos, intermittency, and limit cycle oscillations in a bluff body combustor. They showed that the impingement of vortex on a bluff body generates instantaneous heat release that, in turn, produces acoustic waves in the system. A feedback of these acoustic waves affects the time of impingement of the vortices with the bluff body, which plays a key role in the occurrence of these states in the system dynamics. Furthermore, Unni and Sujith (2017) characterized physics of intermittency, in terms of difference in the flame dynamics, observed prior to the both onset of thermoacoustic instability and the flame blowout.

### **1.5.3 Complexities in Combustion Dynamics of Thermoacoustic Systems**

Thermoacoustic systems are complex systems. Complexities mainly arise through the nonlinear interaction of various components of the system such as chemical kinetics, molecular mixing, the range of turbulent scales and their interaction with the acoustic field of the confinement. The presence of various dynamical states and the interaction of various coupled subsystems leading to the onset of periodic oscillations (order) from the aperiodic oscillations (disorder) reflect the complex nature of thermoacoustic systems. Therefore, understanding the dynamical properties of a base state (or combustion noise)

of the system dynamics from where the emergence of order takes place is important either to predict the onset of thermoacoustic instabilities accurately or to improve the models that capture the transitions in the system behaviour.

The dynamics of stable operation of the combustor were traditionally considered as a fixed point (Lieuwen, 2002). These fluctuations observed during this state were considered to be a result of the signal modulated by the underlying stochastic processes (Lieuwen, 2002). During modeling, such oscillations are usually averaged out or ignored, and the linear stability analysis of the system dynamics was performed through the averaged equations (Lieuwen, 2001, 2003*b*; Noiray and Schuermans, 2013). In such situations, the system dynamics were modeled as an acoustic phenomenon by excluding the effect of hydrodynamics (Candel *et al.*, 2009). However, in practical turbulent combustors, the dynamics observed during stable operation are irregular fluctuations resulting from the broadband frequencies in the signal (Chakravarthy *et al.*, 2007). Therefore, this ‘signal plus noise’ paradigm of the traditional analysis is insufficient in accurately detecting the boundaries of the stable operation of the combustor (Zinn and Lieuwen, 2005).

Nair *et al.* (2013) investigated the dynamical features of the acoustic pressure fluctuations acquired during stable operation (combustion noise) using various tests such as Kaplan-Glass test for determinism (Kaplan and Glass, 1992) and 0-1 test for chaos (Gottwald and Melbourne, 2004). They suggested the possibility of the existence of high dimensional chaos in the dynamics of combustion noise. The onset of thermoacoustic instability corresponds to the emergence of periodic oscillations with a single frequency from the background of broadband fluctuations. Thus, the loss of chaos happens during the onset of order in the thermoacoustic systems. Furthermore, Tony *et al.* (2015) used a surrogate analysis (Theiler *et al.*, 1992) along with different measures such as translation error, permutation entropy, and permutation spectrum to confirm the deterministic behaviour of the acoustic pressure signal. They showed that combustion noise consists of high dimensional chaos contaminated with white and colored noise using the measures of correlation dimension and correlation entropy. Further, Nair *et al.* (2013) suggested describing the combustion noise as ‘combustion chaos’, as the properties of the signal acquired during this state show characteristics of a deterministic chaos.

Nair and Sujith (2014) performed multifractal detrended fluctuation analysis to characterize the dynamics of combustion noise. They showed that the acoustic pressure signal observed during combustion noise has characteristics of multifractality, wherein the magnified view of the signal possesses the features of the entire signal. They suggested that the multifractal nature of combustion noise could arise due to the existence of multiple scales in the combustion dynamics of this state. The multifractal spectrum observed during this state is broad and shows different values of Hurst exponents. They further showed that the onset of thermoacoustic instability is a loss of multifractal nature of combustion dynamics. Unni and Sujith (2015) used the framework of multifractal analysis to study the features of the acoustic pressure and the heat release rate signals obtained for both the state of combustion noise observed prior to thermoacoustic instability and the state observed prior to a lean flame blowout. They observed a shift in the position of the multifractal spectrum during the transition from combustion noise to flame blowout via thermoacoustic instability. Gotoda *et al.* (2012) showed that the acoustic pressure signal obtained prior to the lean blowout of the flame displays multifractal characteristics.

Murugesan and Sujith (2015) used a complex network approach (Newman, 2010) to study the scale invariance property of combustion noise. In their analysis, they constructed complex networks at different operating conditions from the time series of acoustic pressure fluctuations using a visibility algorithm (Lacasa *et al.* 2008). They showed that the degree distribution of the acoustic pressure signal shows a power-law behavior, which is a property of scale-free network. Thus, combustion noise is scale-free, and the transition to thermoacoustic instability happens through the emergence of a regular network. They suggested that hubs in the complex network of combustion noise correspond to the large-scale vortices present in the turbulent flow field, whereas, nodes with a lower degree in such networks correspond to the short-lived eddies. Hence, the cascade of different scale vortices in the reacting field of the combustor leads to the scale-free behaviour of combustion noise. In a similar manner, Godavarthi *et al.* (2017) constructed complex networks using a recurrence based algorithm called as a  $\epsilon$ -recurrence network (Marwan *et al.*, 2009). They studied the transition of a thermoacoustic system from the state of combustion noise to thermoacoustic instability and, finally to blowout. They suggested that the recurrence networks constructed from the pressure time series preserves the structure of the attractor corresponding to a given dy-

namical state. Gotoda *et al.* (2017) showed the presence of small-world networks in the combustion dynamics observed prior to flame blowout using a method of  $\epsilon$ -recurrence network.

#### **1.5.4 Studying Thermoacoustic Systems Using Synchronization Theory**

It is well known that the generation of thermoacoustic instability is a coupled response of the acoustic oscillations and the heat release fluctuations present in the combustor (Rayleigh, 1878). The observation of locking of these processes at the onset of limit cycle oscillations and unlocking of their dynamics during the state of combustion noise naturally motivated some of the researchers to examine thermoacoustic instability using tools from synchronization theory.

Synchronization is an emergent phenomenon that occurs in a broad range of dynamical systems, including neural signals, beating of the heart and flashing of fire-flies. The history dates back to the 17<sup>th</sup> century when Christiaan Huygens first observed synchronization of two pendulum clocks suspended from a common wooden beam (Huygens, 1665). He described the phenomena as ‘sympathy of two clocks’. Later, in the 19<sup>th</sup> century, Lord Rayleigh (Rayleigh, 1945) described the phenomenon of synchronization between two similar but distinct organ-pipes which began to sound in unison while kept side by side. Further, synchronization in a large population of oscillating systems was also observed, e.g., synchronous clapping in a large audience. It is important to note that synchronization is essentially a nonlinear phenomenon and occurs only in the self-sustained oscillations.

Synchronization, in simple terms, is the matching of the rhythm of oscillating objects upon coupling. In the seventeenth century, Huygens discovered this universal phenomenon when he observed the locking of beats of two pendulum clocks hung on a common beam (Huygens 1665; Pikovsky *et al.* 2003). In the ensuing years, this phenomenon has been observed in a variety of disciplines of science and technology (Pikovsky *et al.*, 2003). For the synchronization of oscillators, the strength of the mutual interaction between oscillators is a crucial parameter that determines their arrival at a common frequency or at a constant phase difference. Synchronization among os-

cillators is usually examined by investigating the locking of phase (or frequency) of their signals (Pikovsky *et al.*, 2003). A system of coupled oscillators that are initially desynchronized can become synchronized by means of varying the coupling strength (Boccaletti *et al.*, 2002b), through periodic forcing, or feedback (Wang *et al.*, 2001).

In the case of complex fluid systems, there are instances where the features of synchronization have been observed (Zdravkovich, 1982; Gunnoo *et al.*, 2016). The synchronized shedding of large-scale coherent structures with the vibrating bodies is a well-known phenomenon in the studies involving flow-induced vibrations (Green, 1995). When the fluid flows over a bluff body, a street of the vortex is generated in its wake region, commonly known as von Karman vortex street. The shedding of a vortex induces vibration in the bluff body, which, in turn, affects the shedding process. When the frequency of vortex shedding is close to the frequency of natural oscillations of the bluff body, the frequency of vortex shedding locks in with that of the bluff body. Such lock-in results in the synchronized generation of vortex streets in the wake region of the bluff body. The lock-in mechanism alters the vortex shedding pattern (Zdravkovich, 1982), increases the spanwise correlation in the wake, and shifts the vortex shedding frequency to the frequency of vibrating body (Griffin and Ramberg, 1974; Blevins, 1985; Williamson and Roshko, 1988; Griffin and Hall, 1991). Thus, in the region of lock-in, the interaction between the flow and the vibrating body controls the shedding pattern of the large-scale structures.

Similarly, in the case of a thermoacoustic system with an underlying turbulent flow field, a presence of synchronized behaviour between the acoustic field in the duct and the turbulent reactive flow fluctuations has been observed at the onset of thermoacoustic instability. In this state, a vortex sheds in the combustor after every acoustic cycle (Crump *et al.*, 1986; Poinso *et al.*, 1987; Ken *et al.*, 1991a). Chakravarthy *et al.* (2007) referred to such interaction between the vortex shedding (hydrodynamic) and the acoustic field during the onset of limit cycle oscillations as a phenomenon of vortex-acoustic lock on. During this process, they reported the shifting of the frequency of the acoustic oscillations in the duct to the frequency of vortex shedding in the system.

Recently, synchronization theory is used to study the coupled instantaneous interactions of the acoustic field and the heat release rate oscillations in the temporal (Chiocchini *et al.*, 2017; Mondal *et al.*, 2017a) and also in the spatiotemporal (Mondal *et al.*,

2017b; Kheirkhah *et al.*, 2017) domain of thermoacoustic systems. Using this approach for a bluff-body stabilized combustor, Mondal *et al.* (2017b) performed spatiotemporal analysis of the synchronization transition in the turbulent reactive flow field for the intermittency route to thermoacoustic instability. They characterized the instantaneous phase difference between the local heat release rate fluctuations of the reaction zone and acoustic pressure fluctuations measured inside the combustor. Their study reports an emergence of order from a disordered state in turbulent reactive flow through the occurrence of chimera-like structures where the regions of synchronized and desynchronized behavior coexist simultaneously. Furthermore, Mondal *et al.* (2017a) characterized the coupled interaction of acoustic pressure and heat release rate fluctuation during the quasiperiodicity route to chaos observed in a ducted multiple laminar flame burner. Using synchronization framework, they characterized different states of synchronization observed during this route. They showed that, although the dominant frequencies of acoustic pressure and heat release rate fluctuations are locked during the limit cycle, quasiperiodic and chaotic states, the instantaneous phase difference between these signals can show rich behaviour such as phase-locking, phase trapping, intermittent phase locking and phase drifting during these states. Chiocchini *et al.* (2017) used chaotic synchronization theory to predict the onset of thermoacoustic instability in an industrial swirl burner.

Bellows *et al.* (2008), on the other hand, have investigated the lock-in mechanism of a thermoacoustic system by studying its response to an external periodic forcing. In this case, when the frequency of external forcing is sufficiently close to the natural frequency of the system, or when the amplitude of the forcing is high enough, the system dynamics locks-in to the external forcing (Bellows *et al.*, 2008; Thumuluru and Lieuwen, 2009). Balusamy *et al.* (2015) studied the nonlinear dynamics of a self-excited thermoacoustic system subjected to acoustic forcing using the framework of forced synchronization. They observed the phenomenon of pushing or pulling of the natural frequency towards the forcing frequency, depending on whether the forcing frequency is lesser or greater than the natural frequency, respectively, in the system. They also observed the existence of quasiperiodic oscillations prior to the lock-in of forcing and natural frequencies. The presence of different states of forced synchronization such as phase-drifting, phase-trapping, and phase-locking are also reported.

## 1.6 Control and Early Warning of Thermoacoustic Instabilities

The presence of thermoacoustic instability is undesirable for the life of the system components as well as for the safe operation of the combustor. Researchers have attempted to understand the intricacies involved in the interactions of components of the combustor, and have subsequently exploited the acquired knowledge to devise techniques that either mitigate the strength of such oscillations (Putnam, 1971; Schadow and Gutmark, 1992; McManus *et al.*, 1993) or forewarn their onset (Lieuwen, 2005*b*; Gotoda *et al.*, 2014; Nair and Sujith, 2014).

### 1.6.1 Passive Controls

The control of thermoacoustic instabilities mostly falls into two categories, i.e., passive control and active control. In the earliest stages of development of the combustor, the methodologies to mitigate thermoacoustic instabilities involved with the design of passive controls (Putnam, 1971; Schadow and Gutmark, 1992). The main objectives of the technique are to alter or shift the instability frequency to a non-resonant frequency of the combustor by incorporating geometrical changes in the design of the combustor (Richards and Janus, 1997; Steele *et al.*, 1999; Noiray *et al.*, 2007). This will, in turn, change the phase relation between acoustic field and heat release rate fluctuations, and thus, dampen the acoustic oscillations in the system. Another objective of this technique is to increase the damping in the system by fixing static devices such as baffles, liners, and resonators (Bellucci *et al.*, 2001; Gysling *et al.*, 2000; Eldredge and Dowling, 2003). The fixing of dampers will remove the energy from excited acoustic fluctuations in the combustor and thus lessen the strength of thermoacoustic oscillations. Although the advantage of being simple in nature, the disadvantages of this technique are: (i) more expensive in terms of both cost and time, and (ii) effective only for a few targeted frequencies and mostly used to control high-frequency oscillations (Dowling and Morgans, 2005).

Recently, a novel approach based on the phenomenon of amplitude death of two coupled oscillators has been applied to thermoacoustic systems by Thomas *et al.* (2018).

Their theoretical analysis showed the possibility of quenching of self-sustained limit cycle oscillations developed in two independent thermoacoustic systems through the use of time delay and dissipative couplings between them. They suggested that, in practical situations, such couplings between two combustors can be achieved by incorporating a hollow tube between them. Then the coupling strength between the combustors can be controlled by varying the diameter or the length of this connecting tube. Such behaviour of quenching of oscillations is based on the phenomenon of amplitude death. In 1945, Rayleigh was the first to report the observation of amplitude death between two coupled sounding organ pipes (Rayleigh, 1945). When the organ pipes are sufficiently far apart, they oscillate at their natural frequencies but when these pipes are kept beside each other, the oscillations in both the pipes dies down. Biwa *et al.* (2015) showed the experimental evidence of amplitude death in two coupled thermoacoustic engines. Meanwhile, the experimental evidence of this phenomenon is still unreported in the practical thermoacoustic systems.

## 1.6.2 Active Controls

Active control strategies are a more sophisticated way of controlling thermoacoustic instabilities (McManus *et al.*, 1993). In this technique, the response of the combustor (i.e., pressure oscillations or radical emissions from the flame) is measured using a sensor. After modifying the signal properties (such as filtering or phase shifting), corresponding changes are made in the inlet flow condition through the use of feedback controller or actuator (Candel, 2002; McManus *et al.*, 1993; Dowling and Morgans, 2005). The strategy of feedback can also be referred to as closed-loop control. In one approach, fuel flow rates are altered (Paschereit *et al.*, 1999; Neumeier and Zinn, 1996; Sattinger *et al.*, 1998) so that heat release rate fluctuations in the system are changed, resulting in the dampening of acoustic oscillations in the combustor due to the loss of in-phase relation between them. The use of external velocity perturbations can result in the control of vortex shedding from the shear layer or can help in disrupting the large-scale structures in the combustor (Gutmark *et al.*, 1989; Schadow *et al.*, 1992). In another situation, a secondary injection of fuel is used to alter the heat release rate fluctuations (Langhorne *et al.*, 1990; Yu *et al.*, 1996). Sometimes, an ‘anti-sound’ is generated through the use of loudspeaker that can aid in canceling the acoustic pressure oscillations inside the

combustor (Williams, 1984; Lang *et al.*, 1987; Heckl, 1988; Li *et al.*, 2013).

### 1.6.3 Precursors

In both of these control strategies, the main focus was to control the thermoacoustic instabilities only after they have developed in the system. However, recently an alternate approach has been used wherein the control measures (or precursors) are developed to forewarn the occurrence thermoacoustic instabilities. Various tools based on the linear or nonlinear time series analysis or complex system theory have been developed for the online monitoring of the operation of a combustor. As these early warning measures are purely based on capturing the changes in dynamics of the combustor rather than measuring the changes in the amplitude of the pressure signal, they exhibit a significant change much prior to the onset of thermoacoustic instability in the system. Lieuwen (2005*b*) characterized damping in the system in terms of the autocorrelation function of the acquired pressure signal with the change in the control parameter and suggested the onset of thermoacoustic instability at the point wherein the damping rate becomes zero. Nair and co-workers 2013; 2014; 2014 developed several precursors from the characterization of dynamical properties of the acoustic pressure signal. They used different tools from dynamical systems theory such as the 0-1 test and the recurrence quantification analysis, and a measure based on the fractal nature of the signal called Hurst exponent to forewarn thermoacoustic instabilities. They showed that the values of these measures exhibit a gradual decrease from a high value to a low value with increase in Reynolds number as the system approaches thermoacoustic instability. In these analyses, the presence of intermittency is the major reason for the smooth variation of these parameters. In another approach, Unni *et al.* (2016) used a method of symbolic time series analysis to detect impending thermoacoustic instabilities. Based on the property of critical slowing down or tipping of the system dynamics prior to the approach of bifurcation point, Gopalakrishnan *et al.* (2016*a*) showed that the indicators such as variance and conditional heteroscedasticity can provide the early warning to the critical transitions (such as thermoacoustic instability) of thermoacoustic systems.

In a similar manner, various measures are from dynamical system theory and complex systems theory have been to forewarn the onset of flame blowout. Gotoda *et al.* (2014) used a measure that captures parallelism of the phase space trajectory called

translational error, while Gotoda *et al.* (2017) used a measure that captures complexities in the signal called permutation entropy to prevent lean blowout in the system. Unni and Sujith (2015) characterized transition to thermoacoustic instability as well as transition to flame blowout using a single measure called Hurst exponent. A similar analysis was performed by Murugesan and Sujith (2016), and Godavarthi *et al.* (2017) by using measures obtained from complex network and recurrence network analysis, respectively.

## 1.7 Objectives and Overview of the Thesis

In summary, thermoacoustic instability has been identified as a great concern in the development of practical combustion systems (Culick and Kuentzmann, 2006). Various studies have been dedicated to characterize linear and nonlinear aspects of coupled processes in the combustor that lead to the onset of such instabilities. Studies on identification of routes through which such instabilities are developed are gaining interest in recent times (Kabiraj *et al.*, 2012*b,a*). The dynamic changes that happen during the transition of combustor operation from combustion noise to thermoacoustic instability are characterized using tools from dynamical systems theory and complex systems approach Juniper and Sujith (2018). Traditionally, such a transition to thermoacoustic instability was considered as Hopf bifurcation (Lieuwen, 2002). However, recent studies in turbulent combustors show that the onset of thermoacoustic instability precedes a dynamical state called intermittency (Nair *et al.*, 2014; Domen *et al.*, 2015; Ebi *et al.*, 2017). The presence of intermittency has proven to provide precursors that can forewarn the impending thermoacoustic instabilities (Nair *et al.*, 2013; Nair and Sujith, 2014; Nair *et al.*, 2014; Unni and Sujith, 2015; Murugesan and Sujith, 2016). In spite of intermittency route to thermoacoustic instability being important, the characterization of such a transition to thermoacoustic instabilities has been hitherto done using acoustic pressure alone. In some studies, a qualitative analysis on the coupled behaviour of flame dynamics with acoustic pressure is studied during intermittency (Unni and Sujith, 2017); however, a detailed characterization of coupled interaction of acoustic field and unsteady heat release rate field during intermittency route to thermoacoustic instability has not been studied in the literature. Furthermore, most of the previous studies on the transition to thermoacoustic instability were based on gas fired combustors and the ex-

istence of such studies in spray combustors are rare. Hence, studying the transition to thermoacoustic instability in spray combustion systems needs further attention.

Recently, Emerson *et al.* (2012a) experimentally showed that the preheating of reactants can alter the dynamic stability of reacting wakes of the bluff body stabilized combustor from a convectively unstable mode to a globally unstable mode. In such a situation, the interaction of the reacting flow field with the acoustic field of the combustor could be different for different values of preheating of reactants. Although the fluid mechanic aspect of such an interaction has been studied by Emerson and Lieuwen (2015), characterization of nonlinear dynamics of the interaction between the acoustic field and the unsteady reacting wake dynamics is necessary to reveal hidden features of their coupled behaviour. Further, various control strategies such as passive and active controls have been developed in the past to mitigate thermoacoustic instabilities. Among these methods, active control strategies are found to be more sophisticated and easy to implement as compared to passive controls (McManus *et al.*, 1993). In the active control, the fuel flow rates are automatically modified through a feedback mechanism in response to the dynamics of the combustor (closed-loop control) or continuously modified at a particular frequency (open-loop control) so that a coupling between the acoustic field and the heat release rate fluctuations in the combustor is completely disrupted (Richards *et al.*, 2007). In one of the simplest approaches of active control, the use of external acoustic forcing has been found to control the response dynamics of the unstable combustor operation (Bellows *et al.*, 2008; Balusamy *et al.*, 2015; Kashinath *et al.*, 2018). However, a comprehensive investigation of the experimental investigation of forced response of thermoacoustic instabilities through this method is yet to be performed.

Therefore, the primary aim of the present thesis is to study the coupled interaction of the acoustic field and the unsteady flame dynamics in thermoacoustic systems using a framework of synchronization theory. Further, the study also aims to provide an open-loop control strategy based on the forcing of thermoacoustic instabilities using the external acoustic perturbations. The specific objectives of the work are:

1. We study the coupled interaction of the acoustic pressure and the heat release rate fluctuations in the framework of synchronization theory during the transition from combustion noise to thermoacoustic instability via intermittency in turbulent combustors. We characterize different states of synchronization observed

during this route to thermoacoustic instability. We further compare the process of synchronization transition observed for both bluff body and swirl stabilized combustors.

2. We investigate the transition of system dynamics from combustion noise to thermoacoustic instability in a two-phase flow combustor. We characterize the type of intermittency using various tools from dynamical systems theory. We also investigate the coupled behaviour of acoustic pressure and global heat release rate fluctuations during the intermittency route to thermoacoustic instability.
3. Subsequently, we examine the coupled dynamics of multiple flamelets anchored at the flame holder and the acoustic field of the combustor in the context of complex systems approach such as emergence and collective synchronization. In order to do this, we compare the flame dynamics observed during different dynamical states such as combustion noise, intermittency and thermoacoustic instability with the corresponding acoustic field of the combustor.
4. In order to highlight the importance of preheating of reactants on the interaction of the flame dynamics with the acoustic field of the combustor, we study the response of such flames to the externally imposed acoustic oscillations. We study this flame response to different values of preheating (or the variation in density ratio across the bluff body wake) and also for different forcing parameters. We characterize this nonlinear interaction between the flame and the acoustic forcing using tools from dynamical systems theory and synchronization theory.
5. Finally, we propose the use of framework from forced synchronization theory to devise an open loop-control strategy for thermoacoustic systems. Using this theory, we also characterize different routes of frequency or phase locking existing in thermoacoustic systems.

The organization of the thesis is presented as follows. In **Chapter 2**, a basic introduction of the synchronization theory is provided. It includes, the history, definition, requirements to study synchronization and applications. Two main types of synchronization i.e., mutual synchronization and forced synchronization are explained in detail. The chapter ends with the summary of tools that have been devised to study synchronization behaviour of two coupled oscillators.

**Chapter 3** summarizes the descriptions of experimental setups used in the present study. Primarily four experimental setups are used to investigate the mutual as well as forced synchronization behaviour of coupled oscillators in thermoacoustic systems.

The experimental procedure and the data acquisition for the respective setups are also provided.

The phenomenon of onset of thermoacoustic instability in a bluff body stabilized turbulent combustor is studied in **Chapter 4**. The nature of the coupled behaviour of acoustic pressure and heat release rate oscillations for the transition of a thermoacoustic system from combustion noise to thermoacoustic instability through intermittency is characterized using a framework from synchronization theory. The process of frequency locking of these oscillations is examined using frequency domain analysis. The comparison of different states of synchronization is also performed. The coupled behaviour of acoustic pressure fluctuations, global heat release rate fluctuations and multiple flamelets anchored at the mesh is investigated for laboratory scale two-phase flow combustor in **Chapter 5**. The stability of this system is characterized for the variation of the flame location as a system parameter. The existence of different dynamical states combustion noise, intermittency and thermoacoustic instability are characterized using tools from dynamical systems theory and synchronization theory.

In **Chapter 6**, a forced response of a reacting wake (or flame) in a bluff body combustor is characterized for different conditions of density ratios, flow velocities and forcing parameters (such as amplitude and frequency). The response of the top and bottom branches of the flame to periodic forcing is characterized using recurrence analysis and synchronization theory. The comparison of forced response of both branches of the flame is also performed for different location along the flame length.

The open-loop control strategy of thermoacoustic instabilities using the framework of forced synchronization is described in **Chapter 7**. A comprehensive investigation of 1:1 synchronization of periodically forced limit cycle oscillations in a prototypical thermoacoustic system, a horizontal Rijke tube, is performed. The different routes of frequency entrainment in thermoacoustic systems are also characterized. The idea of using of periodic forcing to quench the amplitude of thermoacoustic instabilities is proposed.

Finally, conclusions derived from the present thesis are provided in **Chapter 8**. This chapter also includes the scope for future work based on the use of synchronization theory to thermoacoustic systems, combustion phenomena, fluid mechanics problems, and control of instabilities.

# CHAPTER 2

## SYNCHRONIZATION

### 2.1 Basics Concepts

Way back in the seventeenth century, Christiaan Huygens discovered the universal phenomenon of synchronization, when he observed the locking of beats of two pendulum clocks hung over a wooden beam in an anti-phase motion (Huygens, 1665; Pikovsky *et al.*, 2003). Such a sympathetic behavior of these pendulum clocks towards the coupling is referred to as *synchronization*. Figure 2.1a shows two nearly identical pendulum clocks suspended over two independent nearby wooden beams. The oscillation periods of these clocks show a small difference in time, even though, both oscillators carry the same natural frequencies. However, when such pendulum clocks are mounted on a single wooden beam, they exhibit a mutual adjustment in their time periods and eventually a complete locking of their motions to a common time (Fig. 2.1b). This temporal locking of motions of oscillatory pendulum clocks is called synchronization. In classical terms, synchronization is defined as the matching of the rhythm of two or more oscillating objects due to weak coupling, i.e., oscillators ‘*share the same time*’ in the synchronization state. This further suggests that the existence of beam is necessary for coupling the motions of two pendulum clocks. If the synchronized motion established between clocks is disturbed through some means, these clocks reestablish their synchronization motion once the disturbance is removed.

Synchronization is a ubiquitous phenomenon in nature. We come across various instances of synchronization in our day-to-day life, namely, the beating of heart cells, firing of neurons in the brain, flashing of fireflies in unison, chirping of crickets, flocking of birds, the motion of fish schools or even clapping of humans in the orchestra (Strogatz and Edwards, 2005). Synchronization has been studied in a variety of disciplines of science and technology ranging from biology (Glass, 2001), ecosystems (Blasius *et al.*, 1999), chemistry (Schreiber and Marek, 1982), communication (Kocarev and Parlitz, 1995), to various types of engineering systems (Roy and Thornburg Jr, 1994; Heagy

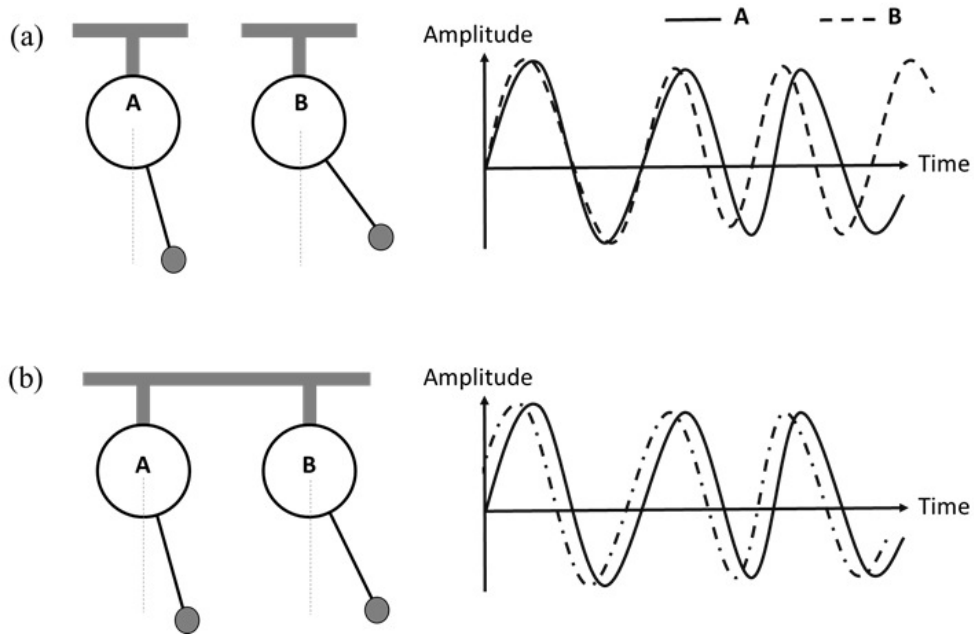


Figure 2.1: Examples of synchronization of two pendulum clocks. (a) The clocks are hung on distinct beams, exhibiting a desynchronized motion with time. (b) The clocks hung on a common beam exhibit synchronization due to the weak coupling exerted through the beam.

*et al.*, 1994). Although the cause of synchronization varies with different systems, the underlying physics of order (synchronization) emerging from disorder (desynchronization), due to change in the coupling parameter, remains conserved.

The requirements for studying the synchronization behavior of two or more oscillators is that, (i) oscillators should be self-sustained (i.e., the motion of the individual oscillator is inherent and is independent of time), and (ii) there should exist a coupling between them. Depending on the value of the coupling strength, the adjustment of rhythms of such oscillators would lead to the locking of either their instantaneous phases or their instantaneous amplitudes. For a low value of coupling strength, coupled oscillators achieve a state of phase (or frequency) synchronization, whereas, for a high value of coupling strength, they reach to a state of amplitude synchronization (Pikovsky *et al.*, 2003). However, it is important to note that, in practical situations, there is no clear demarcation as to what value of coupling strength is to be considered as strong or weak and it is difficult to identify the boundary between them. Furthermore, the synchronization of coupled oscillators can be achieved through different ways, i.e., by varying the coupling strength, by external forcing, or by a feedback mechanism. However, since different types of coupling mechanisms can exist simultaneously in physical systems, due to which it is difficult to identify the effect of each of the coupling mech-

anism individually on the dynamics of the system.

Furthermore, during the process of synchronization, coupled oscillators exhibit an adjustment of frequencies, from different values observed during their uncoupled state to a common value achieved at the state of synchronization. The mode of adjustment of frequencies of such oscillators primarily depends on the type of synchronization that exists between them. Synchronization of coupled oscillators is mainly classified into two basic types, namely, mutual synchronization and forced synchronization. In mutual synchronization, one oscillator affects the other oscillator and also receives influence from it in return. On the other hand, in forced synchronization, one oscillator affects the other oscillator but the reverse coupling is not possible between the oscillators. The difference between these two types of coupling mechanisms of self-sustained oscillators leading to their synchronization can be understood through the following equations of coupled Van der Pol oscillators. The classical Van der Pol oscillator consists of a second-order ordinary differential equation with a nonlinear damping term. It exhibits self-sustained periodic oscillations for positive values of the damping constant (shown by  $\Lambda$  in the following equations 2.1 and 2.2).

*Mutually coupled periodic oscillators*

$$\begin{aligned} \ddot{x}_1 - \Lambda_1(1 - x_1^2)\dot{x}_1 + \omega_1^2 x_1 + K_R(x_1 - x_2) + K_D(\dot{x}_1 - \dot{x}_2) &= 0 \\ \ddot{x}_2 - \Lambda_2(1 - x_2^2)\dot{x}_2 + \omega_2^2 x_2 + K_R(x_2 - x_1) + K_D(\dot{x}_2 - \dot{x}_1) &= 0 \end{aligned} \quad (2.1)$$

where  $x_1$  and  $x_2$  are the dynamical variables of the two oscillators, the dot represents a time derivative,  $\Lambda_{1,2}$  are the nonlinear damping terms, and  $\omega_{1,2}$  are the natural frequencies of oscillators. Both oscillators are coupled through two types of coupling mechanisms, represented by the  $K_R$  and  $K_D$  terms in the equations, which correspond to the reactive and the dissipative coupling strengths, respectively. Thus, the presence of variables  $x_1$  and  $x_2$  (or their derivatives) in both equations indicate the existence of a mutual coupling between oscillators.

*Unidirectionally coupled periodic oscillators*

$$\ddot{x}_1 - \Lambda_1(1 - x_1^2)\dot{x}_1 + \omega_1^2 x_1 = A \cos(\omega_f t + \phi_0) \quad (2.2)$$

where  $A$  is the forcing amplitude,  $\omega_f$  is the forcing frequency, and  $\phi_0$  is the initial phase

of the forcing signal. Here, the forcing signal influences the natural oscillations of the Van der Pol oscillator without being influenced by the dynamics of the Van der Pol oscillator.

The coupling of oscillators can lead to a change in their resultant (or synchronization) frequency. The final frequency of the synchronized oscillators can be equal to the initial frequency of one of the two oscillators (in the case of forced synchronization as shown in Fig. 2.2a), or the final frequency can be in between their initial values (in the case of mutual synchronization as shown in Fig. 2.2b) (Pikovsky *et al.*, 2003). Such adjustment of frequencies is explained in Fig. 2.2. In the case of forced synchronization, depending on the value of the amplitude or the frequency of forcing, the frequency of the driven oscillator (slave system,  $\omega_1$ ) will get locked with that of the driving oscillator (master system,  $\omega_2$ ). In doing so, the frequency  $\omega_1$  will either move towards  $\omega_2$  (if,  $\Delta\Omega = \omega_2 - \omega_1$  is very small), or  $\omega_1$  will get completely suppressed, i.e., the initially dominant natural (unforced) frequency ( $\omega_1$ ) will gradually lose its dominance in favor of the forcing frequency ( $\omega_2$ ), with a change in the forcing parameter. At the time of frequency locking, the frequency corresponding to the natural oscillation gets completely suppressed (Balanov *et al.*, 2008). There is a similar situation in the mutual synchronization case. That is, if the detuning ( $\Delta\Omega$ ) between the oscillators is small, both the frequencies will approach each other and lock-on to a common frequency ( $\omega_3$ ) which is in between their initial values ( $\omega_1$  and  $\omega_2$ , respectively). For large detuning, the original (uncoupled) dominant frequencies ( $\omega_1$  and  $\omega_2$ ) will get completely suppressed, and dominance of the frequencies will be shifted to a common frequency ( $\omega_3$ ) emerged in between these initial frequencies. In this case, the relative position of  $\omega_3$  in between  $\omega_1$  and  $\omega_2$  is decided by the strength of each oscillator. The stronger oscillator tries to pull the weaker one towards it.

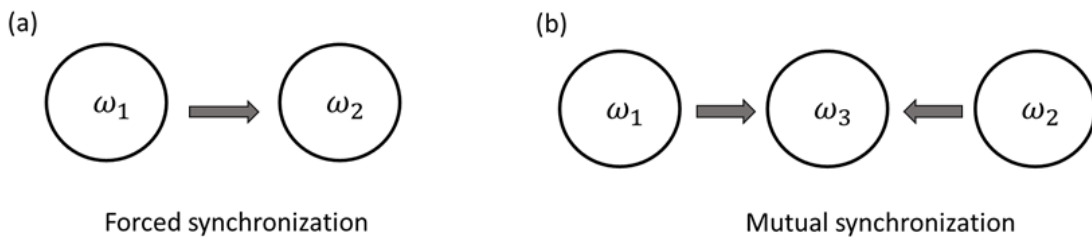


Figure 2.2: A schematic to explain adjustment of frequencies during synchronization for the two different modes of coupling between the oscillators which are (a) forced coupling, and (b) mutual coupling.

## 2.2 Mutual Synchronization

### 2.2.1 Periodic and Chaotic Synchronization

The oscillators that are observed in nature could exhibit periodic or chaotic oscillations (Fig. 2.3). Synchronization of periodic oscillators is commonly observed in nature. For example, if two limit cycle oscillators are coupled and if the coupling between them is weak, one can expect the adjustment of their phases alone without affecting their amplitudes. However, for strong coupling, amplitudes of oscillators can also exhibit locking. If the coupling between such oscillators is phase-attractive, it leads to in-phase synchronization, wherein the phase difference between the oscillators is zero degrees. On the other hand, if the coupling is phase-repulsive, oscillators undergo an anti-phase synchronization, in which the oscillators are locked with a phase shift of 180 degrees. Sometimes in practical systems, more than one mode of the system gets excited. In such a situation, synchronization of two modes of the same system can also be studied, although the modes cannot be split and studied independently (Pikovsky *et al.*, 2003). The change in coupling strength between the modes would result in a condition of mode-locking at the onset of synchronization. Synchronization of two periodic oscillators can be examined through the locking of their dominant frequencies or their instantaneous phases.

On the other hand, chaotic oscillators exhibit deterministic, irregular behavior. The irregularity in their dynamics arises from the broadband nature of their amplitude spectrums. The predictability of the dynamics of such oscillators in time is highly sensitive to their initial conditions. A small change in the initial condition can lead to an exponential divergence of neighboring trajectories in the long-term behavior, but the behavior of such trajectories can be predictable for the initial period of the oscillations. Therefore, synchronization of two coupled chaotic oscillators for different initial conditions has fascinated researchers over the years (Boccaletti *et al.*, 2002*b*). In a similar way as that of period oscillators, the synchronization behavior of coupled chaotic oscillators can be investigated through locking of their time-dependent phases or frequencies. As the amplitude spectrum of the chaotic oscillator is broadband, the period of their oscillation does not remain constant with time. Therefore, the locking behavior of such oscillators is mostly determined through the estimation of their mean frequencies ( $\omega = \langle d\phi/dt \rangle$ ),

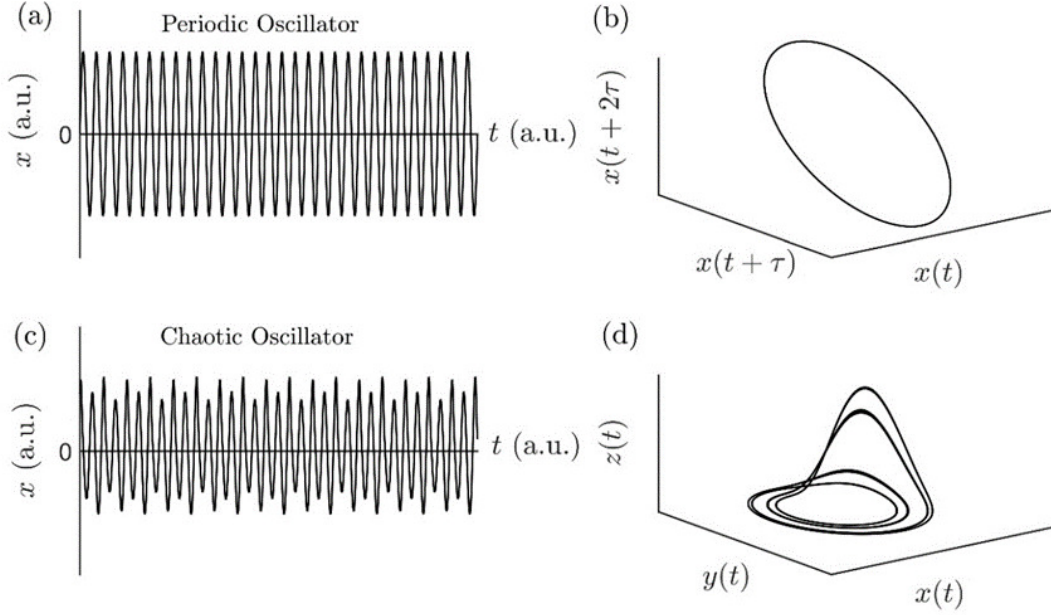


Figure 2.3: The difference between the periodic and chaotic oscillators. (a), (c) The time series and (b), (d) the reconstructed phase portraits of periodic and chaotic oscillations, respectively. The equation for the periodic oscillator is a simple harmonic motion:  $x(t) = A\sin(\omega t)$ , and that for the chaotic oscillator is a Rössler oscillator:  $\dot{x} = -y - z$ ;  $\dot{y} = x + ay$ ;  $\dot{z} = b + z(x - c)$ , where  $a = 0.25$ ,  $b = 0.2$ ,  $c = 10$  are the constants.

where  $\phi$  and  $\omega$  are the instantaneous phase and the angular frequency of the oscillator) and not their dominant frequencies.

The synchronization of coupled chaotic oscillators can display various forms, which have been categorized mainly into phase synchronization (Rosenblum *et al.*, 1996), lag synchronization (Rosenblum *et al.*, 1997), complete synchronization (Fujisaka and Yamada, 1983) and generalized synchronization (Rulkov *et al.*, 1995). In *phase synchronization*, both the oscillators of a coupled system show a perfect locking in their phases; however, their amplitudes remain uncorrelated. This is a weak form of synchronization. During *complete synchronization*, both the amplitudes and the phases of the signals from the coupled oscillators display the exact same behavior. This form of synchronization is the manifestation of stronger coupling between the oscillators. Complete synchronization can only be observed in identical oscillators. A small mismatch between the oscillators can lead to a shift in their instantaneous phases, however, their amplitudes remain perfectly locked. Such state of synchronization is referred to as *lag synchronization*. In the case of *generalized synchronization*, there exists a functional relationship between the signals of coupled non-identical oscillators. This means that, if

$X(t)$  and  $Y(t)$  are two oscillators, they exhibit a functional relation of  $Y(t) = F(X(t))$  during the state of generalized synchronization. In some cases, the state of perfect synchronization is preceded by a state of *intermittent synchronization*, wherein the regions of synchronized and desynchronized oscillations are simultaneously present in the signals of coupled oscillators (Ahn *et al.*, 2011).

## **2.3 Other Phenomena of Mutual Synchronization of Coupled Oscillators**

### **2.3.1 Amplitude Death and Oscillation Death**

As discussed in the previous paragraphs, at a particular value of the coupling parameter, weak coupling between two or more oscillators can induce synchronization (phase-locking) between their oscillations. During synchronization, all oscillators exhibit a common time scale. In contrast, when the coupling between oscillators is sufficiently strong, it can give rise to the phenomenon of oscillation quenching in the dynamics of all oscillators. Thus, self-sustained oscillators that display either periodic or chaotic oscillations in the uncoupled state can undergo a complete annihilation of their oscillations due to coupling. The quenching of oscillations in mutually coupled oscillators is further classified into two types: amplitude death and oscillation death (Koseska *et al.*, 2013). Although these two phenomena of quenching appear to be the same, their occurrence is found to be entirely different. During amplitude death, all oscillators get stabilized to a same steady state due to coupling. The transition of all oscillators to a common steady state is also referred to as a homogeneous steady state. The steady state that appears during amplitude death is of zero amplitude. On the contrary, the occurrence of oscillation death is associated with the phenomenon of symmetry-breaking, in which coupling between the oscillators induces the formation of new steady states that can have non-zero amplitudes. Thus, the occurrence of oscillation death is associated with the occurrence of an inhomogeneous steady state due to coupling.

The quenching of oscillations can be achieved through the application of various types of coupling mechanisms between the oscillators. Different types of coupling schemes such as dissipative coupling, time-delay coupling, conjugate coupling, mean-

field coupling, dynamic coupling or environment coupling can exist between the oscillators (Saxena *et al.*, 2012). In order to attain quenching of oscillations between the instantaneously coupled oscillators, the existence of sufficient amount of detuning (difference in frequencies) is necessary. However, quenching of identical oscillators (zero detuning) is possible, if the oscillators are coupled only through time delay coupling. During conjugate coupling, dissimilar variables of the oscillators are coupled to each other to achieve oscillation quenching between them.

The quenching of self-sustained oscillations has many potential applications in real world. In some cases, the quenching of oscillations is necessary, whereas, in some other cases, it is unwanted. Suppression of oscillations is detrimental in some of the neural disorders such as Alzheimer's and Parkinson's disease (Selkoe, 2000; Caughey and Lansbury Jr, 2003). The stabilization of oscillations is necessary in the case of coupled lasers (Kim *et al.*, 2005; Kumar *et al.*, 2008). Even in thermoacoustic systems (Thomas *et al.*, 2018) and thermoacoustic engines (Biwa *et al.*, 2015), the existence of self-sustained thermoacoustic instabilities are undesirable and the concept of amplitude death can be used to mitigate such instabilities. Several other examples of oscillation quenching can be found in Koseska *et al.* (2013).

### **2.3.2 Emergence and Collective Synchronization**

The existence of a mutual coupling between the population of oscillators can give rise to an emergent phenomenon, wherein the interaction of multiple components of the population at the smaller scale leads to an occurrence of order (or synchronization or self-organized pattern) in the population at the larger scale (Manrubia *et al.*, 2004). One of the simplest example to understand this phenomenon of emergence in the large class of oscillators is the synchronized flashing of fireflies in the forest (Strogatz and Edwards, 2005). The resultant dynamics of such collective interaction of multiple oscillators can exhibit different behaviors. The ensemble of oscillators can transition from a desynchronized state, where all oscillators oscillate at different phases/frequencies, to phase synchronized (for weaker coupling) or amplitude synchronized (for stronger coupling) states of the oscillations. Sometimes, if the coupling between oscillators is not sufficiently strong or if the detuning between the oscillators is large, then a partial state of synchronization can occur in the ensemble of oscillators. During this state of oscil-

lations, the interaction between the oscillators leads to the formation of clusters in the population (Wang *et al.*, 2000, 2001; Wickramasinghe and Kiss, 2013). All elements of an individual cluster exhibit synchronized behavior. Furthermore, depending on the value of the coupling strengths or the inhomogeneity between the oscillators, neighboring clusters of the population can exhibit synchronized or desynchronized behavior. In the case of identical oscillators, a situation can arise where the population of oscillators divides into two parts, in which, one part of the population is desynchronized and the other is synchronized. Such coexistence of synchronized and desynchronized oscillators in the same population is commonly referred to as chimera state (Abrams and Strogatz, 2004; Panaggio and Abrams, 2015). If the coupling between the oscillators is strong, all oscillators can undergo a transition from desynchronized or partially synchronized state to a fully synchronized state, called the condensation transition of the oscillators (Zanette and Mikhailov, 1998).

The investigation of synchronization behavior of a population of oscillators was started by Winfree (1967) and Kuramoto (1984) in biology. Later on, such investigation has received a much attention in revealing and understanding the complexities of different fields of science and technology (Manrubia *et al.*, 2004; Strogatz and Edwards, 2005).

## **2.4 Forced Synchronization**

### **2.4.1 Frequency and Phase Entrainment**

Forced synchronization is a simple case of studying synchronization (phase or frequency entrainment) behavior of a self-sustained oscillator (Balanov *et al.*, 2008). As explained earlier, there exists a unidirectional (one-way) coupling between the coupled oscillators. The coupling between the forced oscillator and the forcing system can be changed either by varying the forcing amplitude or the forcing frequency. The variation of forcing amplitude and forcing frequency required for the forced synchronization of the oscillator exhibits a linear relation. When the detuning, i.e., the difference of frequencies between the natural and the forcing signals is low, the amount of forcing amplitude required for the synchronization of the oscillator is small. An increase in

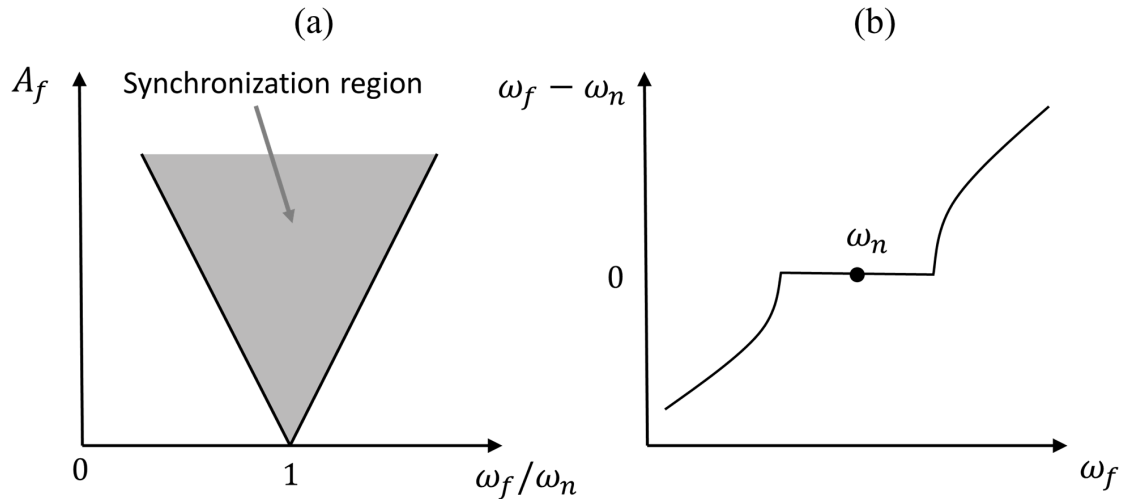


Figure 2.4: (a) A synchronization map or Arnold tongue (i.e., V-shaped plot) showing the forced response of a self-sustained (periodic or chaotic) oscillator for different values of the forcing amplitude ( $A_f$ ) and forcing frequency ( $\omega_f$ ) around the natural frequency of the oscillator ( $\omega_n$ ). The shaded region inside the Arnold tongue represents the phase-locking (forced synchronization) behavior of the oscillator. (b) A frequency response curve of the oscillator showing the variation of the frequency difference ( $\omega_f - \omega_n$ ), calculated across the natural frequency of the oscillations, with the forcing frequency ( $\omega_f$ ) for a constant value of the forcing amplitude. When the forcing frequency approaches the natural frequency, natural frequency gets locked with the forcing frequency. This locking of the two frequencies continues for a finite value of detuning around the natural frequency, as shown by the plateau region around the zero frequency difference before both frequencies get separated out at the boundary of the Arnold tongue. The width of the plateau observed in (b) increases with increase in forcing amplitude.

detuning shows a linear increase in the value of the forcing amplitude required for synchronization. During the state of synchronization, natural oscillations of the forced oscillator get completely suppressed and the system oscillates at the forcing frequency. The forced synchronization behavior of an oscillator can be effectively represented in a two-dimensional parametric plane of forcing amplitude against forcing frequency, commonly referred to as a synchronization map or an Arnold tongue due to its tongue like shape (see Fig. 2.4a). The study of the forced synchronization phenomenon is same for both periodic and chaotic oscillators.

The requirement to study forced synchronization is that the oscillator being forced should be in a state of self-sustained oscillation. Therefore, the amplitude spectrum of the unforced oscillator exhibits a prominent peak at the natural frequency of the oscillations. The application of forcing leads to an appearance of another peak corresponding to the forcing frequency in the amplitude spectrum of the response signal. The inter-

action of these two frequencies governs the resultant dynamics of the forced system. When the forcing frequency approaches the natural frequency of the oscillator, near the synchronization boundary, the frequency of the natural oscillations gets locked with the forcing frequency (Fig. 2.4b). With further increase in the forcing frequency in the synchronization region, both frequencies stay locked for a small frequency range on either side of the natural frequency, referred to as a *frequency-locking* region. The crossing of another synchronization boundary of the Arnold tongue, due to further increase in forcing frequency beyond natural frequency, leads to the separation of these frequencies in the amplitude spectrum of the response signal. Therefore, during the state of forced synchronization, the driven system oscillates only at the forcing frequency and the instantaneous phase difference between the forcing and the natural oscillations remains bounded, exhibiting a constant phase shift with time (plot 1 shown in Fig. 2.5b). This state is also called *frequency locking* or *phase locking* state of the oscillations. When the oscillators are desynchronized, the driven system exhibits oscillations at both the forcing and the natural frequencies. At this condition of oscillations, the instantaneous phase difference between the signals of forced and forcing systems becomes unbounded, displaying a continuous increase or decrease (depending on whether  $\omega_n > \omega_f$  or  $\omega_n < \omega_f$ , respectively) with time, known as the *phase drifting* behaviour of the oscillations (plot 4 shown in Fig. 2.5b).

The effect of forcing on the oscillations of the forced system is different for different values of the forcing amplitude. Weak forcing (i.e., low amplitude forcing) can affect only the phase and not the amplitude of the driven oscillations when detuning is small. Therefore, the amplitude of the driven oscillations can remain the same during the desynchronized as well as synchronized regions of the oscillations. On the contrary, when the frequency detuning is large, a strong forcing required for the synchronization can affect both the phase and the amplitude of the forced oscillations. In the unforced state, the driven system oscillates at the natural frequency. The commencement of forcing with a finite amplitude modulates the amplitude envelope of the forced oscillations, which then resembles the phenomenon of *beating* (Balanov *et al.*, 2008). The oscillations observed during this state display a quasiperiodic motion whose behavior in the phase space shows a 2-torus structure. The amplitude modulation frequency or the beating frequency is same as the difference in frequencies of forcing and natural oscillations present in the response signal. The instantaneous phase difference between the driven

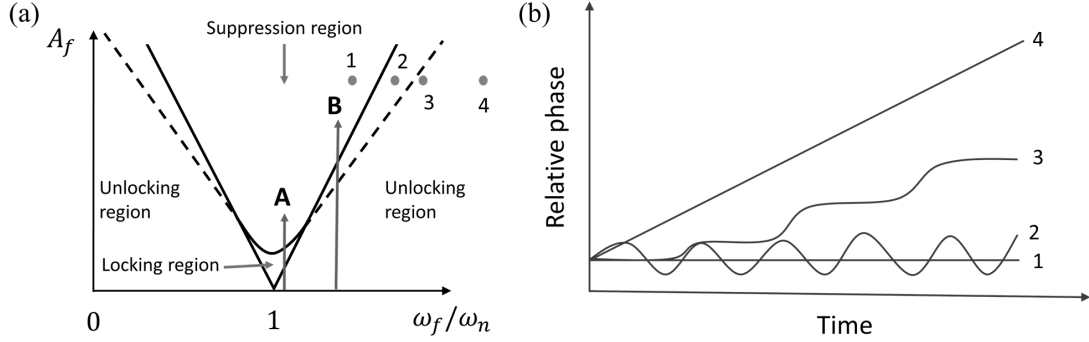


Figure 2.5: (a) A schematic of the Arnold tongue showing different regions of synchronization, i.e., locking, suppression and unlocking regions. A transition from the unlocking to the locking region is shown by path A and a transition to suppression region is shown by path B. The region between the dotted and the continuous lines shows the phase trapping behavior of the forced oscillations. (b) The instantaneous phase difference (or relative phase) between the forcing signal and the forced oscillator signal is shown for four different points (1, 2, 3, and 4) located across the right-hand side synchronization boundary of the Arnold tongue. These points correspond to the phase-locking, phase trapping, intermittent phase locking and phase drifting states of the oscillations, respectively.

and driver systems shows a staircase like structure, wherein the signals are locked for a short range of the oscillations, exhibiting a plateau region in the plot, separated by a phase slip of integer multiples of  $2\pi$  radians (plot 3 shown in Fig. 2.5b). The presence of a phase slip indicates the mismatch in the oscillations of two systems for a short duration, leading to an increase in the phase difference by  $2\pi$  radians. At the onset of forced synchronization, amplitude modulation in the response signal ceases and the forced system oscillates only at the forcing frequency. The bifurcation of the forced oscillation during the synchronization transition in a Poincaré section or a first return map shows a fixed point in the unforced state, a circle during the quasiperiodic state, and again a fixed point in the synchronization state.

## 2.4.2 Routes to Forced Synchronization

The forced synchronization (or phase locking) of limit cycle oscillations can be achieved through two ways, as shown by paths A and B in Fig. 2.5a. Each path to synchronization is associated with a particular type of bifurcation, where path A is related to saddle-node bifurcation and path B is related to torus-birth bifurcation (Balanov *et al.*, 2008). The synchronization region of the Arnold tongue is divided into two regions,

i.e., locking and suppression, depending on whether the forced synchronization of the oscillator is achieved via path A or path B, respectively. The locking region is restricted to a small value of the frequency detuning, while suppression region is achieved when the frequency detuning is high. For a fixed value of the forcing frequency, if the forcing amplitude is increased through path A from a low to a high value, the instantaneous relative phase dynamics of the forcing signal with the forced oscillator signal display a change from phase-drifting to phase-locking behavior. On the other hand, if the forcing amplitude is increased through path B, the relative phase dynamics of these oscillators change from phase drifting to phase trapping and finally to phase locking state of the oscillations. Here, during the *phase trapping* state, the relative phase between these oscillators exhibits periodic fluctuations around a constant phase shift where mean frequencies of both the oscillators are locked but not their instantaneous phases (plot 2 shown in Fig. 2.5b). The region of phase trapping is observed between the dotted line and the continuous line of the Arnold tongue (see Fig. 2.5b).

The amplitude spectrum of the forced oscillator shows a significant difference for the two routes of the synchronization transition (i.e., path A and path B). For the locking route (path A), the frequency peak corresponding to the natural oscillations exhibits a gradual movement towards the forcing frequency during the synchronization transition. On the other hand, for the suppression route (path B), the frequency peak corresponding to the natural oscillations instead of moving towards the forcing frequency, loses its strength gradually at the same location and eventually vanishing at the onset of synchronization. The transition of boundaries of the phase-locking and the suppression regions can also be identified through the variation of the beating frequency ( $|\omega_f - \omega_n|$ ) with the change in forcing frequency ( $\omega_f$ ), obtained for a constant value of the forcing amplitude (Balanov *et al.*, 2008). For the phase locking region, the beating frequency shows a linear decrease to zero with the variation of forcing frequency on either side of the unforced natural frequency of the oscillator. In contrast, for the suppression region, the beating frequency shows a sudden drop to zero at the synchronization boundary.

## 2.5 Tools to Detect Synchronization

### 2.5.1 Instantaneous Phase Calculations

The phase of a signal is an important parameter in analyzing synchronization characteristics of coupled oscillator systems. For instance, a simple harmonic signal can be represented in the form  $x(t) = A\cos(\omega t + \phi_0)$ , where  $A$  is the amplitude,  $\omega$  is the angular frequency and  $\phi_0$  is the initial phase of the signal (see Fig. 2.6). The period of the signal is given by  $T = 2\pi/\omega$ . The phase of the oscillator corresponds to the argument of the cosine term in the equation, i.e.,  $\phi(t) = \omega t + \phi_0$ . The interpretation of the phase of an oscillator can easily be understood through the evolution of the signal in the plane  $(x, \dot{x})$ , where  $\dot{x}$  is the time derivative of  $x$  (Fig. 2.6). In this plane, the oscillations of the signal are represented by a circle whose radius is  $A$ , in which the phase of the oscillation increases by  $2\pi$  radians after every revolution. The mean slope of the plot showing a variation of instantaneous phase with time represents the angular frequency ( $\omega = \langle d\phi/dt \rangle$ ) of the signal.

Various methods are available in the literature to calculate the instantaneous phase of the signal (Pikovsky *et al.*, 2003; Balanov *et al.*, 2008); however, the choice of a specific method depends on the properties of the signal. One of the ways to calculate an instantaneous phase of a signal is to use the analytic signal approach (Gabor, 1946) based on the Hilbert transform (Rosenblum *et al.*, 1996). The analytic signal ( $\zeta(t)$ ) is a complex quantity, whose real part is the original signal ( $x(t)$ ) and imaginary part

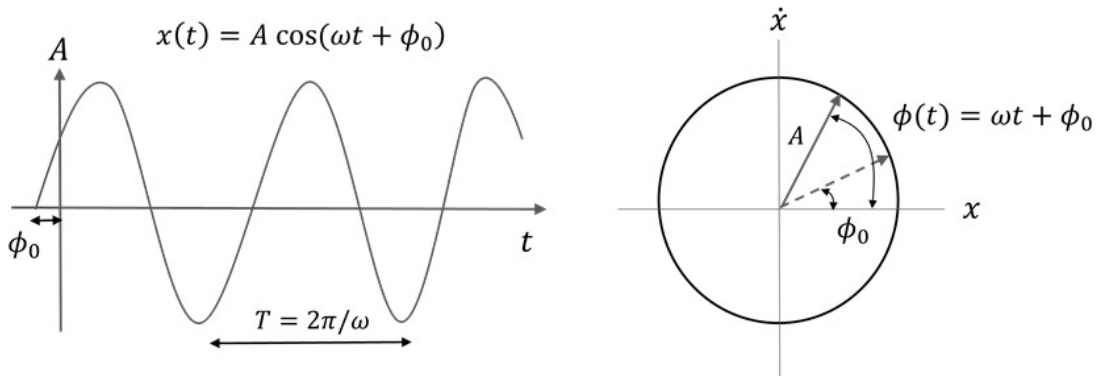


Figure 2.6: The interpretation of the phase of an oscillator is shown through the schematic of a sinusoidal signal and its representation in the 2-D phase portrait.

$(x_H(t))$  is its Hilbert transform

$$x_H(t) = \frac{1}{\pi} P.V. \int_{-\infty}^{\infty} \frac{x(\tau)}{(t - \tau)} d\tau \quad (2.3)$$

where  $P.V.$  is the Cauchy principle value of the integral. Thus, the analytic signal is defined as,

$$\zeta(t) = x(t) + ix_H(t) = A(t) e^{i\phi(t)} \quad (2.4)$$

where  $\phi(t)$  represents the instantaneous phase ( $\phi(t) = \tan^{-1} \frac{x(t)}{x_H(t)}$ ) and  $A(t)$  the instantaneous amplitude ( $A(t) = \sqrt{x^2(t) + x_H^2(t)}$ ) of the signal.

A different method to calculate the instantaneous phase of an oscillator is to project the signal in a two-dimensional plane, say  $(x, y)$ . If the evolution of the signal in this plane exhibits a single center of rotation, the instantaneous phase of the signal can be easily calculated through the argument of rotation of the signal around the origin (Lakshmanan and Senthilkumar, 2011) as

$$\phi(t) = \tan^{-1} \frac{y(t)}{x(t)}. \quad (2.5)$$

Sometimes, a Poincaré section can be used to calculate the instantaneous phase of an oscillator (Pikovsky *et al.*, 2003). In this method, a phase space attractor of the signal is transversely cut through a lower dimensional plane and the crossing of points of the phase space trajectory through this plane demonstrate the evolution of the signal. In such situation, it is presumed that the time instant ( $T_i$ ) of each crossing of the trajectory through the Poincaré section leads to an increase of the phase by  $2\pi$ . Thus, the instantaneous phase calculated through this method exhibit a linear increase in phase and is calculated by the following equation

$$\phi(t) = \frac{t - T_i}{T_{i+1} - T_i} + 2\pi i \quad (2.6)$$

The synchronization feature of coupled oscillators is investigated by analyzing the temporal variation of their relative phase (phase difference) and is calculated as  $\Delta\phi_{i,j}(t) = \phi_j(t) - \phi_i(t)$ . The condition for phase locking is  $|\Delta\phi_{i,j}(t)| < constant$ , which means that the phase difference between the signals remains bounded during the state of synchronization. In an ideal case, synchronization leads to a constant value of the relative

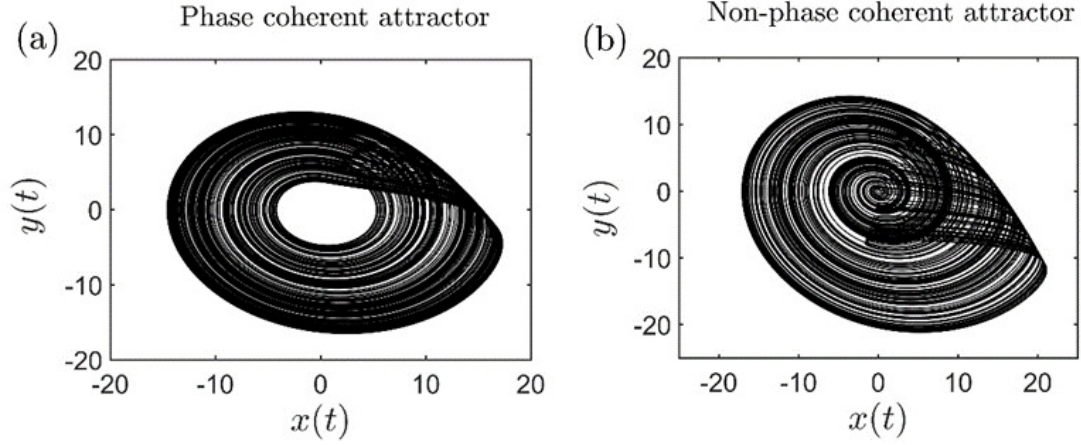


Figure 2.7: The difference between phase coherent and non-phase coherent attractors is shown for Rössler oscillator:  $\dot{x} = -y - z$ ;  $\dot{y} = x + ay$ ;  $\dot{z} = 0.2 + z(x - 10)$ , where  $a = 0.15$  for the phase coherent and  $a = 0.25$  for the non-phase coherent attractor. In (a), the projection of the Rössler attractor in 2-D plane show a smeared limit cycle, where the trajectory revolves around a fixed origin. On the other hand, in (b), the projection of the attractor is filled all over the plane, without showing any distinct center of rotation for the trajectory.

phase, which could be zero (for complete synchronization) or some non-zero value (for other types of synchronization). However, in practice, all signals are contaminated with noise, their relative phases show fluctuations around some constant value of phase shift.

Though the analytical signal approach is desirable, as it gives us the phase at every time instant, there are limitations in calculating the instantaneous phase by this technique. Firstly, it works well only for the narrowband signals, and secondly, the calculated phase has physical meaning only if the projection of a signal in the analytic plane (plot between real and imaginary part of the analytic signal) has a unique center of rotation (Yalçinkaya and Lai, 1997). If the attractor of a signal possesses a unique center of rotation in the analytical plane, it is termed as a phase coherent attractor (Fig. 2.7a), else it is referred to as a non-phase coherent attractor (Fig. 2.7b) (Lakshmanan and Senthilkumar, 2011). In our system, for the signals acquired during combustion noise and intermittency state, we notice the presence of non-phase coherent attractors (figures are not shown here). The presence of multiple centers of rotations makes it difficult to select a single reference point and hence define the instantaneous phase around it. Conversely, in the case of limit cycle oscillations, we observe a single center of rotation (phase coherent attractor) in the analytic plane, and thus, the instantaneous Hilbert phase is well defined for such signals.

There are only a few methods available in the literature to characterize the synchronization features of non-phase coherent signals. In these methods, the attractor of the signal is projected onto a two-dimensional plane or transformed into another plane such that the projected attractor would look like a smeared limit cycle with a proper center of rotation (Boccaletti *et al.*, 2002b; Yalçınkaya and Lai, 1997; Osipov *et al.*, 2003). In these methods, selection of the projection plane or the kind of transformation to use so that the projected signal would have a single origin of rotation is difficult. In contrast to these methods, the requirement of the state space trajectory to rotate about a single origin is not necessary for the method based on recurrence plots (Romano *et al.*, 2005). In addition, this method can be used for signals that are non-stationary and those that are contaminated with noise. Further, the reconstruction of the phase space ensures that the attractor is untangled, as the trajectories in the phase space do not intersect with each other. Since this method is based on the recurrence property of such a trajectory, it eliminates the question of seeking a center of rotation.

## 2.5.2 Synchronization Using Recurrence Theory

Recurrence is a fundamental property of deterministic dynamical systems (Eckmann *et al.*, 1987). The recurrence in the dynamics of the system can be effectively represented by using a two-dimensional binary matrix, known as the recurrence plot (RP) (Marwan *et al.*, 2007). The construction of the RP relies on the reconstruction of the phase space, which is possible on account of Takens' delay embedding theorem (Takens *et al.*, 1981). The time series of an experimental observable, for example, unsteady pressure oscillations  $[p(t) = p'_1, p'_2, p'_3, \dots, p'_N]$  measured at a particular value of the control parameter is embedded in the phase space, by choosing the suitable values of time delay ( $\tau_{opt}$ ) and minimum embedding dimension ( $E$ ) (Abarbanel, 1996). The embedding dimension is obtained from the method suggested by (Cao, 1997), whereas the optimum value of the time delay is chosen as the first minimum of the average mutual information (Fraser and Swinney, 1986).

An important parameter required in the construction of RP is the cut-off threshold ( $\epsilon$ ), which is instrumental in deciding the recurrence of the phase space trajectory (Schinkel *et al.*, 2008). We can choose the threshold as a fraction of the size of the attractor, or assign it values so that there are a fixed number of nearest neighbors for each

point, depending on the applicability of RP to a particular type of problem (Marwan, 2011). The increase in the size of the threshold correspondingly increases the number of recurrences in the RP. The equation used in the construction of the recurrence plot is given by,

$$R_{i,j} = \Theta(\epsilon - \|x_i - x_j\|); \quad i, j = 1, 2, \dots, N_1 \quad (2.7)$$

where,  $\Theta$  is the Heaviside step function,  $N_1 = N - (E - 1)\tau_{opt}$  is the total number of points in the delayed vector, and  $\|\cdot\|$  is the Euclidian norm. Whenever the phase space trajectory falls within the threshold, it is marked as 1 in the recurrence matrix; otherwise, it is marked as 0. Thus, the recurrence plot is a graphical representation of black and white points, where a black point corresponds to  $R_{i,j} = 1$  and white point corresponds to  $R_{i,j} = 0$ .

A measure of synchronization based on the recurrence analysis of the signal is called the probability of recurrence ( $P(\tau)$ ) (or also known as generalized autocorrelation function). It shows the probability with which the trajectory returns to the neighbourhood of a given point in the phase space after a time lag  $\tau$  (Romano *et al.*, 2005). The  $P(\tau)$  is given by,

$$P(\tau) = \frac{1}{(N_1 - \tau)} \sum_{i=1}^{N_1 - \tau} \Theta(\epsilon - \|x_i - x_{i+\tau}\|) \quad (2.8)$$

The recurrence property of a signal can be related to its phase. Whenever the trajectory in the phase space recurs, the phase of the signal can be considered to be increased by  $2\pi$ . During synchronization, both phases as well as frequencies of the signals from the coupled oscillator system are locked, which, in turn, reflects in the locking of positions of the peaks in the plot of  $P(\tau)$  against the lag,  $\tau$ . The locking of the height of the peaks in the plot of  $P(\tau)$  depends on the correlation between the amplitudes of the interacting signals (Lakshmanan and Senthilkumar, 2011). In the case of phase synchronization, the phases of the signals are perfectly locked; nonetheless, their amplitudes may remain uncorrelated. This behavior manifests in the locking of positions of the peaks but a mismatch of their heights in the plot of the probability of recurrence. On the other hand, during generalized synchronization, both the oscillators are bound together by a functional relationship. This translates to the circumstance that if two states in the phase space of one oscillator are close to each other, the states corresponding to the same time instance on the trajectory of the other oscillator are also close to

each other (Fujisaka and Yamada, 1983). The property of recurrence is able to capture this feature of the proximity of the phase space trajectories. If the two oscillators are in generalized synchronization, their recurrence plots become nearly identical, and hence their plots of probability of recurrence also show identical behavior (Romano *et al.*, 2005; Lakshmanan and Senthilkumar, 2011).

### 2.5.3 Use of Cross Wavelet Transform

Synchronization properties (phase and frequency locking) of coupled oscillators can also be detected through a measure based on continuous wavelet transform, known as cross wavelet transform, XWT (Issartel *et al.*, 2015). The wavelet transform demonstrates the localized variation of frequency content in the signal with time, while the cross wavelet transform measures the correlation in common spectral power of two signals. The mathematical formula to calculate continuous wavelet transform, CWT, is given by Torrence and Compo (1998),

$$W(s, t_0) = \int_{-\infty}^{\infty} x(t) \Psi_{s, t_0}^*(t) dt \quad (2.9)$$

where  $x(t)$  is the signal and  $\Psi_{s, t_0}^*(t)$  represents the complex conjugate of the mother wavelet function,  $\Psi_{s, t_0}(t)$ . Here,  $\Psi_{s, t_0}(t) = \frac{1}{\sqrt{s}} \Psi_0\left(\frac{t-t_0}{s}\right)$ , wherein  $s$  is the time scale that determines the width of  $\Psi_0$  and  $t_0$  is the time shift of the wavelet function.

A complex Morlet wavelet (Torrence and Compo, 1998) is used as the mother wavelet for the analysis. Morlet wavelet is the most common mother wavelet function used in the analysis of practical sinusoidal signals. The complex nature of this wavelet further helps in separating the instantaneous phase and amplitude information from the signal, which is not feasible with the real-valued wavelet functions. The mathematical form of the Morlet wavelet can be given as

$$\Psi_0(\eta) = \frac{1}{\sqrt{4\pi}} \exp(j\omega_0\eta) \exp(-\eta^2/2) \quad (2.10)$$

where  $\omega_0$  is a wavenumber and  $\eta$  is a non-dimensional time parameter.

The smallest value of scale ( $s_0$ ) is chosen as the integer multiples of  $dt = 1/(\text{sampling frequency})$  and the largest value of the scale is chosen as  $J = \delta_j^{-1} \log_2(N\delta t/s_0)$ .

Thus, the variation of scale of the Morlet wavelet is given by  $s_j = s_0 2^{j\delta_j}$ , where  $j = 0, 1, 2, \dots, J$ . The parameters of the wavelet that are considered fixed:  $\omega_0 = 6$ ,  $s_0 = 2dt$  and  $\delta_j = 0.5$ .

Thus, the cross wavelet transform (XWT) of two signals  $x(t)$  and  $y(t)$  can be obtained as  $W^{xy} = W^x W^{y*}$ , where  $*$  denotes the complex conjugate of the wavelet transform of  $y(t)$ . The power spectrum of the XWT is calculated as  $|W^{xy}|$ . Since the XWT is a complex function, the localized variation in the relative phase between the signals can be obtained as  $\text{Arg}(W^{xy})$ . The synchronization of signals results in the presence of common power throughout the signal length in XWT as well as the coherent arrangement of arrows, indicative of relative phase between the signals, in the common power band of XWT (Issartel *et al.*, 2015). The direction of arrows from the left to the right indicates that the signals are in-phase with each other, and that from right to left indicates the anti-phase locking of both the signals. The upward direction of arrows shows that one signal leads other by 90 degrees or lags by 270 degrees, and vice versa for the downward directed arrows. Thus, with the single XWT plot, it is possible to characterize the synchronization properties in terms of frequency locking and phase locking of the two signals obtained from a coupled oscillator system.

# CHAPTER 3

## EXPERIMENTAL SETUPS AND MEASUREMENT TECHNIQUES

The study is performed in four different experimental setups. A brief description of these setups, experimental procedures and data acquisition are provided in this chapter. The purpose of using each experimental setup is different: (1) A turbulent gas fired combustor is used to study the coupled interaction between the acoustic field of the confinement and the unsteady heat release rate in the flame during the transition of system behaviour from the state of combustion noise to thermoacoustic instability via intermittency. (2) A two-phase flow spray combustor is used to compare and contrast the similarities observed in the transition to thermoacoustic instability from a state of combustion noise in the turbulent gas fired combustor. (3) A vitiated turbulent gas fired combustor is used to study the effect of preheating of reactants on the coupled interaction of the externally forced acoustic field and the unsteady flame dynamics of a bluff body wake in the combustor. (4) An electrically heated horizontal Rijke tube is used to study the interaction of self-sustained limit cycle oscillations with the external acoustic forcing, and thus, propose an open-loop control strategy to mitigate thermoacoustic instabilities in the system.

### 3.1 Turbulent Gas Fired Combustors

#### Setup Description

The experiments were conducted in a laboratory scale combustor having a partially premixed turbulent flame as shown in Fig. 3.1. The experimental setup consists mainly of three parts: i) a settling chamber, ii) a burner, and iii) a combustor. The airflow is first passed through the settling chamber, which serves the purpose of reducing the effect of hydrodynamic fluctuations at the air inlet from the flow inside the combustion chamber. In the burner, fuel (Liquefied Petroleum Gas; propane 40% and butane 60%

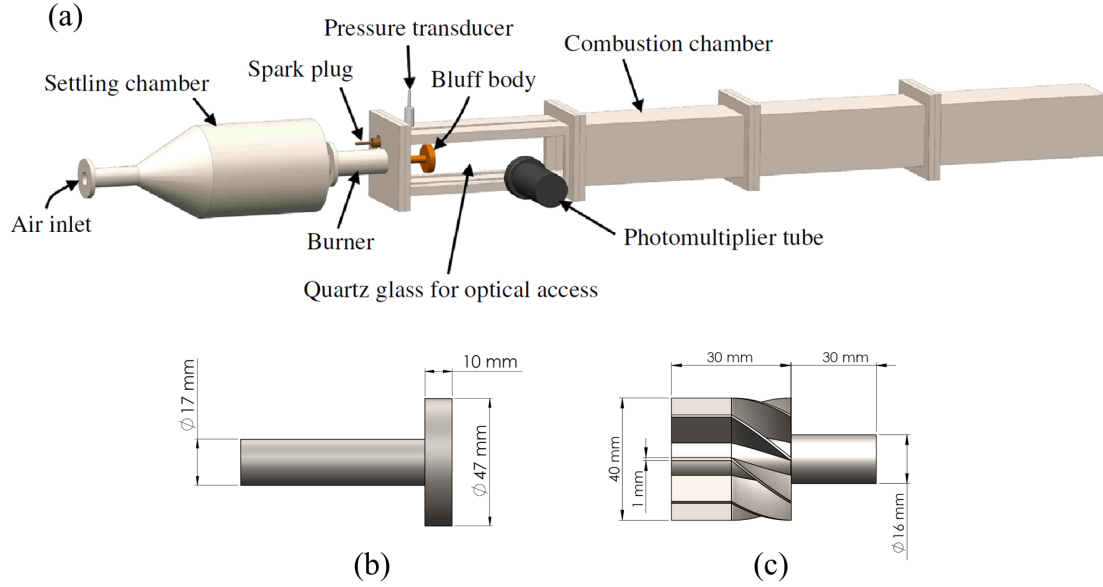


Figure 3.1: (a) A schematic of the turbulent flame combustor. Experiments were performed with two different flame holding mechanisms (b) bluff body and (c) fixed-vane swirler.

by volume) is partially mixed with the incoming airflow from the settling chamber at different equivalence ratios. This partially premixed fuel-air mixture then enters into the main combustor section. The combustor is a rectangular duct which is 1400 mm long and 90 mm  $\times$  90 mm wide, and has a backward facing step (dump plane) at the inlet. The experiments are conducted separately for two configurations of the flame holding mechanisms, i.e., a bluff-body (Fig. 3.1b) and a swirler (Fig. 3.1c). These flame holding devices aid in anchoring the flame in a high velocity turbulent environment of the combustor. A bluff body, circular disc of diameter 47 mm and thickness 10 mm, is located at a distance of 4.5 mm from the inlet of the combustor. The swirler is positioned near the exit of the burner. It consists of eight blades, each having a vane angle of 40°. A central body located flush with the dump plane of the combustion chamber is used for flame stabilization.

The air and fuel flow rates are controlled separately by using mass flow controllers (Alicat Scientific, MCR 2000SLPM - for air, and MCR 100SLPM - for fuel; uncertainty is  $\pm 0.8\%$  of measured reading + 0.2% of full-scale reading) in the system. In bluff body combustor, the fuel flow rate is maintained at a constant value of 25 slpm and the air flow rate is varied from a value of 400 slpm to 940 slpm such that the flow field in the system is turbulent ( $Re = 1.09 \times 10^5$  to  $Re = 2.12 \times 10^5$ ) throughout the experiment. The estimated uncertainties in  $Re$  are  $\pm 1.97 \times 10^3$  to  $\pm 2.71 \times 10^3$ . The equivalence

ratios range from  $0.95 \pm 0.02$  to  $0.46 \pm 0.01$ . In swirl combustor, the fuel flow rate is maintained at a constant value of 21 slpm and the air flow rate is varied from a value of 330 slpm to 950 slpm. For the purpose of initial ignition, a spark plug (along with 11 kV ignition transformer - National Engineering Corporation), fixed at the dump plane, is used to ignite the combustible air-fuel mixture. Quartz windows of size 90 mm  $\times$  360 mm, located on both the side walls of the combustor, provide optical access required for the measurement of heat release rate fluctuations from the flame.

## Measurements and Data Acquisition

We measure the acoustic pressure fluctuations ( $p'$ ) from the combustor using a piezo-electric transducer (PCB Piezotronics, PCB103B02, with a sensitivity of 223.4 mV/kPa, and an uncertainty of  $\pm 0.15$  Pa). The pressure transducer is fixed on the top wall near the inlet step of the combustor. This position of the transducer corresponds to a near maximum amplitude of the acoustic pressure in the duct. It is an appropriate location for the measurement of the acoustic pressure in this combustor, as it always remains a pressure antinode for all the acoustic modes of the duct. The unsteady heat release rate fluctuations ( $\dot{q}'$ ) are captured by using a photomultiplier tube, PMT, (Hamamatsu H10722-01). A CH\* bandpass filter (wavelength = 432 nm and 10 nm FWHM), which captures the CH\* chemiluminescence intensity from the flame, is used to filter the input to the PMT. The chemiluminescence intensity thus recorded is a measure of the heat release rate from the flame. The PMT is positioned at a distance 500 mm normal to the combustor wall near the location of the bluff body. The signals of the pressure fluctuations and the heat release oscillations were acquired for 3 s at a sampling frequency of 10 kHz. A 16-bit analog to digital (NI-6143) card is used for the data acquisition. Since our main objective in the present study is to analyze the synchronization characteristics of  $p'$  and  $\dot{q}'$ , we directly use the raw (mean subtracted) signals obtained in voltage from the pressure transducer and the PMT throughout our analysis. This further ensures that both  $p'$  and  $\dot{q}'$  fluctuations are represented in the comparable scales of voltage. Welch's average method is used to smoothen periodogram of the signals. A Hanning window of 5000 data points with an overlap of 50 percentages is used in the analysis. This method improves the spectral representation of signals in the waterfall diagram by reducing noise from the estimated power spectra.

The local heat release rate fluctuations are captured through flame imaging using a high-speed CMOS camera (Phantom V 12.1) operating at a resolution of  $1280 \times 360$  pixels imaging a  $400 \text{ mm} \times 90 \text{ mm}$  test section on the camera sensor. The camera is outfitted with a ZEISS 50 mm camera lens at  $f/2$  aperture. A narrow bandpass CH\* filter (peak at wavelength 432 nm with 10 nm FWHM) is mounted in front of the lens to capture the CH\* chemiluminescence intensity of the flame. The CH\* flame images are acquired for 1 sec at a frame rate of 2000 Hz.

## 3.2 Two Phase Flow Spray Combustor

### Setup Description

A schematic of the laboratory scale two-phase flow spray combustor used in the present study is shown in Fig. 3.2a. The experimental setup consists of five parts: (i) a fuel supply head, (ii) an air input unit, (iii) a needle spray injector, (iv) the combustion chamber (or resonator), and (v) a flame holder (or mesh unit). The fuel supply head is fixed at the top of the combustor and the fuel is supplied from a gravity feed fuel tank. An air input unit supplies air uniformly from the four sides to the combustor. The combustor is a 1000 mm long quartz glass tube with an inside diameter of 50 mm and a thickness of 2.5 mm.

A novel design of the needle spray injector (see Fig. 3.2b) is used to produce a droplet spray having a one-dimensional velocity field. The injector consists of 70 stainless steel needles of 0.8 mm inner diameter, 1.25 mm outer diameter and 100 mm length. The size of the droplets is reduced by fastening 10 mm long capillary tubes of size 0.4 mm inner diameter and 0.6 mm outer diameter at the end of primary needles of the injector. These needles are fixed over a 5 mm thick stainless steel plate having a diameter of 58 mm. The needles are located on the metal plate in such a manner that each needle is located at the apex of equilateral triangles of side 4 mm. A 5 mm long protrusion of needles is provided on the other side of the metal plate in order to avoid clogging of the needles due to the accumulation of any foreign particles at the plate. This type of placement of the needles helped in producing a uniform, non-coalescing droplet distribution across the combustor.

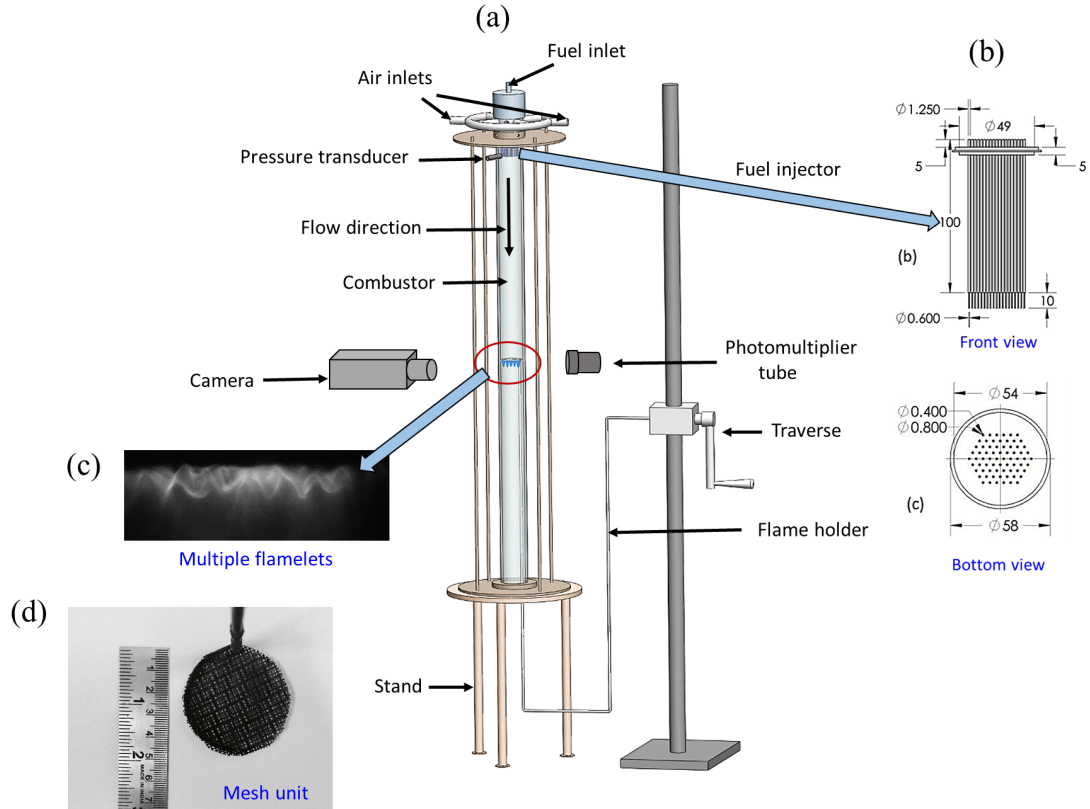


Figure 3.2: (a) Schematic of the spray combustion system used to study the transition of the combustor dynamics from a state of combustion noise to thermoacoustic instability. (b) Schematic of the front and the top view of a needle injector. (c) An image of multiple flamelets anchored at the mesh unit. (d) A photograph of the mesh unit along with a measurement scale.

Secondary atomization is achieved by utilizing two different size stainless steel wire meshes (*gauze 20* and *gauze 12*) that are packed together as a single mesh unit (see Fig. 3.2d). The mesh unit also serves the function of anchoring the flame at a specific location inside the combustor. The relative position of the mesh unit from the bottom of the combustor, defined as  $x_f$ , is varied in the present experiment. Ethanol is used as the fuel. Compressed air maintained at 1 bar (gauge pressure) is used for combustion.

Experiments are conducted at different mass flow rates of fuel (from 8 ccm to 13 ccm) for a fixed air flow rate (100 slpm and 120 slpm). During each experiment, the equivalence ratio is kept constant and the location of the flame is varied. The fuel flow rate is measured manually by collecting the fuel in a 50 ml graduated cylinder (least count of 1 ml and uncertainty of  $\pm 0.5$  ccm) over a period of 60 s before ignition. The air flow rate is measured using a mass flow controller (Alicat Scientific MCR 500SLPM, uncertainty of  $\pm 1.8$  slpm, based on 95% of the confidence interval). The Reynolds number ( $Re = 4\dot{m}_a/\mu D$ ) of the air flow is around  $2842 \pm 49$ , where  $\dot{m}_a$  is the mass

flow rate air,  $\mu$  is the dynamic viscosity of air calculated at ambient conditions, and  $D$  is the inner diameter of the combustor. The fuel-air mixture is ignited from the bottom of the combustor, using a pilot flame. Initially, during ignition, the mesh is lowered down to  $x_f = 110$  mm and once the flame is anchored at the mesh, the mesh is moved upward to  $x_f = 480$  mm. The resonator is preheated at least for 7 min in every experiment before the start of data acquisition. Preheating minimizes the variation of the temperature of the combustor wall from the time of ignition and ensures that the setup temperature reaches a constant value. A fraction of combustion fuel (around 10% of the total fuel supplied) is collected as unburned fuel at the bottom of the combustor due to poor atomization characteristics of the mesh unit and the larger size of the parent drops.

## Measurements and Data Acquisition

Unsteady acoustic pressure fluctuations in the combustor are measured using a data acquisition system, which consists of a pressure transducer, a signal conditioner, and a data acquisition card. The pressure transducer (PCB Piezotronics 103B02, sensitivity of 223.4 mV/kPa, resolution of 0.142 Pa) is fixed on a T-mount, at a location of 140 mm from the injector plate, as shown in Fig. 3.2a. The transducer is connected to the data acquisition card (NI PCI-6221) through a signal conditioner (PCB 480E09). A manual traverse arrangement is employed to move the mesh unit, which, in turn, determines the location of flame inside the combustor. The location of the flame holder (mesh unit) is varied in a step size of 10 mm throughout the experiment (least count on the traverse is 1 mm). Data is acquired for 30 s at the rate of 10 kHz at each location of the flame holder. A settling time of 30 s was ensured before the acquisition of data at every location of the flame. This settling time is necessary to remove the transients associated with the change in flame location. In order to characterize the type of intermittency, a separate experiment was performed to acquire a sufficient number of bursts. The data was acquired for 300 s at the rate of 3 kHz.

In order to study the coupled interaction between acoustic pressure and heat release rate fluctuations, the simultaneous measurements of these fluctuations are performed. The global heat release rate fluctuations in the system are captured using a photomultiplier tube (PMT) equipped with a CH\* bandpass filter (wavelength of 432 nm and

bandwidth of 10 nm) in front of it. Both the data of acoustic pressure and CH\* chemiluminescence from the flame are acquired simultaneously for 30 s at a sampling rate of 10 kHz. Simultaneous high-speed imaging of the multiple flamelets (see Fig. 3.2c) with the acoustic pressure signal is performed using a high-speed CMOS camera (Phantom v 12.1) at a resolution of  $512 \times 288$  pixels. The camera is outfitted with a ZEISS 50 mm camera lens set at  $f/5.6$  aperture. The images are acquired at a sampling frequency of 2.5 kHz for 11 sec.

### 3.3 Vitiated Turbulent Gas Fired Combustors

#### Setup Description

The experimental setup of a bluff body stabilized vitiated turbulent gas fired combustor<sup>1</sup> is shown in Fig. 3.3a. It consists of two premixed combustors connected in series. Natural gas and air are premixed and burned in both the combustors. The first combustor acts as a vitiator, whose purpose is to raise the temperature of reactants going into the second combustor. The second combustor consists of a bluff body, with a 2D ballistic shape (see Fig. 3.3c), used to stabilize the flame in high speed flows. The bluff body span covers the entire combustor width, thus creating a nominal 2D flow in the system as shown in Fig. 3.3b. The aspect ratio, the ratio of the height of the bluff body with a width of the second combustor, is 0.15. Quartz glass window on all four sides of the second combustor provides optical access required for flame imaging.

The experimental rig is designed in a manner that allows independent control of the density ratio of the unburned and burned gases present across the flame ( $\rho_u/\rho_b$ ) and the lip velocity of the flow ( $U_{lip}$ ). Another control parameter is the shape of the bluff body which controls the shear layer thickness and also the alignment between the velocity and density profiles; however, we do not focus on this parameter in the present study. Since  $\rho_u/\rho_b = T_b/T_u$ , the density ratio ( $\rho_u/\rho_b$ ) across the flame is varied by varying the preheating temperature of reactants ( $T_u$ ) entering into the second combustor. Secondary fuel and air supply lines are provided in between the two combustors to have flexibility in varying the density ratio and flow velocity in the second combustor. Thus,

---

<sup>1</sup>The dataset is made available by Emerson and Lieuwen (2015).

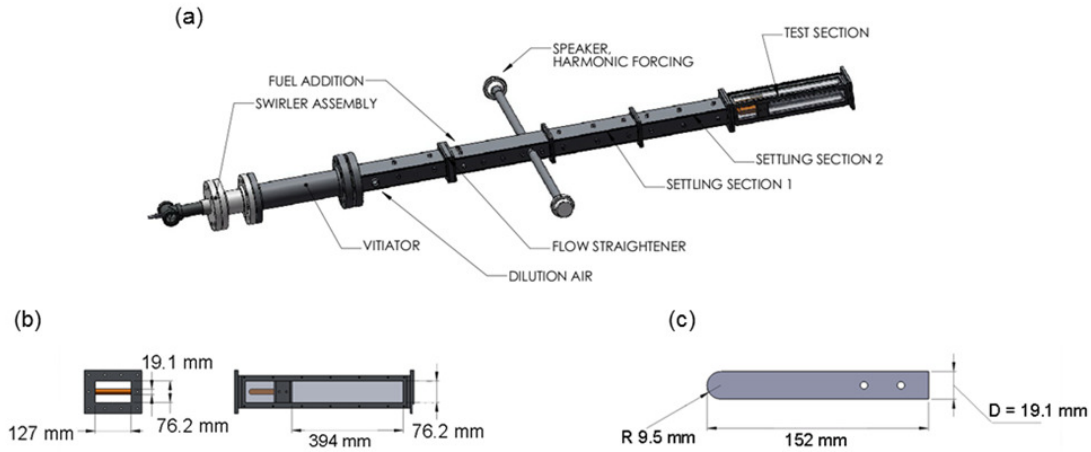


Figure 3.3: (a) Schematic of the bluff body stabilized turbulent gas fired combustion system used to study the effect of density ratio and forcing parameters on the characteristics of a reacting wake. Schematic of (b) the test section (second combustor) and (c) the bluff body. The setup figure is reproduced with permission from Emerson and Lieuwen (2015).

the inlet temperature to the second combustor (after vitiation in the first combustor and after the addition of secondary air and fuel) is varied from 770 K to 1200 K. Thus, the density ratio can be varied systematically aiding in the study of the growth rate of the hydrodynamic global mode in the system. As we sweep the density ratio from a low ( $\rho_u/\rho_b = 1.7$ ) to a high ( $\rho_u/\rho_b = 3.2$ ) value, the flow dynamics gradually transition from a globally unstable to a convectively unstable mode through intermittency. During intermittency ( $\rho_u/\rho_b \approx 2$ ), flow dynamics fluctuate between convectively unstable and globally unstable modes in an apparently random manner. The equivalence ratio and the adiabatic flame temperature in the main combustor were maintained in the range of  $0.7 < \varphi < 0.75$  and  $1950 < T_b < 2030$  K, respectively. Great care was taken to operate this combustor well away from the boundaries of blowoff of the flame, where additional flame and flow dynamics can occur (Shanbhogue *et al.*, 2009b; Chaudhuri *et al.*, 2010, 2011).

## Measurements and Data Acquisition

Two loudspeakers are mounted on the tubes placed 1 m upstream of the second combustor. The harmonic signal generated using a function generator is amplified and then supplied to drive the speakers. As the first transverse mode of the second combustor is 5000 Hz, the multi-dimensional disturbances generated in the system are evanescent

and decay quickly. Thus, the acoustic excitation in the second combustor is effectively planar. In all experiments, the forcing frequency ( $f_f$ ) is fixed at a constant value of 515 Hz and the natural frequency of the global mode is varied across this forcing frequency. To achieve this, the lip velocity of the flow ( $U_{lip}$ ) is varied in such a way that the mean frequency of natural oscillations ( $f_n$ ) in the flame is either less than, equal to or greater than  $f_f$ . This has the additional effect of increasing the global mode limit cycle amplitude as the ratio  $f_n/f_f$  is increased.

The line of sight integrated (along with the bluff body span) imaging of flame CH\* chemiluminescence is performed at different conditions of the forcing parameters and density ratios. The high-speed CH\* chemiluminescence images of the flame are captured using a high-speed CMOS camera (Photron Fastcam SA3) with  $21.7 \mu\text{m}$  pixels, a sampling frequency of 5000 Hz and a pixel resolution of  $768 \times 384$ . The exposure time is fixed at  $1/5000$  s. The camera is outfitted with a 135 mm lens at  $f/2.8$ , with a magnification of 1:17.1. The imaging was performed such that a  $286 \text{ mm} \times 80 \text{ mm}$  region of the main combustor is imaged on  $768 \times 215$  pixels. This captured region of the combustor covers the span from the trailing edge of the bluff body to 15 times bluff body diameters downstream. The flame images are captured through a bandpass filter centered at 434 nm, with 90% transmission between 425.5 nm and 442.5 nm. A total of 4000 images are acquired at every value of the control parameter.

## 3.4 Horizontal Rijke Tube

### Setup Description

Experiments are performed on a horizontal Rijke tube (shown in Fig. 3.4) to study the control of thermoacoustic instabilities using external acoustic forcing. The Rijke tube is 1 m long duct with a square cross-section ( $9.2 \text{ cm} \times 9.2 \text{ cm}$ ). An electrically heated wire mesh is used as a compact heat source in the system. The air flow rate is maintained constant at a value of 100 slpm using a mass flow controller, MFC (Alicat Scientific MCR 500SLPM, the uncertainty of  $\pm 1.8$  slpm). The compressed air is then passed through a rectangular chamber ( $120 \text{ cm} \times 45 \text{ cm} \times 45 \text{ cm}$ ), referred to as a decoupler. The function of the decoupler is to eliminate the hydrodynamic and acoustic

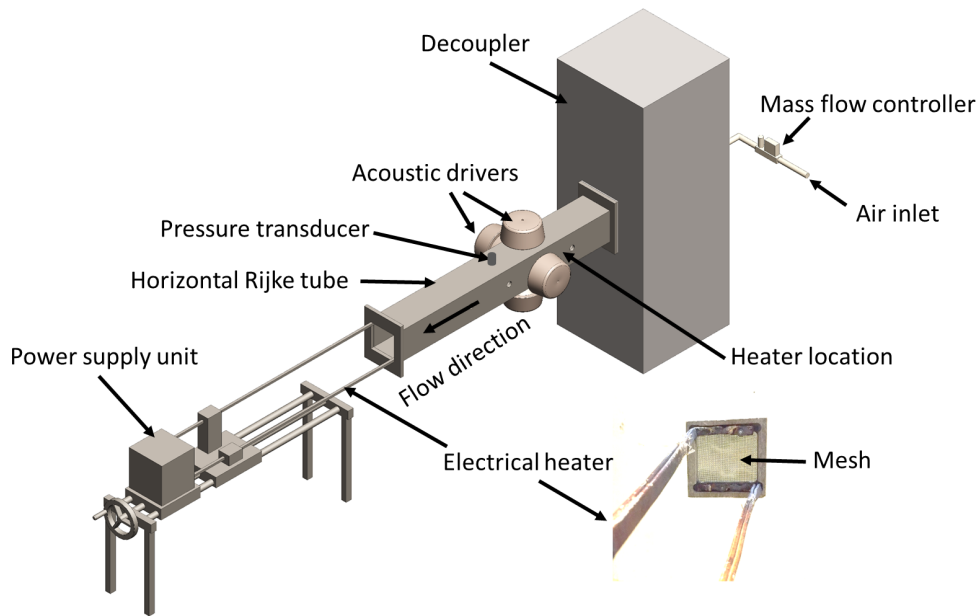


Figure 3.4: (a) A schematic of the horizontal Rijke tube used to study forced synchronization behaviour of limit cycle oscillations in the thermoacoustic system. A photograph of the electrical heater used in the present study is shown in the side figure.

fluctuations associated with the incoming airflow to the combustor and send a steady flow into the Rijke tube.

The system is preheated for 10 min at a constant heater voltage value of 3.5 V to ensure the steady state temperature in the vicinity of the heater. Once the steady state temperature is reached, heater voltage is increased, with a step size of 0.05 V and a waiting time of 30 s at each step, to a value of 4.1 V. A subcritical Hopf bifurcation is observed to occur at a heater voltage value of 4 V. For the forcing study, we maintained the heater voltage at a constant value of 4.1 V throughout the experiments. We note that when the heater voltage is less than the value at Hopf point, i.e., the system is in a bistable region, imposed forcing sometimes lead to the transition of the system behaviour back to its steady state, for certain amplitudes of the forcing.

## Measurements and Data Acquisition

A piezoelectric transducer (PCB 103B02, sensitivity 217.5 mV/kPa and an uncertainty  $\pm 0.15$  Pa) is used to measure the acoustic pressure fluctuations, which in turn, measures the forced response of the limit cycle oscillations in the system. The four acoustic

drivers (loudspeaker, Ahuja AU60), mounted at a distance of 62.5 cm from the inlet on walls of the duct, are used to provide harmonic forcing signal in the system. The response of the system to the forcing is measured for different values of forcing amplitudes and frequencies. The forcing frequency is varied around the unforced natural frequency of the limit cycle oscillations. At a particular value of the forcing frequency, the value of forcing amplitude is increased from 0 mV to the value where the frequency entrainment of natural oscillations with forcing signal is observed. The forcing amplitude is varied at a fine resolution near the natural frequency and at coarse resolution when the forcing frequency is far away from the natural frequency. The forcing frequency is varied from a range of 90 Hz to 220 Hz. The data are acquired at a sampling frequency of 10 kHz for 3 s. The decay rate of the acoustic wave in the system is measured before the start of every experiment by giving an acoustic pulse at no flow conditions. The mean decay rate is found to be approximately  $19 \text{ s}^{-1}$ . To ensure the repeatability, the experiments are conducted only when the decay rate lies within  $\pm 10\%$  of the mean value. The data are acquired using a 16-bit analog to digital (NI-6143) card.

## CHAPTER 4

# ONSET OF THERMOACOUSTIC INSTABILITY AS MUTUAL SYNCHRONIZATION OF THE ACOUSTIC FIELD AND TURBULENT REACTING FLOW

The characterization of the transition of combustion systems from stable to unstable operation has been a topic of intense research during recent times (Lieuwen, 2002; Gotoda *et al.*, 2011; Kabiraj *et al.*, 2012a; Nair *et al.*, 2014). Here, the stable operation, which is manifested as low amplitude aperiodic oscillations, is referred to as combustion noise. The unstable operation, characterized by high amplitude periodic (limit cycle) oscillations, is known as thermoacoustic instability (Lieuwen, 2002). The investigation of the onset of such instabilities is a major concern for practical combustion systems. In most practical turbulent combustion systems, the stabilization of flame is achieved through different devices such as bluff body, swirler or step (dump plane) at the inlet of the combustor. In such combustors, the periodic formation of large-scale vortical structures is observed in the reacting field during the onset of thermoacoustic instability (Keller *et al.*, 1982; Poinso *et al.*, 1987). The breakdown of these coherent structures results in the fine scale mixing of cold unburnt reactants with the hot reacting products, leading to an instantaneous release of heat in the system (Schadow and Gutmark, 1992). This heat release adds energy to the acoustic field, which in turn, affects the vortex formation process and thus establishes a feedback loop. Such a coupled interaction between the duct acoustics and the hydrodynamic field of the reacting mixture has been studied by various researchers in the past (Poinso *et al.*, 1987; Keller, 1995; Ken *et al.*, 1991b; Smith and Zukoski, 1985; Altay *et al.*, 2009; Steinberg *et al.*, 2012); however, the focus of these studies was mostly on the states of the stable and the unstable operation of the combustor.

Chakravarthy *et al.* (2007) examined the transition of combustor operation from combustion noise to thermoacoustic instability. They described such a transition as a

---

The results presented in this chapter are published in S. A. Pawar, A. Seshadri, V. R. Unni, and R. I. Sujith, Thermoacoustic Instability as Mutual Synchronization Between the Acoustic Field of the Confinement and Turbulent Reactive Flow *Journal of Fluid Mechanics*, 827, 664-693, (2017).

phenomenon of vortex-acoustic lock-on, wherein, at the onset of thermoacoustic instability, the frequency of acoustic oscillations locks in with that of the vortex shedding inside the combustor. The process of vortex-acoustic locking or the interaction of the reacting flow field with the acoustic field of the confinement is a nonlinear phenomenon. Recently, studies have focused on understanding such nonlinear interactions using the approach of dynamical systems theory (Juniper and Sujith, 2017). Lieuwen (2002) considered the onset of thermoacoustic instability in turbulent combustors as a Hopf bifurcation, wherein the low amplitude aperiodic oscillations in the acoustic field transition to high amplitude limit cycle oscillations at a particular value of the control parameter. Gotoda *et al.* (2011) described the onset of thermoacoustic instability as the transition of stochastic fluctuations observed near the flame blowout to periodic oscillations through the occurrence of lower-dimensional chaotic oscillations, as the equivalence ratio is increased. The study by Nair *et al.* (2014) has shown the presence of intermittency prior to the occurrence of a full-blown thermoacoustic instability from the state of combustion noise. During intermittency, bursts of seemingly periodic oscillations appear irregularly among the epochs of low amplitude aperiodic oscillations. Most of these studies on the characterization of the route to thermoacoustic instability in turbulent combustion systems are based on nonlinear time series analysis of the acoustic pressure alone. Sometimes the time-resolved flame images or the flow field data acquired simultaneously with the acoustic pressure signal are presented to qualitatively demonstrate the coupled behaviour of these different processes in the combustor.

In this chapter, we view thermoacoustic instability as a synchronization phenomenon between two mutually coupled, non-identical oscillators namely, the acoustic field and the turbulent reactive flow present in the combustor. We perform the experimental investigation of the coupled behaviour of these oscillators during the transition from combustion noise to thermoacoustic instability via intermittency in a bluff body stabilized turbulent gas fired combustor (see Fig. 3.1 in Chapter 3). We use the framework from synchronization theory to study the coupled interaction of these oscillators in both temporal and frequency domain analysis. We characterize different states of coupled dynamics of acoustic pressure and heat release rate fluctuations observed during the transition to thermoacoustic instability in the context of synchronization theory.

## 4.1 Time Domain Analysis of Coupled Acoustic Pressure and Heat Release Rate Fluctuations

We investigate the synchronization behavior of the acoustic pressure ( $p'$ ) and the heat release rate ( $\dot{q}'$ ) oscillations present in a turbulent combustor, as we vary the mean velocity of the flow ( $\bar{u}$ ). Because a turbulent flow generates sound, there will always be acoustic oscillations in the duct. Further, the measured heat release rate fluctuations incorporate the fluctuations from both chemical kinetics and that induced from the associated flow turbulence present in the system (Shanbhogue *et al.*, 2009b). As the resulting effects produced by the fluctuations in hydrodynamic and combustion processes in the combustor are difficult to separate, we consider them as a single oscillator, which we call ‘turbulent reactive flow’. The increase in  $\bar{u}$  results in a decrease in equivalence ratio of the combustible air-fuel mixture from a value close to stoichiometry ( $\varphi = 0.98$ ) to a value of fuel lean condition ( $\varphi = 0.49$ ). At lower values of the mean flow velocity ( $\bar{u} = 9.4$  m/s), we observe low amplitude aperiodic oscillations in both acoustic pressure and heat release rate signals (see Fig. 4.1a). This state of combustion dynamics is traditionally referred to as combustion noise (Strahle, 1978). Recent studies by Nair *et al.* (2013) and Tony *et al.* (2015) have shown that the dynamical features of combustion noise consist of high dimensional chaos contaminated with white and colored noise. With further increase in the mean flow velocity ( $\bar{u} = 11.9$  m/s), we observe the emergence of bursts of periodic oscillations from a background of aperiodic oscillations (Fig. 4.1b). These bursts appear to occur randomly, with no apparent pattern. Nair *et al.* (2014) referred to this state of combustion dynamics as intermittency. The visual comparison of the acoustic pressure and heat release rate signals (in the inset of Fig. 4.1b) shows that both the signals are locked in the burst regions of the periodic oscillations, while unlocked in the relatively silent regions of the aperiodic oscillations.

At sufficiently higher values of the mean flow velocity ( $\bar{u} = 13.2$  m/s), we notice the transition of combustion dynamics from a state of intermittency to a state of weakly periodic oscillations (Fig. 4.1c). During this state, we observe wide cycle-to-cycle variation in the amplitudes of the pressure signal. This variation in the amplitudes of limit cycle oscillations has been postulated to be due to the forcing exerted by background noise (Lieuwen and Neumeier, 2002; Lieuwen, 2003b; Noiray and Schuermans, 2012).

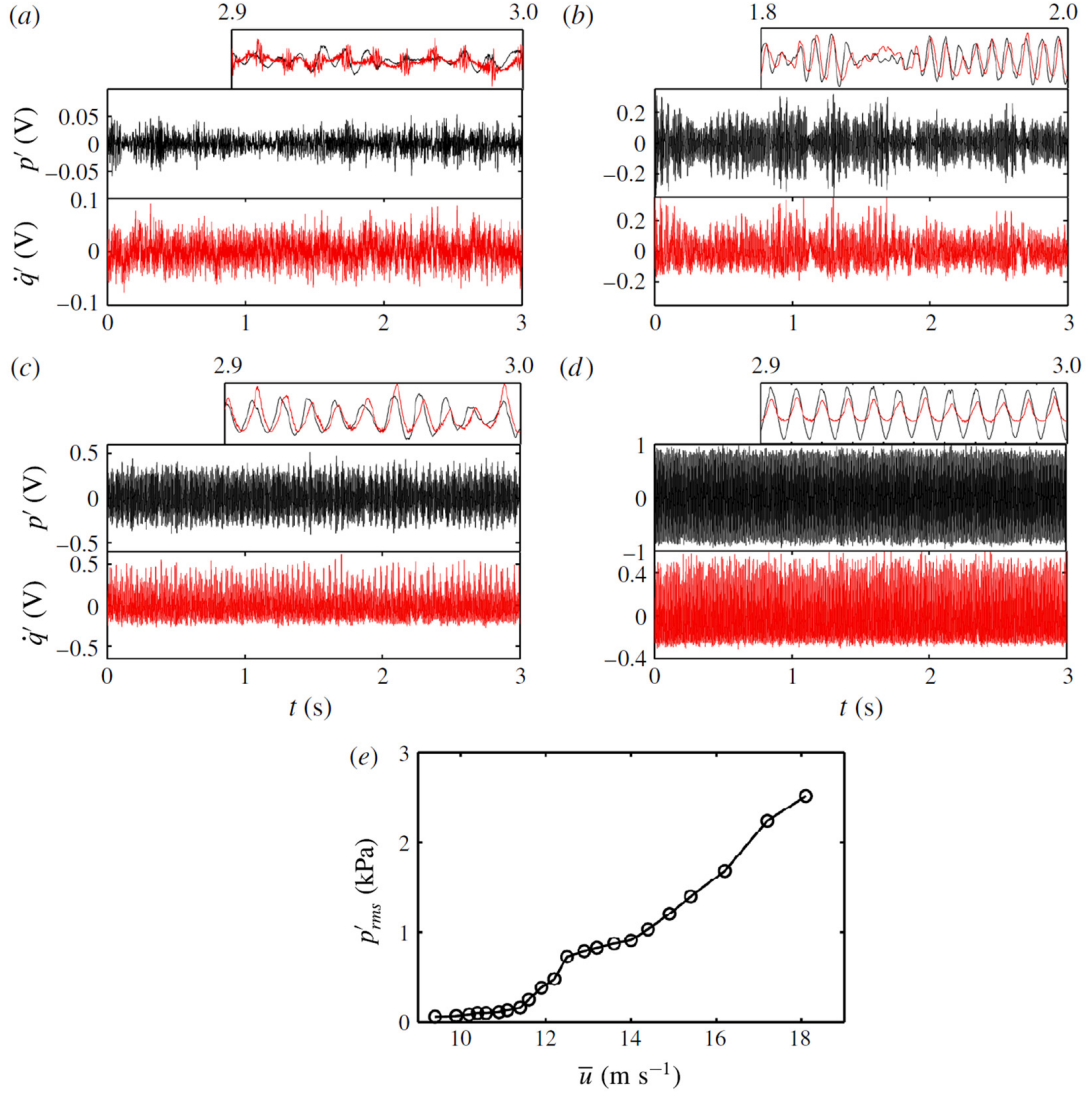


Figure 4.1: (a)-(d) The time series of the acoustic pressure ( $p'$  - black color) and the heat release rate ( $\dot{q}'$  - red color) signals obtained from experiments at  $\bar{u} = 9.4$  m/s,  $\bar{u} = 11.9$  m/s,  $\bar{u} = 13.2$  m/s and  $\bar{u} = 17.2$  m/s, respectively. The magnified views of the corresponding signals are shown in the insets over each figure. (a) A low amplitude aperiodic state, (b) an intermittency, (c) a weakly periodic limit cycle state, and (d) a strongly periodic limit cycle state of oscillations. (e) The variation of root mean square value of the acoustic pressure ( $p'_{rms}$ ) plotted against the mean velocity of the flow ( $\bar{u}$  varies from 9.4 m/s to 18.1 m/s).

With further increase in the mean flow velocity ( $\bar{u} = 17.2$  m/s), we observe the transition of the system dynamics to a state of strongly periodic oscillations (Fig. 4.1d), wherein the amplitude of the pressure oscillations nearly remains the same. Figure 4.1e shows the variation of root mean square value of the acoustic pressure ( $p'_{rms}$ ) acquired for different values of the mean flow velocities ( $\bar{u}$ ). We notice a continuous increase in the amplitude of the pressure oscillations with an increase of  $\bar{u}$  in the system. This plot suggests that the growth in the amplitude of the pressure oscillations is not a linear

function of  $\bar{u}$ , as the slope of the plot varies differently in the different regions of the system dynamics.

## 4.2 Frequency Domain Analysis of Coupled Acoustic Pressure and Heat Release Rate Fluctuations

In order to investigate the coupled interaction between the acoustic pressure and the heat release rate oscillations in the system, we plot a waterfall diagram (see Fig. 4.2a), which demonstrates the variation of power spectral density (PSD) of the signals obtained at different values of  $\bar{u}$ . Figure 4.2a shows the emergence of sharp dominant peaks in the three-dimensional plot of PSD, for both the acoustic pressure and the heat release rate oscillations at large values of  $\bar{u}$ . The presence of sharp peaks in the PSD indicates the existence of periodic oscillations in the dynamics of the system. The variation of dominant frequencies of both acoustic pressure and heat release rate oscillations, for a range of  $\bar{u}$ , is plotted in Fig. 4.2c. This plot reveals the locking behaviour of the dominant frequencies of both the signals, which happens for the first time at  $\bar{u} = 11.1$  m/s. The variation of dominant frequencies of these signals prior to the locking of frequencies (the highlighted portion of Fig. 4.2c), is further explored by plotting a zoomed in view of Fig. 4.2a and is shown in Fig. 4.2b. At low mean velocities of the flow ( $\bar{u} = 9.4$  m/s), the plot of PSD for both  $p'$  and  $\dot{q}'$  show distinct shallow bands of dominant frequencies, around 130.7 Hz for the acoustic pressure signal and around 25.3 Hz for the heat release rate signal (marked by green arrows in Fig. 4.2b). The dominant peak in the acoustic pressure spectrum corresponds to the fundamental mode of acoustics in the combustor, which is around 125 Hz (the calculation is based on the assumption of close-open geometry of the combustor having a length of 1.4 m, and an approximate value of the speed of sound equal to 700 m/s). On the other hand, we observe that the dominant frequency corresponding to 25.3 Hz in the heat release rate signal is the consequence of the underlying turbulent hydrodynamic fluctuations present in the reaction zone of the combustor. When the large-scale fluid structures shed from the dump plane impinge on the bluff-body and on the side walls of the combustor, there is a sudden release of heat in the system (observations are based on the high-speed CH\* chemiluminescence images of the flame). The frequency corresponding to these heat

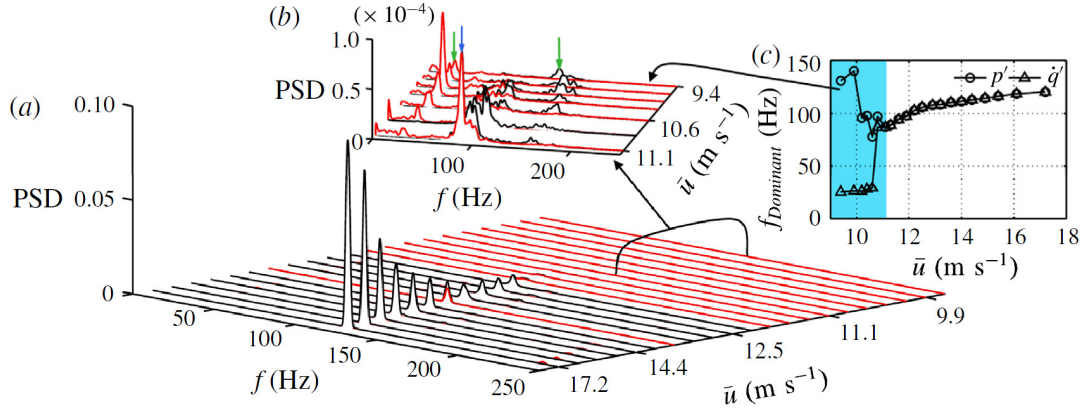


Figure 4.2: (a) The variation of the power spectral density (PSD) of both  $p'$  (black color) and  $q'$  (red color) for a range of  $\bar{u}$  from 9.4 m/s to 17.2 m/s. (b) The magnified view of the PSD for a velocity range of  $\bar{u} = 9.4$  m/s to  $\bar{u} = 11.1$  m/s. (c) The variation of the dominant frequency ( $f_{Dominant}$ ) of both  $p'$  and  $q'$  obtained for a range of  $\bar{u}$  in the system. The magnified view of PSD shown in (b) is highlighted by a blue color in (c). In (b), the separate unlocked frequency bands of  $p'$  and  $q'$ , obtained during initial value of  $\bar{u} = 9.4$  m/s, are shown by green arrows; whereas, the frequency corresponding to the first onset of frequency lock-in is shown by a blue arrow.

release fluctuations is close to 25.3 Hz, which indicates that hydrodynamics has a key role to play in the low-frequency oscillations observed in the power spectra of the heat release rate signal.

The existence of different dominant frequencies indicates that these signals are not locked during the stable operation of the combustor. A close inspection of Fig. 4.2b reveals the emergence of a secondary band of frequencies with increasing  $\bar{u}$ , which is in between the disparate frequency bands that we had for  $p'$  and  $q'$  during aperiodic oscillations. The magnitude of secondary band frequencies gradually grows with  $\bar{u}$ ; yet, the dominant frequencies of pressure and heat release rate oscillations in this secondary band still remain different (see the highlighted portion of Fig. 4.2c). The locking of these dominant frequencies happens at  $\bar{u} = 11.1$  m/s (around  $f_{lock} = 86.6$  Hz). As the heat release fluctuations are highly nonlinear, there is a possibility of excitation of higher harmonics in its spectrum. The value of secondary frequency band appears to be close to the third harmonic of the hydrodynamic frequency (i.e., 25.3 Hz) and also near the subharmonic frequency of the longitudinal mode of acoustic oscillations (125 Hz) in the system. Thus, there is a good chance that the dominant frequencies of these fluctuations could lock for the first time at the secondary frequency band during higher flow velocity conditions, which then exhibit a continuous increase with further increase

in the flow velocity. The presence of distinct frequency peaks for low mean velocities, and the locking of these peaks to a common frequency, which is in between their initial values, indicates the presence of mutual coupling (Pikovsky *et al.*, 2003) between these two oscillators of a thermoacoustic system. We further note that such an observation of switching of the dominant frequencies of  $p'$  and  $\dot{q}'$  to a secondary frequency band, which is sufficiently away from the natural acoustic mode of the duct, is different from the problem of forced flame response, wherein the low frequency associated with heat release rate fluctuations damps and a single peak arises at the forcing frequency. However, whether the phenomenon we observe can be termed as merging or adjustment of frequencies needs to be clarified through further studies.

The frequency analysis of the acoustic pressure and the heat release rate oscillations (Fig. 4.2c) reveals an important feature of the locking of dominant frequencies of these signals in our system: it happens in the intermittency state ( $\bar{u} = 11.1$  m/s), much before the onset of limit cycle oscillations ( $\bar{u} = 13.2$  m/s) in the system. The possible physical mechanisms that bring about the locking of frequencies of  $p'$  and  $\dot{q}'$ , at higher flow velocities, could be the locking of hydrodynamics and acoustics oscillators during periodic epochs of the intermittent oscillations. We further need to keep in mind that vortex shedding affects the combustion dynamics that, in turn, affect the acoustics in the system. Hence, all three of these processes are likely to play a role in the mutual synchronization during the periodic epochs of intermittency. The dominant frequencies of  $p'$  and  $\dot{q}'$  oscillators remain locked as the system dynamics changes from intermittency ( $\bar{u} = 11.1$  m/s) to limit cycle oscillations ( $\bar{u} = 17.2$  m/s). During the onset of limit cycle oscillations, we observe periodic shedding of large-scale vortices, and hence a periodic heat release rate, during every acoustic cycle. We further notice that this locked-in frequency of the signals continuously increases with  $\bar{u}$  till the final state (see the non-highlighted portion of Fig. 4.2c).

### **4.3 Synchronization Behaviour of Coupled Acoustic Pressure and Heat Release Rate Fluctuations**

To ascertain the synchronization behaviour of the acoustic pressure and the heat release rate oscillations, we use a statistical measure of synchronization based on the recurrence

plots known as the probability of recurrence,  $P(\tau)$  (refer Section 2.5.2 in Chapter 2). We compute  $P(\tau)$  for  $p'$  and  $q'$ , and then compare the coincidence of the peaks of  $P(\tau)$  obtained from these signals in order to analyse the synchrony between them (Romano *et al.*, 2005).

Figure 4.3a shows the plot of  $P(\tau)$  as a function of the time lag  $\tau$ , for both the acoustic pressure and the heat release rate signals, obtained during the aperiodic state (as shown in Fig. 4.1a). We see from the figure that there is no correspondence between the peaks of  $P(\tau)$  of these signals. This confirms that the two oscillators are not in synchrony. On the other hand, when the system dynamics undergoes a transition to limit cycle oscillations (see Figs. 4.1c,d) we see a perfect locking of the positions of the peaks of  $P(\tau)$  of both the signals, as shown in Figs. 4.3b,c. The locking of the positions of peaks confirms the synchronization between acoustic pressure and heat release rate oscillations. Furthermore, the absence of exact locking of the heights of these peaks in Fig. 4.3b indicates that we have phase synchronization (PS) in the system (Romano *et al.*, 2005). Figure 4.3c reveals the perfect coincidence of the height as well as the position of the peaks of the probability of recurrence (Fig. 4.3c), obtained from the acoustic pressure and the heat release rate oscillations, suggesting the presence of generalized synchronization (GS) in the system (Romano *et al.*, 2005). Previous studies in synchronization have reported chaotic oscillators synchronizing in the chaotic state (Boccaletti *et al.*, 2002a), or periodic oscillators synchronizing in the periodic state (Blekhman *et al.*, 1995). However, in our system, the chaotic oscillators transition to the periodic state as they synchronize. This makes the study of such a synchronization transition quite interesting.

We, therefore, analyse the synchronization behaviour of acoustic pressure and heat release rate oscillators during intermittency (see Fig. 4.4), as this is the intermediate state of the transition. Since the intermittent oscillations consist of alternating occurrences of high amplitude periodic and low amplitude aperiodic oscillations, we plot  $P(\tau)$  for short windows of the periodic (Fig. 4.4b) and the aperiodic (Fig. 4.4c) regions of the signals. The plot of  $P(\tau)$  for a periodic window (Fig. 4.4b), corresponding to both  $p'$  and  $q'$ , shows the locking of the positions of peaks without locking of their heights, which confirm the phase synchronization of two signals during the periodic epoch. Doing the same for the aperiodic region, we see a mismatch in the locations as well as the heights of the peaks; this depicts the desynchronized behavior during the

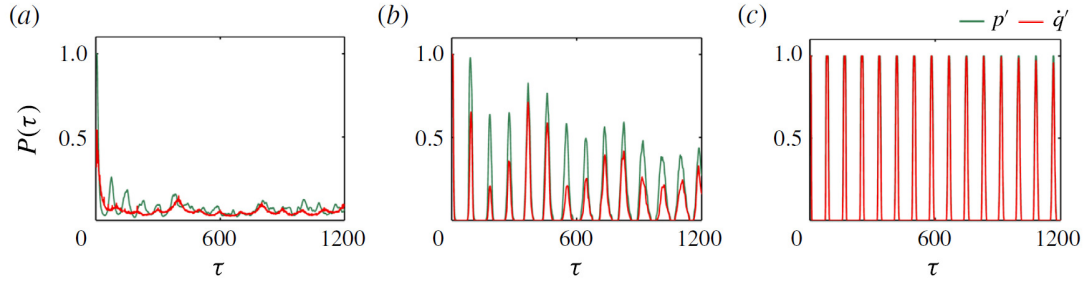


Figure 4.3: The plots of probability of recurrence ( $P(\tau)$ ) of a phase space trajectory at different values of time lags ( $\tau$ ) for  $p'$  (green colour) and  $q'$  (red colour). (a)-(c) represents the plots of  $P(\tau)$  corresponding to three states of synchronization viz., desynchronization (aperiodic oscillations), phase synchronization (periodic oscillations) and generalized synchronization (periodic oscillations) obtained at  $\bar{u} = 9.4$  m/s,  $\bar{u} = 13.2$  m/s and  $\bar{u} = 17.2$  m/s, respectively. The parameters used in plotting are embedding dimension = 12, time delay = 2 ms, recurrence threshold = 25% of the maximum size of the attractor. A data set containing 3000 points (shown for 1200 points).

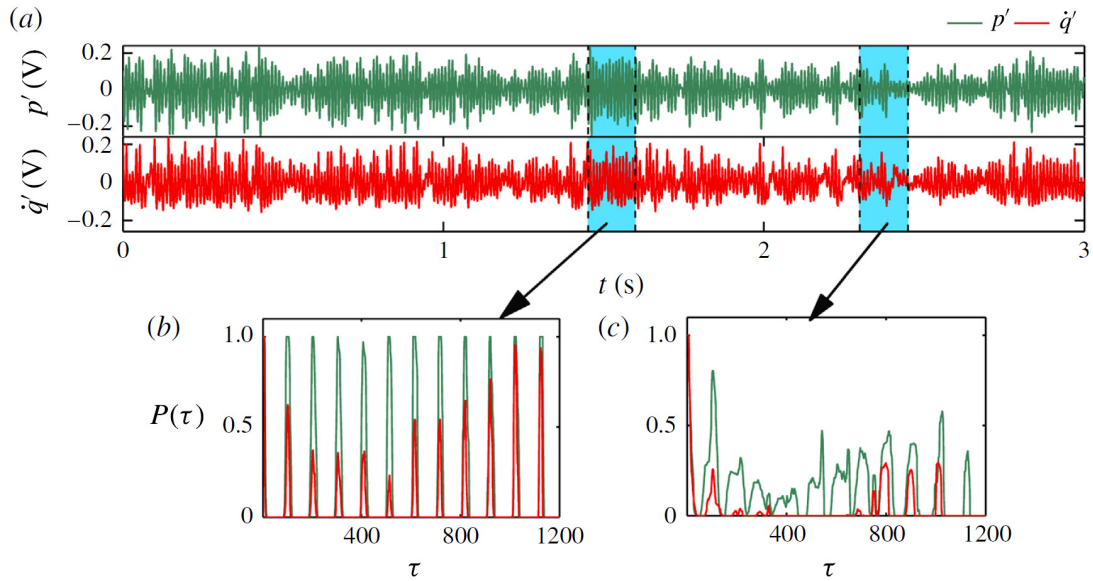


Figure 4.4: (a) Plots of time series of  $p'$  (green colour) and  $q'$  (red colour) acquired during the intermittency state at  $\bar{u} = 11.6$  m/s. (b), (c) The plots of  $P(\tau)$  shown for periodic and aperiodic regions of both  $p'$  and  $q'$ , respectively. The parameters used in plotting (b) and (c) are embedding dimension = 12, time delay = 2 ms, recurrence threshold = 25% of the maximum size of the attractor. A data set containing 3000 points (shown for 1200 points).

aperiodic phase. The alternate switching of the coupled oscillators between synchronized and desynchronized behaviors describes the property of intermittent synchronization in the system. And, since the two oscillators in our system are phase synchronized in the periodic region and desynchronized in the aperiodic region, such a coupling behaviour of the system is referred to as intermittent phase synchronization (IPS). This

state shows that the oscillators in our system gradually change their underlying dynamics from aperiodic to periodic as they synchronize. Recently, Mondal *et al.* (2017b) investigated the spatiotemporal synchronization behaviour of the local heat release rate in the flame with the global acoustic field of the duct. During intermittency, their study demonstrates the coexistence of patches of both synchronized periodic oscillations and desynchronized aperiodic oscillations in the reaction zone. Furthermore, these patterns of spatial synchrony and desynchrony interchange as the flow convects downstream, which they referred to as a breathing chimera like state. Therefore, IPS is arguably an apt intermediate state that we observe during the transition of combustion dynamics from a state of completely desynchronized oscillations to a state of perfectly phase synchronized oscillations. Thus, it is evident from Figs. 4.3 and 4.4 that, in the turbulent flame combustor examined in the present study, the desynchronized oscillations pave the way to PS through IPS, and subsequently to GS with an increase in the mean velocity of the flow ( $\bar{u}$ ).

#### 4.4 Comparison of Phase Synchronization and Generalized Synchronization States

As discussed earlier, the unstable operation of a turbulent combustor has been traditionally perceived in terms of limit cycle oscillations (Lieuwen, 2002). We, however, observe two different types of limit cycles in our system, which exhibit different dynamical characteristics. We call them weakly correlated (phase synchronization) and strongly correlated (generalized synchronization) limit cycle oscillations. In order to identify the distinguishing features of these two states, we compare the temporal variation in instantaneous phase difference (relative phase) between the acoustic pressure and the heat release rate oscillations. The instantaneous phases of these signals are calculated using the Hilbert transform. Figures 4.5a,b show the relative phase plots ( $\Delta\phi_{p',q'}$ ) of these signals obtained during PS and GS states, respectively. The fluctuation of relative phase around a constant phase shift (as shown in Figs. 4.5a,b) suggests the synchronization of the signals of the coupled oscillator system (Pikovsky *et al.*, 2003). The enlarged view of the relative phase for PS state shows a noisy behavior (Fig. 4.5a), while for the GS state shows an apparently periodic behavior (Fig. 4.5b). In Fig. 4.5c,

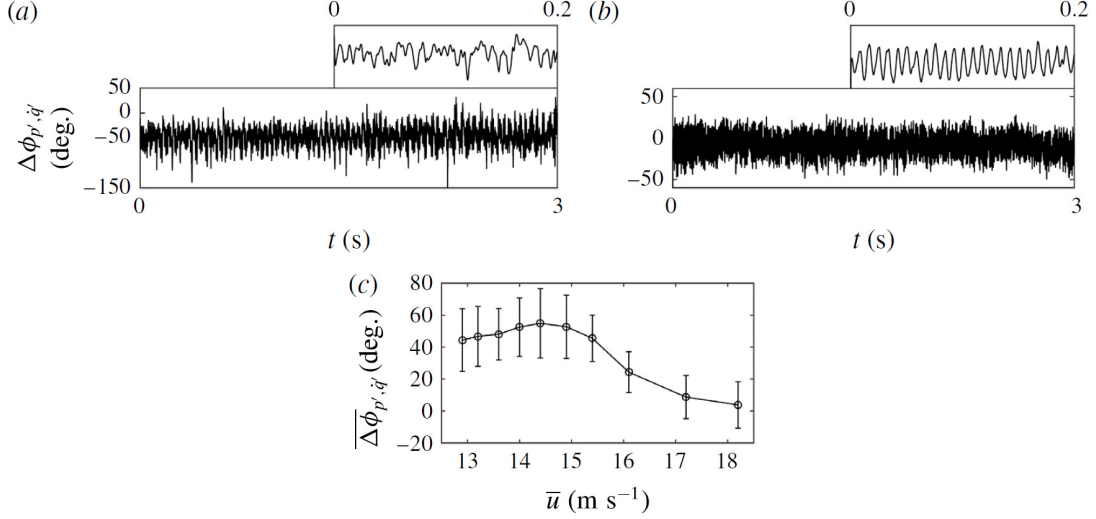


Figure 4.5: (a), (b) The temporal variation of the relative phase ( $\Delta\phi_{p',q'}$ ) between  $p'$  and  $q'$  calculated using the analytic signal approach based on the Hilbert transform (refer Section 2.5.1 in Chapter 2). (a) The phase synchronization ( $\bar{u} = 13.2$  m/s) and (b) the generalized synchronization ( $\bar{u} = 17.2$  m/s) state of oscillations. (c) The plot depicting the variation of mean value of relative phase ( $\langle \Delta\phi_{p',q'} \rangle$ ) with mean velocities of the flow observed during the transition from PS to GS states.

we plot the temporal mean value of the relative phase ( $\langle \Delta\phi_{p',q'} \rangle$ ), wrapped in the interval -180 to 180 degrees, versus different values of the mean velocities of the flow. The plot shows the velocity range corresponding to PS and GS states alone. During PS state, we notice that the mean value of the relative phase remains close to 50 degrees, whereas, during GS state (figure 6b), it approaches a value closer to zero degrees (refer Fig. 4.5c). Thus, we observe the reduction in the mean phase angle between acoustic pressure and heat release rate fluctuations as the system dynamics transition from PS to GS state.

Recall that when two oscillators are in GS, there exists a functional relation between the dynamics of these oscillators (Rulkov *et al.*, 1995). Say, we have two non-identical oscillators viz.,  $X(t)$  and  $Y(t)$ . When these oscillators are in the state of GS, there exists a functional relationship between them, which can be expressed as  $Y(t) = F(X(t))$ . It means that the response of  $Y(t)$  can be uniquely determined from  $X(t)$ , if the functional form of their relationship is known (Pyragas, 1998). However, the determination of the exact functional form for experimental signals is not straightforward.

In our system, we can obtain an approximate functional relation between the acoustic pressure ( $p'$ ) and the unsteady heat release rate ( $q'$ ) during the GS state, using the

knowledge obtained from experiments. During the GS state (see Fig. 4.6a), the visual inspection of the acoustic pressure signal hints the features of a sinusoidal function, whereas the heat release rate signal shows the features of a spiky signal. By saying spiky, we mean that the signal is relatively flat for some time, then rises up, decays and becomes flat again. The behavior of these signals can then be qualitatively mimicked by the following equations

$$P' = [a_1 + n_{p1}(t)] \times \sin[\omega t \pm \phi_1 + n_{p2}(t)] \quad (4.1)$$

$$Q' = [a_1 + n_{q1}(t)] \times \sin[\omega t + a_3 \sin(\omega t \pm \phi_2) + n_{q2}(t)] \quad (4.2)$$

where  $P'$  and  $Q'$  are the assumed functional forms of  $p'$  and  $q'$ ,  $\omega$  is the angular frequency of the signals,  $a_1, a_2, a_3$  are the constants, and  $\phi_1$  and  $\phi_2$  are the initial phases of  $P'$  and  $Q'$ , respectively.  $n_{p1}, n_{p2}, n_{q1}$ , and  $n_{q2}$  are Gaussian white noise terms added to the amplitude and the phase parts of the signals.

The values of the constants in the assumed functional forms of  $P'$  and  $Q'$  are derived from statistical properties of the corresponding  $p'$  and  $q'$  signals obtained from experiments. This is to ensure an approximate fit between the data generated from numerical results and the signals obtained from experiments.

The relative phase between the two signals can then be expressed as,

$$\begin{aligned} \Delta\phi &= [\omega t + a_3 \sin(\omega t \pm \phi_2)] - [\omega t \pm \phi_1] + G(t) \\ &= a_3 \sin(\omega t \pm \phi_2) \pm \phi_1 + G(t) \end{aligned} \quad (4.3)$$

where  $G(t)$  is the phase noise present in the relative phase of both  $P'$  and  $Q'$ . The parameters selected in plotting Fig. 4.6b are  $a_1 = 0.8$ ,  $a_2 = 0.35$ ,  $a_3 = 0.7$ ,  $\omega = 120.2$  Hz,  $\phi_1 = 0$  rad,  $\phi_2 = \pi/2$  rad, and the strength of noise is 0.05. Figure 4.6b qualitatively simulates the features of the acoustic pressure and the heat release rate oscillations observed in experiments during the GS state (Fig. 4.6a). The plot of the relative phase between two signals obtained from the experiments (Fig. 4.6c) is qualitatively captured by the proposed functional form for these signals (Fig. 4.6d). These analogies between the experimental results and the assumed functional relation are completely drawn from the characteristics of the acoustic pressure and the heat release oscillations observed during the GS state. In reality, the functional relationship may be considerably more

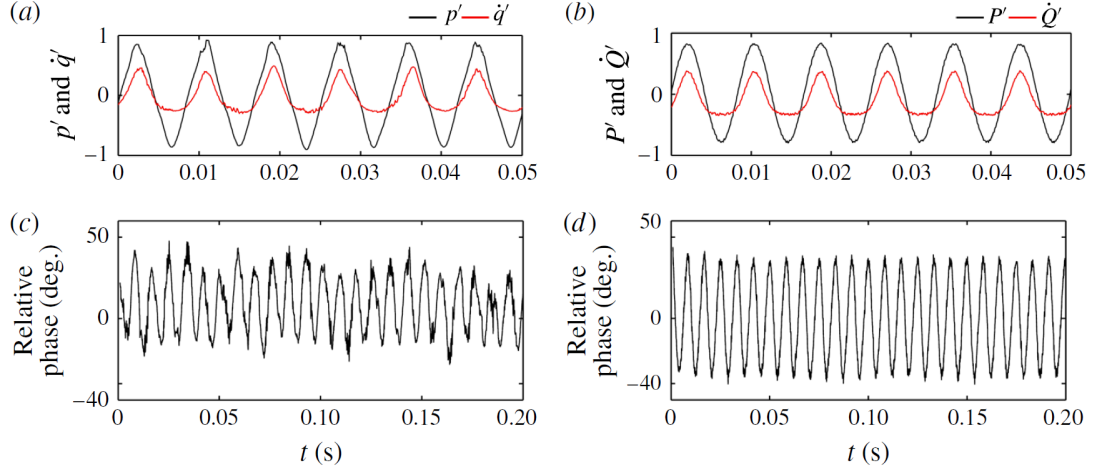


Figure 4.6: (a) A portion of the time series of  $p'$  (black color) and  $q'$  (red color) obtained from experiments during the GS state ( $\bar{u} = 17.2$  m/s). (b) A portion of the signal obtained from an assumed functional form for both acoustic pressure ( $p'$  - black color) and heat release rate ( $q'$  - red color) oscillations. (c), (d) are the temporal variation of the relative phases obtained from Hilbert transform for the signals shown in (a), (b) respectively.

complicated involving different combinations of sine and cosine functions along with inherent turbulent fluctuations present in the combustion system. The identification of the exact functional form of these signals is difficult, mainly because the complex interaction between acoustic pressure and heat release rate oscillations is still not completely known.

We now try to elucidate the possible physical reason for having separate PS and GS states in our turbulent flame combustor. Towards this purpose, we calculate the amplitude difference (Fig. 4.7a) and the time difference (Fig. 4.7b) between the consecutive cycle peaks of the acoustic pressure and the heat release rate oscillations respectively, and subsequently compare them for the PS (Figs. 4.7c,d) and GS (Figs. 4.7e,f) states. The time at which  $q'$  reaches a local maximum is referred to as a kicking time (Fig. 4.7b). The reason for using such a terminology is to relate it to the kicked oscillator model (Matveev and Culick, 2003). The term kick refers to the release of heat in a very short time span when the shed vortex from the dump plane impinges on the bluff body. This sudden generation of heat leads to the spiky behavior in  $q'$ . Figures 4.7d,f show the difference in the impingement time (i.e., the kicking time) of two consecutive vortices (normalized by the period,  $T = 1/f_{Dominant}$ ) obtained during the PS and GS states, respectively. We observe a wide variation in the kicking times of the vortex during PS

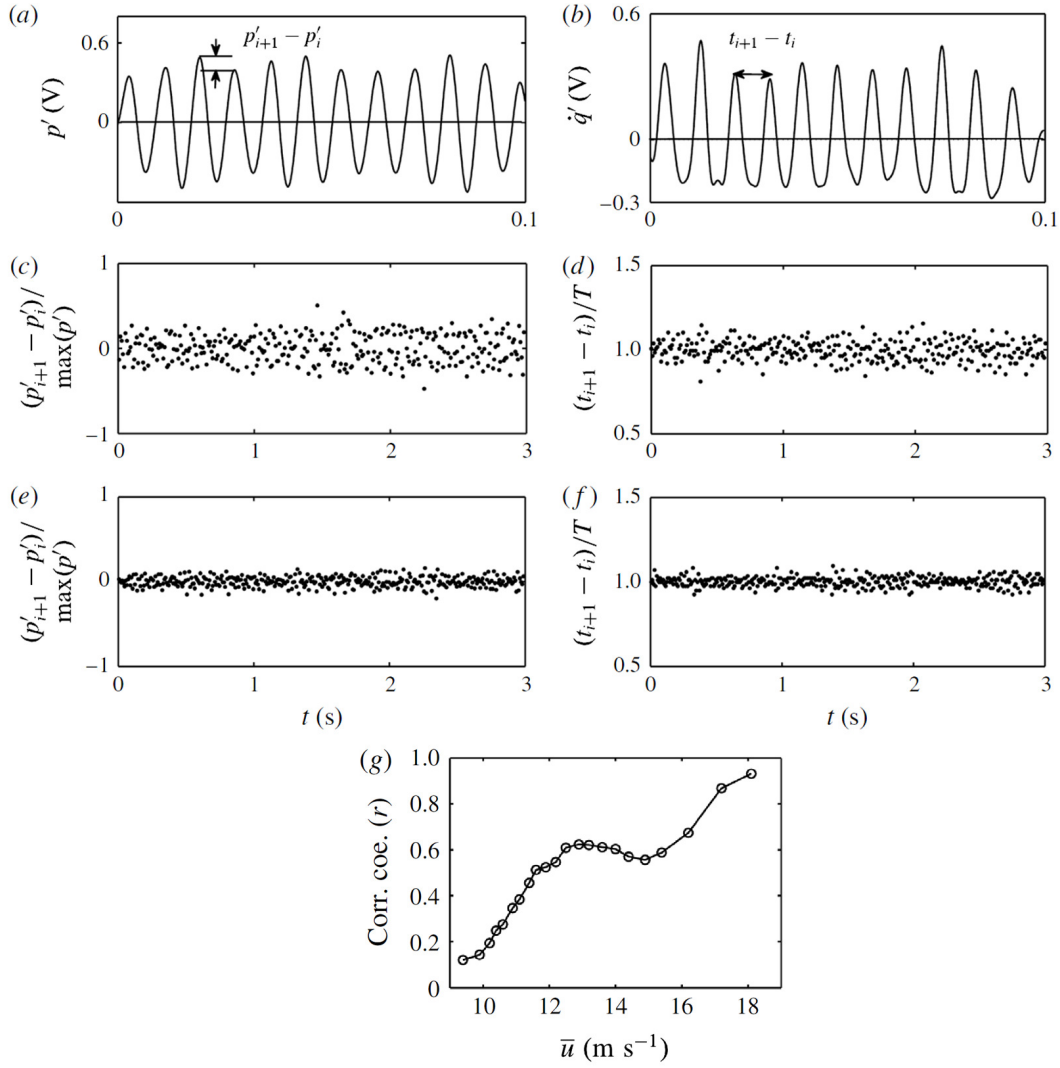


Figure 4.7: (a) The portion of acoustic pressure and (b) heat release rate oscillations depicting the computation procedure for the amplitude difference and the kicking times, respectively. (c), (e) The temporal variation of the amplitude difference (normalized by signal global maxima) between consecutive peaks of the acoustic pressure oscillations obtained for PS and GS states, respectively. (d), (f) The temporal variation of the time difference (normalized by signal period  $T = 1/f_{Dominant}$ ) between the consecutive peaks of the heat release rate oscillations, referred to as kicking times, obtained for PS and GS states, respectively. PS state corresponds to  $\bar{u} = 13.2$  m/s and GS state corresponds to  $\bar{u} = 17.2$  m/s. (g) A variation of the cross-correlation coefficient ( $r$ ) between  $p'$  and  $q'$  with different values of mean velocity of the flow ( $\bar{u}$ ).

as compared to what is seen during GS.

The variation in the kicking times is possibly reflected in the irregular nature of amplitudes of the acoustic pressure oscillations observed during PS. Figures 4.7c,e show plots of the amplitude difference between the consecutive cycles of the acoustic pres-

sure ( $p'$ ) signal, normalized by the global maxima ( $p'_{max}$ ) of the respective signal, for the PS and GS states, respectively. We notice that the cycle-to-cycle variation in the amplitude of  $p'$  is comparatively much larger during PS state than that during GS state. The consequence of such cycle-to-cycle variation in the kicking times as well as in the amplitudes of the signals, observed during PS and GS, is further investigated by plotting a linear measure of correlation between  $p'$  and  $q'$  for the whole range of  $\bar{u}$  used in this study (see Fig. 4.7g). The cross-correlation coefficient ( $r$ ) (or Pearson's coefficient) is a measure of the strength of the linear relationship between the two signals. It further helps in determining the synchronization of amplitudes of the signals obtained from a coupled oscillator system (Gonzalez-Miranda, 2002; Bove *et al.*, 2004), and is given by the following equation

$$r = \frac{n \sum_{i=1}^n x_i y_i - \sum_{i=1}^n x_i \sum_{i=1}^n y_i}{[(n \sum_{i=1}^n x_i^2 - (\sum_{i=1}^n x_i)^2)(n \sum_{i=1}^n y_i^2 - (\sum_{i=1}^n y_i)^2)]^{0.5}} \quad (4.4)$$

where  $x_i$  and  $y_i$  are the samples of the bivariate data obtained from the experiments and  $n$  is the total number of samples in the signal.

The values of  $r$  range from -1 to +1;  $r = -1$  corresponds to strong negative correlation and  $r = 1$  corresponds to a strong positive correlation between the signals. The value of  $r = 0$  indicates zero linear correlation between the signals. In our system, we observe the values of  $r$  greater than zero suggesting the presence of a positive correlation between acoustic pressure and heat release rate oscillations (Fig. 4.7g). We notice an increase in the values of linear correlation as the system dynamics transitions from combustion noise to a final state of limit cycle oscillation. During PS, the weak correlation of the oscillators is reflected in the relatively low values of  $r$ , which is around 0.5-0.6. Although the amplitude of the acoustic pressure oscillations shows a significant increase for all values of the mean flow velocity ( $\bar{u} = 12.9$  m/s to 15.4 m/s) during PS (Fig. 4.1e), the values of  $r$  show a marginal variation during this state (Fig. 4.7g). The transition from PS to GS results in the increase in the value of  $r$  from a value close to 0.5 to a value close to 1. Thus, the oscillators in GS ( $\bar{u} = 16.1$  m/s to 18.5 m/s) in our system are very strongly correlated. Change in the behaviour of both the kicking times and the cycle-to-cycle amplitude variation have a major impact on the linear correlation during the transition from PS to GS state.

## 4.5 Conclusions

We studied the dynamical transition of a turbulent combustion system from stable to unstable operation in the framework of synchronization theory. Using a measure based on recurrence plots, we showed that the onset of thermoacoustic instability in the systems involving turbulent flow is a synchronization phenomenon of two mutually coupled non-identical oscillators viz., the acoustic field in the confinement and the turbulent reactive flow present in the system. A bidirectional coupling that exists between these oscillators is responsible for their transition from a non-synchronous state of aperiodic oscillations to a synchronous state of periodic oscillations with a variation in the mean velocity of the flow. The system dynamics culminates in a state of generalized synchronization (GS), having gone through intermittent phase synchronization (IPS) and phase synchronization (PS). During IPS, the oscillators are periodic in the synchronized phase while harboring aperiodicity in the desynchronized phase.

Furthermore, we characterized the distinguishing features of PS and GS states. These two states correspond to two different types of limit cycle oscillations; one that is weakly correlated, the other being strongly correlated. The observation of the presence of two types of limit cycle oscillations seems to have been overlooked in the study of turbulent combustion systems. The variation of the linear correlation coefficient between the signals of coupled subsystems showed a significant increase, during the transition from PS to GS state. The observation of kicking times showed a wide variation in the cycle-to-cycle amplitude of acoustic pressure signals during PS, whereas, such amplitude variation is nearly constant during GS. Thus, during GS, a stronger form of lock-in mechanism is observed in the system.

Another experimental study on the coupled behaviour of the acoustic field and the unsteady heat release rate field is performed on a swirl-stabilized combustor (see APPENDIX A). The qualitatively similar behaviour of the synchronization transition, as compared to the bluff body stabilized combustor, is observed in the swirl combustor. A detailed analysis of the coupled behaviour of the acoustic pressure and the heat release rate fluctuations in the time-frequency domain is provided. Further, a comparison of the spatiotemporal fields of phase synchronization and generalized synchronization states is also performed.

## CHAPTER 5

# INTERMITTENCY, SYNCHRONIZATION AND COLLECTIVE INTERACTION IN A TWO-PHASE FLOW SPRAY COMBUSTOR

In the previous chapter, we studied the transition of a turbulent gas fired combustor operation from the state of combustion noise to thermoacoustic instability through intermittency. Various studies have shown the occurrence of intermittency in other gaseous flame combustors (Gotoda *et al.*, 2014; Murugesan and Sujith, 2015; Domen *et al.*, 2015; Sampath and Chakravarthy, 2016; Wilhite *et al.*, 2016; Unni and Sujith, 2015; Kheirkhah *et al.*, 2017; Ebi *et al.*, 2018). The intermittency route to thermoacoustic instability is further characterized to investigate the type of intermittency. Knowing the type of intermittency gives the information about the kind of bifurcation the system undergoes while transitioning from one state to another through intermittency. Nair *et al.* (2013) mentioned the existence of type-II or type-III intermittency in the turbulent bluff body combustor. Furthermore, Unni and Sujith (2017) compared the intermittent oscillations observed in the turbulent combustor prior to both thermoacoustic instability and flame blowout, and confirmed the presence of type-II intermittency in both the cases. Murugesan and Sujith (2018) showed the existence of type-II intermittency in the turbulent lifted jet flame combustor. Furthermore, the presence of intermittency prior to thermoacoustic instability as well as flame blowout has aided various researchers in devising different control measures that can forewarn the occurrence of such instabilities (Nair *et al.*, 2014; Nair and Sujith, 2014; Unni and Sujith, 2015; Unni *et al.*, 2015; Murugesan and Sujith, 2016; Godavarthi *et al.*, 2017).

In spite of these recent advances in gaseous combustion systems in understanding the route to thermoacoustic instability, the existence of such studies in spray combus-

---

The results presented in this chapter are published in S. A. Pawar, R. Vishnu, M. Vadivukkarasan, M. V. Panchagnula and R. I. Sujith, Intermittency Route to Combustion Instability in a Laboratory Spray Combustor *Journal of Engineering for Gas Turbines and Power*, 138(4), 041505:1-8, (2016).

S. A. Pawar, M. V. Panchagnula and R. I. Sujith, Phase Synchronization and Collective Interaction of Multiple Flamelets in a Laboratory Scale Spray Combustor *Proceeding of the Combustion Institute*, (Accepted).

tion systems is rare. Most combustion systems in practice utilize liquid fuels as a source of energy. Further, most of the previous studies (numerical as well as experimental) on spray combustion systems were focused on characterizing the effect of acoustic oscillations (self-excited or externally forced) on the physical processes such as atomization, evaporation, and combustion of the spray combustor observed during the state of thermoacoustic instability (Young, 1995). On the contrary, the characterization of the route through which such instabilities are developed in spray combustion systems has not yet received much attention. Therefore, it is important to understand the phenomena of the onset of thermoacoustic instabilities in such systems.

In this chapter, we investigate the phenomenon of occurrence of a thermoacoustic instability in a laboratory scale spray combustion system (shown in Fig. 3.2, Chapter 3). A unique design of the spray injector is fabricated to generate a droplet spray across the combustor section. The stability of the system dynamics is tested against the variation of two control parameters: (a) the location of flame inside the combustor, and (b) the mass flow rate of fuel for a fixed value of mass flow rate of air. Various tools from the dynamical systems theory such as the statistical distributions of durations of aperiodic (turbulent) phases observed between bursts of periodic oscillations with respect to the control parameter, first return map and recurrence plot (RP) analysis are used to quantify the type of intermittency. We, further, study the coupled behaviour of the acoustic pressure fluctuations and the global heat release rate fluctuations during the intermittency route to thermoacoustic instability. We also examine the collective interaction of coupled multiple flamelets anchored at the flame holder with the acoustic field of the confinement during the different dynamical states observed in the combustor.

## **5.1 Characterization of Transition to Thermoacoustic Instability Using Acoustic Pressure Signal**

### **5.1.1 Intermittency Route to Thermoacoustic Instability**

In this section, we study the effect of variation of two different control parameters (i.e., the location of the flame and the fuel mass flow rate) on the transition of the system behaviour from a state of combustion noise to thermoacoustic instability via intermittency.

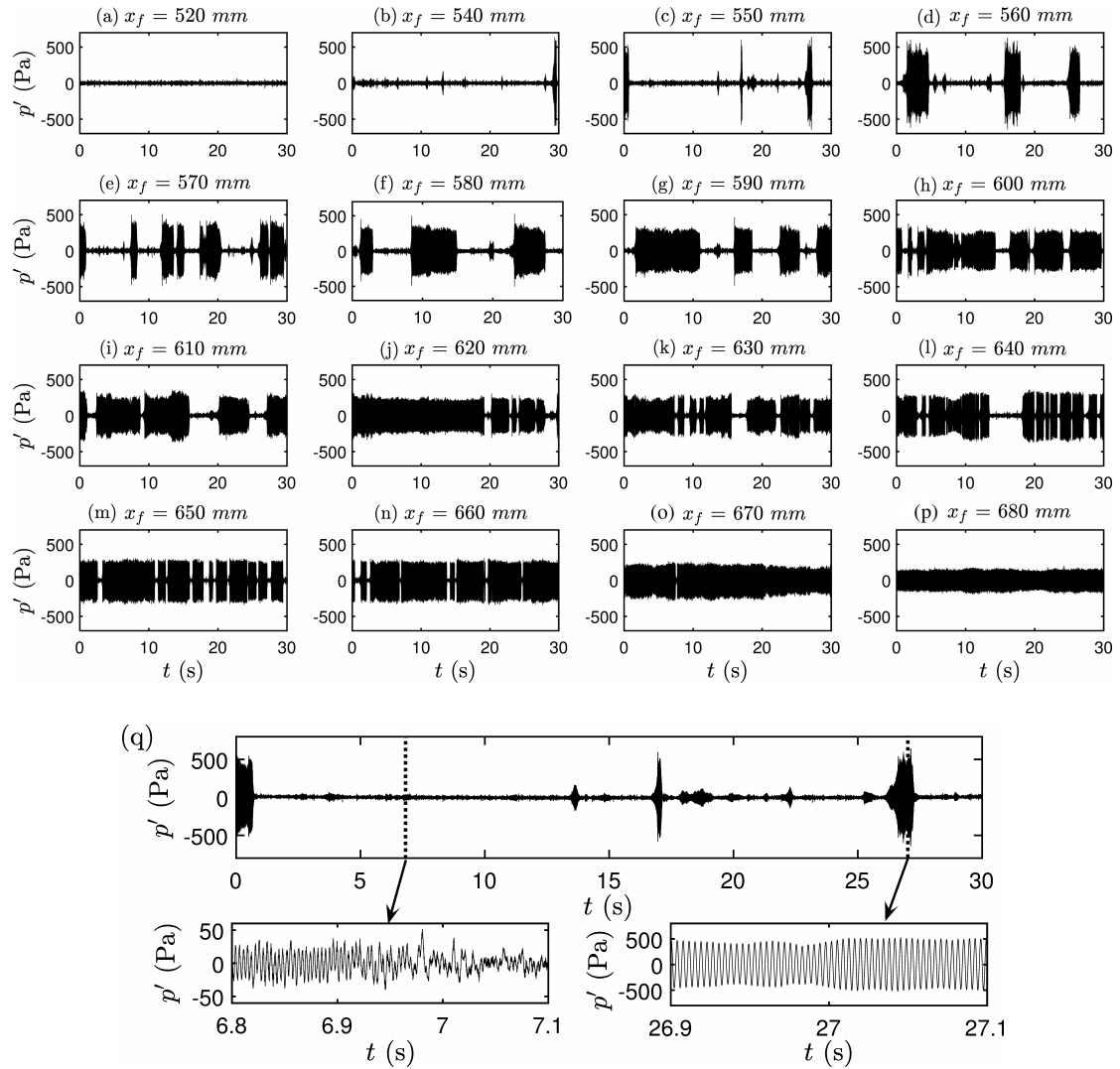


Figure 5.1: Time series data of the acoustic pressure fluctuations acquired at different locations of flame in the combustor. (a) combustion noise state ( $x_f = 520$  mm), (b)-(o) intermittency state ( $x_f = 540$  mm to  $x_f = 670$  mm) and (p) limit cycle state ( $x_f = 680$  mm). These plots show the intermittency route to limit cycle oscillations in a spray combustion system. (q) A magnified portion of intermittency signal obtained at  $x_f = 550$  mm shows the low amplitude aperiodic oscillations and the burst of high amplitude periodic oscillations present in the signal. The value of air and fuel flow rates are fixed at  $\dot{m}_a = 100$  slpm and  $\dot{m}_f = 8$  mlpm, respectively.

During each experiment, only one control parameter is varied at a time. We first show the effect of a change in the location of the flame inside the combustor for a constant value of the equivalence ratio. Fixing equivalence ratio ensures the fixing of values of mass flow rates of fuel and air in the system. The flame location is varied from the lower half ( $x_f = 480$ mm) to the upper half ( $x_f = 740$ mm) of the combustor, in a step size of 10 mm, using a traverse mechanism. The dynamics of the combustor is analysed from the recordings of acoustic pressure signal acquired at each location of the flame inside

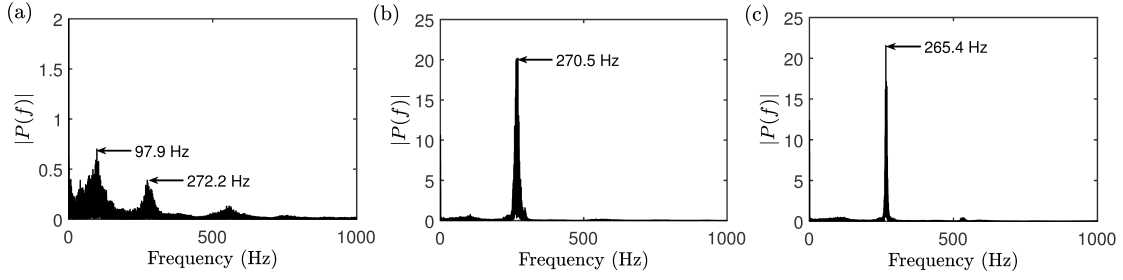


Figure 5.2: The amplitude spectrum of the acoustic pressure signals acquired during the state of (a) combustion noise ( $x_f = 520$  mm), (b) intermittency ( $x_f = 590$  mm), and (c) limit cycle ( $x_f = 680$  mm) oscillations in the combustor.

the duct. Figure 5.1 displays a sequence of time series plots of the acoustic pressure fluctuations acquired at different locations of the flame inside the duct. With variation in the flame location, we notice that dynamics of the system transitions from a state of low amplitude aperiodic oscillations (combustion noise, Fig. 5.1a) to a state of high amplitude limit cycle oscillations (thermoacoustic instability, Fig. 5.1p) via a regime of intermittency (Figs. 5.1b-o). During intermittency, a series of bursts of periodic oscillations occur in between the relatively silent regions of aperiodic oscillations in an apparently random manner (see Fig. 5.1q). During the onset of intermittency ( $x_f = 540$  mm), we notice that the bursts are short-lived, large amplitude periodic oscillations. As the flame location is further increased, we note an increase in the size (duration) of the bursts with the corresponding decrease in their amplitudes. Eventually, at a critical value of the flame location, all bursts get merged to constitute the sustained periodic oscillations (limit cycle) in the system dynamics.

The amplitude spectra of acoustic pressure signals obtained during three major states of the combustion dynamics, i.e., combustion noise, intermittency and thermoacoustic instability are shown in Figs. 5.2a-c, respectively. We observe two low amplitude bands of broadband frequencies during the state of combustion noise (Fig. 5.2a). In these bands, the lower frequency band ( $f_{dominant} = 97.9$  Hz) possibly corresponds to the heat release rate fluctuations present in the flame, whereas the larger frequency band ( $f_{dominant} = 272.7$  Hz) shows the frequencies associated with the natural acoustic mode of the duct. As the system dynamics enter into a state of intermittency (Fig. 5.2b) and limit cycle (Fig. 5.2c), a sharp frequency peak corresponding to the periodic oscillations is observed in the frequency range of 260 to 280 Hz. This frequency range matches well with the value of second longitudinal mode of the acoustic oscillations developed in a close-open configuration of the setup ( $f_n = 3c/4L$ , where  $c = 360$  m/s,

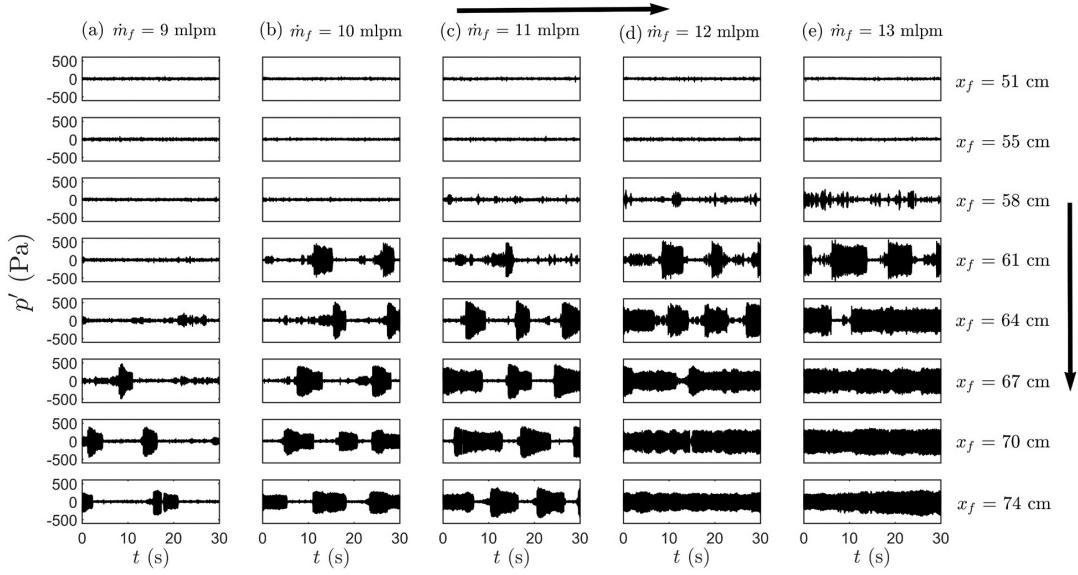


Figure 5.3: (a)-(e) The time series of acoustic pressure representing the effect of increasing fuel flow rate ( $\dot{m}_f$ ) on the occurrence of intermittency and eventually the onset of thermoacoustic instability when the control parameter, the location of flame in the duct ( $x_f$ ), is varied in the system. The value of air flow rate is fixed at  $\dot{m}_a = 120$  slpm during all experiments.

$L = 1$  m). The effect of a change in fuel flow rate for a constant air flow rate on the occurrence of intermittency or on the transition of the system dynamics from combustion noise to thermoacoustic instability is further investigated in Fig. 5.3. The increase in fuel flow rate has effect on the increase in energy content of the combustible of fuel-air mixture.

Initially, the value of fuel flow rate is kept fixed at a low value and the location of flame is varied from  $x_f = 51$  cm to 74 cm. The experiments are repeated for a gradual increase in the value of fuel flow rate. For the lower value of the fuel flow rate ( $\dot{m}_f = 9$  mlpm), we observe that the intermittency occurs at a larger distance from the open end of the combustor (Fig. 5.3a). The number of bursts observed in the signal is also low. Further, we do not observe the onset of thermoacoustic instability at this condition of equivalence ratio. With further increase in  $\dot{m}_f$  ( $= 10$  and  $11$  mlpm), we notice advancement (or early occurrence at lower  $x_f$  as compared to  $\dot{m}_f = 9$  mlpm) in the onset of intermittency, however, the occurrence of thermoacoustic instability is still not observed in the system dynamics (Figs. 5.3b,c). However, we notice an increase in the frequency of the occurrence of bursts in the signals for  $\dot{m}_f = 10$  and  $11$  mlpm, as compared to the condition of  $\dot{m}_f = 9$  mlpm. When  $\dot{m}_f = 12$  mlpm, we see a further advancement in the onset of intermittency at lower  $x_f$  in the acoustic pressure signal

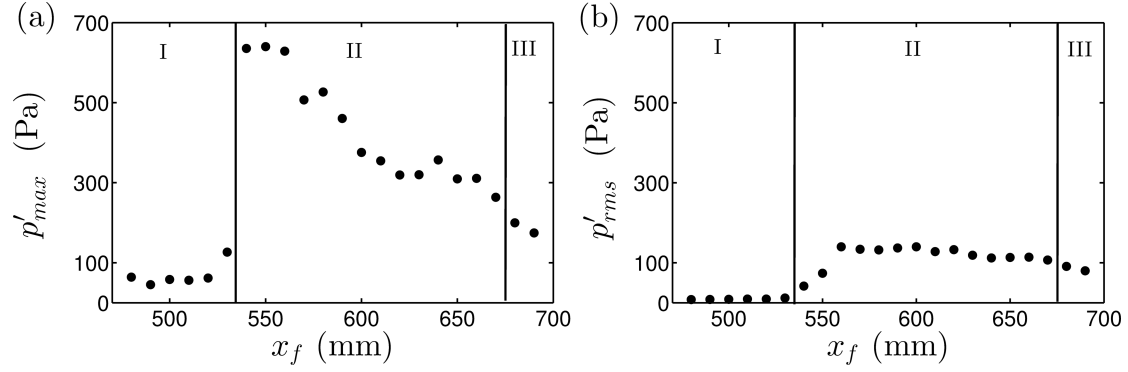


Figure 5.4: The variation of (a) a global maximum ( $p'_{max}$ ) and (b) a root mean square ( $p'_{rms}$ ) value of the acoustic pressure signal versus the location of flame ( $x_f$ ) inside the combustor. The plots are divided into three distinct regions of system dynamics as (I) low amplitude aperiodic oscillations, (II) intermittency, and (III) limit cycle oscillations. The value of air and fuel flow rates are fixed at  $\dot{m}_a = 100$  slpm and  $\dot{m}_f = 8$  mlpm, respectively.

(Fig. 5.3d). We also observe the occurrence of lengthy bursts with small regions of aperiodic oscillations in between the consecutive bursts. At this condition of fuel flow rate, we notice the presence of sustained limit cycle oscillations in the system dynamics (refer  $x_f = 74$  cm in Fig. 5.3d). With further increase in  $\dot{m}_f$  (13 mlpm), we see that the occurrence of sustained thermoacoustic instabilities happens even at lower  $x_f$  in the system (refer  $x_f = 67$  cm in Fig. 5.3e). The number of bursts observed at  $x_f = 58$  cm are also more for the case of  $\dot{m}_f = 13$  mlpm than that for  $\dot{m}_f = 12$  mlpm. These observations of change in fuel flow rate at a constant value of air flow rate suggest that the amount of fuel burnt during combustion has a significant effect on the characteristics of the onset of intermittency as well as thermoacoustic instability in the system dynamics.

The bifurcation analysis of the acoustic pressure fluctuations is presented in Fig. 5.4. The bifurcation plots showing the variation of the global maxima,  $p'_{max}$  (Fig. 5.4a) and the root mean square,  $p'_{rms}$  (Fig. 5.4b) values of the acoustic pressure signal for the variation of location of flame holder inside the combustor at a constant value of equivalence ratio. The plots are divided into three regions: region I - combustion noise, region II - intermittency and region III - thermoacoustic instability. During stable operation of the combustor, up to  $x_f = 530$  mm, low amplitude aperiodic oscillations are observed (see region I of Fig. 5.4). At  $x_f = 540$  mm, as the system dynamics enter into a zone of intermittency, a jump in the maximum amplitude of the acoustic pressure signal is noticed. This sudden hike in the pressure amplitude is due to the occurrence of bursts of high amplitude periodic oscillations from the background of low amplitude

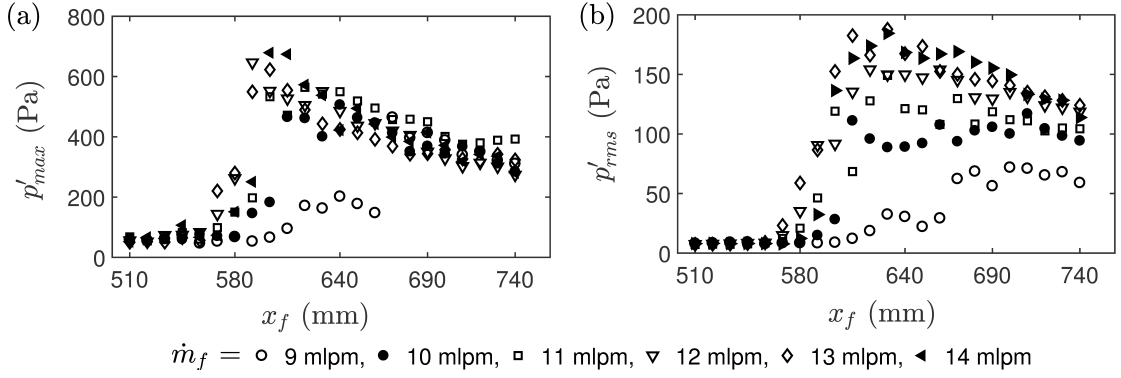


Figure 5.5: The effect of increase in the value of fuel flow rate  $\dot{m}_f$  from 9 to 14 mlpm for a constant value of  $\dot{m}_a = 120$  slpm, on the variation of (a)  $p'_{max}$  and (b)  $p'_{rms}$  of the acoustic pressure signal for different values of  $x_f$  in the system.

aperiodic oscillations. This point is further referred to as the onset of intermittency in the system dynamics. The intermittent state of oscillations is observed from  $x_f = 540$  mm to  $x_f = 670$  mm, as shown in region II of Fig. 5.4. Finally, for  $x_f = 680$  mm and  $x_f = 690$  mm (see region III of Fig. 5.4), the system enters into a region of limit cycle oscillations, where sustained periodic oscillations are observed in the system dynamics. We found that during the onset of intermittency, the maximum amplitude of bursts (in the start of region II of Fig. 5.4a) is much higher in magnitude than that of the limit cycle oscillations (region III of Fig. 5.4a). We notice a decrease in maximum amplitude of acoustic pressure oscillations from the point of onset of intermittency to that of limit cycle oscillations (refer region II in Fig. 5.4a). However, this behaviour of a decrease in the pressure amplitude is not effectively seen in the plot of the variation of  $p'_{rms}$  with the flame location,  $x_f$  (see region II in Fig. 5.4b). This is because  $p'_{rms}$  averages out the values of high amplitude pressure oscillations that occur for a short duration amongst the lengthy regions of low amplitude aperiodic oscillations during the onset of intermittency.

The effect of an increase in the value of fuel mass flow rate on the bifurcation plots of  $p'_{max}$  and  $p'_{rms}$  is shown in Fig. 5.5. In a similar manner to Fig. 5.4, the jumps in the plot of  $p'_{max}$  at a particular value of  $x_f$ , represent the onset of high amplitude bursts during the state of intermittency in the system (Fig. 5.5a). Further, we notice that the jump in the plot for  $\dot{m}_f = 9$  mlpm happens at a higher  $x_f$  as compared to that happen for  $\dot{m}_f = 14$  mlpm. This observation also suggests that a decrease in the value of fuel flow rate ( $\dot{m}_f$ ), in a given air-fuel mixture, delays the onset of intermittency in the system dynamics. After the onset of intermittency, the maximum amplitude of the acoustic pressure

signal exhibit a continuous decrease with further increase in  $x_f$ . This plot demonstrates an interesting feature of the system behaviour, wherein we notice almost collapse of all data points observed after the onset of intermittency in the system dynamics, for a range of fuel flow rates used in the experiment. This behaviour of the system dynamics reasserts the fact that the maximum amplitude achieved by self-excited periodic oscillations (observed during intermittency and/or thermoacoustic instability) in the system, at a particular value of air flow rate and flame location in the combustor, is independent of the amount of fuel burned in the system. On the contrary, we observe a nearly gradual increase in the values of  $p'_{rms}$  with  $x_f$ , for different values of  $\dot{m}_f$ , during the transition from combustion noise to intermittency (see Fig. 5.5b). This plot also indicates that the *rms* value of the acoustic pressure signal, after the onset of intermittency in the system dynamics, has nearly direct relation with the amount of fuel burned for a given air flow rate in the system. For a constant value of  $x_f$ , the increase fuel flow rate increases the *rms* value of the acoustic pressure signal. This is in contrast with the variation of the maximum value of the acoustic pressure signal, where it remains nearly the same for all values of fuel flow rates (Fig. 5.5a).

Nair *et al.* (2014) reported the observation of intermittency route to thermoacoustic instability in their turbulent gaseous flame combustor. They noticed that the root mean square values of the acoustic pressure fluctuations ( $p'_{rms}$ ) increases continuously from the point of onset of intermittency to limit cycle oscillations due to change in Reynolds number of the flow in the system. In stark contrast with Nair *et al.* (2014), it was witnessed that the amplitude (local maxima as well as root mean square values) of intermittent oscillations of acoustic pressure fluctuations is much higher than that observed for limit cycle oscillations. Historically, it was considered that the limit cycle oscillations are dangerous to the combustion systems. The problems associated with the high-amplitude limit cycle oscillations have been described by various researchers in the past (Culick and Kuentzmann, 2006). The continuous loading of the system during the state of sustained instability may lead to severe vibrations of mechanical parts of the combustor that may induce thermal as well as hoop stresses in the combustor walls or can cause compressor surge and damage to the turbine blades. The accumulation of these stresses over a period of time may lead to catastrophic failure of the engine during operation (Suresh, 1998). However, our experimental results highlight that the intermittent states can be more dangerous than the sustained limit cycle oscillations. This

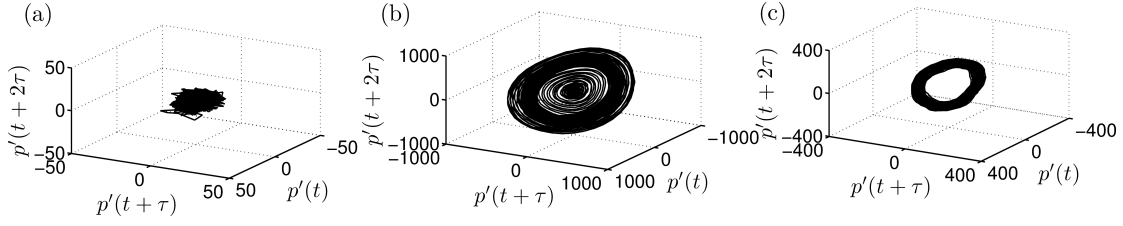


Figure 5.6: Reconstructed phase portrait of a portion of the pressure time series (0.5 s) obtained during three different dynamical states system dynamics such as (a) combustion noise ( $x_f = 520$  mm,  $\tau_{opt} = 3$ ,  $E = 11$ ), (b) intermittency ( $x_f = 590$  mm,  $\tau_{opt} = 10$ ,  $E = 9$ ), and (c) thermoacoustic instability ( $x_f = 680$  mm  $\tau_{opt} = 10$ ,  $E = 9$ ).

is because during intermittency, combustor experiences significantly higher amplitude intermittent loads (due to large amplitude bursts of periodic oscillations) over a shorter duration. Such loads can have a greater impact on the structural properties of the engine than the low-amplitude cyclic loading exercised during sustained limit cycle oscillations (Schmid *et al.*, 2014). A sudden rise in the pressure amplitude, during intermittency, may lead to fracture of the brittle material or may cause deformation of the ductile material (Ditlevsen and Madsen, 1996; Schmid *et al.*, 2014). Sometimes, the damage due to a single intermittent shock may not be seen, but the continuous exposure of system components to intermittent loads of different amplitude may result in fatigue failure (Schmid *et al.*, 2014). Therefore, the intermittent oscillations wherein high-amplitude bursts occur pose a great concern to the structural integrity of the thermoacoustic systems and there is a need to understand the mechanism of such intermittent oscillations.

## 5.1.2 Phase Space Reconstruction

The dynamics of the acoustic pressure fluctuations acquired at different states of the combustor operation is explored through tools from dynamical systems theory. Using the approach of nonlinear dynamics, a single variable time series of the experimental signal can be visualized into a higher dimensional reconstructed phase space. Such phase space is reconstructed using delay embedding theorem proposed by Takens *et al.* (1981). Figure 5.6 shows three-dimensional phase portraits of the acoustic pressure fluctuations ( $p'$ ) measured at three states of the combustor operation which are combustion noise, intermittency, and thermoacoustic instability. In Fig. 5.6a, the phase portrait of  $p'$  acquired during the combustion noise state is shown. As the acoustic pressure oscillations are aperiodic in nature, the phase portrait corresponding to this state displays

a clutter of trajectories. During intermittency, it is observed that the phase space trajectory continuously switches between high amplitude periodic (outer regular circle) and low amplitude aperiodic (central disordered region) oscillations as shown in Fig. 5.6b. During limit cycle oscillations, the phase space of the signal displays a thick circular structure (see Fig. 5.6c), in which the thickness of the circle is caused by the amplitude variation of the acoustic pressure oscillations observed during this state.

### 5.1.3 Detection of Chaos

We further characterize the nature (random or chaotic) of acoustic pressure fluctuations obtained during the state of combustion noise. Such classification of the signal observed during this state is necessary to develop an appropriate model required for the analysis of the combustor dynamics. Various methods are available in the literature to distinguish chaotic signals from the noisy ones. These include Lyapunov exponent, surrogate analysis, test for determinism, permutation entropy, etc. (Kantz and Schreiber, 2004). However, in the present analysis, we discuss the use of an approach based on recurrence plots<sup>3</sup>, RPs. The advantage of this method is that it requires a shorter time series, unlike other cases, to analyse the data. Further, it helps in better visualization of divergence of the phase space trajectory compared to the other methods.

The difference between a random process and a chaotic process is examined through recurrence plot analysis and measures of recurrence quantification analysis. Towards this purpose, a comparison test is performed between the experimental signal of acoustic pressure fluctuations obtained at  $x_f = 520$  mm and the signal generated by random shuffling of its data points, using a method of surrogate analysis (Theiler *et al.*, 1992). Surrogate test aids in distinguishing the nonlinear behaviour of the real-world data from the linear process by using an appropriate null hypothesis. In order to reject the hypothesis, a significance of the test against the null hypothesis is examined. Many realizations of the null hypothesis are generated and the significance of the test is estimated empirically. This check is important in showing that the underlying dynamics present during the aperiodic state of oscillations is deterministic chaos and not random noise.

The structural patterns present in RPs further represent the typical behaviour of the

---

<sup>3</sup>The mathematical description for recurrence plots is provided in Section 2.5.2, Chapter 2

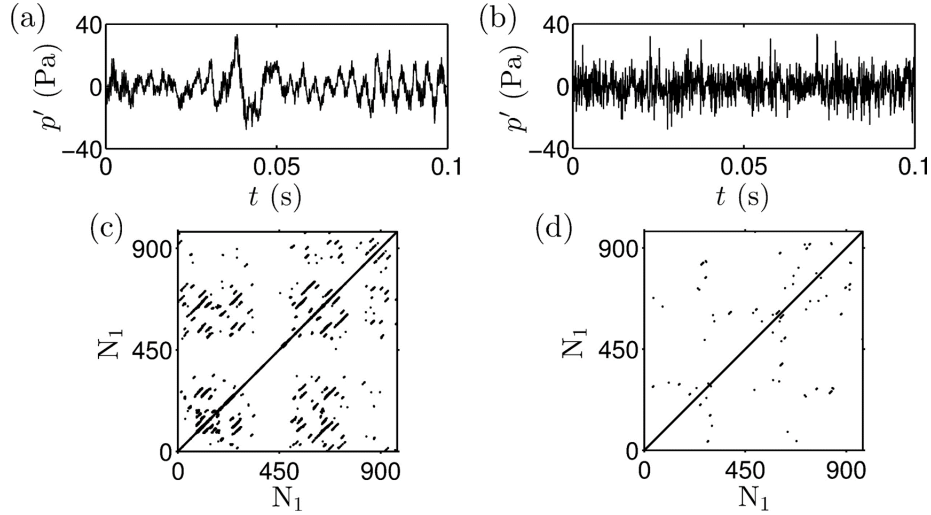


Figure 5.7: (a), (b) The acoustic pressure signals measured at  $x_f = 520$  mm and that obtained from a random shuffling of its data points, respectively. The recurrence plots corresponding to these signals are shown in (c), (d). The parameters that are fixed, number of data points in a signal  $N = 1000$ , optimum delay  $\tau_{opt} = 3$ , embedding dimension  $E = 10$ , and recurrence threshold  $\epsilon = 30\%$  of the mean diameter of the attractor.

phase space trajectory. The long lines parallel to the main diagonal represent a periodic (deterministic) process, whereas homogeneously distributed black points indicate white noise (random) process. On the other hand, a chaotic process is shown by the apparently random distribution of short diagonal lines along with a few isolated black points in RP (Marwan *et al.*, 2007). The characteristic of chaotic oscillations is that the neighbouring trajectories in the phase space of such signals remain nearby for a short duration and then diverge exponentially at far distances. Hence, when the trajectories are adjacent, they recur inside the recurrence threshold and do not recur after the exponential divergence. Conversely, in the case of random signals, every event of the signal is independent of the previous one. Hence, for such signals, the possibility of recurrence of the phase trajectory is very low.

The RPs of the aperiodic oscillations observed during the state of combustion noise and its surrogate signal are shown in Figs. 5.7c,d, respectively. During the random shuffling of data points, the statistical properties of the signal such as sample mean, variance, and autocorrelation function are maintained same as that of the original signal used for the construction. In Fig. 5.7c, we notice the presence of short (broken) diagonal lines along with few single points in RP suggesting the possibility of chaotic oscillations during the state of combustion noise. In contrast, Fig. 5.7d shows the grainy structure with the apparently random distribution of isolated black points in RP confirming the

noisy behavior of the oscillations in the signal.

### 5.1.4 Determining the Transition to Thermoacoustic Instability Using Recurrence Quantification Analysis

We further use measures of recurrence quantification analysis (RQA), mainly based on the characterization of diagonal patterns from RP (i.e., determinism,  $\%DET$ , and the length of the maximum diagonal structures,  $L_{max}$ ), to investigate the transition points of the system dynamics from aperiodic to periodic oscillations and vice versa. In order to do this, we divide the entire time series into non-overlapping time windows of 1000 data points. The values of  $\%DET$  and  $L_{max}$  are then calculated for each time window and plotted against the number of windows for the given signal.

Determinism ( $DET$ ) quantifies the recurrence behaviour of lines that are parallel to main diagonal in RP. It is the ratio of a number of black points in RP that form a diagonal line to the total number of black points present in RP.

$$DET = \frac{\sum_{i=l_{min}}^N lP(l)}{\sum_{i=1}^N lP(l)}$$

where  $P(l)$  is the histogram of the lengths  $l$  that form diagonal lines in RP and  $l_{min} = 2$  points. Determinism is a measure of predictability of the dynamical system and shows a higher value close to 1 for the regular behavior and lower value close to zero for the irregular behavior.

Further,  $L_{max}$  characterizes the length of maximum diagonal structures, other than the main diagonal line, present in RP. The inverse of  $L_{max}$  is called divergence. It is also referred to an estimator for the largest positive Lyapunov exponent of the signal (Marwan *et al.*, 2007). Since the largest positive Lyapunov exponent is a measure of the divergence of the phase space trajectory, its value is more for chaotic oscillations and less for periodic oscillations.

Figure 5.8 shows the variation of  $\%DET$  and  $L_{max}$  obtained for the states of combustion noise (Fig. 5.8a), intermittency (Fig. 5.8b), and thermoacoustic instability (Fig. 5.8c). The length of the diagonal line has a direct connection with the property of determinism of the system dynamics. The points along the diagonal line show evolution of

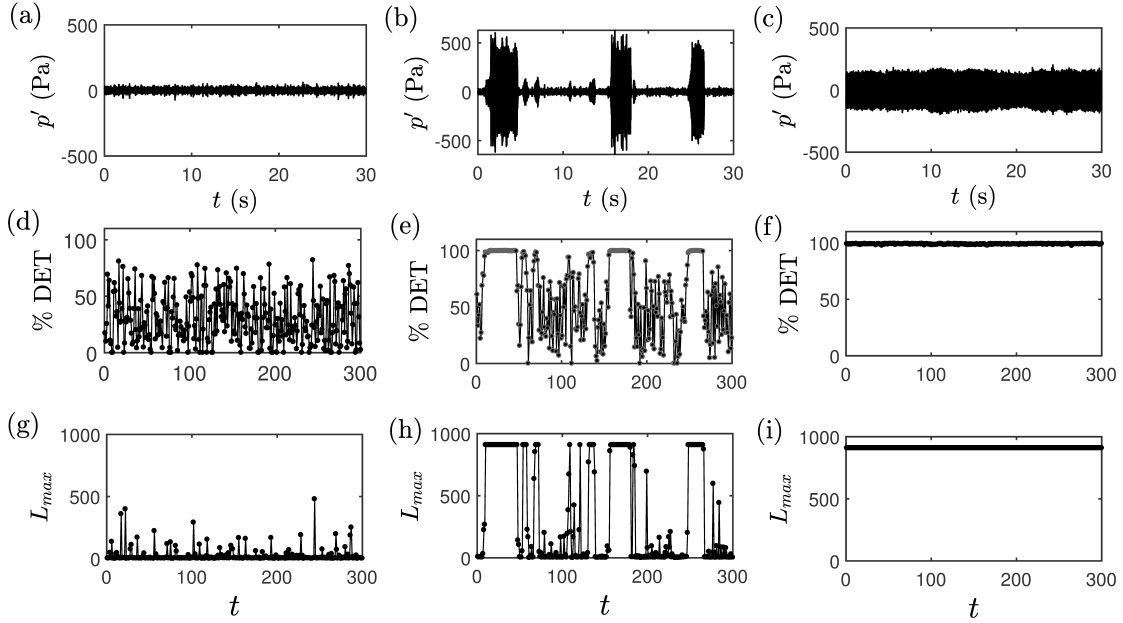


Figure 5.8: (a)-(c) The acoustic pressure signals obtained at  $x_f = 520$  mm (combustion noise),  $x_f = 560$  mm (intermittency) and  $x_f = 680$  mm (thermoacoustic instability), respectively. (d)-(i) The variations of  $\%DET$  and  $L_{max}$  for a non-overlapping time window of 1000 data points. The parameters that are fixed, number of data points in a signal  $N = 300000$ , optimum delay  $\tau_{opt} = 10$ , embedding dimension  $E = 10$ , and recurrence threshold  $\epsilon = 25\%$  of the mean diameter of the attractor.

similar situations in the future time. Moreover, short diagonal lines indicate the short-term predictability and long diagonal lines demonstrate the long-term predictability of the system dynamics. The values of  $\%DET$  and  $L_{max}$  are sufficiently higher than zero for every time window, indicating the possibility of chaotic oscillations (Marwan *et al.*, 2007) in the underlying dynamics of aperiodic oscillations observed during the state of combustion noise (see Figs. 5.8d,g). The values of  $\%DET$  and  $L_{max}$  reach a maximum during the periodic epoch of oscillations. During the state of intermittency, the values of recurrence quantifiers display lower value for aperiodic epochs of oscillations and reach a maximum value during periodic epochs of oscillations (see Figs. 5.8e,h). For a proper value of the recurrence threshold, the temporal variation of these recurrence measures will clearly manifest the transition points of the system dynamics from aperiodic to periodic oscillations, and vice versa, in the time series displaying intermittency. This is observed from the strong change displayed by  $\%DET$  and  $L_{max}$  values across the transition point, as shown in Figs. 5.8e,h. The ability of these RQA measures in discerning even low amplitude periodic oscillations from the low amplitude aperiodic oscillations observed during intermittency is also illustrated in Figs. 5.8e and 5.8h. For the periodic oscillations (or thermoacoustic instability) of any amplitude (low or high)

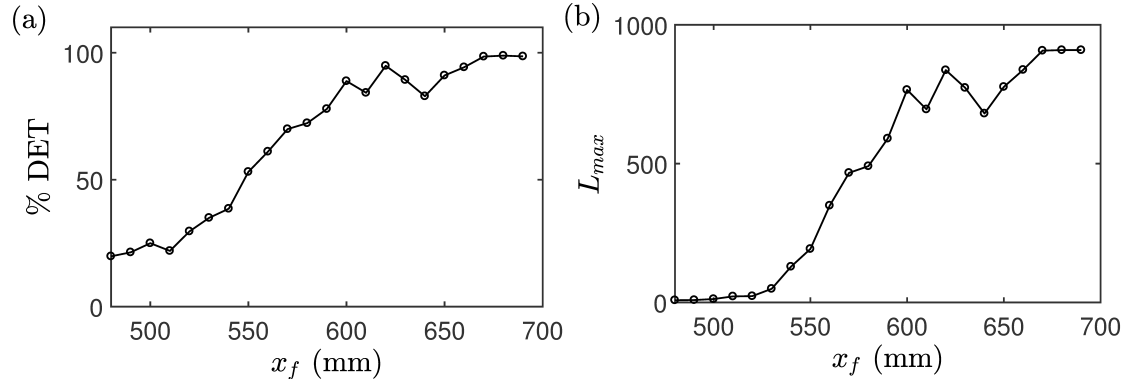


Figure 5.9: (a), (b) The variation of average values of the percentage of determinism ( $\%DET$ ) and the length of the maximum diagonal structures ( $L_{max}$ ) with the location of flame in the combustor. The parameters fixed during the analysis are  $\tau_{opt} = 10$ ,  $E = 10$ ,  $\epsilon = 25\%$  of the mean diameter of the attractor.

in the pressure signal, the values of  $\%DET$  and  $L_{max}$  stay at maxima throughout the signal, as seen in Figs. 5.8f,i. Thus, the periodic oscillations observed during thermoacoustic instability establish the highest predictability by showing only continuous diagonal lines in the RP.

The transition of system dynamics from combustion noise to thermoacoustic instability can be quantitatively explained by plotting the time average values of  $\%DET$  and  $L_{max}$  with control parameter as shown in Fig. 5.9. The values of  $\%DET$  and  $L_{max}$  are calculated for every time window of 1000 data points and averaged over the entire signal. The average value of  $\%DET$  is close to 1 for the state of thermoacoustic instability, as the observed dynamics during this state is completely periodic. On the contrary, the value of  $\%DET$  is around 0.2 for the state of combustion noise, as the observed dynamics is mostly aperiodic during this state. During intermittency, the value of this measure lies in between these extreme values. Similar behaviour is observed in the variation of the average value of  $L_{max}$ . The increase in the average values of  $\%DET$  and  $L_{max}$  with control parameter indicates the increase in predictability of the system dynamics. Other types of RQA measures namely recurrence rate, entropy and trapping time have been previously used by Nair *et al.* (2014) to forewarn the impending instability of the practical gas turbine combustor. Controlling the operation of combustor at the onset of the first burst in the pressure signal, by detecting the changes in  $\%DET$  and  $L_{max}$  plots, will help in protecting the system components from any further damage.

## 5.2 Characterizing the Type of Intermittency

In the following analysis of intermittency, the low amplitude aperiodic regions present between the consecutive bursts are defined as the turbulent phases, and the regions of high amplitude bursts of periodic oscillations are called the laminar phases. The terms turbulent phase and laminar phase are completely different from the terminology of turbulent flow and laminar flow used in the fluid mechanics. The lengths of the turbulent phases ( $L_T$ ) present in the unsteady pressure signal are determined to quantify the type of intermittency. Furthermore, the conventions of laminar and turbulent phase used in the present analysis may contradict with that used in the literature of dynamical systems theory, wherein the bursts of chaotic oscillations are described as turbulent phases and the regions of periodic oscillations observed in between the bursts are described as laminar phases.

Figure 5.10 shows a portion of the acoustic pressure signal acquired during a state of intermittent dynamics. For the calculation of the length of turbulent phase ( $L_T$ ), we adopt a method suggested by Hammer *et al.* (1994). Using this approach, an amplitude threshold is expressed in terms of fraction of maximum pressure such that  $\text{threshold} = \max(p')/(2^n)$ , where  $1 \leq n \leq 6$ . Here, we present the results corresponding to  $n = 4$ , which is equal to a pressure amplitude threshold of 54 Pa. The duration in the acoustic pressure signal having an amplitude below the selected threshold (i.e., the signal length between consecutive bursts) is defined as the length of the turbulent phase, as described in Fig. 5.10. The turbulent phase starts when the last waveform of the periodic burst

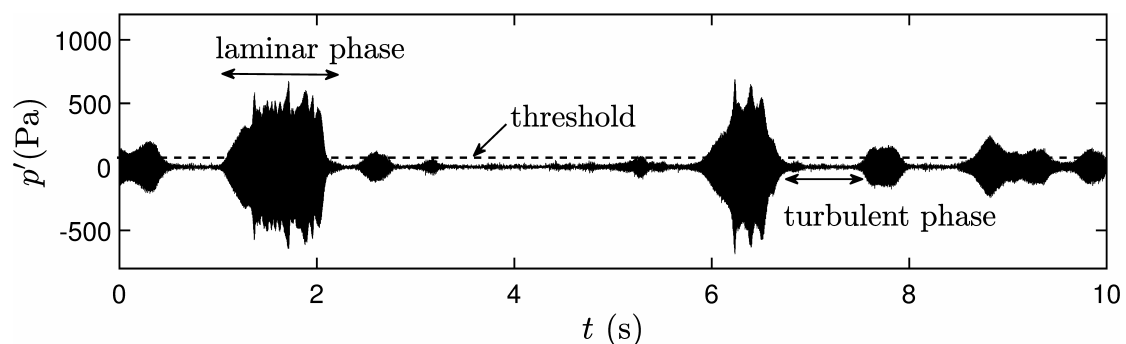


Figure 5.10: The intermittency signal consists of epochs of low amplitude aperiodic oscillations, referred to as turbulent phases, in between consecutive bursts of high amplitude periodic oscillations, referred to as laminar phases. A pressure threshold demarks the high amplitude periodic oscillations from low amplitude aperiodic oscillations.

falls below the threshold and ends when the first waveform of the next burst exceeds the threshold. These turbulent lengths are binned to calculate their probability distribution (using histogram) near the critical point. The critical point ( $x_{f0}$ ) is the value of control parameter corresponding to the onset of intermittency. In order to characterize the type of intermittency, a separate experiment was performed to acquire a sufficient number of bursts near the critical point. The acquisition of such lengthy data is necessary to confirm the statistical convergence of the obtained results. Towards this purpose, the data was acquired for 300 s at a sampling rate of 3 kHz.

### 5.2.1 Distribution of the Length of the Turbulent Phase

The histogram of the length of the turbulent phase present in the acoustic pressure signal acquired at  $x_{f0} = 540$  mm is shown in Fig. 5.11. An optimum pressure amplitude threshold of 54 Pa was chosen to ensure that the dynamics of the signal is aperiodic below the threshold and solely periodic above the threshold. Figure 5.11 shows an exponential decrease in the probability distribution of the length of the turbulent phase. Such distribution is consistent with the distribution shown for type-II and type-III intermittency (Xiao *et al.*, 2009; Frank and Schmidt, 1997; Sacher *et al.*, 1989; Schuster and Just, 2006). Therefore, this distribution of turbulent lengths eliminates the possibility of type-I intermittency, which is characterized by a bimodal distribution (Schuster and Just, 2006; Feng *et al.*, 1996).

Figure 5.11b shows the variation of the average length of the turbulent phase with the normalized control parameter. Since the appearance of bursts is apparently random

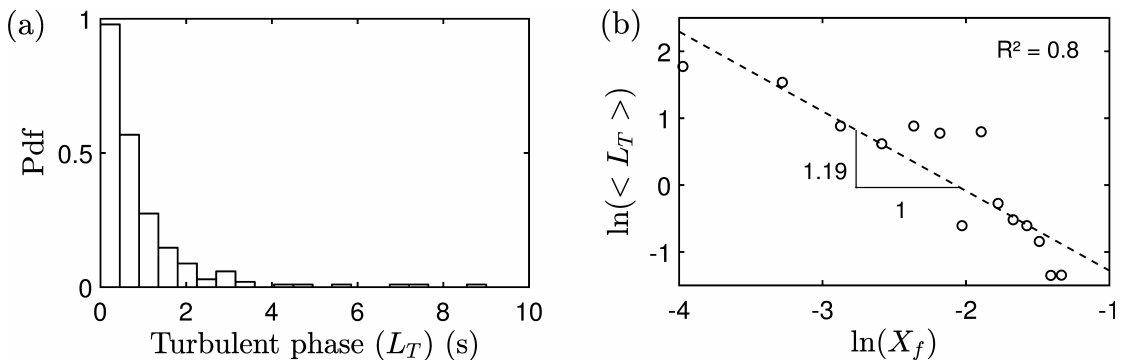


Figure 5.11: (a) The distribution of the length of the turbulent phases obtained at  $x_f = 540$  mm shows an exponential tail. (b) A log-log plot of the average value of the length of the turbulent phase ( $\langle L_T \rangle$ ) versus the normalized flame location ( $X_f$ ) shows a scaling law behaviour of type-II intermittency.

during intermittency, the average length of the turbulent phases,  $\langle L_T \rangle$ , is used as a representative total length of turbulent phases existing in the corresponding pressure signal obtained at a particular  $x_f$ . The normalized flame location is given by  $X_f = (\tilde{x}_f - \tilde{x}_{f0})/\tilde{x}_{f0}$ ; where  $\tilde{x}_f (= x_f/L)$  and  $\tilde{x}_{f0} (= x_{f0}/L)$  are the locations of the flame holder, measured from the open end of the combustor ( $x_f$ ) and that corresponding to the onset of intermittency ( $x_{f0}$ ), respectively, normalized by the length of the duct ( $L$ ). The mean duration of the turbulent phase plotted against each location of the flame holder on a log-log plot shows a power law behaviour. The variation of  $\langle L_T \rangle$  with  $X_f$  shows a linear relationship of slope  $-1.19$ , which is close to the theoretical value predicted for type-II and type-III intermittency, i.e.,  $\langle L_T \rangle \sim X_f^{-1}$  (Pomeau and Manneville, 1980; Sacher *et al.*, 1989; Chatterjee and Mallik, 1996; Ringuet *et al.*, 1993); on the contrary, for type-I intermittency, it is  $\langle L_T \rangle \sim X_f^{-1/2}$  (Pomeau and Manneville, 1980; Feng *et al.*, 1996). This statistical distribution again rules out the possibility of type-I intermittency in our experimental data. The difference in the values of slope obtained from a theory ( $-1$ ) and from experiments ( $-1.19$ ) could be the result of the finite length of the experimental signal, unavoidable noise in experiments and also in measurements, and challenge in detecting the length of turbulent phases accurately.

## 5.2.2 Analysis Using First Return Map

Finally, a method of first return map is used to differentiate type-II intermittency from type-III intermittency (Sacher *et al.*, 1989). It is a two-dimensional plot between the first local maxima of the signal versus the next local maxima. Here, we plot the local maxima, say  $X_n$ , of the oscillations in laminar phases present in between the consecu-

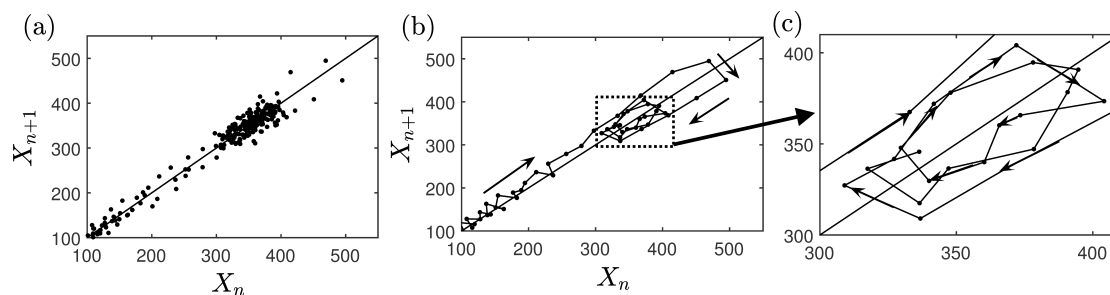


Figure 5.12: (a) First return a map of the intermittency signal shows a scatter of points along the diagonal line. (b), (c) The time evolution of these points indicates a spiraling behaviour of the trajectory, which confirms the possibility of type-II intermittency in the system dynamics.

tive turbulent phases, against the next local maxima, i.e.,  $X_{n+1}$ . In the first return map, the scatter of points along the main diagonal line is observed (Fig. 5.12a), whereas the evolution of these points shows a spiral-like structure in the plot (Figs. 5.12b,c). Such spiraling structure of the phase space trajectory is a typical characteristic property of type-II intermittency (Frank and Schmidt, 1997; Sacher *et al.*, 1989; Ringuet *et al.*, 1993). In Fig. 5.12b, the evolution of some of the initial points from Fig. 5.12a is plotted to show the spiraling behaviour of the phase space trajectory. For type-I intermittency, the first return map shows an open channel between the diagonal line and the phase space trajectory (Schuster and Just, 2006; Feng *et al.*, 1996), whereas for type-III intermittency, it is represented by a two-fold trajectory crossing the diagonal line with increasing trend for sub-harmonic amplitude and decreasing trend for fundamental amplitude (Schuster and Just, 2006; Griffith *et al.*, 1997), which are different from that shown in Fig. 5.12. This confirms the presence of type-II intermittency in the present study.

### 5.2.3 Investigation Based on Recurrence Plot

Another way to identify the type of intermittency is based on recurrence plot analysis, RP (Klimaszewska and Żebrowski, 2009). The occurrence of different types of intermittency will result in various characteristic patterns in the RP.<sup>4</sup> The recognition of the structure in RP will help in determining the type of intermittency. Figures 5.13b-d show the RPs of small portions of the time series displaying intermittency (see Fig. 5.13a) obtained at  $x_f = 540$  mm. Figure 5.13c shows a kite-like structure, representative of type-II intermittency, observed during the transition of system dynamics from low amplitude aperiodic to high amplitude periodic oscillations. A sinusoidal shape at the right upper corner of the kite with white perforations inside the kite (Fig. 5.13c) is the characteristic of type-II intermittency. Figure 5.13d shows the diagonal lines parallel to the main diagonal line representing the periodic behaviour present in the burst. Kabiraj and Sujith (2012) and Unni and Sujith (2017) reported the presence of such kite-like structures, observed prior to blowout of the flame, for confirming type-II intermittency in gaseous laminar premixed and turbulent partially premixed combustors, respectively.

<sup>4</sup>We have used a recurrence quantification analysis software package developed by Hasson *et al.* (2008) to obtain RPs of the experimental signal.

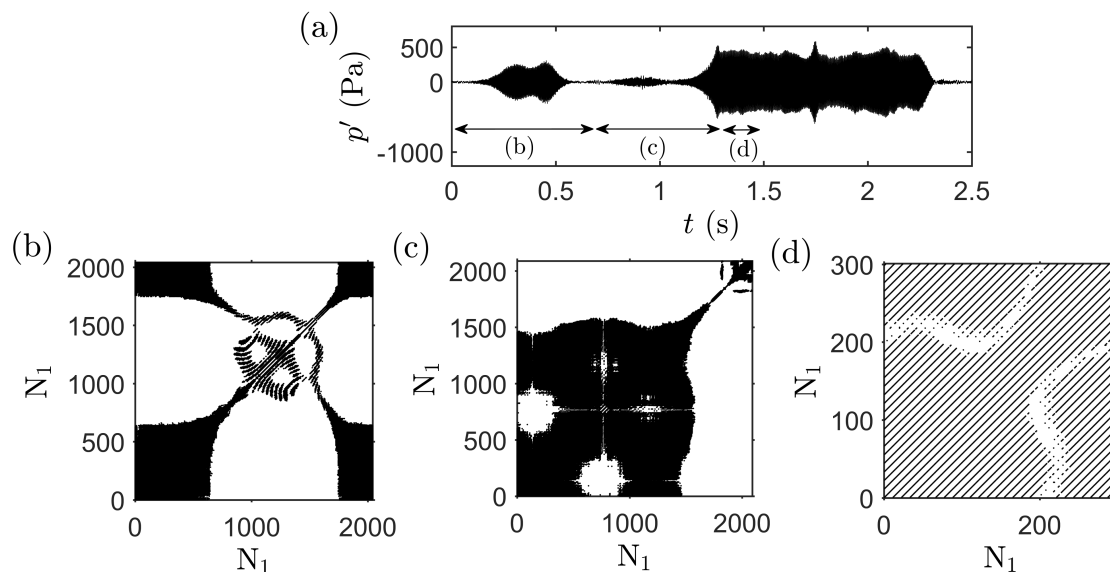


Figure 5.13: (a) A portion of the signal displaying intermittency. (b)-(d) Recurrence plots (RP) obtained from different regions of the intermittency signal. (c) RP shows a kite-like structure of type-II intermittency. Data points ( $N$ ) = 7500,  $\tau_{opt} = 3$ ,  $E = 10$ ,  $\epsilon = 20\%$  of the mean diameter of the attractor.

### 5.3 Interim Summary

We investigated the transition of the system dynamics from a state of combustion noise to thermoacoustic instability through intermittency using acoustic pressure alone. The intermittency is characterized by the presence of high amplitude bursts of periodic oscillations amongst regions of low amplitude aperiodic fluctuations. The analysis of recurrence plot and recurrence quantification of the experimental data proves that the low amplitude aperiodic fluctuations possibly exhibit chaotic behaviour. Furthermore, the transitions of the system dynamics, from aperiodic to periodic oscillations and vice versa, can be clearly detected by the recurrence quantification measures such as  $\%DET$  and  $L_{max}$  during intermittency. The characterization of the type of intermittency demonstrates the presence of type-II intermittency in the dynamics of the spray combustion system.

The bifurcation study of the acoustic pressure oscillations demonstrates the presence of higher amplitude bursts during intermittency compared to that during limit cycle oscillations. The maximum amplitude of such bursts can grow as high as three times than that of the sustained periodic oscillations. Further, we observed that the maximum amplitude attained by bursts of acoustic pressure oscillations, at a particular value of the flame location, is independent of the amount of fuel burned in the combustor. The

presence of these high amplitude intermittent loads during intermittency may possibly be more dangerous to the system components than the low amplitude continuous cyclic loads observed during limit cycle oscillations. A sudden jump in the pressure amplitude can cause fracture of the brittle materials or can lead to deformation of the ductile materials. Sometimes, the damage caused by a single burst cannot be recognized easily but the continuous exposure of different amplitude intermittent loads over a long-term operation can lead to fatigue failure of the system parts. As a result, the intermittent oscillations wherein the high amplitude bursts occur, pose a major challenge to the engine operator to protect the system before reaching a state of sustained limit cycle oscillations. Such behaviour of intermittent oscillations might be present in the practical combustion systems and should be considered during the construction of models of the thermoacoustic systems.

## **5.4 Coupled Behaviour of Acoustic Pressure and Global Heat Release Rate Fluctuations**

Separate experiments are performed to investigate the nature of the coupled interaction between the acoustic fluctuations in the confinement and heat release rate fluctuations present in the flame. As the location of the flame ( $x_f$ ) is moved from the bottom to the top region of the combustor, we observe a transition of the system dynamics from a state of combustion noise (Fig. 5.14a) to thermoacoustic instability (see Fig. 5.14c) through the occurrence of intermittency (see Fig. 5.14b) in both the acoustic pressure ( $p'$ ) and the heat release rate ( $\dot{q}'$ ) signals. During intermittency, bursts of large amplitude periodic oscillations (Fig. 5.14b-II) appear in between regions of low amplitude aperiodic oscillations (Fig. 5.14b-III) in an apparently random manner in both the signals. We notice two types of bursts, one having a low amplitude (Fig. 5.14b-I) and the other having a high amplitude (Fig. 5.14b-II) periodic oscillations, in the intermittency signal. The low amplitude aperiodic oscillations are mostly observed to precede the high amplitude bursts of periodic oscillations in the signal.

Further, we investigate the coupling between the acoustic field and the heat release rate field by examining the locking of frequencies and phases of their simultaneously acquired signals. The frequency locking behaviour of such signals is analyzed using

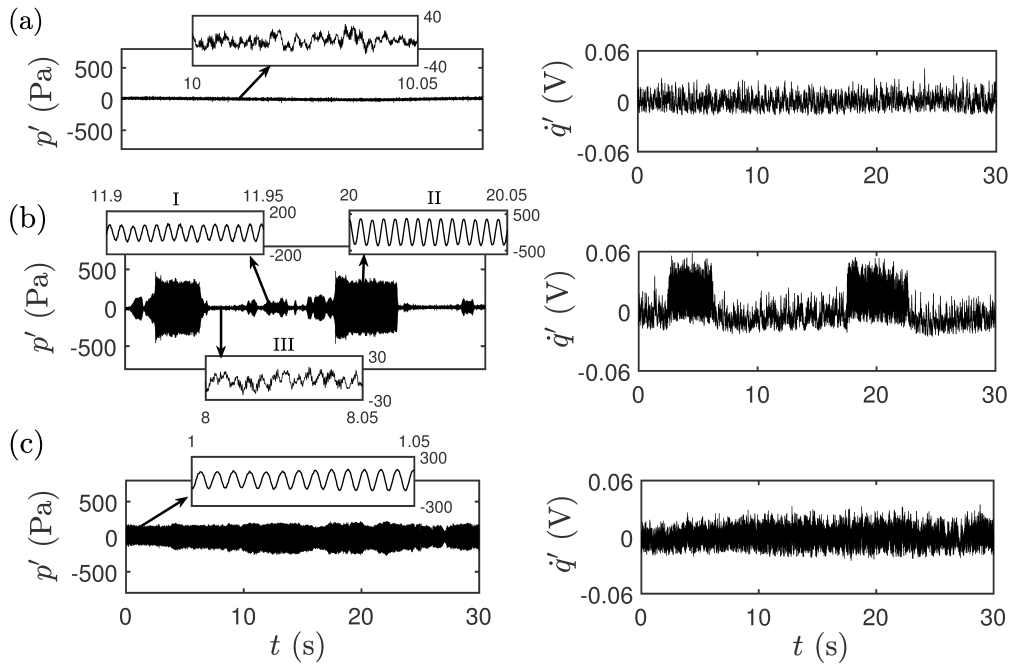


Figure 5.14: Time series of the simultaneously acquired acoustic pressure and the heat release rate fluctuations during different states of the combustion dynamics as (a) combustion noise ( $x_f = 500$  mm), (b) intermittency ( $x_f = 530$  mm) and (c) thermoacoustic instability ( $x_f = 640$  mm). Insets in the plots show zoomed in view of the signal observed during a particular state of oscillation.

a measure of cross wavelet transform (Grinsted *et al.*, 2004; Issartel *et al.*, 2015) for different dynamical states of the combustor operation such as combustion noise, intermittency and thermoacoustic instability (shown in Fig. 5.15). The description of the use of cross wavelet transform to study synchronization properties of two signals is provided in Section 2.5.3, Chapter 2.

When two signals are synchronized, their cross wavelet transform will show maximum spectral power at a common frequency band throughout the signal. The arrows in the plots (refer Fig. 5.15) indicate the value of the instantaneous phase difference between the signals calculated at a particular frequency of the oscillation. The orientation of the arrows signifies the phase angle between the signals. Alignment of the arrows from left to right represents the presence of 0 degrees of phase shift (in-phase), while their alignment from right to left shows the presence of 180 degrees of phase shift (anti-phase) between the signals. The upward and downward orientations of arrows represent the leading of one signal with respect to the other signal by 90 degrees and 270 degrees, respectively (Issartel *et al.*, 2015). A black thin line at the bottom of every figure represents the region of the ‘cone of influence’ of the plot (Grinsted *et al.*,

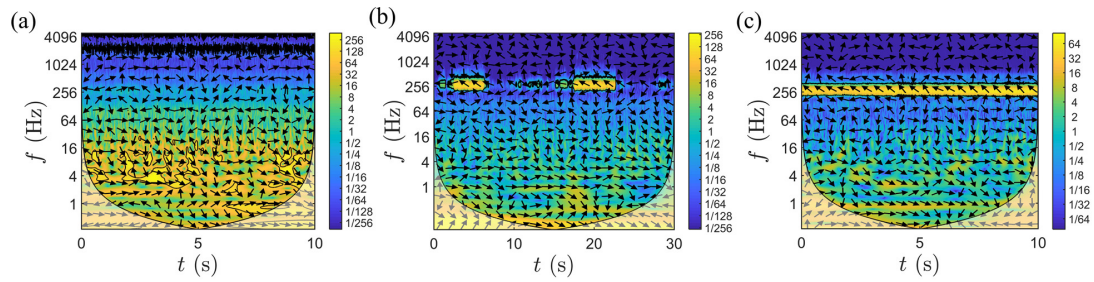


Figure 5.15: The cross wavelet transforms of both acoustic pressure and heat release rate fluctuations obtained from a continuous wavelet transform of the complex Morlet wavelet during different states of the combustion dynamics as (a) combustion noise ( $x_f = 500$  mm), (b) intermittency ( $x_f = 530$  mm) and (c) thermoacoustic instability ( $x_f = 640$  mm).

2004).

During the state of combustion noise, we notice an apparently random (incoherent) distribution of the spectral power in the lower frequency region of the cross wavelet transform, indicating the absence of a distinct common frequency in both  $p'$  and  $\dot{q}'$  signals (Fig. 5.15a). The lack of feedback between these signals further leads to incoherence in their instantaneous phase difference, as seen from the random orientation of the arrows throughout the plane of the XWT plot. During the onset of intermittency, we observe the regions of enhanced coupling between the acoustic pressure and the heat release rate fluctuations, mostly during epochs of bursts of periodic oscillations. The existence of such a short-term coupling results in the intermittent occurrence of regions of common frequency between the signals (Fig. 5.15b), which is around the three-quarter mode of acoustic field of the duct ( $f_a = 267.6$  Hz). The constant orientation of arrows in this frequency-locked band represents the existence of a nearly constant phase-shift (or phase-locking) between the signals (Fig. 5.15b).

It can further be noted that, as the direction of arrows is from right to left, the signals appear to be “out-of-phase” with each other (i.e., phase difference  $> 90$  degrees). However, note that the signals of acoustic pressure and heat release rate fluctuations are actually “in phase” with each other at the flame location. The artifact of the “out-of-phase” of signals is due to the positioning of acoustic pressure and heat release rate measurements in different regions of the three-quarter standing wave developed in the system. The position of the pressure transducer is in the first quarter (towards the closed end), and the location of the flame is in the other half (towards the open end) of the standing wave. Since the phase of the acoustic oscillations in between the consecutive

lobes of the standing wave show a phase jump of 180 degrees (Lieuwen, 2012), we can conclude that the fluctuations in acoustic pressure at the flame zone and the heat release rate are “in-phase” with each other.

When the system dynamics enter into a state of sustained periodic oscillations, we observe the appearance of a common frequency band around the acoustic mode frequency ( $f_a = 266.9$  Hz) for the entire length of the signal (Fig. 5.15c). The constant orientation of arrows in the common frequency-locked band further reasserts the phase locking behaviour of these signals at the acoustic frequency of the combustor. Thus, the system dynamics change its behaviour from a state of desynchronization (observed during combustion noise) to phase synchronization (observed during thermoacoustic instability) through the occurrence of intermittent bursts of phase synchronization (observed during intermittency).

## **5.5 Collective Interaction of Acoustic Field and Multiple Flamelets**

Finally, we will discuss the coupled behaviour of the flame dynamics with the acoustic field in the system. It is well known that the unsteady heat release rate in the flame adds energy to the acoustic field of the thermoacoustic system (Lieuwen, 2012). Acoustic perturbations in the combustor modulate the flame surface area, which, in turn, causes the heat release rate to fluctuate. The fluctuating heat release rate generates an acoustic wave, which reflects from the boundaries. These reflected waves, in turn, affect the flame surface and thus establish a feedback process. When the feedback is positive, the acoustic oscillations in the system are amplified and attain limit cycle oscillations in the system (Lieuwen, 2012). Therefore, the study of the interaction of the flame with the acoustic field of the combustor is important for understanding the nature of coupling that leads to the onset of such oscillations in the system dynamics. Most of the previous studies analyse the flame dynamics while the system is operating either in the stable or unstable state (Rogers and Marble, 1956; Poinsot *et al.*, 1987). Some of the studies analyzed the response of the flame to an external forcing and characterized such a response for different conditions of the forcing parameters (Jarosinski and Veyssiere, 2009). In the contrast, Unni and Sujith (2017) characterized the flame behaviour during

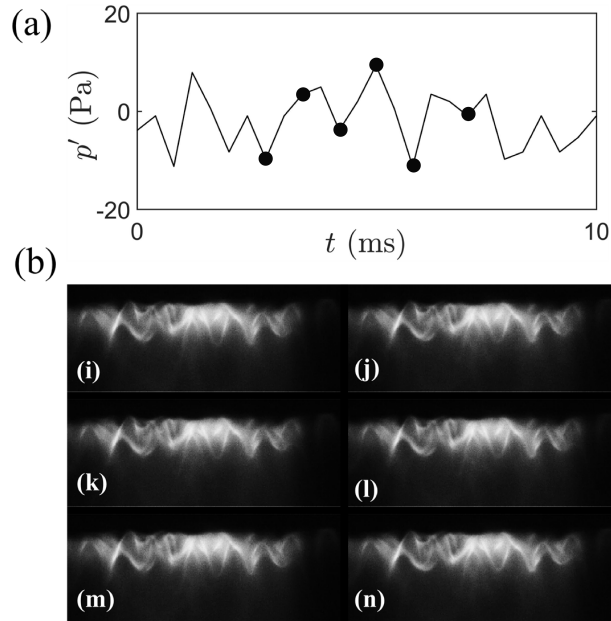


Figure 5.16: (a) A portion of the acoustic pressure signal acquired during combustion noise state ( $x_f = 540$  mm), wherein the dynamics of the signal show low amplitude aperiodic oscillations. (b) The simultaneously acquired instantaneous images of the flame corresponding to dotted points marked in (a).

intermittency in a gaseous flame, stabilized with the bluff-body in a dump combustor. In the present study, we examine the coupled response of the multiple flamelets anchored at the flame holder and the acoustic field in the system for different regimes of the combustor dynamics such as combustion noise, intermittency, and thermoacoustic instability.

### 5.5.1 Combustion Noise

Figure 5.16 shows the simultaneously acquired instantaneous images of the flame during the state of combustion noise with the acoustic pressure signal. The dynamics of the acoustic pressure during this state is of low amplitude and aperiodic (refer Fig. 5.16a). The flame shape observed during this state is small and conical, wherein we observe a steady (non-oscillatory) burning of the multiple flames. The flamelets are randomly anchored in the empty flow passages of the mesh unit. Further, we notice minute movements exhibited by the flamelets, which is mainly due to the hydrodynamic fluctuations of the flow passing through the mesh, and not due to their positive feedback with acoustic fluctuations in the system.

## 5.5.2 Intermittency

The existence of a positive coupling between the acoustic pressure and the heat release rate fluctuations is perceived for the first time during intermittency (Fig. 5.14b). Such a coupling is observed to exist for short duration, wherein the amplitude of the pressure oscillations grows to a high amplitude value where it stays constant for a small duration, and then decays gradually as the coupling between these fluctuations weakens. We observe a collective behaviour of individual flamelets anchored at the mesh with the acoustic field of the duct during the onset of periodicity in the system. In order to characterize the change in the behaviour of such flamelets in response to the acoustic oscillations, we compare the dynamics of the flamelets over different regimes of the intermittency signal. These regimes include (i) epoch of low amplitude aperiodic oscillations (Fig. 5.17b-I), (ii) epoch of growth in the amplitude of the burst (Fig. 5.17b-I), and (iii) epoch of constant amplitude oscillations in the burst (Fig. 5.17b-III). Since the system dynamics is periodic during bursts, we restrict our comparison over an acoustic cycle of the oscillation.

In the region of low amplitude aperiodic oscillations (Fig. 5.17b-I), we observe a steady (non-oscillatory) burning of the flamelets (Fig. 5.17c-I), which is similar to the observation shown in Fig. 5.16b for the state of combustion noise. Figure 5.17c-II shows the flame images corresponding to the region of amplitude growth in the acoustic pressure signal. In this region, we observe the emergence of periodic oscillations in conjunction with the occurrence of collective order in all the multiple flamelets anchored at the mesh. Here, all flamelets exhibit a synchronized axial motion with acoustic cycle while retaining their individual distinct shapes without interacting with the neighbors (Fig. 5.17c-II-k). We further notice an increase in the maximum heights attained by individual flamelets with an increase in the amplitude of pressure oscillations in this region.

As the amplitude of the acoustic pressure signal approaches a region of constant amplitude oscillations (Fig. 5.17b-III), we observe a radical change in the behaviour of all flamelets. We observe an increase in the width as well as the height of all flamelets anchored at the mesh, resulting in the merging of boundaries of neighboring flamelets, which now appear to form a compound flame (see Fig. 5.17c-III-l). During the oscillation cycle, we observe two dominant motions exhibited by the flamelets; one is the axial

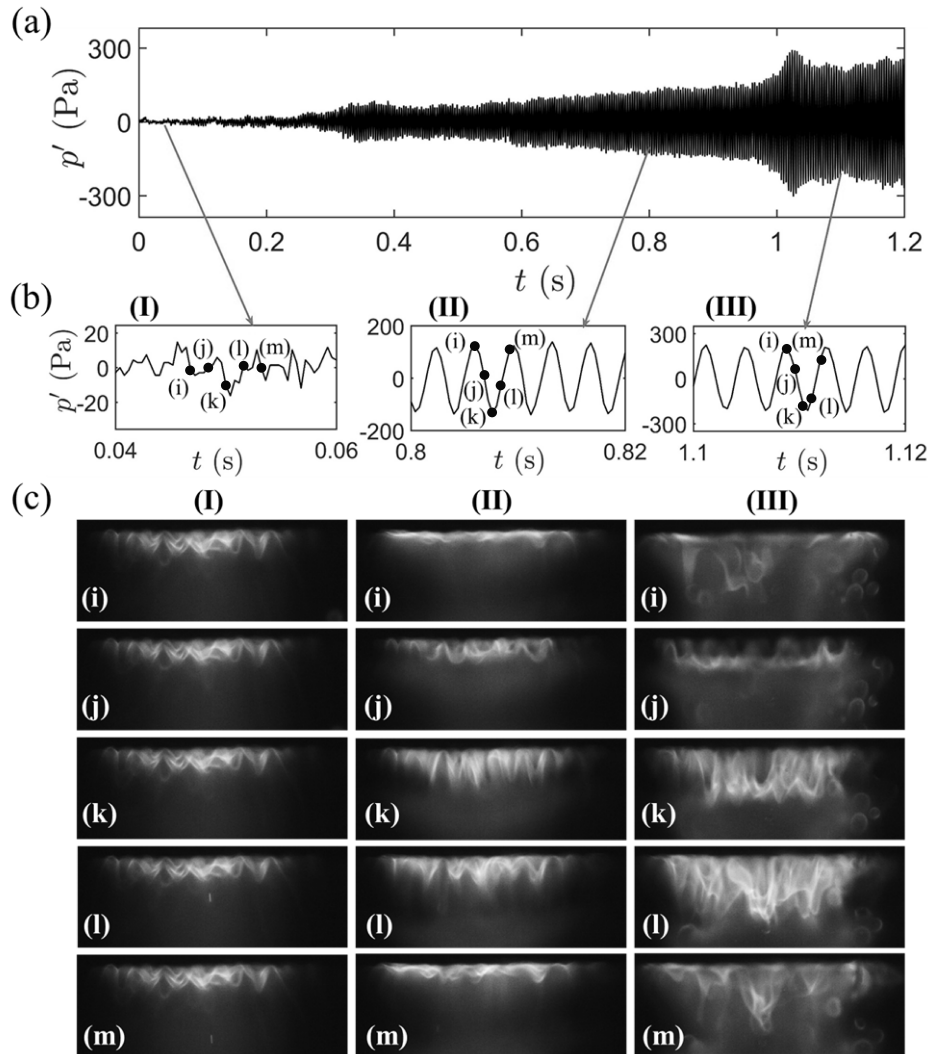


Figure 5.17: (a) A portion of the acoustic pressure signal showing the transition from low amplitude aperiodic to high amplitude periodic oscillations of the burst observed during the state of intermittency ( $x_f = 570$  mm). (b) The different regions of the signals are classified as (I) low amplitude aperiodicity, (II) growth in the amplitude of the burst, and (III) constant amplitude oscillations of the burst. (c) The simultaneously acquired instantaneous images of the flame corresponding to dotted points marked in (b).

motion observed in the central region of the mesh, and the other is the flapping (cross-wise) motion exhibited by the flamelets on the periphery, located near the combustor wall. The interaction of these two motions while all flamelets attain their respective maximum heights causes merging as well as an impingement of the boundaries of the neighboring flamelets, resulting in the occurrence of intense heat release rate in the system. In contrast, during an epoch of low amplitude bursts (shown in Fig. 5.14b-I) in the intermittency signal, the boundaries of individual flamelets remain distinct while all flamelets exhibit collective synchrony with the acoustic pressure oscillations in the

system (not shown here).

When the acoustic oscillations transition to a region of decay in the amplitude of burst (not shown here), we observe that all flamelets gradually recover their distinct shapes while oscillating in synchrony with the acoustic pressure. During this region of oscillation, we notice that the maximum height attained by all flamelets decreases gradually as the amplitude of the pressure oscillations decrease with time. Ultimately all flamelets stop oscillations as the periodicity in the acoustic pressure ends. This decrease in the amplitude of the acoustic pressure is a result of the weakening of the coupling between the acoustic oscillations and the energy supplied by multiple flamelets through the heat release rate fluctuations. This process of collective flame dynamics with acoustic pressure repeats during the onset of the next burst in the intermittency signal.

### **5.5.3 Thermoacoustic Instability**

When the system dynamics is in the state of thermoacoustic instability (Fig. 5.18a), we observe the presence of sustained periodicity in the oscillations of all flamelets anchored at the flame holder (Fig. 5.18b). During this state of oscillations, the boundaries of the neighboring flamelets merge to form a compound flame. The oscillation behaviour of such a compound flame is very much similar to what is shown for the constant amplitude epoch of bursts in the intermittency signal (Fig. 5.17c-III). During the acoustic cycle, all flamelets exhibit a collective growth from a nearly zero height (Fig. 5.18b-i) to a maximum height (Fig. 5.18b-k). During the contraction part of the cycle, the interaction of axial and lateral motions (as explained previously) of the flamelets disturbs the surfaces of individual flamelets (Fig. 5.18b-l). This disturbance further induces a small delay in reaching of individual flamelets to their respective minimum height at the flame holder (Fig. 5.18b-n). Nevertheless, all flamelets hold a collective (global) phase synchrony in their oscillation with the acoustic signal.

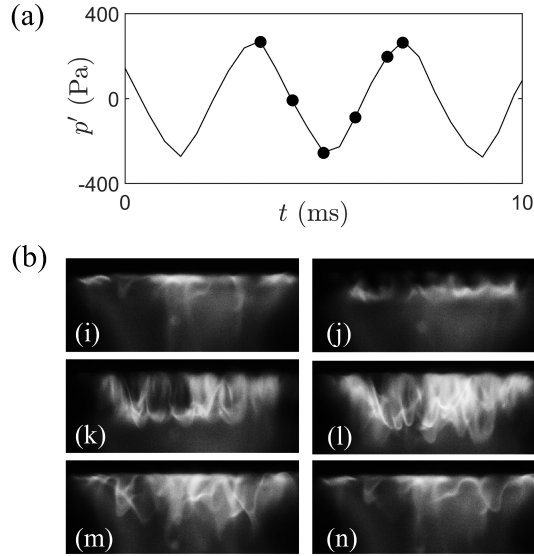


Figure 5.18: (a) A portion of the acoustic pressure signal acquired during the state of thermoacoustic instability ( $x_f = 720$  mm), wherein the system dynamics exhibits self-sustained periodic oscillations. (b) The simultaneously acquired instantaneous images of the flame corresponding to dotted points marked in (a).

## 5.6 Conclusions

The coupled interaction of the acoustic field of the combustor and the dynamics of the multiple flamelets is studied during the intermittency route to thermoacoustic instability when the location of flame is varied as the system parameter. By examining the cross wavelet transform of the acoustic pressure and the heat release rate signals, it is shown that these signals are desynchronized during the state of combustion noise, while they are phase synchronized during the onset of thermoacoustic instability. During intermittency, both signals exhibit intermittent synchronization, wherein they are phase synchronized during bursts of periodic oscillations and desynchronized during the epochs of aperiodic oscillations. Further, the collective behaviour of multiple flamelets anchored at the flame holder is studied during different regimes of the combustor dynamics. During the state of combustion noise, all flamelets appear steady. In contrast, during the epochs of growth and decay of bursts in the intermittency signal, flamelets retain their regular shape while exhibiting synchronized oscillation in their heights with the acoustic field. The shapes of neighboring flamelets are merged and appear to form a compound flame during the epochs of constant amplitude periodicity, wherein the presence of synchronous behaviour of all flamelets with the acoustic field is witnessed. Similar behaviour of the constant amplitude periodicity is also observed in the flamelet

dynamics during the state of thermoacoustic instability. Thus, our study reveals that the emergence of periodicity in the dynamics of a laboratory scale spray combustor is an emergence of collective synchronization phenomena between the acoustic field of the confinement and the multiple flamelets anchored at the flame holder. This result could have implications for the gas turbine or rocket engines which usually consist of multiple flames.

## CHAPTER 6

# NONLINEAR DYNAMICS AND SYNCHRONIZATION BEHAVIOUR OF A FORCED DENSITY STRATIFIED REACTING WAKE

It is well known that the onset of thermoacoustic instability is a coupled response of the acoustic field, the hydrodynamic field and the reacting field of the combustor. The inherent dynamics of each of these subsystems play an important role in the resultant behavior of the thermoacoustic system. In the previous chapters, we studied the coupled response of the acoustic field and the unsteady combustion dynamics on the occurrence of a thermoacoustic instability in the gas fired as well as liquid fuel combustors when the incoming reactants to the combustors are non-preheated. In this chapter, we discuss the effect of preheating of the reactants on the coupled interaction the reacting flow field inside the combustor with the externally driven acoustic field in the system.

Experiments are conducted in the bluff body stabilized turbulent combustor. Another combustor, which acts as a vitiator, is used to preheat the reactants at different temperatures. Preheating of reactants results in the variation of density ratio [i.e., the ratio of the unburnt gas density ( $\rho_u$ ) to the burnt gas density ( $\rho_b$ )] across the flame region (or across the reacting wake of the bluff body) in the combustor. The introduction of the density variation alters the global stability of the bluff body wake field (McMurtry *et al.*, 1989; Bush and Gutmark, 2007). Density ratios far from unity tend to stabilize the global mode, rendering the wake convectively unstable (Huerre and Monkewitz, 1990). This is the situation in wakes of premixed combustors with highly exothermic combustion and/or little preheat of the reactant mixture. At density ratios closer to 1 (where the density ratio equal to 1 represents a non-reacting wake), high Reynolds number wakes are globally unstable (Yu and Monkewitz, 1990), which happens due to weak exothermic combustion and/or high degree preheating of the reactant mixture. When

---

The results presented in this chapter are published in S. A. Pawar, R. I. Sujith, B. Emerson and T. Lieuwen, Characterization of Forced Response of Density Stratified Reacting Wake *Chaos: An Interdisciplinary Journal of Nonlinear Science*, 28(2), 023108: 1-14, (2018).

the density ratio is decreased from one extreme to the other in a high Reynolds number flow, the transition from convective to global instability is observed to be not sudden; it happens gradually via intermittency (Emerson *et al.*, 2012a; Suresha *et al.*, 2016). Convectively unstable and globally unstable flows exhibit substantially different forced response characteristics. Convectively unstable flows are seemingly linear amplifiers (Huerre and Monkewitz, 1990), i.e., such flows display response to both low and high values of the forcing amplitudes. Therefore, the effect of forcing is most prominent in convectively unstable flows, such as the shear layers separating from a bluff body. In contrast, globally unstable flows exhibit a nonlinear response to external disturbances (Huerre and Monkewitz, 1990). These flows will tend to oscillate at their own natural frequency in the presence of low amplitude external forcing but may respond to the forcing when the amplitude of forcing is large. In such a situation, a nonlinear phenomenon of frequency-locking may be observed for the conditions of high amplitude forcing (Masselin and Ho, 1985; Bellows *et al.*, 2008). During the frequency-locking condition, the frequency associated with the global mode oscillations in the wake locks-in with that of the external forcing.

Furthermore, to note that although the response of the forced wake to the forcing could be linear or nonlinear, the underlying flow being turbulent is highly nonlinear and inherently complex. The effect of forcing on non-reacting wakes has been widely studied (Bishop and Hassan, 1964; Tanida *et al.*, 1973; Griffin and Ramberg, 1976; Blevins, 1990; Sheridan *et al.*, 1998; Carberry *et al.*, 2005). In the absence of forcing, the vortex shedding frequency exhibits a certain amount of phase noise that is centered around a particular frequency, often parameterized by a Strouhal number. The application of forcing results in synchronized shedding of vortices at the frequency of forcing. The locking of this forcing frequency with the frequency of vortex shedding depends on the difference between these frequencies and the amplitude of forcing. For larger frequency spacing, a higher value of forcing amplitude is required for the entrainment of these frequencies (Barbi *et al.*, 1986). For reacting wakes, the effect of forcing on the dynamics of the flame for high density ratios ( $\rho_u/\rho_b > 1$ , convectively unstable flow) and low density ratios ( $\rho_u/\rho_b \rightarrow 1$ , globally unstable flow) is quite different due to the difference in the stability of the underlying hydrodynamic flow field. Emerson and Lieuwen (2015) performed a systematic study to quantify the response of the reacting wake to harmonic forcing, for different conditions of the density ratio. They found that

although the longitudinal forcing naturally excites the varicose mode (symmetric vortex shedding), the sinuous mode (asymmetric vortex shedding) is the fastest-growing mode downstream of the bluff body wake for a wide range of density ratios. When the forcing frequency is near the natural frequency of the global mode, the sensitivity of the external forcing is different for the flame edge fluctuations and for the heat release rate fluctuations. At this condition of forcing, the heat release rate fluctuations are minimum, and the transversely induced flame edge fluctuations are maximum, referred to as resonant amplification.

In this chapter, we study the nonlinear response of the highly turbulent, density stratified, bluff body stabilized reacting wake (see Fig. 3.3 in Chapter 3) using various tools from the dynamical systems theory. In the previous studies, the characterization of reacting wakes was based on measures from linear theory (Emerson and Lieuwen, 2015; Shin *et al.*, 2011; Shanbhogue *et al.*, 2009b). However, since the response of the reacting wake (or flame) to the external forcing is nonlinear (Lieuwen and Neumeier, 2002), it is necessary to adopt a framework based on dynamical systems theory to understand the interactions between the signals of forcing and forced response of the wake in a better manner. Recently, for a case of the hydrodynamically unstable flow field, Juniper and co-workers used the framework of forced synchronization (Li and Juniper, 2013a) to study the forced response of a low density jet (Li and Juniper, 2013d), a diffusion flame (Li and Juniper, 2013b), and a swirl-stabilized flame (Balusamy *et al.*, 2015) at different conditions of the forcing parameters. Using the theory of synchronization, they characterized various dynamical states of the forced flame response, such as quasiperiodicity, phase drifting, phase trapping, and phase locking, which were unnoticed previously in the literature.

In a similar manner, we characterize the various other aspects of the forced wake dynamics such as determinism, symmetry of phase locking of the top and bottom branches of the wake with the forcing, and the relative phase angle of the vortex shedding from the trailing edges of the bluff body. We first compare the dynamics of the flame in the absence of forcing with that in the presence of forcing when the forcing amplitude is sufficiently high. We subsequently move our attention to detect the phase-locking (or synchronization) behaviour of the oscillations in the flame (reacting wake) with the forcing signal. Towards this purpose, we compute the local heat release rate fluctuations from the top and bottom halves of the flame at an unforced state ( $A_f = 0$ ) as well

as forced at an amplitude of  $A_f = 0.02$ . Here,  $A_f = |u'_{lip}(f_f)/(2f_f D)|$  is the normalized amplitude of the forcing obtained from the ratio of unsteady axial velocity at the bluff body lip ( $u'_{lip}$ ) acquired from PIV measurement (discussed in detail in Emerson and Lieuwen, 2015) to the diameter of the bluff body ( $D$ ), and  $f_f$  is the frequency of periodic forcing.

## 6.1 Comparison of the Dynamics of Unforced and Forced Oscillations of Reacting Wake

We see from Figs. 6.1a-d that, during the state of unforced oscillations, the flame edge is weakly modulated, wherein the oscillations in the flame are mainly due to the underlying hydrodynamic instability of the reacting flow. In contrast, the forced flame exhibits oscillatory corrugations on both sides of its surface, as seen in Figs. 6.1e-h. These wavy patterns in the flame edge are the result of shedding of large-scale vortical structures from the trailing edges of the bluff body at a frequency equal to that of the external perturbations (since  $f_n/f_f \approx 1$ ). The vertical lines shown in the flame images (in Figs. 6.1a,e) with different colors divide the near field of the wake into two equal halves representing the top (red line) and the bottom (yellow line) branches of the flame. The location of the line is chosen at  $x/D = 3$ . The instantaneous local heat release rate fluctuations of the top ( $I_T$ ) and bottom ( $I_B$ ) portions of the flame are obtained by summing all the pixel intensities lying along the respective lines. The time series corresponding to these local heat release rate fluctuations ( $I_T$  and  $I_B$ ) for the conditions of unforced and forced states are shown in Figs. 6.1i,k and Figs. 6.1j,l, respectively. During the unforced state, the oscillations in the flame are aperiodic, which thereafter, transition to seemingly periodic oscillations due to the application of high amplitude forcing to the flame. We notice an increase in the amplitude of the local heat release rate fluctuations due to forcing.

We, further, characterize the dynamics of these local heat release rate fluctuations in a higher dimensional phase space by using a time-delay embedding theorem proposed by Takens *et al.* (1981). According to this theorem, a univariate time series can be appropriately embedded into a higher dimensional space, if a proper value of the time delay ( $\tau_{opt}$ ) and the embedding dimension ( $E$ ) are chosen. The optimum value of the

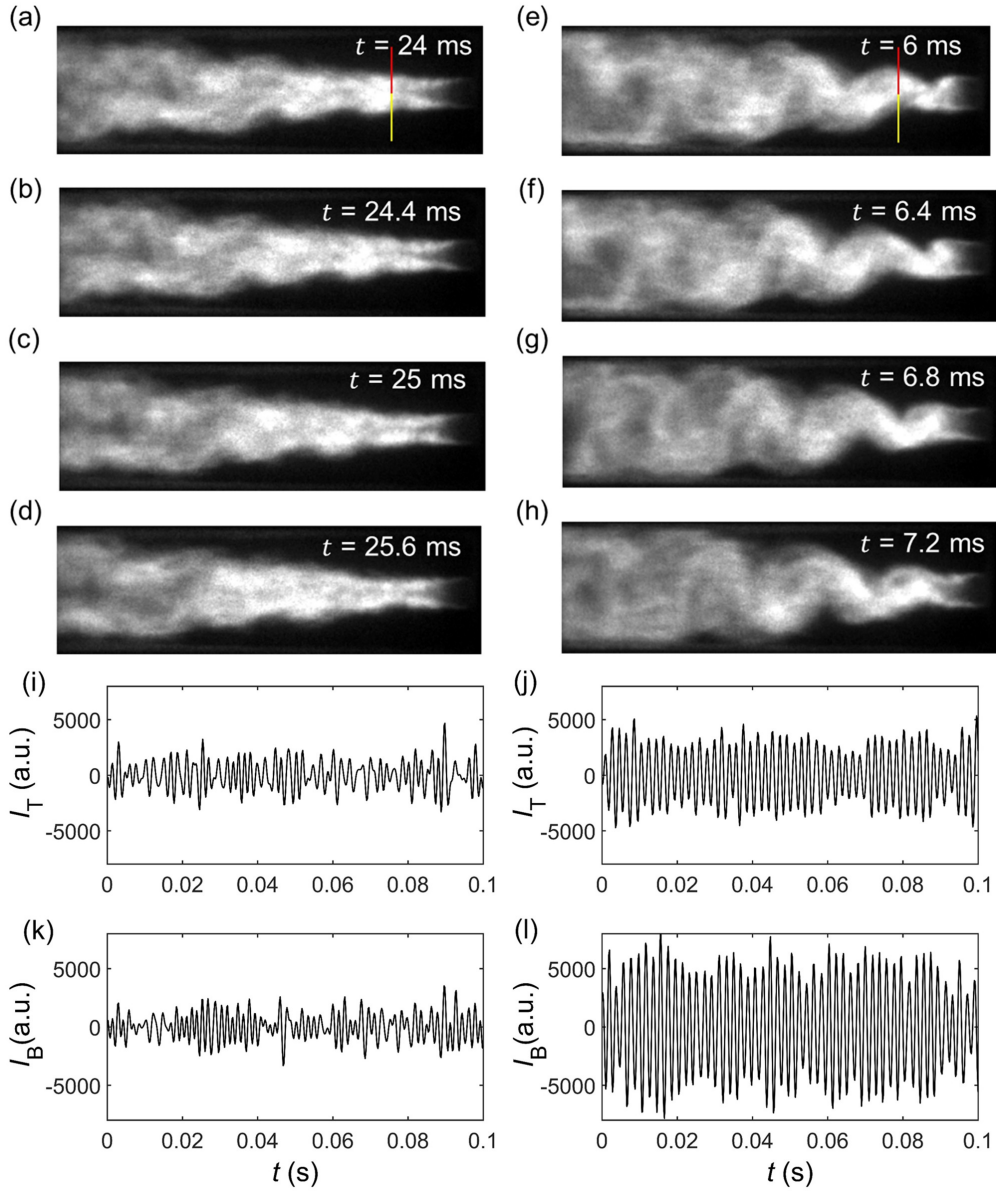


Figure 6.1: The instantaneous  $\text{CH}^*$  chemiluminescence images of the flame shown for different time instances of the oscillation cycle captured during (a)-(d) unforced ( $A_f = 0$ ) and (e)-(h) forced ( $A_f = 0.02$ ) states. (i), (j) and (k), (l) The time series of the local heat release rate fluctuations acquired from top (shown by red line in a) and bottom (shown by yellow line in a) branches of the flame correspond to  $A_f = 0$  and  $A_f = 0.02$ , respectively. The parameters that are fixed:  $x/D = 3$ ,  $\rho_u/\rho_b = 2$ ,  $U_{lip} = 40$  m/s, and  $f_n/f_f \approx 1$ . The flow direction is from right to left.

time delay can be calculated from the average mutual information (Fraser and Swinney, 1986) and the minimum embedding dimension can be calculated from the method of false nearest neighbors (Kennel *et al.*, 1992). A detailed description of the use of Takens' embedding theorem to construct a phase space is found in Abarbanel *et al.* (1993). The value of optimum time delay corresponds to the first local minimum of the average mutual information (Fraser and Swinney, 1986), and the minimum embedding

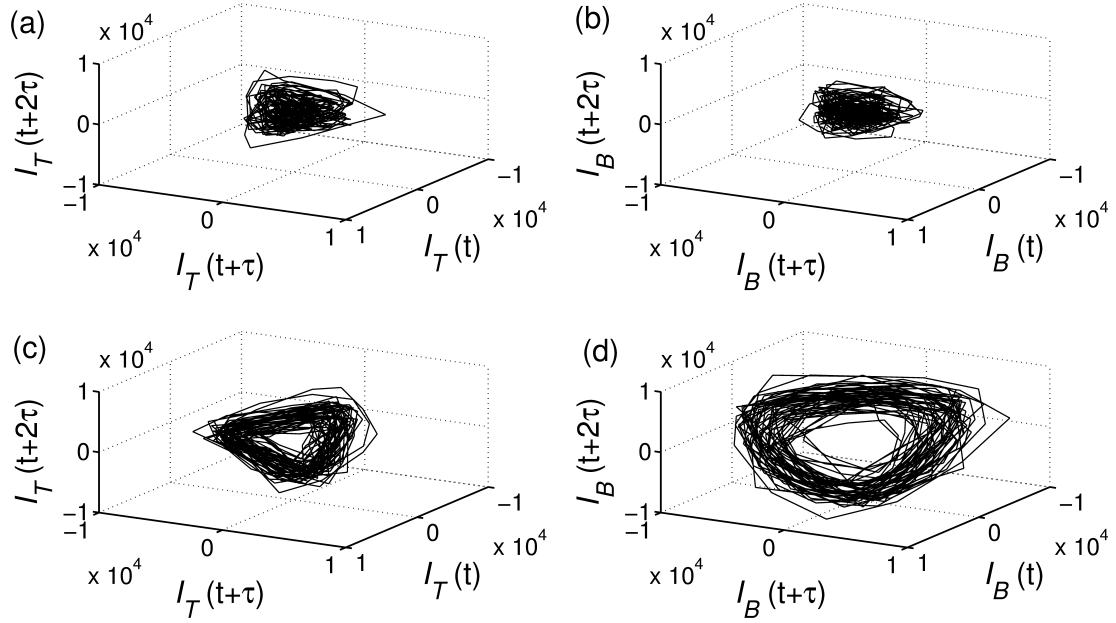


Figure 6.2: The reconstructed phase portraits of the local heat release rate fluctuations obtained from the top ( $I_T$ ) and bottom ( $I_B$ ) halves of the flame for the conditions of (a), (b) unforced ( $A_f = 0$ ) and (c), (d) forced at amplitude  $A_f = 0.02$ . The parameters chosen for the reconstruction of the phase space are:  $\tau_{opt} = 0.6$  ms and  $E = 6$ . The conditions that are fixed:  $x/D = 3$ ,  $U_{lip} = 40$  m/s,  $f_n/f_f \approx 1$  and  $\rho_u/\rho_b = 2$ .

dimension is chosen as the next dimension to the value where the percentage of false nearest neighbors becomes zero for the first time (Kennel *et al.*, 1992).

Figure 6.2 shows a three-dimensional reconstructed phase space of the local heat release rate fluctuations obtained from the top ( $I_T$ ) and bottom ( $I_B$ ) branches of the flame corresponding to unforced (Figs. 6.2a,b) and forced at  $A_f = 0.02$  (Figs. 6.2c,d) states, respectively. For the unforced case, the attractors of the local flame dynamics show a clutter of trajectories in the phase space, due to their aperiodic nature. Whereas, during the condition of high amplitude forcing, the phase portraits show a relatively regular behaviour wherein the trajectories are arranged into a distorted oval structure. The scatter of these trajectories in the phase space is a result of variation in the amplitudes of the periodic oscillations observed in the local heat release rate fluctuations.

The recurrence behaviour of these phase space trajectories is further characterized by using recurrence plots, RP (Eckmann *et al.*, 1987). Recurrence is a property of deterministic dynamical systems (Eckmann *et al.*, 1987) in which the recurrent behaviour of a phase space trajectory is captured in a region which has been previously visited by the same trajectory.<sup>2</sup>

<sup>2</sup>The mathematical formulation of the construction of recurrence plots is shown in Section 2.5.2.

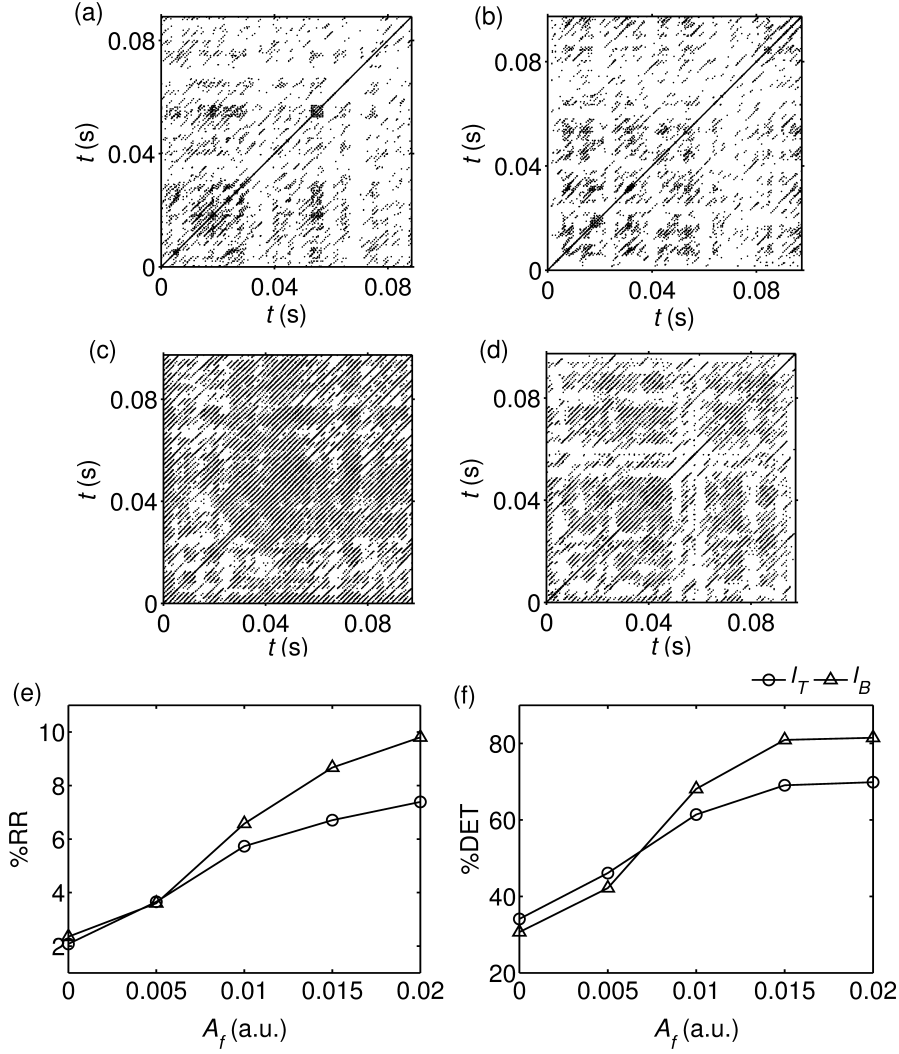


Figure 6.3: The recurrence plots of the local heat release rate fluctuations obtained from the top ( $I_T$ ) and bottom ( $I_B$ ) portions of the flame for (a), (b) the absence of forcing and (c), (d) the presence of forcing at  $A_f = 0.02$ . The variation of recurrence quantification measures such as (e) %RR and (f) %DET are plotted for different values of the forcing amplitude. The conditions that are fixed:  $x/D = 3$ ,  $U_{lip} = 40$  m/s,  $f_n/f_f \approx 1$ , and  $\rho_u/\rho_b = 2$ . Recurrence parameters used for plotting are: time delay ( $\tau_{opt}$ ) = 0.6 ms, embedding dimension ( $E$ ) = 6, recurrence threshold ( $\epsilon$ ) = 20% of the maximum size of the attractor and the number of data points equal to 1000.

In Fig. 6.3, the RPs of the local heat release rate fluctuations obtained from the top and bottom halves of the flame in the absence of forcing (Figs. 6.3a,b) and in the presence of forcing at  $A_f = 0.02$  (Figs. 6.3c,d) are shown. In the absence of forcing, the RP shows rarer structures of broken lines that are aligned parallel to the main diagonal in the plot. We further note that these short (or broken) diagonal lines are distributed in an apparently random manner. During the state of maximum forcing, the RP appears to be denser with most of the recurrence points aligned along the broken diagonal lines. The lesser the density of the black points, the weaker the recurrence of the phase

space trajectory. The existence of short (or broken) diagonal lines in RPs indicates the possibility of the presence of deterministic chaos (Aparicio *et al.*, 2008; Marwan *et al.*, 2002) in the oscillations of unforced local heat release rate fluctuations. In contrast, for white noise signals, the RPs exhibit only single isolated black points due to their non-recurring behaviour. Furthermore, we quantify the recurrence properties of the phase space trajectories when the amplitude of the forcing is varied.

In Figs. 6.3e,f, we plot the variation of two quantitative measures of recurrence (Webber and Zbilut, 1994; Marwan *et al.*, 2002) known as recurrence rate ( $\%RR$ ) and determinism ( $\%DET$ ), respectively, for different values of the forcing amplitude. Recurrence rate captures the percentage of the total number of state points of a phase space trajectory that recurs inside the threshold. It is calculated as

$$RR = \frac{1}{N_1^2} \sum_{i,j=1}^{N_1} R_{i,j} \quad (6.1)$$

On the other hand, determinism captures the percentage of a total number of recurrence points that align in parallel with the main diagonal line in the RP. The determinism is calculated as

$$DET = \frac{\sum_{i=l_{min}}^{N_1} lP(l)}{\sum_{i,j=1}^{N_1} R_{i,j}} \quad (6.2)$$

where  $P(l)$  is the histogram of the lengths  $l$  that form diagonal lines in the RP ( $l_{min} = 2$  Points). Determinism is a measure of predictability of the dynamical system. It takes higher and lower values for the regular and irregular behaviours of the system dynamics, respectively.

We notice an increase in the values of  $\%RR$  and  $\%DET$  with an increase in the forcing amplitude. Significantly higher value (as compared to zero) of  $\%DET$ , during the unforced state, indicates the presence of deterministic or possibly a chaotic behaviour (Trulla *et al.*, 1996; Hołyst *et al.*, 2001; Aparicio *et al.*, 2008; Marwan *et al.*, 2002) in the local dynamics of the heat release rate signal. The amount of determinism and also periodicity increases with increase in the forcing amplitude and reaches a maximum value for  $A_f = 0.02$ .

## 6.2 Symmetry and Asymmetry of Forced Response of Reacting Wake

The dynamics of the forced flame response obtained in terms of local heat release rate fluctuations is further investigated for off-resonance conditions (i.e.,  $f_n/f_f < 1$  and  $f_n/f_f > 1$ ) of forcing. As the heat release rate fluctuations obtained from the top and bottom branches of the flame during the unforced state are broadband (see Figs. 6.5a-I,II), the detection of the exact value of natural frequencies of the signal from visual inspection of their frequency spectrums is difficult. Nevertheless, the flow velocity conditions can be maintained in such a way that the mean frequency ( $f_n = (1/2\pi) \langle d\phi/dt \rangle$ , where  $\phi$  is the instantaneous phase of the signal) of the overall selected frequency range of the heat release rate fluctuations, at a given condition of the frequency ratio, is either lower than, nearly equal to, or greater than  $f_f$ .

Figure 6.4 shows the comparison of the reconstructed phase portraits of the top and bottom halves of the flame obtained for both conditions of frequency ratios,  $f_n/f_f < 1$  and  $f_n/f_f > 1$ , and four different values of the density ratios (i.e.,  $\rho_u/\rho_b = 1.7, 1.9, 2$  and  $2.4$ ). Here,  $\rho_u/\rho_b = 1.7$  and  $1.9$  (low density ratios) correspond to the globally unstable flow,  $\rho_u/\rho_b = 2$  (intermediate density ratio) corresponds to the situation of intermittency where the reacting flow dynamics fluctuates between globally unstable flow and convectively unstable flow characteristics, and  $\rho_u/\rho_b = 2.4$  (high density ratio) corresponds to convectively unstable flow. We observe in Figs. 6.4a,b that during the case of low density ratio ( $\rho_u/\rho_b = 1.7$  &  $1.9$ ) and when  $f_n/f_f < 1$ , the phase space trajectories of the top side of the flame display a cluttered behaviour, whereas that for the bottom side of the flame show a seemingly regular structure. The situation reverses at these density ratios when  $f_n/f_f > 1$ , wherein the top side of the flame has a seemingly regular behaviour and the bottom side of the flame has a noisy behaviour in the phase space. We hypothesize that small, inherent asymmetry in the geometry may provide a “reference” to the fluid dynamics. This reference allows the flow to respond with a repeatable directionality to its asymmetry. An interesting pair of observations is (a) the repeatability of this phenomenon, which demonstrates a high degree of sensitivity to small geometrical imperfections and (b) the switching of the directionality of this asymmetry as the frequency ratio ( $f_n/f_f$ ) is varied.

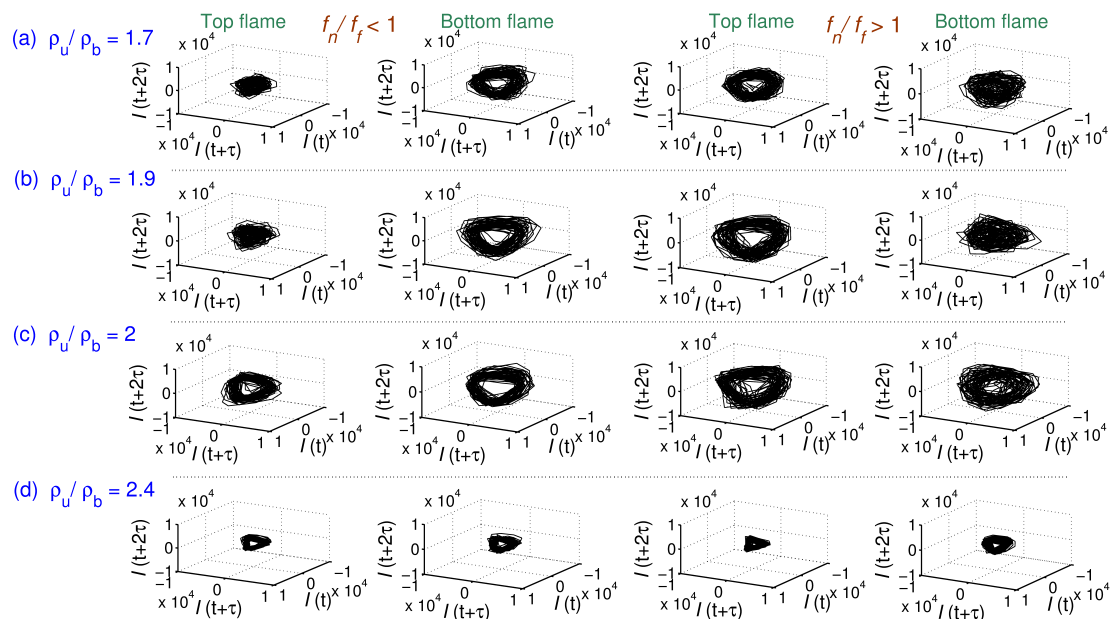


Figure 6.4: The reconstructed phase portraits of the local heat release rate fluctuations obtained from the top and bottom sides of the flame are shown for the conditions of two frequency ratios  $f_n/f_f < 1$  and  $f_n/f_f > 1$ , and four density ratios (a)  $\rho_u/\rho_b = 1.7$ , (b)  $\rho_u/\rho_b = 1.9$ , (c)  $\rho_u/\rho_b = 2$ , and (d)  $\rho_u/\rho_b = 2.4$ . The flow velocity conditions, for  $\rho_u/\rho_b = 1.7$  ( $U_{lip} = 35$  m/s and 44 m/s), for  $\rho_u/\rho_b = 1.9$  ( $U_{lip} = 35$  m/s and 46 m/s) for  $\rho_u/\rho_b = 2$  ( $U_{lip} = 34$  m/s and 46 m/s), and for  $\rho_u/\rho_b = 2.4$  ( $U_{lip} = 34$  m/s and 45 m/s), are chosen such that the conditions of frequency ratios are  $f_n/f_f < 1$  and  $f_n/f_f > 1$ , respectively. The parameters chosen for the reconstruction of the phase space are optimum time delay  $\tau = 0.6$  ms and embedding dimension  $d = 6$ . The conditions that are fixed:  $x/D = 3$  and  $A_f = 0.02$ .

Further, we notice a seemingly regular behaviour of the phase space trajectory for intermediate ( $\rho_u/\rho_b = 2$ ) and sufficiently higher value ( $\rho_u/\rho_b = 2.4$ ) of the density ratios (in Figs. 6.4c,d) irrespective of the values of frequency ratios ( $f_n/f_f < 1$  or  $f_n/f_f > 1$ ). These observations of the flame dynamics in the phase space suggests that the response of the flame to the periodic forcing is asymmetric for the values of lower density ratios ( $\rho_u/\rho_b = 1.7$  and 1.9), where the unforced reacting flow dynamics is globally unstable (Emerson *et al.*, 2012a). On the contrary, such behaviour of the flame dynamics is relatively symmetric for the intermediate ( $\rho_u/\rho_b = 2$ ) and the higher ( $\rho_u/\rho_b = 2.4$ ) density ratios, where the unforced reacting flow dynamics is observed to be intermittent and convectively unstable, respectively (Emerson *et al.*, 2012a; Suresha *et al.*, 2016). This behaviour of flame dynamics is, however, expected in convectively unstable cases due to the symmetric nature of the forcing (Emerson and Lieuwen, 2015).

The qualitative observations of the symmetry in the forced flame response during off-resonance conditions at different density ratios (as shown in Fig. 6.4) further moti-

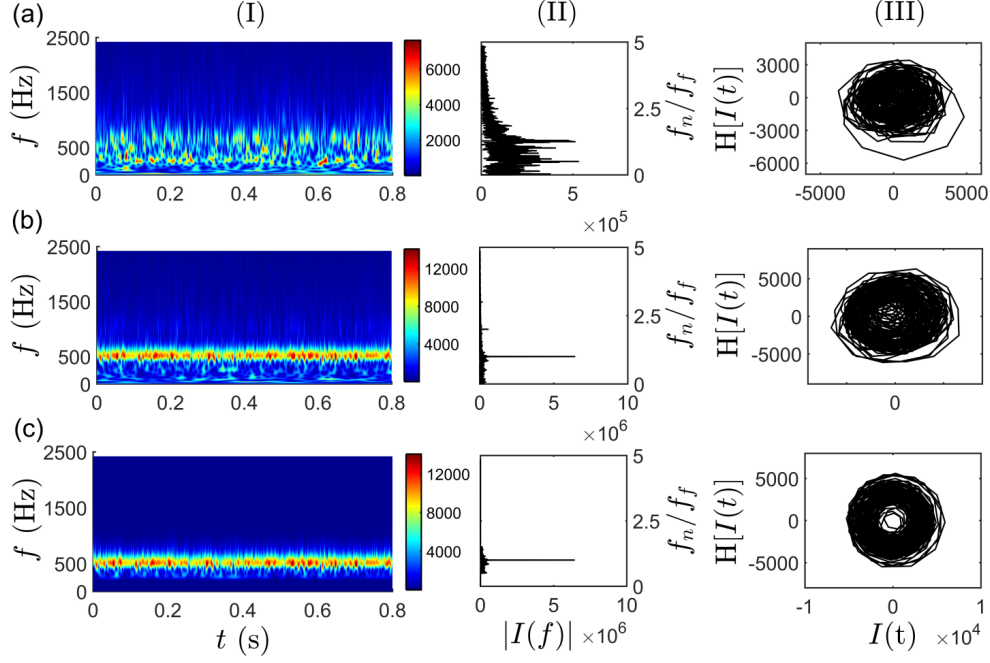


Figure 6.5: (I) Time-frequency plot obtained from wavelet transform, (II) amplitude spectrum obtained from Fourier transform, and (III) analytic plane representation of the signal. These plots demonstrate the different properties of local heat release rate fluctuations obtained from the bottom half of the flame (I) for different conditions (a) unforced ( $A_f = 0$ ), (b) forced at high amplitude ( $A_f = 0.02$ ), and (c) filtered signal corresponding to the forced state. The conditions that are fixed  $x/D = 3$ ,  $U_{lip} = 35$  m/s,  $f_n/f_f < 1$  and  $\rho_u/\rho_b = 1.7$ . The forcing frequency ( $f_f$ ) is fixed at 515 Hz. The frequency range chosen for bandpass filtering of the heat release rate signals is  $0.5f_f < f_f < 1.5f_f$ .

vates us to quantify this symmetry aspect using a framework of synchronization. Here, we turn our attention to characterize the phase-locking behaviour of the local heat release rate fluctuations obtained from top and bottom branches of the flame with the forcing signal. In doing so, we calculate the instantaneous phases of these signals from an analytic signal approach based on the Hilbert transform (refer Section 2.5.1 for more details on the instantaneous phase calculations).

Figures 6.5-I,II show two different ways of representing spectral properties of the signals, where Fig. 6.5-I corresponds to a time-frequency plot based on the wavelet transform and Fig. 6.5-II demonstrates the amplitude spectrum of the signal obtained from the fast Fourier transform. Here, we use the continuous wavelet transform, CWT, (Farge, 1992) to represent the localized time varying frequency content of the heat release rate signal. The mathematical description of the CWT is provided in Section 2.5.3. The spectral properties of the unforced local heat release rate fluctuations ob-

tained from the bottom half of the flame are shown in Figs. 6.5a-I and 6.5a-II. These plots suggest that the heat release rate fluctuations observed during the unforced state are broadband. This wide distribution of frequencies is further reflected in the representation of the signal in its analytic plane (plot between  $I(t)$  and  $H[I(t)]$ ). In such a plane (Fig. 6.5a-III), the behaviour of the trajectory is seemingly irregular exhibiting multiple centers of rotations about its origin. In Figs. 6.5b-I and 6.5b-II, the spectral properties of  $I$  corresponding to the situation of high amplitude forcing ( $A_f = 0.02$ ) are shown. When the amplitude of forcing is sufficiently large (observed as a sharp amplitude peak in the frequency spectrum), the spectral properties of the unforced signal gets organized around the forcing frequency (as shown in Fig. 6.5b-I). Even though the signal is forced at high amplitude (see Fig. 6.5b-II), the analytical plane corresponding to this signal (Fig. 6.5b-III) still shows multiple centers of rotation, which results in an improper definition of the instantaneous phase of the signal.

The application of filtering to the heat released rate signals within a frequency band of  $0.5f_f < f < 1.5f_f$  removes the multiple centers of rotation in the analytic plane. We note that the interpretation of synchronization behaviour of the forcing signal with that of the heat release rate fluctuations is sensitive to the size of the frequency band. The change in the frequency range might lead to additional phase slips in the relative phase plot of the two signals. Here, the phase slip is related to an increase in the value of the unwrapped relative phase of the signals by integer multiples of  $2\pi$ . Figures 6.5c-I and 6.5c-II depict the spectral properties of the bandpass signal. Bandpass filtering removes the noisy fluctuations associated with low as well as high-frequency components (outside the selected frequency band) present in the signal. The removal of such frequencies smoothens the signal. The effect of filtering is clearly reflected in the representation of the signal in the analytic plane, where the plot (see Fig. 6.5c-III) shows a clear center of rotation, and thus enabling a proper definition of phase in the signal.

Synchronization behaviour of the filtered local heat release rate signal ( $I$ ) with the forcing signal ( $F$ ) is examined by computing the instantaneous phase difference [ $\Delta\phi_{F,I}(t) = \phi_F(t) - \phi_I(t)$ ] between them. The effect of external forcing on the top and the bottom branches of the flame is analyzed for three different conditions of the frequency ratios as (i)  $f_n < f_f$ , (ii)  $f_n \approx f_f$  and (iii)  $f_n > f_f$  at a constant value of the forcing amplitude ( $A_f = 0.02$ ). This investigation is necessary to quantitatively detect the aspect of symmetry in the response dynamics obtained from both branches

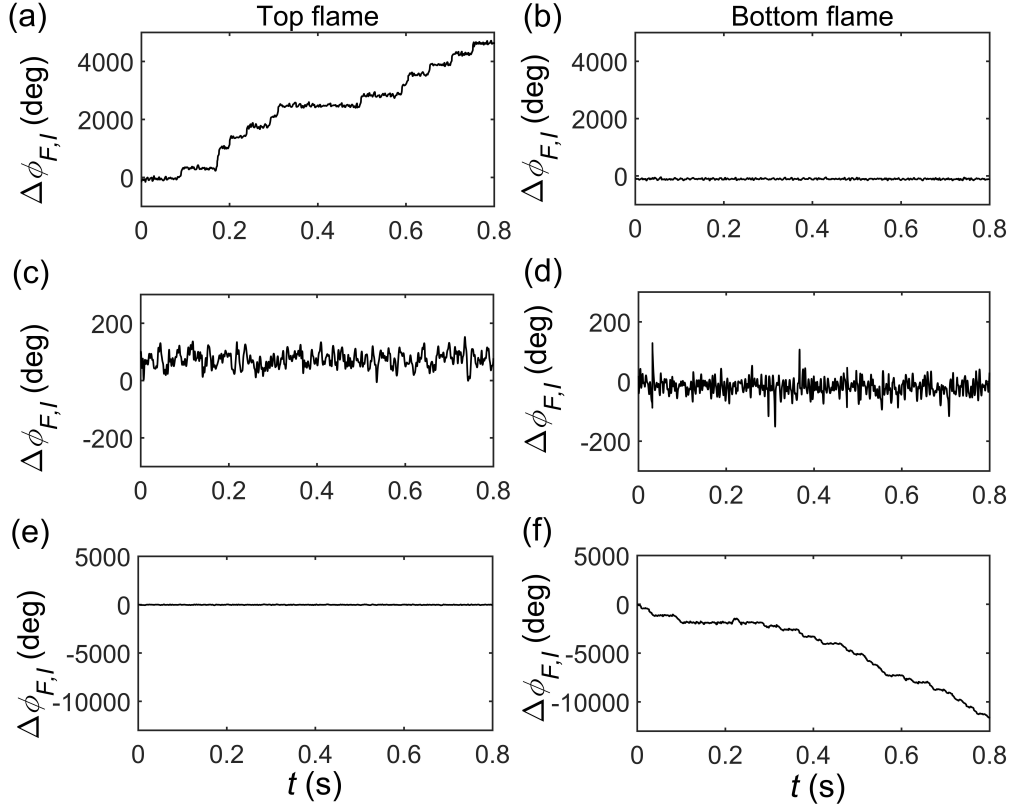


Figure 6.6: The temporal variation of the relative phase of local heat release rate fluctuations obtained from the top and bottom branches of the flame with the external forcing for a low density case. The test conditions correspond to three values of the forcing frequency such that (a), (b)  $f_n/f_f < 1$  ( $U_{lip} = 35$  m/s), (c), (d)  $f_n/f_f \approx 1$  ( $U_{lip} = 41$  m/s), and (e), (f)  $f_n/f_f > 1$  ( $U_{lip} = 46$  m/s). The parameters that are maintained constant are  $x/D = 3$ ,  $\rho_u/\rho_b = 1.9$  and  $A_f = 0.02$ .

of the flame to the external forcing, as shown qualitatively in Fig. 6.4. Furthermore, we compare such a behaviour of the forced flame response for two different conditions of the density ratios i.e.,  $\rho_u/\rho_b = 1.9$  and  $3.2$ . The density ratios are chosen such that the low density ratio ( $\rho_u/\rho_b = 1.9$ ) and high density ratio ( $\rho_u/\rho_b = 3.2$ ) correspond to the globally unstable and convectively unstable modes, respectively (Emerson *et al.*, 2012a).

The response of the top and bottom branches of the flames to the forcing, calculated in terms of the instantaneous phase difference, for  $\rho_u/\rho_b = 1.9$  is shown in Fig. 6.6. We note that the heat release rate fluctuations obtained from the top branch of the flame exhibit phase drifting behaviour (see Fig. 6.6a), whereas that corresponding to the bottom branch of the flame is perfectly phase-locked with the forcing signal (see Fig. 6.6b). The increasing trend in the plot of the instantaneous relative phase (Fig. 6.6a) suggests that the mean frequency ( $f_n$ ) of the heat release rate fluctuations is lesser than

the forcing frequency i.e.,  $f_n/f_f < 1$ . Here, the phase difference is calculated between the instantaneous phases of the forcing signal with that of the natural oscillations of local heat release rate in the flame. When the value of flow velocity is such that  $f_n/f_f \approx 1$  (Figs. 6.6c,d), we witness a perfect locking of the instantaneous phases of the signals obtained from both branches of the flame with the forcing signal. Conversely, when  $f_n/f_f > 1$ , we observe the switching of phase locking behaviour of the heat release rate fluctuations from bottom to top branch of the flame. In this condition, we observe that the top branch of the flame is perfectly phase-locked with the forcing (Fig. 6.6e), while the bottom branch of the flame shows a phase drifting behavior (Fig. 6.6f). The decreasing trend of the instantaneous relative phases in the plot further validates the condition of  $f_n/f_f > 1$  (see Fig. 6.6f). This suggests that the response of two branches of the flames to the symmetric longitudinal forcing is asymmetric during off-resonance conditions of the frequency ratios, for the case of low density ratio. In such a situation, external forcing sheds synchronized vortices from either (bottom or top) lip of the bluff body, depending on whether  $f_n/f_f < 1$  or  $f_n/f_f > 1$ , respectively.

Figure 6.7 shows the temporal variation of instantaneous phase difference of the local heat release rate fluctuations obtained from the top and bottom branches of the flame with the forcing signal, for  $\rho_u/\rho_b = 3.2$  and three different conditions of frequency ratios, i.e.,  $f_n/f_f < 1$  (Figs. 6.7a,b),  $f_n/f_f \approx 1$  (Figs. 6.7c,d) and  $f_n/f_f > 1$  (Figs. 6.7e,f). We notice that, during all conditions of the frequency ratios, the instantaneous phase difference of the heat release rate fluctuations of both branches of the flame display a perfect phase locking with the forcing signal. This observation of the relative phase further suggests that the effect of forcing is nearly symmetric on both branches of the flame during high density ratio case. Thus, in the case of high density ratio, forcing simultaneously sheds a synchronized pair of vortices at the forcing frequency from the lip of both sides the bluff body.

The low density ratio wakes, where the flow is globally unstable, exhibit a stronger sensitivity to the frequency ratio ( $f_n/f_f$ ). We notice that when the density ratio is low (see Fig. 6.6), the maximum amplitude of the acoustic perturbations considered in the present study is insufficient to simultaneously synchronize the heat release rate fluctuations obtained from both branches of the flame with the forcing signal. Conversely, for the case of high density ratio (see Fig. 6.7), this value of the forcing amplitude is sufficiently high to synchronize the instantaneous phases of the heat release rate fluctua-

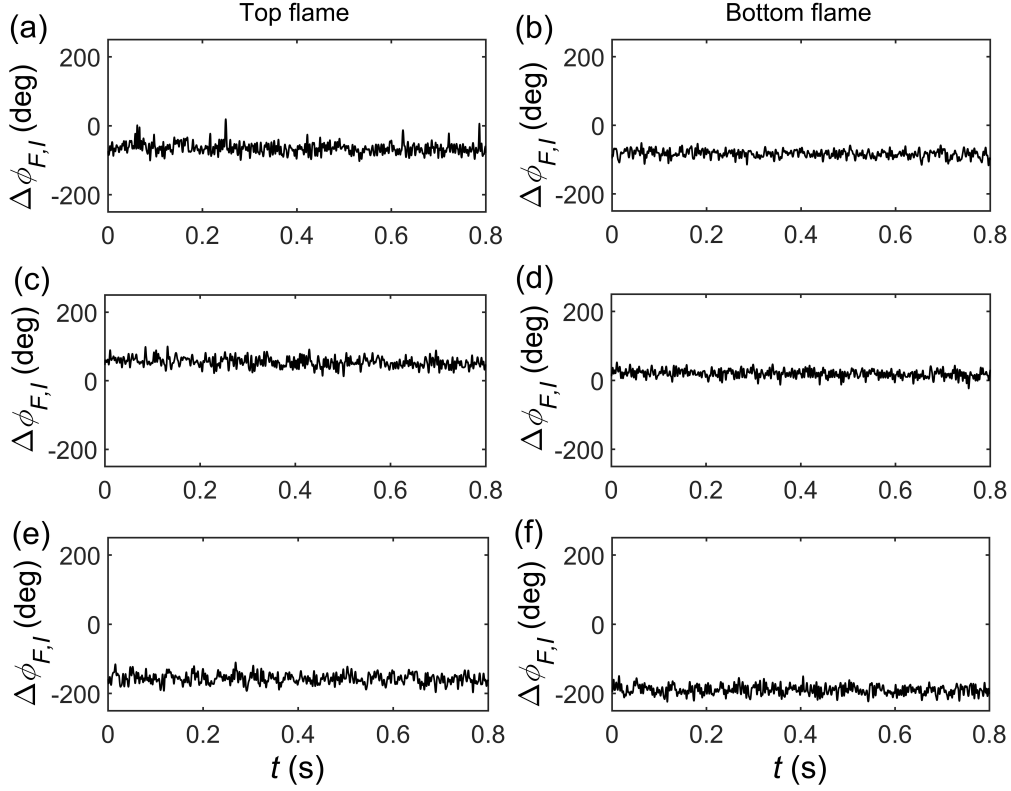


Figure 6.7: The temporal variation of the relative phase of the local heat release rate fluctuations obtained from top and bottom branches of the flame with the external forcing for a high density case. The test conditions correspond to three values of the forcing frequency such that (a), (b)  $f_n/f_f < 1$  ( $U_{lip} = 24$  m/s), (c), (d)  $f_n/f_f \approx 1$  ( $U_{lip} = 41$  m/s), and (e), (f)  $f_n/f_f > 1$  ( $U_{lip} = 44$  m/s). The parameters that are maintained constant are  $x/D = 3$ ,  $\rho_u/\rho_b = 3.2$  and  $A_f = 0.02$ .

tions obtained from both branches of the flame with the forcing signal. Previous studies (Emerson *et al.*, 2012b; Emerson and Lieuwen, 2015) on the same experimental dataset have not noticed the sensitivity of the low density ratio flame asymmetry to  $f_n/f_f$ . Specifically, the asymmetry exhibits phase synchronization of the bottom flame branch when  $f_n/f_f < 1$  and phase synchronization of the top flame branch when  $f_n/f_f > 1$ .

In the case of intermediate density ratios, i.e.,  $\rho_u/\rho_b = 2$  or  $2.2$ , we notice a perfect phase locking of the top and the bottom branches of the flame with the forcing signal, irrespective of whether  $f_n/f_f < 1$  or  $f_n/f_f > 1$ . The results for these density ratios are similar to that observed for the high density ratio case ( $\rho_u/\rho_b = 3.2$ ), as shown in Fig. 6.7. Emerson *et al.* (2012a) and Suresha *et al.* (2016) have reported the presence of intermittency during  $\rho_u/\rho_b = 2$  and showed that the features of such intermittent oscillations vanish at  $\rho_u/\rho_b = 2.4$ . Intermittency, here, refers to the apparently random switching of the flow dynamics from a region of convectively unstable (features of high

density ratio) to a globally unstable (features of low density ratio) mode of oscillations. Thus, during  $\rho_u/\rho_b = 2$ , we expect that the phase-locking behaviour of the top and bottom branches of the flame will have features that are observed in Fig. 6.6 and 6.7 for different conditions of the frequency ratios. That is, when the intermittent flow dynamics exhibit globally unstable behavior, an asymmetry in the phase locking behaviour of both branches of the flame is expected to occur. Conversely, when the intermittent flow dynamics exhibit convectively unstable behavior, the perfect phase locking of both branches of the flame is expected to happen. However, we do not observe such features at this density ratio or at the other intermediate density ratio of  $\rho_u/\rho_b = 2.2$ . This might be because the maximum amplitude of forcing used in all the experiments is high enough to diminish such expected features of the phase dynamics during intermediate density ratios and responsible for the entrainment of the phases of both branches of the flame with the forcing signal.

### **6.3 Characterization of Phase-Locking Behavior Between Top and Bottom Branches of the Flame**

We now move our attention to investigate the phase locking behaviour between the heat release rate signals obtained from the top and bottom branches of the flame. This analysis, in turn, helps in quantifying the relative phase between the vortices that are shed from the top and bottom sides of the bluff body during a high Reynolds number flow condition. This also helps in identifying the kind of vortex shedding pattern (sinuous or varicose) exhibited by the bluff body wake at a given density ratio. During the sinuous type of vortex shedding, both branches of the flame move in the same direction such that the relative phase between the oscillations of their edges is near to zero degrees or the relative phase between the fluctuations of their local heat release rate is near to 180 degrees. The opposite happens for the varicose mode of vortex shedding (Emerson and Lieuwen, 2015). Figure 6.8 shows the temporal variation of the phase difference between the heat release rate fluctuations obtained from the top and bottom branches of the flame for different density ratios. The flow velocity (hence, the mean frequency of natural oscillations of the flame) and the amplitude of forcing are maintained constant at  $U_{lip} = 41$  m/s and  $A_f = 0.02$ , respectively. The choice of  $U_{lip}$  is such that the mean

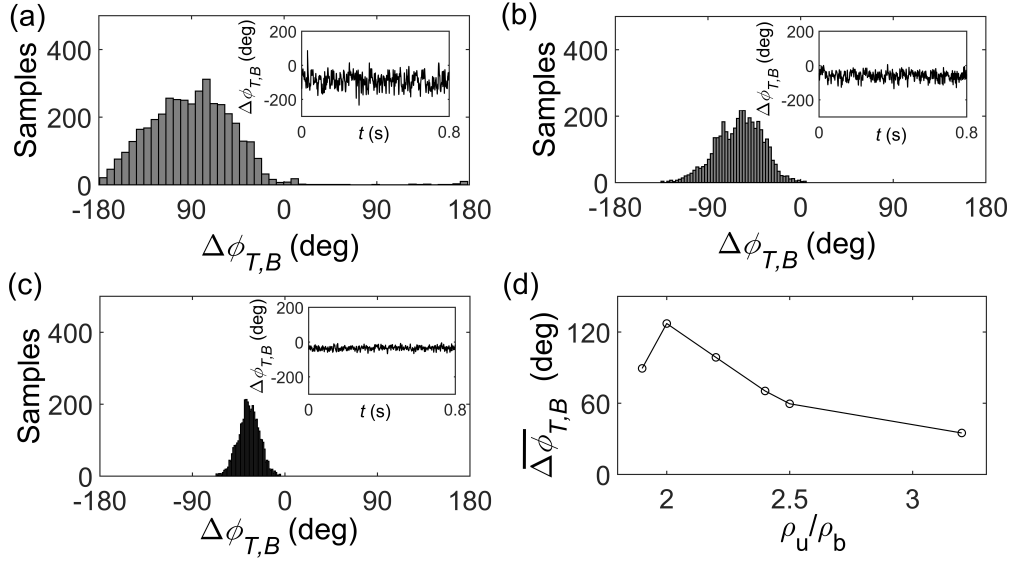


Figure 6.8: (a)-(c) The distribution and the temporal variation (in insets) of the instantaneous phase difference between the signals of heat release rate fluctuations obtained from top and bottom branches of the flame for three different conditions of density ratios as  $\rho_u/\rho_b = 1.9, 2.5$  and  $3.2$ , respectively. (d) The plot showing the variation of mean relative phase angle between the top and bottom branches of a reacting wake with different values of the density ratio i.e.,  $\rho_u/\rho_b = 1.9, 2, 2.2, 2.4, 2.5$  and  $3.2$ . The parameters that are fixed  $U_{lip} = 41$  m/s,  $f_n/f_f \approx 1$ ,  $A_f = 0.02$ , and  $x/D = 3$ . During  $f_n/f_f \approx 1$ , the flame dynamics is such that both branches of the flame are perfectly phase locked state with each other (see insets of a-c).

frequency of the unforced natural oscillations in the local heat release rate fluctuations is nearly same as the frequency of the external forcing (i.e.,  $f_n/f_f \approx 1$ ).

In order to detect synchrony between the heat release rate signals of the top and the bottom branches of the flame, we compute the instantaneous phase difference between them (i.e.,  $\Delta\phi_{T,B}(t) = \phi_T(t) - \phi_B(t)$ , where  $T$  and  $B$  correspond to the top and the bottom branches of the flame, respectively). We notice that for  $A_f = 0.02$ , as the forcing amplitude is sufficiently high and since  $f_n/f_f \approx 1$ , the instantaneous phases of the heat release rate fluctuations obtained from both branches of the flame are perfectly phase locked. This phase locking is confirmed from the fluctuations of the relative phase of these signals around a constant phase shift (refer to insets of Figs. 6.8a-c). In Figs. 6.8a-c, we plot the histogram of the relative phase wrapped in the interval of  $-180$  to  $+180$  degrees. We observe that, for the case of low density ratio (shown in Fig. 6.8a), the histogram of the relative phase displays a wider distribution, whereas that of the higher density ratio (shown in Fig. 6.8c) shows a narrower distribution. On the other hand, for an intermediate case of the density ratio (Fig. 6.8b), the width of the distribution

is in between the value observed for the cases of low and high density ratios. The observation of narrow distribution in the relative phase, for the high density ratio case, demonstrates that the cycle-to-cycle variation of instantaneous phases of the heat release rate fluctuations obtained from both branches of the flame is very low. In contrast, this cycle-to-cycle variation of instantaneous phases of the heat release rate signals is high during the low density ratio case. This further supports the observation that the low density ratio flames are less receptive to external forcing than high density ratio flames (Huerre and Monkewitz, 1990).

Figure 6.8d shows the variation in mean phase difference ( $\overline{\Delta\phi} = \frac{1}{N} \sum_{i=1}^N \Delta\phi_i$ ) between the signals of heat release rate fluctuations obtained from the top and bottom branches of the flame, for different values of the density ratios. The value of flow velocity is maintained such that  $f_n/f_f \approx 1$ . We observe that with an increase in the density ratio, the mean relative phase between the top and bottom branches of the flame shows a monotonic decrease after a small initial increase in the plot. This indicates that the increase in preheating temperature of the reactant mixture changes the relative shedding frequency of the vortex from the top and bottom edges of the bluff-body. This change follows the transition of vortex shedding pattern from predominantly sinuous (phase difference  $> 90$  degrees) to predominantly varicose (phase difference  $< 90$  degrees) mode (Emerson and Lieuwen, 2015).

Furthermore, we compare the influence of external forcing on the phase locking behaviour of the heat release rate signals obtained from both branches of the flame for different locations along the flame length. In order to do this, we quantify the relative phase between these signals acquired at three different locations of the flame such as  $x/D = 3, 5$  and  $7$  for  $\rho_u/\rho_b = 1.9$  (Figs. 6.9a-c) and  $3.2$  (Figs. 6.9d-f). We notice that, in the near field of the bluff body wake, as shown in Figs. 6.9a,d, the relative phase shows fluctuations around a constant phase shift (i.e., a perfect phase-locking condition). Nevertheless, as we move away from near field of the bluff body (shown in Figs. 6.9b,c,e,f), the relative phase shows multiple phase slips depicting the lack of perfect synchronization between these signals. This indicates that the response of the flame dynamics to the external perturbations weakens as we move away from the bluff body location. We notice that the lack of synchrony observed in the flame response is more for the high density ratio case compared to the low density ratio case, as the number of phase slips is more and less for the former and latter cases in the plot of

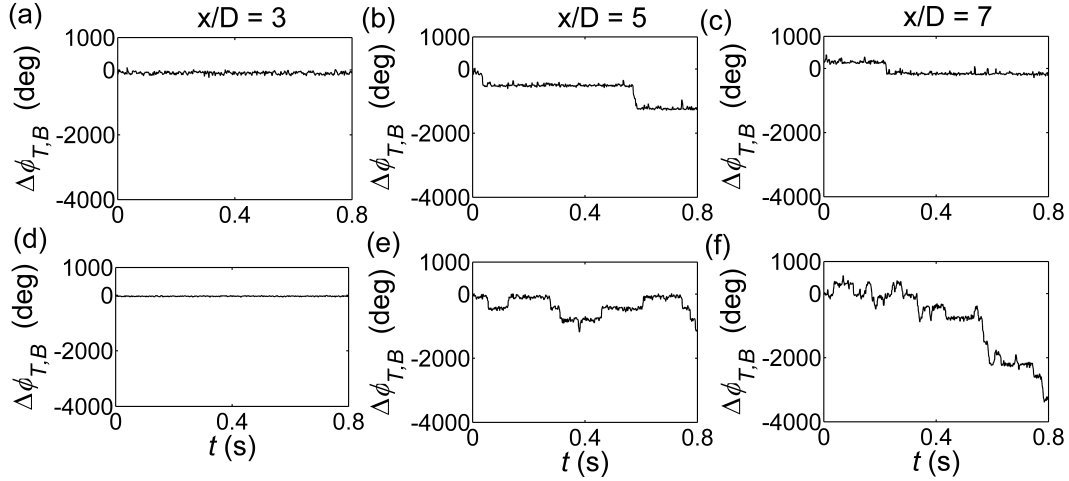


Figure 6.9: The plots of relative phase between the local heat release rate fluctuations obtained from the top and bottom branches of the flame at three different locations along the flame length as  $x/D = 3, 5,$  and  $7$ , for two different values of the density ratios (a)-(c)  $\rho_u/\rho_b = 1.9$  and (d)-(f)  $\rho_u/\rho_b = 3.2$ . The parameters that are fixed  $U_{lip} = 41$  m/s,  $f_n/f_f \approx 1$  and  $A_f = 0.02$ .

relative phase. Thus, it is to be noted that the detection of phase locking between the signals obtained from the top and bottom branches of the flame is highly dependent on the choice of the flame location.

Lastly, we examine the variation of recurrence properties such  $\%RR$  and  $\%DET$  of the local heat release rate fluctuations obtained from the top and the bottom branches of the flame, at various distances downstream of the bluff body, for different values of the forcing amplitude. In Fig. 6.10, we plot the variation of these recurrence measures for the top (Figs. 6.10a,b) and the bottom (Figs. 6.10c,d) sides of the flame separately, when  $\rho_u/\rho_b = 2$ . We notice the variation in the values of these measures for both sides of the flame with an increase in the forcing amplitudes. For the top side of the flame (Fig. 6.10a), the values of  $\%RR$  display an increasing trend for  $x/D = 3, 4, 5,$  and that remains nearly the same for  $x/D = 6, 7,$  with an increase in the forcing amplitude. Whereas, in Fig. 6.10b, we notice a continuous increase in the values of  $\%DET$  with the forcing amplitude for all locations along the flame length. Furthermore, the value of  $\%DET$  is observed to decrease at a particular forcing amplitude with the increase in the distance along the flame length. This reasserts that the response of oscillations in the top side of the flame to the forcing decreases (hence there is a decrease in the periodicity of oscillations) as we move away from the bluff body location. The opposite behaviour is observed in the oscillations of the bottom side of the flame, where we notice a near collapse of all the plots of recurrence measures,  $\%RR$  (Fig. 6.10c)

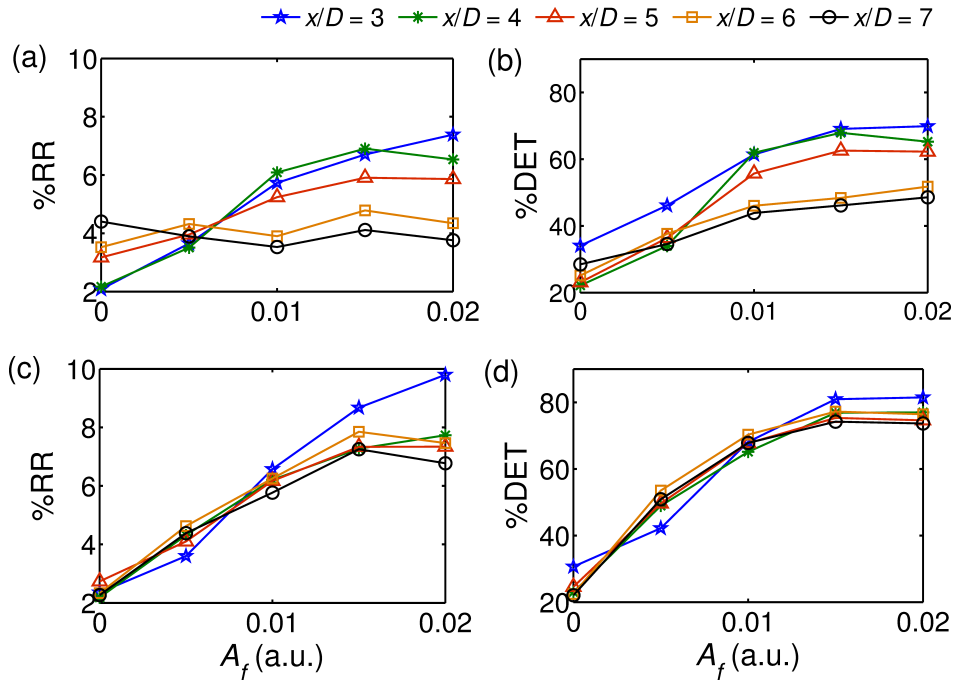


Figure 6.10: The variation of recurrence quantities  $\%RR$  and  $\%DET$  for (a), (b) top and (c), (d) bottom sides of the flame with different values of forcing amplitudes obtained at various locations along the flame length. The flame distances are  $x/D = 3, 4, 5, 6$  and  $7$ , and the forcing amplitude values are  $A_f = 0, 0.005, 0.01, 0.015$ , and  $0.02$ . The conditions that are fixed  $\rho_u/\rho_b = 2$ ,  $U_{tip} = 40$  m/s, and  $f_n/f_f \approx 1$ .

and  $\%DET$  (Fig. 6.10d), obtained for different locations along the flame length with increase in the forcing amplitude. This suggests that the response of forcing is nearly same along the length of the bottom side of the flame. The application of forcing periodically sheds vortices from the bluff body, however, the persistence of these vortices along the flame length is asymmetric for both sides of the bluff body. In particular, at the density ratio of 2 and when the frequency ratio is such that  $f_n/f_f \approx 1$ , we observe that the structures shed from the top side of the bluff body lose coherence faster than those shed from the bottom side. Thus, even though the application of external forcing is symmetric in the system, the response of the system dynamics to the forcing may not be always symmetric and is highly dependent on the various factors such as the geometry of the system, conditions of the underlying hydrodynamic field and that of the external forcing.

## 6.4 Conclusions

This chapter describes a study of the forced response of longitudinally excited, reacting wake for different density and excitation frequency ratios. By using tools from nonlinear dynamics, we showed that the dynamics of the local heat release rate fluctuations during the unforced state have low determinism, and the value of this determinism gradually increases with an increase in the forcing amplitude. We further characterized the symmetry of forced flame response by computing the instantaneous relative phases of the local heat release rate fluctuations obtained from the top and the bottom branches of the flame with the forcing signal. We observed that, for the low density ratio case, when  $f_n < f_f$ , the bottom branch of the flame exhibits more receptivity to forcing and get easily phase-locked. In contrast, the top branch of the flame oscillations displays a weak response to forcing and does not get phase-locked with the forcing signal. The reverse happens when  $f_n > f_f$ , i.e., the top branch of the flame oscillations shows a perfect phase-locking with forcing and not the bottom branch of the flame oscillations. In the case of high density ratio, the effect of forcing is nearly the same for all conditions of forcing ( $f_f < f_n$  or  $f_f > f_n$ ), where both (top and bottom) branches of the flame show perfect phase-locking with the forcing signal.

By comparing the instantaneous phase difference between the top and bottom branches of the flame, when  $f_f \approx f_n$ , we noticed that the mean phase difference between the top and bottom branches of the flame decreases from a high value close to 130 degrees to a low value close to 35 degrees with an increase in the density ratio. This results in the transition of the vortex shedding pattern from a sinuous (predominantly asymmetric) to a varicose (predominantly symmetric) mode. The distribution of the relative phase between the top and bottom branches of the flame is narrower for the high density ratio case, as compared to, the broader distribution observed for the low density ratio case. This suggests that the globally unstable low density ratio reacting wakes are more resistant to harmonic forcing than the high density ratio convectively unstable reacting wakes, as the correlation in phases between the signals is weaker for the former and stronger for the latter.

# CHAPTER 7

## OPEN-LOOP CONTROL OF THERMOACOUSTIC INSTABILITIES USING SYNCHRONIZATION APPROACH

From the investigation of the coupled interaction between the acoustic field of the combustor and the heat release rate fluctuations from the flame in the previous chapters, it is evident that the coupling between these processes plays a vital role in the occurrence as well as the sustenance of thermoacoustic instabilities in combustors. Various strategies have been devised over the years of research to control or to avoid the occurrence of such detrimental instabilities (Poinsot *et al.*, 1989; McManus *et al.*, 1993; Paschereit *et al.*, 1998). Most of these control strategies are based on breaking the coupling between the acoustic pressure and the heat release rate fluctuations or shifting the natural frequency of the acoustic field to a non-resonant mode of the combustor. In this chapter, we propose an approach based on synchronization theory to control the properties such as phase, frequency, and amplitude of thermoacoustic instabilities, which in turn, help in reducing the amplitude of such instabilities to a very low value.

Towards this purpose, we conduct experiments in a prototypical thermoacoustic system, a horizontal Rijke tube (see Fig. 3.4 in Chapter 3). This simple thermoacoustic system has been observed to mimic many of the dynamical features of practical thermoacoustic systems (Matveev and Culick, 2003; Subramanian *et al.*, 2010; Gopalakrishnan and Sujith, 2014). The observation of clean, noise-free limit cycle oscillations can further aid in identifying different states of synchronization observed prior to the phase-locking in a clear manner. The system primarily consists of a horizontal duct with a concentrated heat source, an electrically heated wire mesh. By changing any of the control parameters (heater power, heater location or mass flow rate of the air), the system behaviour can transition from a steady state to limit cycle oscillations (LCO) through a Hopf bifurcation (Etikyala and Sujith, 2017). Here, we employ external forcing through acoustic drivers when the system is in a state of LCO. During experiments,

we set the heater location (27 cm from the inlet), heater power (1.244 kW) and the air flow rate (100 slpm) in such a way that the Rijke tube exhibits self-sustained, large amplitude periodic (limit cycle) oscillations in acoustic pressure with a natural frequency ( $f_{n0}$ ) of 168.8 Hz. The dynamics of such a system with the variation of the parameters mentioned above have been well-studied (Mariappan and Sujith, 2011; Gopalakrishnan and Sujith, 2014; Etikyala and Sujith, 2017). By varying the forcing parameters such as the forcing amplitude and the forcing frequency (on both sides of the natural frequency of the oscillations), we analyze the response dynamics of the acoustic pressure signal captured from the system and also examine the synchronization behavior between the response and the forcing signals.

## 7.1 Synchronization Map

In a particular experiment, we fix the value of one forcing parameter (for instance, forcing amplitude) at a time and vary another parameter (for instance, forcing frequency). In the first experiment, the forcing amplitude ( $A_f$ ) is varied from zero to a value which includes the state of phase locking, while the forcing frequency ( $f_f$ ) is kept constant at different values. In another experiment, the forcing frequency ( $f_f$ ) is varied across the natural oscillation frequency  $f_n$  of the forced system, for the fixed values of  $A_f$ . The response dynamics of acoustic pressure is then plotted in a plane of forcing amplitude against the forcing frequency, also known as the *Arnold tongue* (Fig. 7.1). The different regimes of forced synchronization such as phase locking, phase trapping, and phase drifting are classified and illustrated in Fig. 7.1. The characterization of states of synchronization is based on the features of the plot of the instantaneous phase difference ( $\Delta\phi$ ) between the forcing signal ( $\phi_F$ ) with that of the forced system ( $\phi_{p'}$ ), i.e.,  $\Delta\phi = |\phi_F - \phi_{p'}|$ . During the *phase locking* state, the instantaneous phases as well as the frequencies of the forcing and the response signals show a perfect locking ( $|\Delta\phi| = \text{constant}$ ) (Pikovsky *et al.*, 2003). On the other hand, in the *phase trapping* state, the relative phase ( $\Delta\phi$ ) between these signals show an oscillatory behaviour; however, these oscillations are bounded resulting in the condition of mean frequency locking without exhibiting the perfect phase locking (Thévenin *et al.*, 2011; Li and Juniper, 2013d). *Phase drifting* corresponds to the unbounded variation in the unwrapped relative phases of the signals. The synchronization region indicated by phase locking (I), is observed

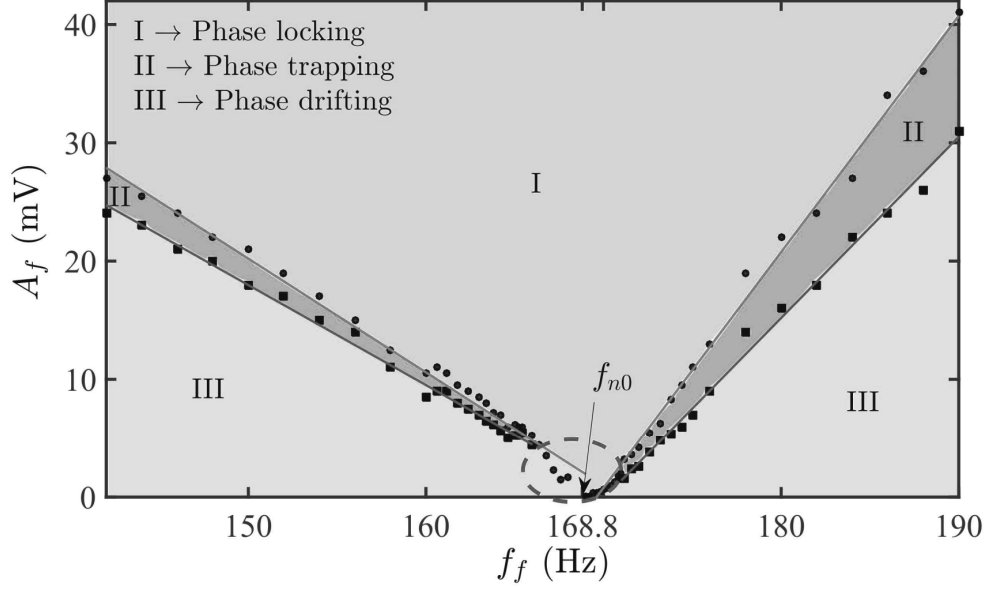


Figure 7.1: A map of 1:1 forced synchronization of the periodically forced limit cycle oscillations in a horizontal Rijke tube, where the forcing amplitude ( $A_f$ ) is plotted against the forcing frequency ( $f_f$ ). Regions of phase locking, phase trapping and phase drifting are indicated as I, II and III, respectively. The synchronization region indicated by phase locking forms the Arnold tongue. The linear fit is applied to the experimental data points shown at the boundaries between regions I and II (●) and between regions II and III (■). The regime where phase trapping is not observed is indicated with a dashed circle near  $f_n$ .

to form the Arnold tongue (Balanov *et al.*, 2009; Pikovsky *et al.*, 2003).

We notice a region of phase trapping (region II, Fig. 7.1) between the regions of phase drifting (region III, Fig. 7.1) and phase locking (region I, Fig. 7.1) on both side of the natural frequency ( $f_n$ ), when detuning is sufficiently high. This route to synchronization is also referred to as *suppression* route of the Arnold tongue (Balanov *et al.*, 2009). We further observe a small region in the parameter space where phase drifting directly transitions to phase locking behaviour without exhibiting the intermediate phase trapping state when the forcing frequency is very close to the  $f_n$  (shown as a dashed circle in Fig. 7.1). This route to synchronization is also referred to as *locking* route of the Arnold tongue (Balanov *et al.*, 2009).

Further, we notice the asymmetries about the  $f_n$  in the Arnold tongue plot. The curves are less steep for  $f_f < f_n$  as compared to that observed for  $f_f > f_n$ . This indicates that, for  $f_f < f_n$ , lower  $A_f$  is required to achieve phase locking for the same value of detuning. A similar asymmetry in the Arnold tongue has been observed in forced low density jets (Hallberg and Strykowski, 2008) and hydrodynamically self-excited jets (Li

and Juniper, 2013a,d). However, in another study with a jet diffusion flame, the asymmetry showed the opposite trend having steeper curves for  $f_f < f_n$  (Li and Juniper, 2013c). Further, we observe a narrower region of phase trapping for  $f_f < f_n$ . Such asymmetries in the Arnold tongue could be the result of stronger nonlinearities existing in the systems dynamics (Balanov *et al.*, 2009). Having described the overall synchronization map of the forced limit cycle oscillations, we now proceed to investigate the response of the system for the individual variation of the forcing parameters.

## 7.2 Effect of Change in Forcing Frequency at Constant Forcing Amplitude

Figure 7.2 shows the variation in different properties of the forced response of the system while the forcing frequency is swept across the natural frequency of the oscillations for a fixed value of the forcing amplitude ( $A_f = 5$  mV). In Fig. 7.2, we show the variation of  $f_f$  around  $f_n (= 168.8$  Hz) in the range of 90 Hz to 220 Hz. The natural frequency of the limit cycle oscillations, in the presence of forcing, is denoted as  $f_n$  and, in the unforced condition, it is denoted by  $f_{n0}$ . In Fig. 7.2a, the variation in the normalized magnitudes of the frequencies corresponding to natural oscillations ( $A_n$ ) and that corresponding to the forcing signal ( $A_f$ ), observed in the amplitude spectrum of the acoustic pressure signal, are plotted against the variation in normalized forcing frequency ( $f_f$ ). The normalization of amplitude and frequency is performed by the respective quantities observed in the amplitude spectra of the unforced signal, i.e.,  $A_0$  and  $f_{n0}$ .

We observed that when the forcing frequency is far away from the frequency of natural oscillations, the presence of forcing does not affect the natural oscillations. This effect can be seen from the variation of  $A_n/A_0$  around one, when  $f_f$  is far away from  $f_n$ . As the forcing amplitude approaches the natural frequency (from the left-hand side), near the boundary of frequency locking region (highlighted in Fig. 7.2a), the magnitude of the natural oscillations exhibits a gradual decrease and becomes zero at the onset of frequency locking in the system dynamics. At the same time, the magnitude of the forcing frequency shows a gradual amplification and a sudden jump to a high value at the onset of frequency locking in the system dynamics. During the state of frequency locking, the frequency of the natural oscillations shifts to the frequency of the external

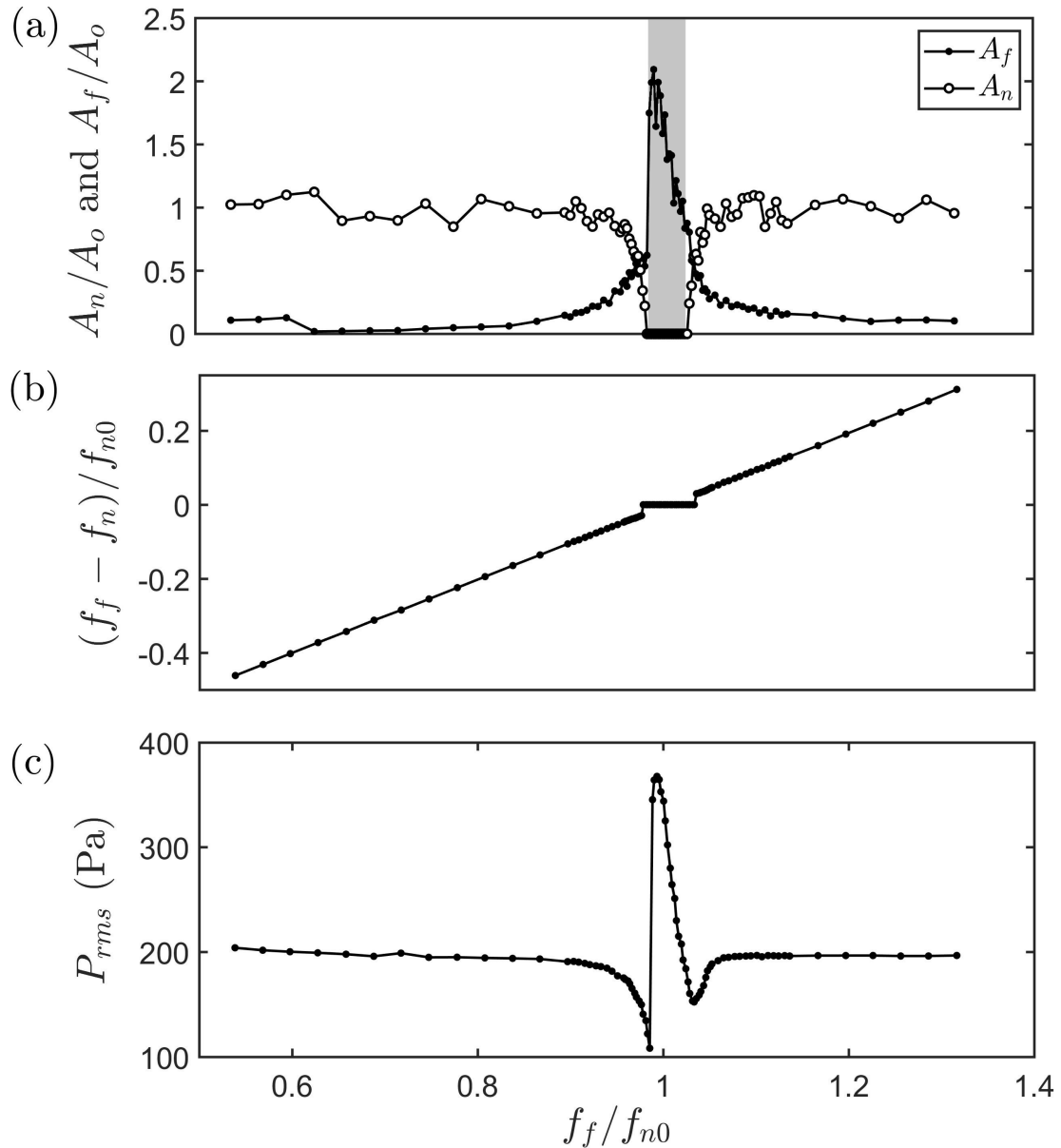


Figure 7.2: (a) Variation of the spectral amplitudes of the self-excited mode or natural oscillations ( $A_n/A_0$ , in open circles) and that of the forcing mode ( $A_f/A_0$ , in filled circles) when the forcing frequency is varied across the natural frequency ( $f_n$ ) of the system at a constant value of the forcing amplitude ( $A_f = 5$  mV). A region of frequency locking is highlighted. (b) A frequency response plot shows the variation of normalized frequency difference  $((f_f - f_n)/f_{n0})$  with the normalized forcing frequency ( $f_f/f_{n0}$ ), where  $f_n$  is the frequency corresponding to the natural oscillations in the presence of forcing. (c) Response characteristics of the acoustic pressure signal shown in terms of the variation of root mean square amplitude  $P_{rms}$  with the normalized forcing frequency ( $f_f$ ).

forcing and stays locked for a finite range of the frequency detuning around the natural frequency. In the frequency locking region, with further increase in the forcing frequency, the magnitude of the forcing frequency shows a gradual decrease while that of the natural frequency stays at zero value. After the crossing of the frequency locking

region, natural frequency regains its amplitude, and thus, two independent frequencies corresponding to the forcing and the natural oscillations are observed in the amplitude spectra of the response acoustic pressure signal. Therefore, the variation of the normalized frequency difference  $[(f_f - f_n)/f_{n0}]$  display a linear variation with an increase in the forcing frequency ( $f_f/f_{n0}$ ) outside the frequency locking region and shows a plateau in the frequency locking region (see Fig. 7.2b). The variation in the magnitude of the natural frequency is apparently symmetric around 1; however, that of the forcing frequency is asymmetric around 1. Such asymmetry in the response of the forcing signal could arise due to the phenomenon of nonlinear resonance of the system (Rajasekar and Sanjuan, 2016). We notice that, in the frequency locking region, both the phenomena of forced synchronization and resonance (amplification the response signal) happen simultaneously. We refer to this behaviour of the system as synchronance amplification (synchronization-resonance). Further, we note that the region of synchronance amplification also corresponds to the phase locking region shown in the Arnold tongue (refer Fig. 7.1).

Figure 7.2c displays the variation of the response amplitude of the acoustic pressure, measured in terms of root mean square value ( $P_{rms}$ ), with different values of the forcing frequency. The response amplitude ( $P_{rms}$ ) shows significant variations near and inside the frequency locking region, as we sweep the forcing frequency ( $f_f$ ) around the natural frequency ( $f_n$ ). When  $f_f$  is far from  $f_n$  (e.g.,  $f_f = 90$  Hz or  $220$  Hz), the effect of the external forcing on the response amplitude of the signal is not discernible, because  $P_{rms}$  remains nearly the same as that of the unforced signal. On the other hand, when  $f_f$  is very close to  $f_n$  (both sides of  $f_n$ ), the effect of forcing on  $P_{rms}$  is more pronounced (Fig. 7.2c). We observe a drop in the response amplitude, as the forcing frequency approaches the natural frequency from both sides of the frequency locking region. Such decrease in the response amplitude of the signal from its unforced amplitude value, due to the forcing, is referred to as suppression of the natural oscillations. Further, we notice that this relative decrease of  $P_{rms}$  with respect to the unforced amplitude is higher for  $f_f < f_n$  than for  $f_f > f_n$ . Inside the frequency locking region, the response amplitude shoots up to a very high value (almost double the amplitude of unforced signal) and, as  $f_f$  is varied across  $f_n$  from left to right,  $P_{rms}$  exhibit a gradual decrease. This behaviour of the response amplitude of the acoustic pressure signal is very much similar to that is seen for the magnitude of the forcing frequency in the frequency locking region in

Fig. 7.2a. Thus, in the frequency locking region, the forced response of the system is dominated by the effect of external forcing, while, in the region outside the frequency locking, the forced response of the system is dominated by the effect of natural oscillations in the system. At the boundaries of the frequency locking region, a combined effect of the nonlinear interaction of both (forcing and natural) the frequencies on the response amplitude of the acoustic pressure signal is observed.

Further, we study the effect of periodic forcing on the phase dynamics of the response signal due to the variation of the forcing frequency across natural frequency at a constant value of the forcing amplitude. To that end, we choose four values of forcing frequencies ( $f_f$ ) corresponding to  $f_f < f_n$  and show different states of forced synchronization observed during the onset of phase locking in the system dynamics. The response dynamics of the acoustic pressure signals, due to the periodic forcing, can be inferred from the first return map and the time series (inset) plots shown in Fig. 7.3-I. The spectral properties, such as frequency and instantaneous phase difference (calculated through Hilbert transform) of the response signals, are shown in Fig. 7.3-II. The forcing frequencies are indicated by dots in the amplitude spectra (Fig. 7.3-II).

When  $f_f$  (= 90 Hz) is far from  $f_n$  (Fig. 7.3a-II), the forcing hardly affects the response signal (inset of Fig. 7.3-I). This is evident from the observation that the amplitude of the response signal does not change due to forcing and the presence of a cluster of points on the diagonal line in the first return map. The relative phase shows a continuous drift with time (inset of Fig. 7.3a-II), indicating desynchronization behaviour of the forcing and the natural oscillations. With a value of  $f_f$  (= 161.5 Hz) close to  $f_n$  (Fig. 7.3b-II), the amplitude of the response signal shows a *beating* behaviour (inset of Fig. 7.3b-I) with a beating frequency,  $|f_n - f_f|$ , where  $f_n$  is the frequency corresponding to the natural oscillations in the presence of forcing. The first return map of such modulated oscillations shows an oval structure around the diagonal line, indicating the existence of *quasiperiodic* oscillations during this state of the forcing. Furthermore, a staircase like structure in the dynamics of the relative phase (inset of Fig. 7.3b-II) indicates the presence of intermittent phase locking between the signals, where the regions of phase locked (plateau region) are separated by jumps (also referred to as *phase slips*) of integer multiples of  $2\pi$  radians.

When  $f_f$  (= 164.3 Hz) is very near to  $f_n$ , however, outside the synchronization

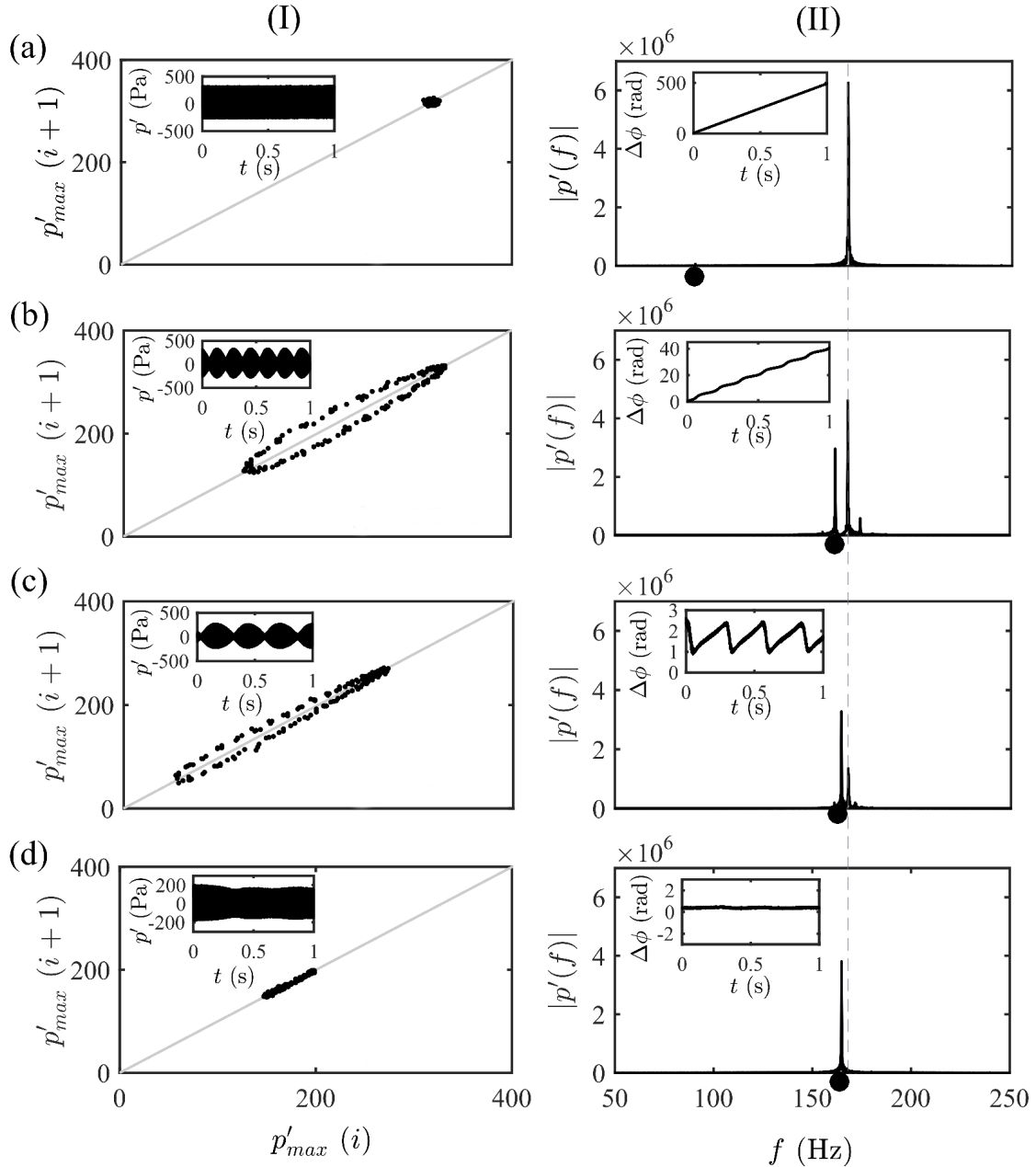


Figure 7.3: The effect of change in the forcing frequency ( $f_f$ ) on the response dynamics of the acoustic pressure signal when  $f_f < f_n$  and the forcing amplitude ( $A_f$ ) is constant. The forced response of the system dynamics is characterized in terms of first return map (I), time series (inset of I), amplitude spectrum (II), and instantaneous phase difference (inset of II). The forcing frequencies ( $f_f$ ) corresponding to (a)-(d) are 90 Hz (phase drifting), 161.1 Hz (intermittent phase locking), 164.3 Hz (phase trapping), and 164.7 Hz (phase locking), respectively. The frequency corresponding to natural oscillations is indicated by a dotted line in II. The frequency corresponding to external forcing is marked by a dot in I.

boundary (Fig. 7.3c-II), the relative phase indicates the presence of a phase trapping state, as inferred from bounded but periodically oscillating behavior of the relative phase with a frequency equal to the beating frequency of the signals (inset of Fig. 7.3c-II).

Although the mean frequencies ( $\omega = \langle \frac{d\phi}{dt} \rangle$ ) of these signals are perfectly locked, the frequency spectrum still shows two distinct frequency peaks corresponding to  $f_f$  and  $f_n$ . This is further reflected in the beating structure observed in the response signal (inset of Fig. 7.3c-I), and a closed loop structure along the diagonal line in the first return map (Fig. 7.3c-I). During the onset of phase locking (Fig. 7.3d), the frequency peak corresponding to  $f_n$  gets completely suppressed and the system dynamics exhibit a single peak at the forcing frequency ( $f_f = 164.7$  Hz). During this state, the relative phase between the response signal and the forcing signal becomes constant with time (inset of Fig. 7.3d-II). The small fluctuations about the mean phase difference observed in the relative phase plot indicate the possibility of inherent noise in the response signal of the system. The first return map corresponding to this state hence shows a cluster of points congregated along the diagonal line (Fig. 7.3d-I). When  $f_f$  is varied beyond  $f_n$  in such a way that it crosses the boundary towards right side of the synchronization region (see Arnold tongue in Fig. 7.1), the observations of forced synchronization states such as phase trapping, intermittent phase locking and phase drifting are repeated in the response dynamics (not shown).

### 7.3 Effect of Change in Forcing Amplitude at Constant Forcing Frequency

Now, we investigate the effect of variation in the forcing amplitude on the response dynamics Rijke tube. For that purpose, we vary the forcing amplitude maintaining the forcing frequency constant (here,  $f_f = 155$  Hz, shown by dots in Fig. 7.4). When the amplitude of forcing is very small ( $A_f = 3$  mV), the external forcing does not show any effect of the natural oscillations, resulting in phase drifting between the forcing and the response signals (inset of Fig. 7.4a). With the increase of forcing amplitude to 12 mV, we observe a beating structure in the amplitude of the response signal. This corresponds to a state of intermittent phase locking, confirmed from the observation of a wavy staircase-like structure in the time series of the relative phase (inset of Fig. 7.4b). As we increase  $A_f$  further ( $A_f = 18$  mV), we notice a shift in dominance of the peak frequencies from  $f_n$  to  $f_f$  in the frequency spectra (see Fig. 7.4c). This results in the bounded nature of the relative phase, where the phase difference between two signals is

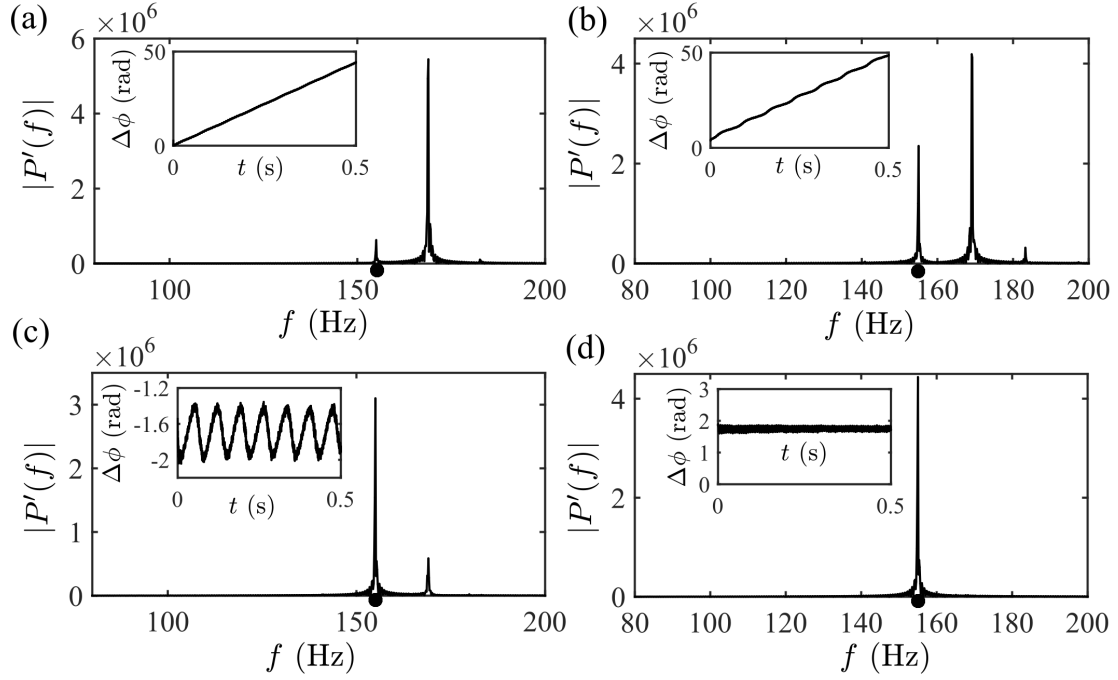


Figure 7.4: The plots showing frequency spectra of the response signal, and temporal variation of the relative phase between the response dynamics and the forcing signal (insets) at different values of  $A_f = 3$  mV (a), 12 mV (b), 18 mV (c), and 24 mV (d), when  $f_f$  is maintained constant at 155 Hz which is sufficiently away from  $f_n$  (168.8 Hz). The dots in the frequency spectra correspond to the location of forcing frequencies ( $f_f$ ).

trapped between finite values (less than  $2\pi$ ) and oscillates in a periodic manner (inset of Fig. 7.4c). This state is referred to as the phase trapping. When the forcing amplitude is sufficiently high ( $A_f = 24$  mV), we observe a perfect locking of phases of two signals (inset of Fig. 7.4d), wherein the natural oscillations get completely suppressed and the system oscillates with the forcing frequency (Fig. 7.4d). We note that these observations are very much similar to the dynamical transitions that we observed when the forcing frequency is varied at a constant value of the forcing amplitude (as shown in Fig. 7.3).

Contrary to this, when  $f_f$  is very close to the natural frequency (shown by a dotted circle in Fig. 7.1), we do not observe the state of phase drifting (see Fig. 7.5). According to Balanov *et al.* (2009), the region of the Arnold tongue wherein the state of phase trapping is absent is referred to as the locking region. And, the region where all the states of forced synchronization such as phase drifting, phase trapping and phase locking present is referred as suppression region. Phase locking and suppression regions are approached through saddle-node and torus-birth bifurcation respectively (Balanov *et al.*, 2009). We observe the existence of locking region when  $f_f$  is fixed at 168 Hz (where  $f_n = 168.8$  Hz) and  $A_f$  is varied from a low to a high value. When  $A_f$  is very

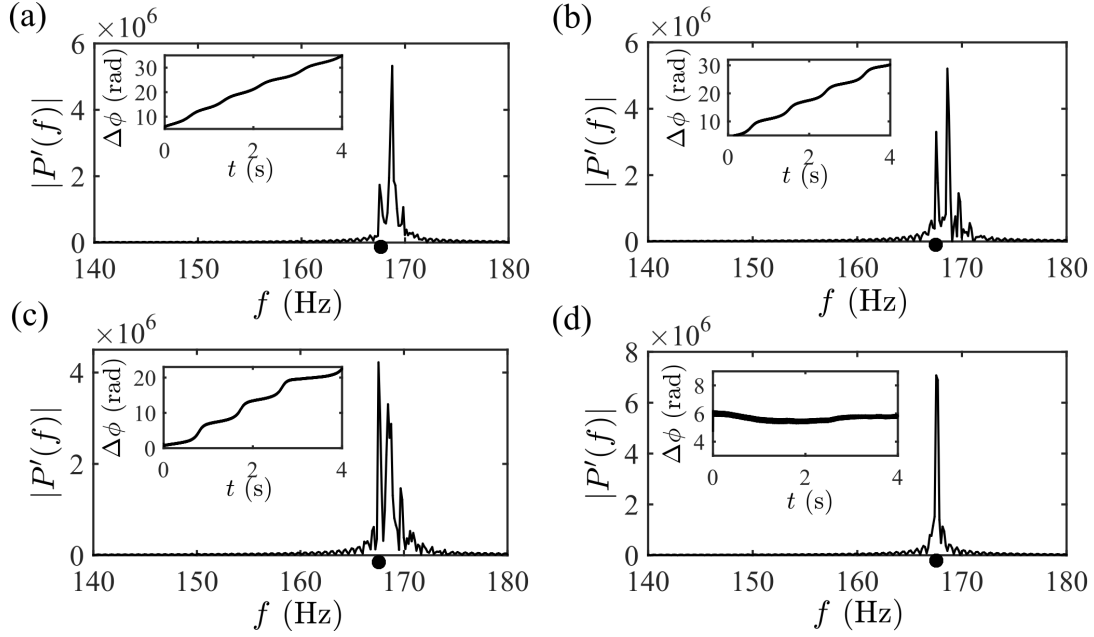


Figure 7.5: The plots showing frequency spectra of the response signal, and instantaneous relative phase variation between the response and the forcing signal (insets), obtained for different values of  $A_f$  as (a) 0.4 mV, (b) 0.8 mV, (c) 1.2 mV, and (d) 1.7 mV, when  $f_f$  (168 Hz) is very close to  $f_n$  (168.8 Hz).

small (0.4 mV, see Fig. 7.5a), the plot of relative phase shows a phase drifting behavior, which subsequently transitions to a staircase like structure at a higher value of the forcing amplitude ( $A_f = 0.8$  mV, see Fig. 7.5b). When  $A_f = 1.2$  mV, we notice a shift in the dominance of the frequencies from  $f_r$  to  $f_f$  (as shown in Fig. 7.5c). We, however, observe that the relative phase between the signals still shows an intermittent phase locking behavior (inset of Fig. 7.5c), unlike that observed when the forcing frequency is sufficiently far from the natural frequency of the oscillations (see inset of Fig. 7.4c). When the amplitude of forcing is high ( $A_f = 1.7$  mV), the relative phases of the signals show a direct transition to the phase locking state (inset of Fig. 7.5d) without showing the presence of phase trapping.

Now, we examine the effect of periodic forcing on the response amplitude (measured in terms of root mean square value,  $P_{rms}$ ) of the acoustic pressure signal, by varying  $A_f$  for fixed values of  $f_f$  (Fig. 7.6). Four values of  $f_f$  are chosen in such a manner that two of them are close to  $f_n$  and other two are far away from  $f_n$ . We observe that the response amplitude of the acoustic pressure signal first decreases to a minimum value and then exhibits a linear increase with further increase in the forcing amplitude. This behavior of the response signal is observed for  $f_f < f_n$  (Fig. 7.6a,b) and also for  $f_f > f_n$  only when the detuning is small (Fig. 7.6c). The suppression in the

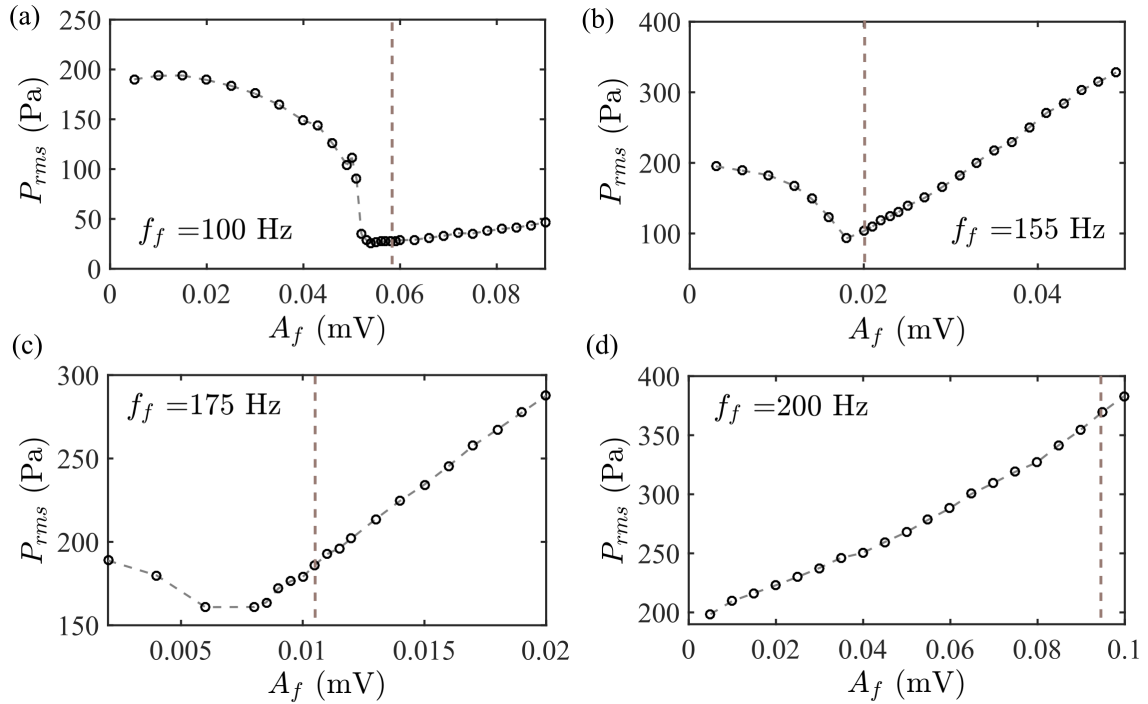


Figure 7.6: The variation of response amplitude ( $P_{rms}$ ) of the acoustic pressure signals with the variation of  $A_f$  for different  $f_f$  as (a) 100 Hz, (b) 155 Hz, (c) 175 Hz, and (d) 200 Hz. Suppression of response amplitude is observed for all forcing frequency except when  $f_f$  is sufficiently higher than  $f_n$  (d). On the right hand side of the vertical dashed line shown in (a)-(d), the instantaneous phases of the response signal are perfectly locked with the forcing signal; thus, it indicate the phase locking region.

amplitude of the acoustic pressure signal is not observed when  $f_f$  is much higher than  $f_n$  (Fig. 7.6d), wherein the response amplitude shows a continuous increase without showing any distinct minima in the plot. From the analysis of relative phase between the response signal and the forcing signal, as shown in Figs. 7.4 and 7.5, we notice that the minimum point in the plot of response amplitude (see Fig. 7.6) is close to the boundary of phase locking regime (shown as the vertical dashed line in Fig. 7.6a-c). In the region of perfect phase locking, the response amplitude of the pressure oscillations demonstrates almost a linear growth with an increase of  $A_f$ . This behaviour of increase in the amplitude response signal is due to the effect of *synchronance* amplification, as explained in the previous Section 7.2. Such a growth in the response amplitude of acoustic pressure signal in the locking region is significantly steep when  $f_f$  is close to  $f_n$  (Figs. 7.6b,c) and is moderate when  $f_f$  is much lower than  $f_n$  (Fig. 7.6a). We further notice that the minimum value of the response amplitude obtained due to the forcing, observed prior to the onset of perfect phase locking state, increases as  $f_f$  is increased from the condition of  $f_f \ll f_n$  to  $f_f > f_n$ .

## 7.4 Asynchronous Quenching of Response Amplitude

The results shown in Figs. 7.2c and 7.6a-c demonstrate the possibility of a reduction in the amplitude of the unforced limit cycle oscillations observed in a thermoacoustic system due to forcing. The occurrence of large amplitude pressure oscillations as a consequence of thermoacoustic instability, are undesirable (Culick and Kuentzmann, 2006) in practical combustors. For such systems, the suppression of amplitude of thermoacoustic instability is, in principle, possible through the application of external acoustic forcing. We notice that the amount of amplitude suppression achieved by forcing depends on the frequency difference between the forcing and the natural oscillations and also depends on the amplitude of the applied forcing signal. Therefore, in order to characterize the amplitude suppression of the response signal due to forcing, we evaluate the *rms* value ( $P_{rms}$ ) of the acoustic pressure signal for different values of  $A_f$  at a particular value of forcing frequency (similar to that is shown in Fig. 7.6). For each  $f_f$ , the maximum suppression in the amplitude of the response signal ( $P_0 - P_{min}$ ) for a range of  $A_f$  is calculated, where  $P_{min} = \min\{P_{rms}(A_f)\}$ , and  $P_0$  is the  $P_{rms}$  when the system is unforced.

We, therefore, analyze the variation of amplitude suppression of the response signal achieved for different values of  $f_f$  in the region where  $f_f < f_n$  (see Fig. 7.7). Suppression in amplitude ( $P_0 - P_{min}$ ) is normalized with *rms* value of the unforced signal ( $P_0$ ).

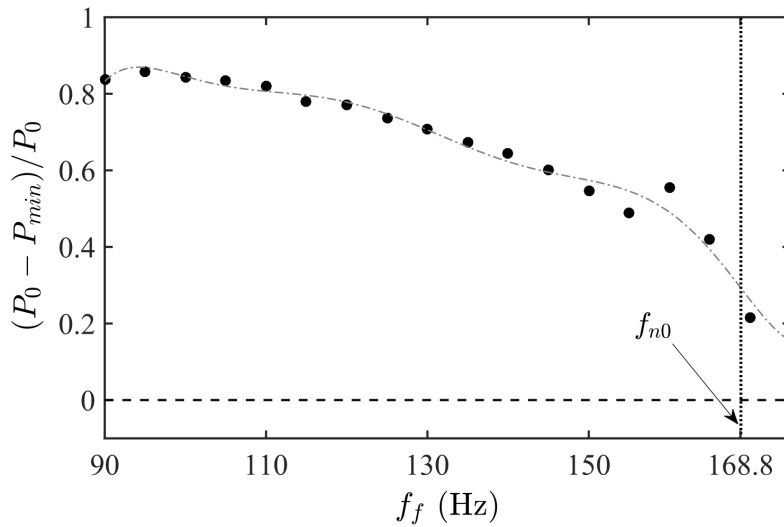


Figure 7.7: Suppression in response amplitude for different forcing frequency. Suppression is normalized with *rms* value of the unforced amplitude ( $P_0$ ) and  $P_{min}$  represents the minimum amplitude ( $P_{max}$ ) obtained forcing the signal with different forcing amplitude and keeping  $f_f$  constant.

We observe the maximum suppression in the amplitude of the response signal when  $f_f$  is far lower than the natural frequency ( $f_n$ ) of the signal. As we approach the natural frequency, the amount of amplitude suppression attained by the forcing reduces. This further indicates that the applied forcing is ineffective in reducing the amplitude of the unforced oscillations for  $f_f$  close to  $f_n$  and  $f_f > f_n$ . When  $f_f$  is near 90 Hz, the response amplitude of limit cycle oscillations is observed to reduce to a minimum value, almost equal to the amplitude of the external forcing. Such reduction in the amplitude of the response signal to a value close to the amplitude of forcing signal is generally referred to as asynchronous quenching (Minorsky, 1967; Staubli, 1987). We notice that forcing the system with a frequency higher than  $f_n$  does not result in the reduction in amplitude of the self-sustained oscillations (Fig. 7.7). The identification of the physical reason behind such a behaviour of the forced system needs further investigation. We observe that this reduction in the amplitude of natural oscillations is approximately 80% when the forcing frequency is close to the subharmonic frequency of the natural oscillations. Therefore, by appropriately choosing the forcing frequency and the forcing amplitude, thermoacoustic instabilities can be suppressed to a great extent through the phenomenon of asynchronous quenching.

## 7.5 Conclusions

A systematic experimental investigation of forced synchronization of limit cycle oscillations in a prototypical thermoacoustic system, the horizontal Rijke tube, is performed. The forced response of the system is captured in terms of acoustic pressure fluctuations. By varying the forcing parameters such as forcing frequency and forcing amplitude, we established a 1:1 synchronization map (or Arnold tongue) of forced response of the system. Further, different routes (such as locking and suppression) to forced synchronization of limit cycle oscillations, and different states (such as phase drifting, phase trapping and phase locking) of couple behaviours of the system response and the forcing signals are identified. When the system is forced with a frequency which is close to the natural frequency, a phenomenon of synchronous amplification (synchronization + resonance) is observed in the phase locking region of the Arnold tongue. A maximum suppression in the unforced amplitude (almost 80% of the unforced amplitude) of the acoustic pressure fluctuations is achieved only when the forcing frequency is near the

subharmonic frequency of the natural oscillations. We showed that such reduction in the amplitude of the response signal is possible due to the phenomenon of asynchronous quenching.

# CHAPTER 8

## CONCLUSIONS AND SCOPE FOR FUTURE WORK

The main focus of this thesis is to investigate the coupled interaction between the acoustic field of the confinement and the unsteady dynamics of the flame existing in thermoacoustic systems. Using a framework of synchronization theory, we aimed to characterize the transition of system dynamics from a state of stable operation (or combustion noise: low amplitude aperiodic fluctuations) to a state of unstable operation (or limit cycle oscillations) happening via intermittency. In order to study this interaction, we performed separate experiments on two configurations of thermoacoustic systems; one with gaseous fired turbulent bluff-body-stabilized and swirl-stabilized combustors having backward facing step at the inlet, and another with a liquid-fueled spray combustor.

We showed that thermoacoustic instability in the system involving turbulent flow is associated with a synchronization phenomenon of two mutually coupled non-identical oscillators viz., the acoustic field in the confinement and the turbulent reactive flow present in the system. We observed that a bidirectional coupling exists between these oscillators, which is responsible for their transition from a non-synchronous state of aperiodic oscillations to a perfectly synchronous state of periodic the oscillations with a variation in the mean velocity of flow. Using the theory of synchronization, we provide a new description for the intermittency route to thermoacoustic instability in a turbulent combustion system. We observe that the system dynamics culminate in a state of generalized synchronization (GS), having gone through intermittent phase synchronization (IPS) and phase synchronization (PS). During IPS, the oscillators are periodic in the synchronized phase while harboring aperiodicity in the desynchronized phase. We further characterized the distinguishing features of PS and GS states. We show that these two states correspond to two different types of limit cycle oscillations; one that is weakly correlated, the other being strongly correlated.

Our study, further, provides a description for the onset of vortex-acoustic lock-in by analyzing the system dynamics in the frequency domain. This analysis suggests that during the onset of intermittency, the distinct dominant peaks of the acoustic pressure

and the heat release rate fluctuations, observed during combustion noise, shift their dominant frequencies to a common lock-in mode (referred to as partial lock-in mode). The value of this lock-in mode frequency exhibits a continuous increase in the IPS and PS states, and finally stays nearly constant (referred to as synchronization mode) during the state of GS.

A spatiotemporal analysis of the coupled acoustic pressure oscillations and the local heat release rate oscillations in the flame performed for the swirl-stabilized combustor showed the emergence of order from the underlying disordered turbulence, as the system dynamics transitions to a state of weakly correlated periodicity (PS). However, with very high flow rates where the strongly correlated periodic oscillations (GS) persist, the coherent reaction zone is observed to be contaminated by small regions of disorder, seemingly due to the higher turbulence. Even then, the state of GS exhibits a higher global synchrony than that of IPS and a higher acoustic driving than that of PS.

The dynamics of a laboratory scaled spray combustion system is studied to understand the transition of the system behavior from a stable to an unstable operation. As we varied the location of the flame inside the combustor, we observe the presence of intermittent oscillations prior to the onset of sustained thermoacoustic instability. The analysis based on recurrence plot and recurrence quantification showed the possibility of chaotic oscillations in the dynamics of combustion noise. The characterization of the type of intermittency demonstrates the presence of type-II intermittency in the dynamics of the spray combustion system. The experimental results also highlight that the intermittent states consisting of significantly high-amplitude bursts can be more dangerous than the sustained low-amplitude limit cycle oscillations. By examining the cross wavelet transform of the acoustic pressure and the heat release rate signals in the spray combustor, we showed that these signals are desynchronized during the state of combustion noise, while they are phase synchronized during the onset of thermoacoustic instability. During intermittency, both signals exhibit intermittent synchronization, wherein they are phase synchronized during bursts of periodic oscillations and desynchronized during the epochs of aperiodic oscillations. Further, the study on the coupled interaction of multiple flamelets anchored at the flame holder with the acoustic field of the confinement during different regimes of the combustor dynamics reveals that the emergence of periodicity in the system dynamics is an emergence of collective synchronization between these subsystems of the spray combustor. The investigation on

the effect of a change in the temperature of reactants reveals the importance of hydrodynamic instability of the underlying flow field on the coupled interaction of the unsteady flame dynamics and the acoustic fluctuations present in the combustor. Such interaction is analyzed by studying the forced response of a longitudinally excited, reacting wake for different density and excitation frequency ratios. We observed that, for the low-density ratio case, when the natural frequency of the flame oscillations ( $f_f$ ) is away from the forcing frequency ( $f_n$ ), i.e.,  $f_f \neq f_n$ , the phase locking behaviour of the top and the bottom branches of the flame with the forcing signal is asymmetric. On the contrary, in the case of high-density ratio, the effect of forcing is nearly symmetric for all conditions of forcing ( $f_f < f_n$  or  $f_f > f_n$ ), where both (top and bottom) branches of the flame show perfect phase-locking with the forcing signal. This behaviour further suggests that the globally unstable low-density ratio reacting wakes are more resistive to harmonic forcing than high-density ratio convectively unstable reacting wakes.

Finally, we studied the effect of periodic forcing on controlling the properties (such as phase, frequency, and amplitude) of thermoacoustic instabilities in the context of forced synchronization theory. The systematic experiments showed the existence of two routes (i.e., locking and suppression) for the forced synchronization of limit cycle oscillations in a system of horizontal Rijke tube. When the system is forced with a frequency which is close to natural frequency, a phenomenon of synchronous amplification is observed, wherein the natural oscillations of the system exhibit a phase locking with the forcing signal along with a substantial increase in the amplitude of response oscillations in the system. In contrast, when the forcing frequency is fairly lower (near the subharmonic frequency) than the natural frequency of the system, a substantial amount of amplitude suppression (80% of unforced amplitude) is observed due to the phenomenon of asynchronous quenching. Such suppression in the amplitude of the response signal is not observed when the forcing frequency is greater than the natural frequency of the oscillations.

## Scope for Future Work

Our approach to viewing thermoacoustic instability in combustors with turbulent flow as a synchronization phenomenon of acoustic field and reacting field is a step towards

the understanding of complex nonlinear interactions occurring between the coupled subsystems of such combustors. As the prerequisite for examining the synchronization phenomenon in a system of coupled oscillators is that the oscillators should be distinct and self-sustained, it is not clear at the outset whether such an approach of mutual synchronization could be further extended to thermoacoustic systems involving laminar flows. In the class of systems having turbulent flow, due to the intrinsic hydrodynamic fluctuations, there will always be an oscillatory behavior in the flow. Hence, the framework of synchronization is valid for such systems, as we show in the present study. On the other hand, in the case of laminar systems, such as Rijke tube and ducted laminar premixed flames, we do see synchronous behavior between the acoustic field and the heat release rate oscillations at the onset of thermoacoustic instability. However, in the absence of noise or inherent fluctuations in the flow during a steady state, the acoustic field is silent (hardly any perceptible pressure or velocity fluctuations) and the heat release rate field is not oscillatory (no perceptible oscillations in the flame or in the heat release rate). As a consequence, the use of synchronization theory to describe the route to thermoacoustic instability in laminar combustors may not be fruitful and need further investigation to explore the use of synchronization theory to such systems.

For turbulent combustors, in a similar manner to the acoustic pressure fluctuations, the coupling of the acoustic velocity with heat release rate fluctuations also plays an important role in the onset of thermoacoustic instability. The acoustic velocity has a direct consequence on the fluctuations of heat release rate with a finite value of the time delay (i.e.,  $u' \approx \dot{q}'(t - \tau)$ ). The large fluctuations in the acoustic velocity can affect the inlet bulk flow velocity or the vortex shedding process happening at the dump plane or at the bluff body. The breaking of these hydrodynamic structures after a time delay  $\tau$  results in the intense release of heat in the system. In the absence of combustion with ideal boundary conditions, the phase difference between the acoustic pressure and the acoustic velocity is nearly 90 degrees. However, the presence of combustion can cause this phase relationship between acoustic variables to alter. Therefore, the characterization of synchronization properties of the acoustic velocity and the heat release rate also needs to be investigated further.

We showed that preheating of reactants plays a crucial role in altering the stability of the reacting flow field inside the combustor, and the response of such flows to the acoustic forcing is not the same for the low and the high levels of preheating temper-

atures. Further, we observed that forcing induces different vortex shedding patterns such as symmetric (varicose mode) and asymmetric (sinuous mode) for the high and low-density ratios, respectively, vitiated combustors. Thus, the application of synchronization theory to study the transition of such density stratified reacting wakes to a state of self-sustained thermoacoustic instability could be a promising avenue for future work, as these kinds of studies have more relevance in exploring the complexities of practical combustion systems.

Similar to the phenomenon of thermoacoustic instability, another dynamic phenomenon that is of great concern to practical combustion systems is the flame blowout (Shanbhogue *et al.*, 2009a; Chaudhuri *et al.*, 2010). Recently, Unni and Sujith (2015) showed that, with decrease in equivalence ratio, the state of thermoacoustic instability transitions to stable operation, consisting low amplitude aperiodic oscillations observed just prior to flame blowout, via intermittency. During such a transition, studying the coupled behaviour of the acoustic pressure and the unsteady flame dynamics (especially, in spatial as well as in temporal domain) in the framework of synchronization theory would shed more light in understanding the occurrence of this dynamic event of combustion.

With the help of periodic forcing, we observed almost 80% decrease in the response amplitude of limit cycle oscillations in a Rijke tube system. Such suppression in the amplitude of thermoacoustic instabilities is desirable for practical combustion systems such as gas turbine engines and rocket motors. Therefore, devising different active open-loop control strategies based on the phenomena of asynchronous quenching can be helpful to mitigate thermoacoustic instabilities in such systems. In addition to this, suppressing the oscillations in practical combustors (for instance, can combustors) by using a phenomenon of amplitude death, where two thermoacoustically unstable combustors are coupled through some means which can lead to the annihilation of self-sustained oscillations due to coupling.

Furthermore, the approach of synchronization theory can likely be used in other real fluid mechanical systems involving turbulent flow, in which, the coupled response of two or more interacting subsystems leads to an unstable phenomenon of flow-induced vibrations. In such systems, the quantitative analysis of synchronization phenomena is still an open topic of research.

# APPENDIX A

## SYNCHRONIZATION TRANSITION IN A SWIRL STABILIZED COMBUSTOR

In this chapter, we analyse the various aspects of coupled interactions of the acoustic pressure and the heat release rate fluctuations due to change in the control parameter, the mean velocity of the air flow ( $\bar{u}$ ) in a swirl-stabilized combustor. An increase of  $\bar{u}$  results in a decrease in the equivalence ratio of the combustible mixture from a value near one to a low fuel lean value, as the fuel flow rate is maintained constant. With an increase in  $\bar{u}$ , the system dynamics transition from a state of combustion noise to thermoacoustic instability through the occurrence of intermittency. We first discuss the time and frequency domain analysis of these coupled oscillations. Subsequently, we study the spatiotemporal coupling of the acoustic pressure with the local heat release rate fluctuations present in the flame during the transition to thermoacoustic instability.

### A.1 Temporal Analysis of Acoustic Pressure and Heat Release Rate Signals

#### A.1.1 Coupled Analysis of Acoustic Pressure and Global Heat Release Rate Fluctuations

Figure A.1 shows the overlapped time series of the acoustic pressure ( $p'$ ) and the global heat release rate ( $\dot{q}'$ ) fluctuations corresponding to different dynamical states of the thermoacoustic system. For low values of the mean flow velocity ( $\bar{u} = 7.8$  m/s), we observe the occurrence of a combustion noise state wherein both the signals show low amplitude aperiodic oscillations (Fig. A.1a). With the increase in the mean flow velocity

---

The results presented in this chapter are published in S. A. Pawar, S. Mondal, N. B. George, and R. I. Sujith, Synchronization Behaviour During the Dynamical Transition in Swirl-Stabilized Combustor: Temporal and Spatiotemporal Analysis *AIAA SciTech Forum*, Kissimmee, Florida, USA, January 8 - 12, (2018).

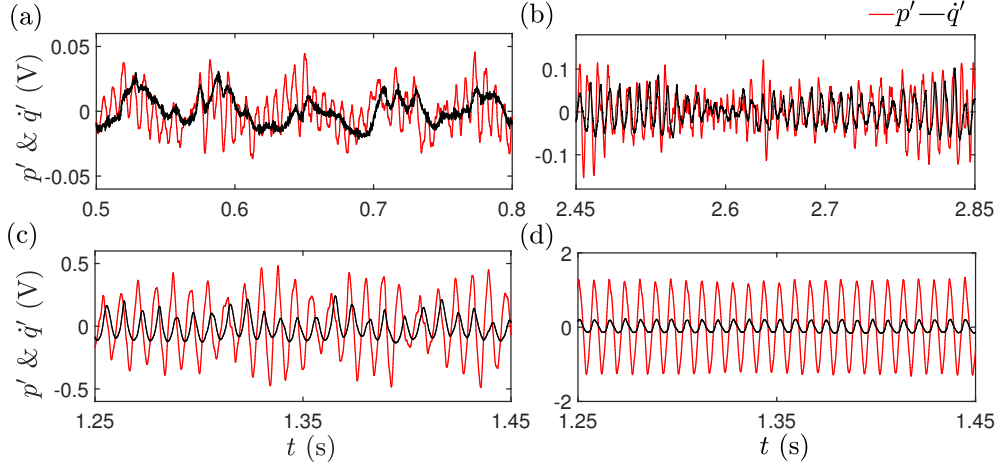


Figure A.1: (a)-(d) The time trace of acoustic pressure ( $p'$ ) and heat release rate ( $q'$ ) fluctuations obtained during the different states of combustion dynamics such as combustion noise ( $\bar{u} = 7.8$  m/s), intermittency ( $\bar{u} = 9.6$  m/s), weakly correlated periodic oscillations ( $\bar{u} = 10.4$  m/s), and strongly correlated periodic oscillations ( $\bar{u} = 11.4$  m/s), respectively.

( $\bar{u} = 9$  m/s), bursts of high amplitude seemingly periodic oscillations begin to appear amongst the regions of relatively low amplitude aperiodic oscillations (Fig. A.1b). We refer to this state as intermittency (Nair *et al.*, 2014; Domen *et al.*, 2015; Ebi *et al.*, 2017). When the value of the mean flow velocity ( $\bar{u} = 10.8$  m/s) is sufficiently high, we notice almost a complete disappearance of the regions of aperiodic oscillations in the system dynamics, resulting in the occurrence of weakly correlated periodic oscillations throughout the signal (Fig. A.1c). For an even higher value of the mean flow velocity ( $\bar{u} = 11$  m/s), the system dynamics transition to a state of thermoacoustic instability, wherein both  $p'$  and  $q'$  signals show a strong correlation in their periodic oscillations (Fig. A.1d). The visual inspection of these signals suggests that the oscillations in both  $p'$  and  $q'$  do not follow each other during the state of combustion noise (Fig. A.1a). On the contrary, the oscillations in these signals are seemingly locked and unlocked at the instances of periodic and aperiodic epochs, respectively, during the occurrence of intermittency (Fig. A.1b). During the weakly correlated periodic and strongly correlated periodic states of the combustion dynamics (Figs. A.1c,d), we observe a wide and relatively small variation in the amplitudes of both  $p'$  and  $q'$  signals, respectively, while their phases appear to be locked in both the cases.

## A.1.2 Frequency Domain Analysis of Acoustic Pressure and Heat Release Rate Signals

The frequency variation of both  $p'$  and  $\dot{q}'$  signals during different dynamical states of the combustor dynamics is shown in Fig. A.2. We also analyse the locking behaviour of the dominant frequencies of these signals during the transition to thermoacoustic instability in Figs. A.3 and A.4. Towards this purpose, we plot both the time-varying frequency (scalogram) utilizing the wavelet transform (Torrence and Compo, 1998) and the amplitude spectra using the fast Fourier transform for both the signals (see Fig. A.2). We notice that during the state of combustion noise (Fig. A.2a),  $p'$  and  $\dot{q}'$  signals possess dominant frequencies at different values. For the heat release rate fluctuations (Fig. A.2a-IV) a sharp frequency peak is observed at  $f_h = 16.3$  Hz (most likely due to unstable hydrodynamic mode in the swirling flow), and for the acoustic pressure fluctuations (Fig. A.2a-II) a broadband frequency peak is observed around  $f_a = 146.3$  Hz (a theoretically predicted fundamental acoustic mode of the combustor). Further, we notice that the spectrum of  $p'$  also contains a peak at a frequency  $f_h$  (possibly due to the presence of the vorticity wave), which eventually vanishes as  $\bar{u}$  is increased. The scalogram of  $p'$  shows an intermittent switching between the modes of  $f_h$  and  $f_a$  throughout the span of the signal (Fig. A.2a-I), whereas the scalogram for  $\dot{q}'$  shows an intermittent occurrence of  $f_h$  alone in the signal (Fig. A.2a-III). When the velocity of the flow is increased beyond a particular value, we notice an emergence of a secondary band of frequencies in between the previously observed frequency bands of  $f_h$  and  $f_a$  (Fig. A.2b). We refer to this band as a partial lock-in mode ( $f_l = 95.7$  Hz), and it is observed during the occurrence of intermittency in the system dynamics. The term partial lock-in signifies the fact that, although both  $p'$  and  $\dot{q}'$  signals possess dominant frequency at a common value, the occurrence of such common frequency is intermittent or inconsistent throughout the signal span (refer Figs. A.2b-I,III). During this state, we observe a substantial reduction in the magnitudes of the previously observed modes (i.e.,  $f_a$  and  $f_h$ ) in the combustion noise state (Figs. A.2a-II,IV), and the appearance of a strong broadband peak at  $f_l$  for both the signals (Figs. A.2b-II,IV).

During the state of weakly correlated periodic oscillations, we observe a continuous presence of the lock-in frequency mode ( $f_l$ ) throughout the span of both signals (Figs. A.2c-I,III). Here, the value of  $f_l$  is observed to approach the frequency of the acoustic

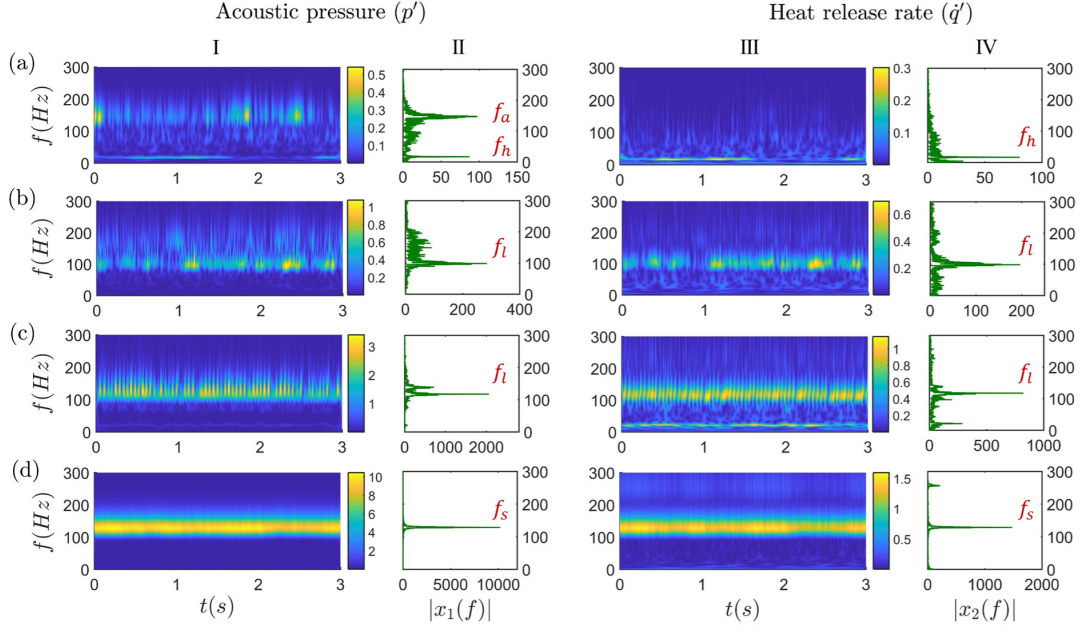


Figure A.2: (a)-(d) The scalograms (I, III) and amplitude spectra (II, IV) of the acoustic pressure ( $p'$ ) and the heat release rate ( $\dot{q}'$ ) signals corresponding to the states of combustion noise ( $\bar{u} = 7.8$  m/s), intermittency ( $\bar{u} = 9.6$  m/s), weakly correlated periodic oscillations ( $\bar{u} = 10.4$  m/s), and strongly correlated periodic oscillations (thermoacoustic instability) ( $\bar{u} = 11.4$  m/s), respectively.

mode ( $f_a$ ) in the pressure signal (see Fig. A.2c-II) and, a small peak associated with  $f_h$  is also noticed in the heat release rate signal (see Fig. A.2c-IV). When the system dynamics is in a state of strongly correlated periodic oscillations, we observe a sharp peak in the amplitude spectra of both  $p'$  and  $\dot{q}'$  signals (Figs. A.2d-II,IV). We find that during the onset of this state, the frequency of the partial lock-in mode shifts to that of synchronization mode of both the signals ( $f_s = 128.3$  Hz), resulting in the onset of large amplitude highly correlated periodic oscillations in both the acoustic pressure and the heat release rate signals. We conjecture that the synchronization mode corresponds to the modified value of the acoustic mode frequency  $f_a$ , which happens possibly due to the increased driving of the flame-acoustic interaction, change in the temperature of reacting flow of the combustor or modification in the flame structure observed during this state. Further, we refer to this state as the onset of perfect vortex-acoustic locking in the system dynamics, wherein the synchronized shedding of strong large-scale vortices is observed at the acoustic mode frequency in the system. We also notice a higher harmonic frequency ( $f_{s,sup} = 219.1$  Hz) in the spectrum of  $\dot{q}'$  (Fig. A.2d-IV), which suggests the presence of strong nonlinearities in the heat release rate signals in comparison to that in the acoustic pressure signals (Nayfeh and Balachandran, 2008).

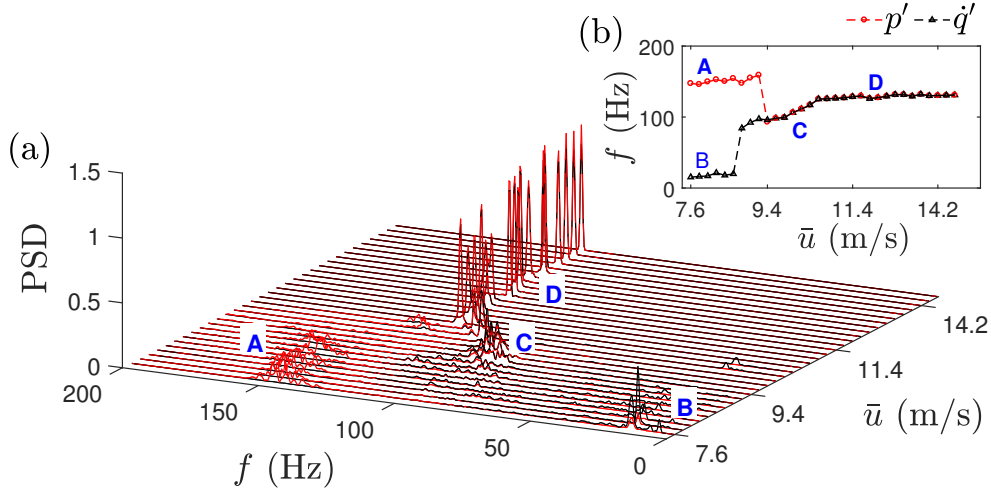


Figure A.3: (a) The waterfall diagram representing the variation of power spectral density of the acoustic pressure ( $p'$ -red color) and the heat release rate ( $q'$ -black color) signals for different values of  $\bar{u}$ , while the system dynamics transition from combustion noise to thermoacoustic instability. (b) The variation in the dominant frequencies of both  $p'$  and  $q'$  signals corresponding to the velocity range shown in (a). In (a), the regions A, B, C and D correspond to the frequency bands of the natural acoustic mode of the duct ( $f_a$ ), hydrodynamic mode of the reacting flow ( $f_h$ ), partial lock-in mode ( $f_l$ ), and perfect lock-in or synchronization mode ( $f_s$ ) of the coupled dynamics of acoustic and heat release rate fluctuations, respectively.

In Fig. A.3, we plot a waterfall diagram representing the variation of the power spectral density of both  $p'$  and  $q'$  (Fig. A.3a) and the variation in their dominant frequencies (Fig. A.3b), when  $\bar{u}$  is varied in the system. The waterfall diagram depicts the overall change in the frequency content of the combustor dynamics during the transition from combustion noise to thermoacoustic instability. For the low values of flow velocity (Figs. A.3a,b), we observe the separate band of frequencies in the regions A and B (represented by  $f_a$  and  $f_h$ , respectively, for  $p'$  and  $q'$  signals in Fig. A.2a). We further notice that, prior to the locking of dominant frequencies of these signals, another band of frequencies (shown by region C in Fig. A.3a and represented by  $f_l$  in Fig. A.2b) emerges in between the earlier frequency bands associated with regions A and B.

After the locking of dominant frequencies of both  $p'$  and  $q'$  signals, we notice that the frequency band corresponding to  $f_l$  exhibits a nearly linear increase with an increase in  $\bar{u}$  (as shown by region C in Figs. A.3a,b), which is similar to that was previously reported by (Lieuwen, 2002; Chakravarthy *et al.*, 2007; Singaravelu and Mariappan, 2017). When the frequency corresponding to the partial lock-in mode ( $f_l$ ) approaches the frequency of the acoustic mode ( $f_a$ ) of the combustor, we notice the locking of

$f_l$  happens with  $f_a$ , which is subsequently referred to as  $f_s$ . After the onset of this frequency lock-in, the value of  $f_l (= f_s)$  stays nearly constant for a large range of values of  $\bar{u}$  (see region  $D$  in Figs. A.3a,b). Further, one should note that the value of the synchronization mode frequency ( $f_s$ ) observed in region  $D$  is lower than the value of acoustic mode frequency ( $f_a$ ) observed during the state of combustion noise, which also suggests that the acoustic mode frequency might have shifted to a lower value due to the change in the flow and flame properties of the system during the onset of thermoacoustic instability. The frequency locking behavior of the acoustic pressure and the heat release rate signals shown in Fig. A.3 for the swirl-stabilized combustor is very much similar to that is observed for the bluff-body stabilized combustor in Chapter 4, Section 4.1.2.

### A.1.3 Synchronization Analysis of Acoustic Pressure and Heat Release Rate Signals

In order to measure the correlation in frequencies of both  $p'$  and  $\dot{q}'$  signals in the time-frequency domain, we compute the cross wavelet transform (XWT) of these signals (refer Fig. A.4). The XWT shows the regions of maximum common spectral power observed in both the signals (as explained in Chapter 2, Section 4.5.3). The color bar indicates the variation of common power in the XWT of the two signals. The black colored arrows in the plots indicate the instantaneous variation of the relative phase angle between  $p'$  and  $\dot{q}'$  signals at different frequencies of the scalogram. When two signals of the coupled oscillators are synchronized, their XWT will show a common power at the synchronization frequency and the arrows will have alignment in the same direction. The direction of arrows further quantifies the value of the phase angle between the signals. The orientation of arrows from left to right (i.e., 0 degrees) indicates that the signals of  $p'$  and  $\dot{q}'$  are in-phase with each other and that from right to left (i.e., 180 degrees) indicates the anti-phase locking of both the signals. The upward direction of arrows show that  $p'$  leads  $\dot{q}'$  by 90 degrees or lags by 270 degrees, and vice versa for the downward directed arrows. The U-shaped regime with a black color border represents the 'cone of influence' (Grinsted *et al.*, 2004). Outside of this region, the edge effects due to the finite length of the signal are significant.

Figure A.4 displays XWTs of  $p'$  and  $\dot{q}'$  signals obtained for the different states of combustor dynamics shown in Figs. A.1 and A.2. During the state of combustion noise

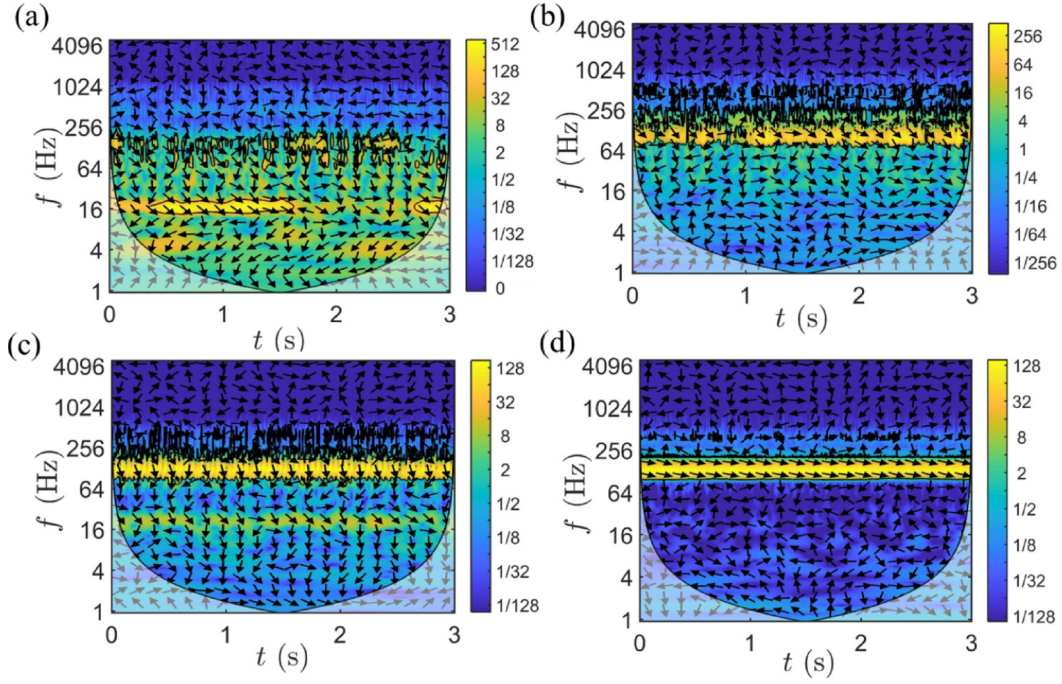


Figure A.4: (a)-(d) The cross wavelet transforms of the acoustic pressure ( $p'$ ) and the heat release rate ( $q'$ ) signals obtained for different states of the combustor dynamics such as combustion noise ( $\bar{u} = 7.8$  m/s), intermittency ( $\bar{u} = 9$  m/s), weakly correlated periodic oscillations ( $\bar{u} = 10.8$  m/s), and strongly correlated periodic oscillations ( $\bar{u} = 11$  m/s), respectively.

(Fig. A.4a), we notice an apparently random distribution of the common frequency around  $f_a$ ; however, a small region of both the signals is observed to share a common power, highlighted by bright yellow color, around  $f_h$  (refer Fig. A.4a). This common power in XWT is due to the presence of frequency  $f_h$  in both  $p'$  and  $q'$  signals for a short duration of time. However, as the dominant frequencies of these signals are at different values (Fig. A.3b) and the relative phase arrows are mostly randomly oriented in the plot of XWT, we confirm the desynchronization in the acoustic pressure and the heat release rate signals during this state of oscillations. In the case of intermittency, the presence of maximum correlation in the frequencies is observed around  $f_l$  (Fig. A.4b). In the regions of common spectral power, we notice a seemingly synchronized alignment of arrows in the periodic epochs of the signals, suggesting the phase-locking behaviour of  $p'$  and  $q'$  signals during this region of oscillation. The breaks in this frequency band point out the absence of a common frequency (or desynchronization) during epochs of aperiodic oscillations of the intermittency signals. Thus, the behaviour of relative phase during intermittency suggests the presence of intermittent phase synchronization between the  $p'$  and  $q'$  signals.

When the signals are in a state of weakly correlated periodic oscillations, a common frequency region associated with them is present throughout their time span (Fig. A.4c). Further, we note that the row of arrows, indicating the relative phase between the signals in the common frequency region, display almost a constant alignment throughout the signal span. This evokes the phase-locking behaviour of both the signals. The distortions in the common frequency band at higher frequencies might contribute to the variation in the amplitudes of both  $p'$  and  $q'$  signals observed during this state (refer Fig. A.1c). As the system dynamics enter into the state of strongly correlated periodic oscillations, we find a strong correlation in the frequencies of coupled  $p'$  and  $q'$  signals exhibited by a clean common frequency band in the scalogram (Fig. A.4d). The relative phase arrows observed in the common frequency band display a constant orientation throughout the signal illustrating a perfect synchronization (or phase-locking) of these signals during this state. We can see that the orientation of the arrows observed in the common power band changes as the system dynamics shifts from the state of weakly correlated periodic oscillations to the strongly correlated periodic oscillations. During the state of strongly correlated periodic oscillations, the phase angle between  $p'$  and  $q'$  signals is observed to approach a value close to 16 degrees, while that during the weakly correlated periodic oscillations remains close to 78 degrees. This decrease in the relative phase angle between the signals possibly enhances the driving between both the oscillations, that further leads to the onset of high amplitude pressure oscillations in the system.

The amplitude correlation between the signals of two oscillators can further be understood by plotting the values of one signal against other, as a two-dimensional phase portrait. In Fig. A.5, we show such plots between the acoustic pressure and the heat release rate oscillations, wherein we demonstrate the difference in the evolution of the phase space trajectories obtained during different states of the combustor dynamics. We observe that during the state of combustion noise (Fig. A.5a), the plot between  $p'$  and  $q'$  shows an irregular behavior of the trajectories, indicating the presence of a lower correlation between the signals. During the state of intermittency (Fig. A.5b), these plots display an emergence of seemingly regular trajectories, corresponding to the burst of periodic oscillations (Fig. A.5b-i), among the regions of aperiodic oscillations that fills the central portion of the phase portrait (see Fig. A.5b-ii). In the state of weakly correlated periodic oscillations (Fig. A.5c), a noisy elliptic structure emerges in the phase

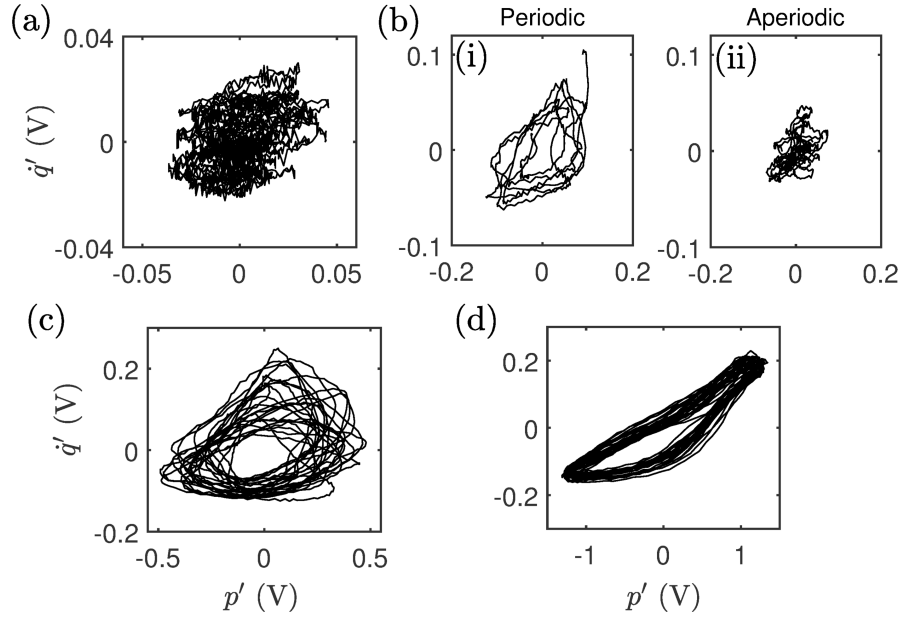


Figure A.5: (a)-(d) The sequence of plots between the acoustic pressure ( $p'$ ) and the heat release rate ( $\dot{q}'$ ) oscillations representing the evolution of the phase space trajectories corresponding to the signals shown in Fig. A.1 for different states of the combustor dynamics. The flow velocities corresponding to (a)-(d) are  $\bar{u} = 7.8, 9.6, 10.4,$  and  $11.4$  m/s, respectively.

space, wherein the trajectories of the signals show a non-overlapping nature indicating a weak correlation in the amplitudes of these signals. Finally, during the onset of strongly correlated periodic oscillations (Fig. A.5d), we notice an overlapping of nearly all the trajectories in the phase portrait displaying a nearly distorted elliptic structure.

Now, we move our attention to characterize the difference in the dynamical as well as the synchronization properties of the acoustic pressure and the heat release rate signals acquired during the states of weakly and strongly correlated periodic oscillations. In order to do this, we use recurrence plots (RP) and a measure of synchronization based on it (Romano *et al.*, 2005; Marwan *et al.*, 2007). Figures A.6a,b show the RPs of the respective states for both the acoustic pressure and the heat release rate signals. The weak correlation in the amplitudes of the former state (Fig. A.5c) is reflected as the broken diagonal lines (except the main diagonal) in the RPs of both  $p'$  and  $\dot{q}'$  signals. However, during the latter case of the strongly correlated periodic oscillations (Fig. A.5d), the RPs of these signals display only continuous diagonal lines reflecting the existence of strong correlation in the amplitudes of these signals. Further, we note that the RPs of  $p'$  and  $\dot{q}'$  shown in Fig. A.6a are non-identical, whereas those shown in Fig. A.6b are perfectly identical.

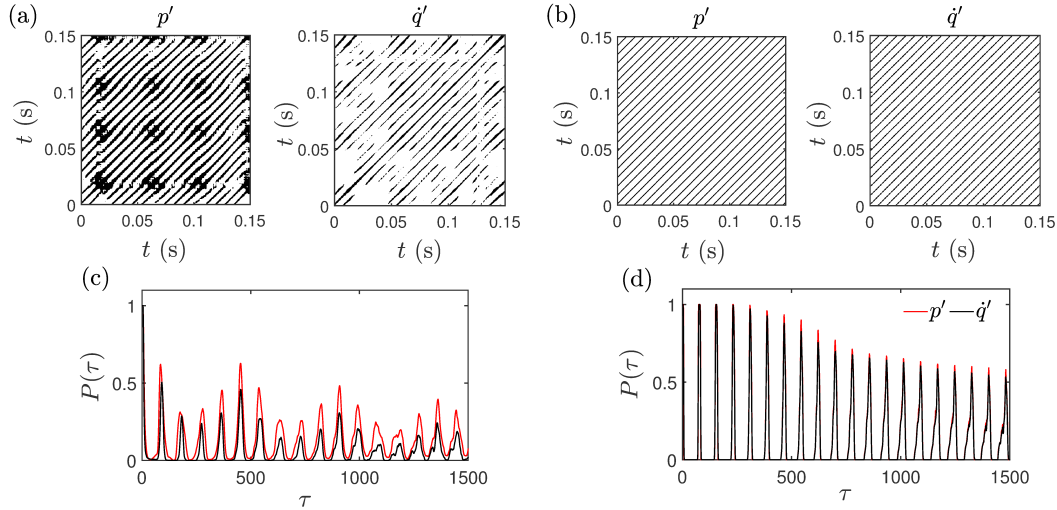


Figure A.6: (a), (b) The recurrence plots of the acoustic pressure ( $p'$ ) and heat release rate ( $q'$ ) signals acquired during the weakly correlated and the strongly correlated periodic oscillations at  $\bar{u} = 10.4$  m/s and  $\bar{u} = 11.4$  m/s, respectively. (c), (d) The plots of the probability of recurrence ( $P(\tau)$ ) with respect to delay time ( $\tau$ ) for both  $p'$  and  $q'$  signals obtained during the states shown in (a), (b), respectively, representing the states of phase synchronization and generalized synchronization. The parameters being used in plotting the recurrence plots are: embedding dimension = 6, time delay = 2.1 ms, recurrence threshold = 20% of maximum size of the attractor, and data length = 3000 points.

To characterize the synchronization properties of  $p'$  and  $q'$  signals observed during the states of weakly correlated and strongly correlated periodic oscillations, we compare the properties of a recurrence measure called the probability of recurrence ( $P(\tau)$ ) (Romano *et al.*, 2005) obtained for these states. The variation of  $P(\tau)$  as a function of the delay time ( $\tau$ ) aids in differentiating the different types of synchronization observed during these states. Figures A.6c,d show such plots of  $P(\tau)$  obtained for both  $p'$  and  $q'$  signals shown in Figs. A.6a,b, respectively. In Fig. A.6c, we notice that the positions of peaks of  $P(\tau)$  for both the signals are perfectly matched, however, their heights remain mismatched. Here, the time scale corresponding to the occurrence of peaks in the  $P(\tau)$  plot is associated with the mean frequency of the signals. This hints at the occurrence of phase synchronization (PS) between the signals during the weakly correlated state of periodic oscillations (Romano *et al.*, 2005). In the PS state, the instantaneous phases between the signals are perfectly locked (see Fig. A.4c), while their amplitudes remain uncorrelated (see Fig. A.5c). On the other hand, when the system is in the state of strongly correlated periodic oscillations, we observe a perfect matching of the positions as well as the heights of peaks in the plots of  $P(\tau)$  for both the signals (Fig. A.6d). This

suggests the occurrence of generalized synchronization (GS) between the signals (Romano *et al.*, 2005). During the GS state, both the signals of coupled oscillators exhibit a functional relationship between them, and hence their RPs show a perfect similarity, as seen in Fig. A.6b (Lakshmanan and Senthilkumar, 2011).

## **A.2 Spatiotemporal Analysis of Coupled Acoustic Field and Reacting Field**

Further, we investigate the spatiotemporal aspects of the coupled behaviour of the acoustic field and the local heat release rate fluctuations of reacting field of the combustor during the transition to thermoacoustic instability. To that end, we consider the reaction zone as a network of local heat release rate oscillators. The local heat release rate fluctuations are obtained from the intensity variation observed at each pixel of the time-resolved chemiluminescence images of the reaction zone of the combustor. Then, the instantaneous phase difference between the acoustic pressure and the local heat release rate oscillations is calculated using the Hilbert transform (Mondal *et al.*, 2017b). This instantaneous phase difference is represented by the phasors in Fig. A.7 for different dynamical states observed during the transition to thermoacoustic instability.

### **A.2.1 Analyzing Spatial Synchrony of the Local Heat Release Rate Fluctuations With the Acoustic Pressure Fluctuations**

The state of combustion noise corresponds to the spatial asynchrony in the phasor field (Fig. A.7a), whereas the spatial synchrony is visible during the state of weakly correlated periodic oscillations (Fig. A.7c). The coexistence of spatial synchrony and asynchrony in the phase field, visible during the state of intermittency (Fig. A.7b), mimics a chimera-like state, which is similar to the observation of Mondal *et al.* (2017b) in a bluff-body stabilized turbulent combustor. However, a counter-intuitive pattern in the phasor plot of the strongly correlated periodic oscillations state is observed. Instead of an increase in the spatial synchrony or coherence in the phasor plot, the regions of spatial asynchrony are observed to grow in the flow field during the state of strongly correlated periodic oscillations (Fig. A.7d). The reason for this growth in the incoherence

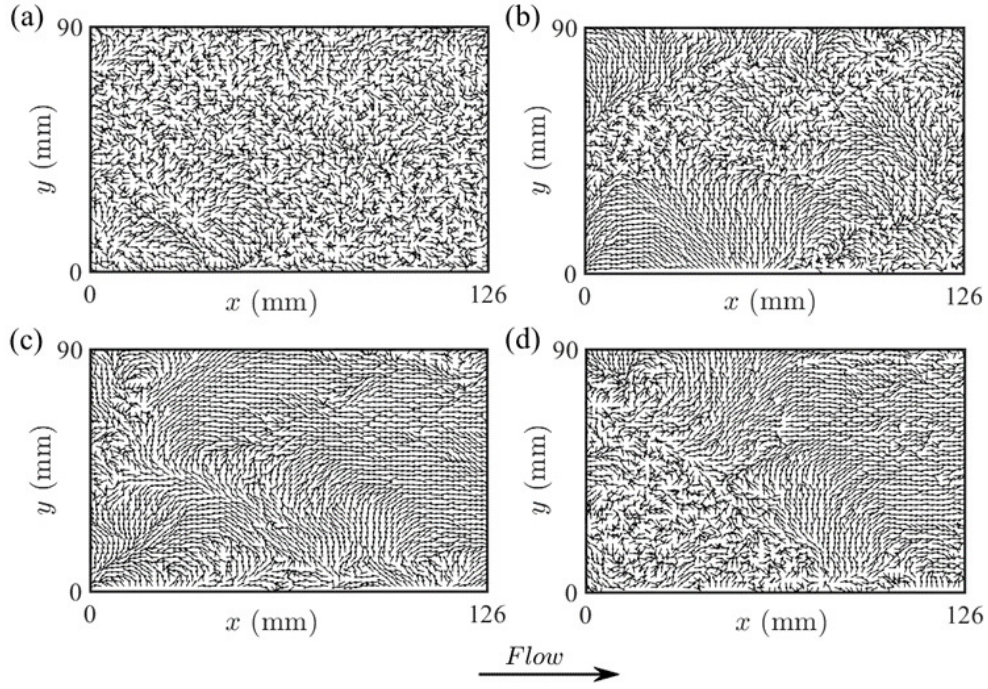


Figure A.7: (a)-(d) Typical phasor plots depicting the instantaneous phase difference (by arrows) between the acoustic pressure and the local heat release rate fluctuations. A pattern of phasors for a time instant (arbitrarily chosen) is shown for each of the dynamical states such as (a) combustion noise ( $\bar{u} = 8.2$  m/s), (b) intermittency ( $\bar{u} = 8.8$  m/s), (c) weakly correlated periodic oscillations ( $\bar{u} = 10.8$  m/s) and (d) strongly correlated periodic oscillations ( $\bar{u} = 11.4$  m/s), similar to that described previously in Fig. A.1.

might be the result of increased turbulence associated with the higher flow Reynolds number in the system.

The global synchrony in the reaction zone is further quantified by calculating the time-averaged value of a Kuramoto order parameter ( $R$ ), which is defined as (Kuramoto, 1984) -

$$R(t) = \frac{1}{N} \left| \sum_{j=1}^N e^{i\theta_j(t)} \right| \quad (\text{A.1})$$

where,  $R(t)$  is the time dependent order parameter,  $\theta_j(t)$  is the instantaneous phase of  $j^{\text{th}}$  oscillator, and  $N$  is the total number of oscillators in the network. The values of the order parameter ranges from zero for a completely disordered state to one for a perfectly ordered state.

We observe a gradual increase in  $R$  when the system dynamics transition to the state of thermoacoustic instability from the combustion noise state (Fig. A.8). The increase in  $R$  indicates a growth in the global synchrony in the system, which has been observed earlier in the bluff-body stabilized combustor (Mondal *et al.*, 2017b). Here, we

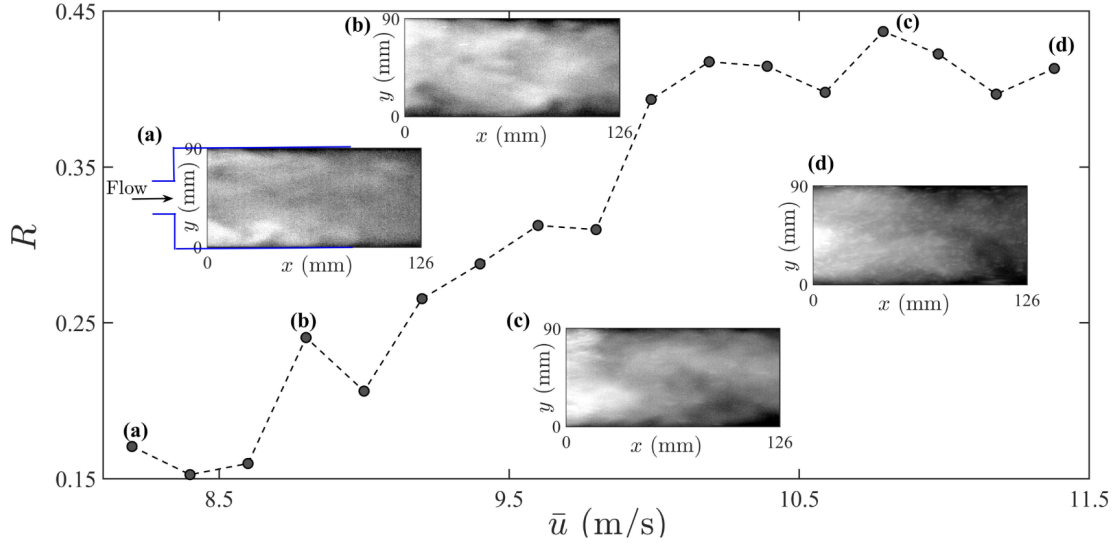


Figure A.8: Time-averaged Kuramoto order parameter ( $R$ ) is plotted against the mean velocity of the flow ( $\bar{u}$ ). Different dynamical states are indicated in the plot as (a) combustion noise ( $\bar{u} = 8.2$  m/s), (b) intermittency ( $\bar{u} = 8.8$  m/s), (c) weakly correlated periodic oscillations ( $\bar{u} = 10.8$  m/s) and (d) strongly correlated periodic oscillations ( $\bar{u} = 11.4$  m/s). For each state we show a typical CH\* intensity field at the time instant for which the phasor field is shown in Fig. A.7.

note that, during the transition from the weakly correlated periodic oscillations (phase synchronization) to the strongly correlated periodic oscillations (generalized synchronization), although the amount of spatial asynchrony is increased, the global synchrony does not exhibit much of a difference (points c, d in Fig. A.8).

Further, we show the instantaneous reaction flow field, acquired in terms of CH\* chemiluminescence of the flame (see insets of Fig. A.8), corresponding to the time instants for which phasor plots are shown in Fig. A.7. We notice that the flame zone is large and grainy during the state of combustion noise (Fig. A.8a). The observed scattering in the CH\* intensity field may be caused due to the underlying turbulence, which results in incoherence in the phasor field (Fig. A.5a). During the occurrence of intermittency (IPS), the flame zone still remains large (Fig. A.8b), however, the local CH\* intensities are apparently more coherent, which is manifested as a chimera-like pattern in the phasor field (Fig. A.7b). For a sufficiently high  $\bar{u}$  (Fig. A.8c), most of the heat is being periodically released near the dump plane during the state of weakly correlated periodic oscillation (PS). The local CH\* intensities observed in the reaction zone are clustered, which subsequently leads to the spatial synchrony noticed in their phasor field (Fig. A.7c). With further increase in the value of  $\bar{u}$ , we observe

a diminishment of CH\* intensities in the region downstream to the dump plane during the state of strongly correlated periodic oscillation (GS). The large amplitude pressure and velocity oscillations occur during this state, and the heat release rate field shows the presence of coherent oscillations very close to the region of dump plane (Fig. A.8d).

We observe that the phasor field during GS (Fig. A.7d) contains more significant regions of incoherence in comparison to that of PS (Fig. A.7c). Essentially, with an increase in the flow velocity, we expect the flow turbulence to increase. However, during the states of IPS and PS, there is an order which is emerging in the spatial dynamics of the disordered phase field. This order keeps increasing (as observed in Fig. A.7) with an increase in the flow velocity. With further increase in the flow velocity, during the state of GS, we conjecture that the amount of turbulence in the flow field is large enough to partially diminish the order in the phasor field. The local synchrony appears to be lost in some places of the reaction zone as the turbulence at higher flow velocities dominates over the coherence emerged due to the thermoacoustic oscillations. Nevertheless, even with slightly lower values of the Kuramoto order parameter ( $R$ ) during the state of GS in comparison to that of PS, we have larger amplitude correlation between the  $p'$  and  $\dot{q}'$  signals (as observed earlier in Fig. A.5d). However, the reason for the higher amplitude correlation during the state of GS in spite of higher spatial incoherence in the phasor field, in comparison with the PS state, needs to be investigated further with simultaneous measurements of the flow field and the flame images.

## **A.2.2 Comparison of Spatial Fields of Phase Synchronization and Generalized Synchronization States**

To reassure the fact that the acoustic driving is higher in the state of generalized synchronization even with the presence of small regions of incoherence in their phasor field, we analyze the instantaneous fields of local  $p'\dot{q}'$  (acoustic power) of the reaction zone. Further, the instantaneous fields of  $p'(t)\dot{q}'(x, y, t)$  and the local distribution of CH\* chemiluminescence intensity field are compared over a period of oscillation in Fig. A.9 for the states of phase synchronization or PS (Fig. A.9-I) and generalized synchronization or GS (Fig. A.9-II). The data points corresponding to these images are marked in the time series shown in Figs. A.9f,g for PS and GS states, respectively. At certain instants of the signals, we observed clusters of positive  $p'\dot{q}'$ , wherein, within

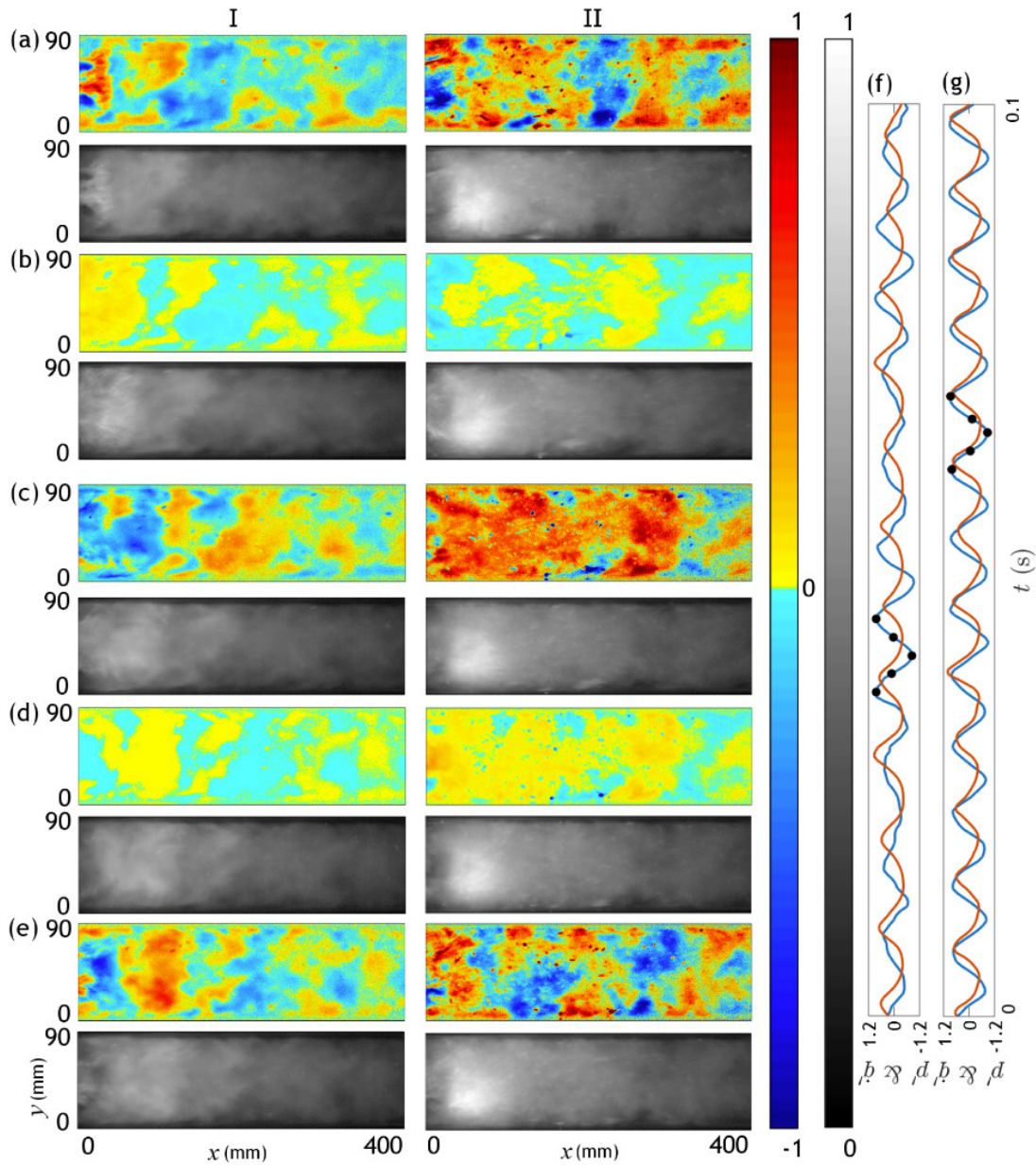


Figure A.9: (a)-(e) The instantaneous field of local  $p'(t)q'(x, y, t)$  during the states of (I) phase synchronization (PS) and (II) generalized synchronization (GS) along with the corresponding CH\* chemiluminescence images of the flame. The simultaneous time traces of the pressure oscillations and the global heat release rate oscillations are presented in (f) and (g) for the states of PS and GS, respectively.

each cluster similar values of positive  $p'q'$  exist for both PS and GS states. The regions of positive  $p'q'$  appear to be more for the case of GS state in comparison to those for PS state (refer Fig. A.9c). We associate this behavior to the larger driving observed during the GS state, when compared to PS state. Further, although the maximum heat release rate occurs near the dump plane as inferred from the higher intensity of light in the chemiluminescence images, the regions of positive  $p'q'$  are distributed in the space

downstream to the dump plane.

### **A.3 Summary**

We performed both temporal and spatiotemporal analysis of the coupled acoustic pressure and heat release rate fluctuations present in a swirl-stabilized combustor. For the temporal analysis, we studied the interaction between the acoustic pressure oscillations and the global heat release rate oscillations in the flame, whereas, for the spatiotemporal analysis, we analyzed the coupling of the acoustic pressure oscillations with the local heat release rate oscillations in the flame. Using the framework of synchronization, we studied the transition of these coupled oscillations from the state of combustion noise to thermoacoustic instability through intermittency. With this, we characterized such a transition into four different states of synchronization: desynchronization (during combustion noise), intermittent phase synchronization (IPS, during intermittency), phase synchronization (PS, during weakly correlated periodicity) and generalized synchronization (GS, during strongly correlated periodicity). Our study, further, provided a description for the onset of vortex-acoustic lock-in by analyzing the system dynamics in the frequency domain. This analysis suggests that during the onset of intermittency, the distinct dominant peaks of the acoustic pressure and the heat release rate fluctuations, observed during combustion noise, shift their dominant frequencies to a common lock-in mode (referred to as partial lock-in mode). The value of this lock-in mode frequency exhibits a continuous increase in the IPS and PS states, and finally stays nearly constant (referred to as synchronization mode) in the state of GS. In the spatiotemporal analysis, an order is observed to emerge from the underlying disordered turbulence as the system dynamics transitions to the state of weakly correlated periodicity (PS). However, with very high flow rates where the strongly correlated periodic oscillations (GS) persist, the reaction zone is observed to be contaminated by the small regions of disorder seemingly due to the higher turbulence. Even then, the state of GS exhibits a higher global synchrony than that of IPS and a higher acoustic driving than that of PS.

## REFERENCES

1. **Abarbanel, H.**, *Analysis of observed chaotic data*. Springer Science & Business Media, 1996.
2. **Abarbanel, H. D., R. Brown, J. J. Sidorowich, and L. S. Tsimring** (1993). The analysis of observed chaotic data in physical systems. *Reviews of modern physics*, **65**(4), 1331.
3. **Abrams, D. M. and S. H. Strogatz** (2004). Chimera states for coupled oscillators. *Physical review letters*, **93**(17), 174102.
4. **Ahn, S., C. Park, and L. L. Rubchinsky** (2011). Detecting the temporal structure of intermittent phase locking. *Physical Review E*, **84**(1), 016201.
5. **Altay, H. M., R. L. Speth, D. E. Hudgins, and A. F. Ghoniem** (2009). Flame–vortex interaction driven combustion dynamics in a backward-facing step combustor. *Combustion and Flame*, **156**(5), 1111–1125.
6. **Ananthkrishnan, N., S. Deo, and F. E. Culick** (2005). Reduced-order modeling and dynamics of nonlinear acoustic waves in a combustion chamber. *Combustion science and technology*, **177**(2), 221–248.
7. **Anderson, W., K. Miller, H. Ryan, S. Pal, R. Santoro, and J. Dressler** (1998). Effects of periodic atomization on combustion instability in liquid-fueled propulsion systems. *Journal of Propulsion and Power*, **14**(5).
8. **Aparicio, T., E. F. Pozo, and D. Saura** (2008). Detecting determinism using recurrence quantification analysis: Three test procedures. *Journal of Economic Behavior & Organization*, **65**(3), 768–787.
9. **Baillet, F., D. Durox, and R. Prud’Homme** (1992). Experimental and theoretical study of a premixed vibrating flame. *Combustion and flame*, **88**(2), 149–168.
10. **Balachandran, R., B. Ayoola, C. Kaminski, A. Dowling, and E. Mastorakos** (2005). Experimental investigation of the nonlinear response of turbulent premixed flames to imposed inlet velocity oscillations. *Combustion and Flame*, **143**(1-2), 37–55.
11. **Balanov, A., N. Janson, D. Postnov, and O. Sosnovtseva**, *Synchronization: from simple to complex*. Springer Science & Business Media, 2008.
12. **Balanov, A., N. Janson, D. Postnov, and O. Sosnovtseva**, *Synchronization: from simple to complex*, volume 17. Springer, 2009.
13. **Balasubramanian, K. and R. Sujith** (2008a). Non-normality and nonlinearity in combustion–acoustic interaction in diffusion flames. *Journal of Fluid Mechanics*, **594**, 29–57.
14. **Balasubramanian, K. and R. Sujith** (2008b). Thermoacoustic instability in a rijke tube: Non-normality and nonlinearity. *Physics of Fluids*, **20**(4), 044103.

15. **Balusamy, S., L. K. Li, Z. Han, M. P. Juniper, and S. Hochgreb** (2015). Nonlinear dynamics of a self-excited thermoacoustic system subjected to acoustic forcing. *Proceedings of the Combustion Institute*, **35**(3), 3229–3236.
16. **Barbi, C., D. Favier, C. Maresca, and D. Telionis** (1986). Vortex shedding and lock-on of a circular cylinder in oscillatory flow. *Journal of Fluid Mechanics*, **170**, 527–544.
17. **Bazarov, V. G. and V. Yang** (1998). Liquid-propellant rocket engine injector dynamics. *Journal of Propulsion and Power*, **14**(5), 797–806.
18. **Bellows, B., A. Hreiz, and T. Lieuwen** (2008). Nonlinear interactions between forced and self-excited acoustic oscillations in premixed combustor. *Journal of propulsion and power*, **24**(3), 628–631.
19. **Bellows, B. D., Y. Neumeier, and T. Lieuwen** (2006). Forced response of a swirling, premixed flame to flow disturbances. *Journal of propulsion and power*, **22**(5), 1075–1084.
20. **Bellucci, V., C. O. Paschereit, P. Flohr, and F. Magni**, On the use of helmholtz resonators for damping acoustic pulsations in industrial gas turbines. *In ASME Turbo Expo 2001: Power for Land, Sea, and Air*. American Society of Mechanical Engineers, 2001.
21. **Bishop, R. and A. Hassan**, The lift and drag forces on a circular cylinder oscillating in a flowing fluid. *In Proceedings of the Royal Society of London A: Mathematical, Physical and Engineering Sciences*, volume 277. The Royal Society, 1964.
22. **Biwa, T., S. Tozuka, and T. Yazaki** (2015). Amplitude death in coupled thermoacoustic oscillators. *Physical Review Applied*, **3**(3), 034006.
23. **Blasius, B., A. Huppert, and L. Stone** (1999). Complex dynamics and phase synchronization in spatially extended ecological systems. *Nature*, **399**(6734), 354.
24. **Blekhman, I., P. S. Landa, and M. G. Rosenblum** (1995). Synchronization and chaos in interacting dynamical systems. *Applied Mechanics Reviews*, **48**, 733–752.
25. **Blevins, R.** (1985). The effect of sound on vortex shedding from cylinders. *Journal of Fluid Mechanics*, **161**, 217–237.
26. **Blevins, R. D.**, *Flow-induced vibration*. New York, NY (USA); Van Nostrand Reinhold Co., Inc., 1990.
27. **Blomshield, F.**, Lessons learned in solid rocket combustion instability. *In 43rd AIAA/ASME/SAE/ASEE Joint Propulsion Conference & Exhibit*. 2007.
28. **Blomshield, F., J. Crump, H. Mathes, R. A. Stalnaker, and M. Beckstead** (1997). Stability testing of full-scale tactical motors. *Journal of Propulsion and Power*, **13**(3), 349–355.
29. **Bloxside, G., A. Dowling, and P. Langhorne** (1988). Reheat buzz: an acoustically coupled combustion instability. part 2. theory. *Journal of fluid mechanics*, **193**, 445–473.
30. **Boccaletti, S., E. Allaria, R. Meucci, and F. Arecchi** (2002a). Experimental characterization of the transition to phase synchronization of chaotic c o 2 laser systems. *Physical review letters*, **89**(19), 194101.

31. **Boccaletti, S., J. Kurths, G. Osipov, D. Valladares, and C. Zhou** (2002*b*). The synchronization of chaotic systems. *Physics reports*, **366**(1), 1–101.
32. **Bove, I., S. Boccaletti, J. Bragard, J. Kurths, and H. Mancini** (2004). Frequency entrainment of nonautonomous chaotic oscillators. *Physical Review E*, **69**(1), 016208.
33. **Boyer, L. and J. Quinard** (1990). On the dynamics of anchored flames. *Combustion and flame*, **82**(1), 51–65.
34. **Bush, S. M. and E. J. Gutmark** (2007). Reacting and nonreacting flowfields of a v-gutter stabilized flame. *AIAA journal*, **45**(3), 662.
35. **Candel, S.** (2002). Combustion dynamics and control: Progress and challenges. *Proceedings of the combustion institute*, **29**(1), 1–28.
36. **Candel, S., D. Durox, S. Ducruix, A.-L. Birbaud, N. Noiray, and T. Schuller** (2009). Flame dynamics and combustion noise: progress and challenges. *International Journal of Aeroacoustics*, **8**(1), 1–56.
37. **Cao, L.** (1997). Practical method for determining the minimum embedding dimension of a scalar time series. *Physica D: Nonlinear Phenomena*, **110**(1-2), 43–50.
38. **Carberry, J., J. Sheridan, and D. Rockwell** (2005). Controlled oscillations of a cylinder: forces and wake modes. *Journal of Fluid Mechanics*, **538**, 31–69.
39. **Carvalho, J., M. Ferreira, C. Bressan, and J. Ferreira** (1989). Definition of heater location to drive maximum amplitude acoustic oscillations in a rijke tube. *Combustion and Flame*, **76**(1), 17–27.
40. **Caughey, B. and P. T. Lansbury Jr** (2003). Protofibrils, pores, fibrils, and neurodegeneration: separating the responsible protein aggregates from the innocent bystanders. *Annual review of neuroscience*, **26**(1), 267–298.
41. **Chakravarthy, S., R. Sivakumar, and O. Shreenivasan** (2007). Vortex-acoustic lock-on in bluff-body and backward-facing step combustors. *Sadhana*, **32**(1), 145–154.
42. **Chatterjee, S. and A. Mallik** (1996). Three kinds of intermittency in a nonlinear mechanical system. *Physical Review E*, **53**(5), 4362.
43. **Chaudhuri, S., S. Kostka, M. W. Renfro, and B. M. Cetegen** (2010). Blowoff dynamics of bluff body stabilized turbulent premixed flames. *Combustion and flame*, **157**(4), 790–802.
44. **Chaudhuri, S., S. Kostka, S. G. Tuttle, M. W. Renfro, and B. M. Cetegen** (2011). Blowoff mechanism of two dimensional bluff-body stabilized turbulent premixed flames in a prototypical combustor. *Combustion and Flame*, **158**(7), 1358–1371.
45. **Chiocchini, S., T. Pagliaroli, R. Camussi, and E. Giacomazzi** (2017). Chaotic and linear statistics analysis in thermoacoustic instability detection. *Journal of Propulsion and Power*, 1–12.
46. **Chishty, W. A.** (2005). *Effects of thermoacoustic oscillations on spray combustion dynamics with implications for lean direct injection systems*. Ph.D. thesis, Virginia Tech.

47. **Cho, J. H.** and **T. Lieuwen** (2005). Laminar premixed flame response to equivalence ratio oscillations. *Combustion and flame*, **140**(1-2), 116–129.
48. **Chu, B.-T.** (1965). On the energy transfer to small disturbances in fluid flow (part i). *Acta Mechanica*, **1**(3), 215–234.
49. **Correa, S. M.** (1993). A review of nox formation under gas-turbine combustion conditions. *Combustion science and technology*, **87**(1-6), 329–362.
50. **Crocco, L.**, Research on combustion instability in liquid propellant rockets. *In Symposium (International) on Combustion*, volume 12. Elsevier, 1969.
51. **Crocco, L.** and **S.-I. Cheng** (1956). Theory of combustion instability in liquid propellant rocket motors. Technical report, PRINCETON UNIV NJ.
52. **Crump, J. E., K. C. Schadow, V. Yang, and F. E. Culick** (1986). Longitudinal combustion instabilities in ramjet engines identification of acoustic modes. *Journal of Propulsion and Power*, **2**(2), 105–109.
53. **Culick, F.** (1970). Stability of longitudinal oscillations with pressure and velocity coupling in a solid propellant rocket. *Combustion Science and Technology*, **2**(4), 179–201.
54. **Culick, F.** (1976). Nonlinear behavior of acoustic waves in combustion chambers. *Acta Astronautica*, **3**(9-10), 735–757.
55. **Culick, F.** (1994). Some recent results for nonlinear acoustics in combustion chambers. *AIAA journal*, **32**(1), 146–169.
56. **Culick, F.** and **P. Kuentzmann** (2006). Unsteady motions in combustion chambers for propulsion systems. Technical report, Nato Research and Technology Organization Neuilly-Sur-Seine (France).
57. **Culick, F. E.** and **V. Yang** (1995). Overview of combustion instabilities in liquid-propellant rocket engines. *Liquid Rocket Engine Combustion Instability*, **169**, 3–37.
58. **Datta, S., S. Mondal, A. Mukhopadhyay, D. Sanyal, and S. Sen** (2009). An investigation of nonlinear dynamics of a thermal pulse combustor. *Combustion Theory and Modelling*, **13**(1), 17–38.
59. **Dattarajan, S., A. Lutomirski, R. Lobbia, O. Smith, and A. Karagozian** (2006). Acoustic excitation of droplet combustion in microgravity and normal gravity. *Combustion and Flame*, **144**(1), 299–317.
60. **Ditlevsen, O.** and **H. O. Madsen**, *Structural reliability methods*, volume 178. Wiley New York, 1996.
61. **Domen, S., H. Gotoda, T. Kuriyama, Y. Okuno, and S. Tachibana** (2015). Detection and prevention of blowout in a lean premixed gas-turbine model combustor using the concept of dynamical system theory. *Proceedings of the Combustion Institute*, **35**(3), 3245–3253.
62. **Dowling, A. P.** (1997). Nonlinear self-excited oscillations of a ducted flame. *Journal of fluid mechanics*, **346**, 271–290.

63. **Dowling, A. P.** and **A. S. Morgans** (2005). Feedback control of combustion oscillations. *Annu. Rev. Fluid Mech.*, **37**, 151–182.
64. **Dubey, R., M. McQuay,** and **J. Carvalho**, An experimental and theoretical investigation on the effects of acoustics on spray combustion. *In Symposium (International) on Combustion*, volume 27. Elsevier, 1998.
65. **Ducruix, S., D. Durox,** and **S. Candel** (2000). Theoretical and experimental determinations of the transfer function of a laminar premixed flame. *Proceedings of the combustion institute*, **28**(1), 765–773.
66. **Ducruix, S., T. Schuller, D. Durox,** and **S. Candel** (2003). Combustion dynamics and instabilities: Elementary coupling and driving mechanisms. *Journal of propulsion and power*, **19**(5), 722–734.
67. **Durox, D., T. Schuller,** and **S. Candel** (2005). Combustion dynamics of inverted conical flames. *Proceedings of the combustion Institute*, **30**(2), 1717–1724.
68. **Durox, D., T. Schuller,** and **S. Gandel** (2002). Self-induced instability of a premixed jet flame impinging on a plate. *Proceedings of the Combustion Institute*, **29**(1), 69–75.
69. **Duvvur, A., C. Chiang,** and **W. Sirignano** (1996). Oscillatory fuel droplet vaporization-driving mechanism for combustion instability. *Journal of propulsion and Power*, **12**(2), 358–365.
70. **Ebi, D., A. Denisov, G. Bonciolini, E. Boujo,** and **N. Noiray**, Flame dynamics intermittency in the bi-stable region near a subcritical hopf bifurcation. *In ASME Turbo Expo 2017: Turbomachinery Technical Conference and Exposition*. American Society of Mechanical Engineers, 2017.
71. **Ebi, D., A. Denisov, G. Bonciolini, E. Boujo,** and **N. Noiray** (2018). Flame dynamics intermittency in the bistable region near a subcritical hopf bifurcation. *Journal of Engineering for Gas Turbines and Power*, **140**(6), 061504.
72. **Eckmann, J.-P., S. O. Kamphorst,** and **D. Ruelle** (1987). Recurrence plots of dynamical systems. *EPL (Europhysics Letters)*, **4**(9), 973.
73. **Elaskar, S.** and **E. Del Río**, *New Advances on Chaotic Intermittency and Its Applications*. Springer, 2017.
74. **Eldredge, J. D.** and **A. P. Dowling** (2003). The absorption of axial acoustic waves by a perforated liner with bias flow. *Journal of Fluid Mechanics*, **485**, 307–335.
75. **Emerson, B.** and **T. Lieuwen** (2015). Dynamics of harmonically excited, reacting bluff body wakes near the global hydrodynamic stability boundary. *Journal of Fluid Mechanics*, **779**, 716–750.
76. **Emerson, B., J. O'Connor, M. Juniper,** and **T. Lieuwen** (2012a). Density ratio effects on reacting bluff-body flow field characteristics. *Journal of Fluid Mechanics*, **706**, 219–250.
77. **Emerson, B., J. O'Connor, D. Noble,** and **T. Lieuwen**, Frequency locking and vortex dynamics of an acoustically excited bluff body stabilized flame. *In 50th AIAA Aerospace Sciences Meeting including the New Horizons Forum and Aerospace Exposition*. 2012b.

78. **Erickson, R.** and **M. Soteriou** (2011). The influence of reactant temperature on the dynamics of bluff body stabilized premixed flames. *Combustion and Flame*, **158**(12), 2441–2457.
79. **Etikyala, S.** and **R. Sujith** (2017). Change of criticality in a prototypical thermoacoustic system. *Chaos: An Interdisciplinary Journal of Nonlinear Science*, **27**(2), 023106.
80. **Farge, M.** (1992). Wavelet transforms and their applications to turbulence. *Annual review of fluid mechanics*, **24**(1), 395–458.
81. **Feng, D., J. Zheng, W. Huang, C. Yu, and W. Ding** (1996). Type-i-like intermittent chaos in multicomponent plasmas with negative ions. *Physical Review E*, **54**(3), 2839.
82. **Fisher, S. C.** and **S. A. Rahman** (2009). Remembering the giants: Apollo rocket propulsion development.
83. **Fleifil, M., A. M. Annaswamy, Z. Ghoneim, and A. F. Ghoniem** (1996). Response of a laminar premixed flame to flow oscillations: A kinematic model and thermoacoustic instability results. *Combustion and flame*, **106**(4), 487–510.
84. **Frank, M.** and **M. Schmidt** (1997). Time series investigations on an experimental system driven by phase transitions. *Physical Review E*, **56**(3), 2423.
85. **Fraser, A. M.** and **H. L. Swinney** (1986). Independent coordinates for strange attractors from mutual information. *Physical review A*, **33**(2), 1134.
86. **Fujisaka, H.** and **T. Yamada** (1983). Stability theory of synchronized motion in coupled-oscillator systems. *Progress of theoretical physics*, **69**(1), 32–47.
87. **Gabor, D.** (1946). Theory of communication. part 1: The analysis of information. *Journal of the Institution of Electrical Engineers-Part III: Radio and Communication Engineering*, **93**(26), 429–441.
88. **Ghoniem, A. F., S. Park, A. Wachsman, A. Annaswamy, D. Wee, and H. M. Altay** (2005). Mechanism of combustion dynamics in a backward-facing step stabilized premixed flame. *Proceedings of the Combustion Institute*, **30**(2), 1783–1790.
89. **Gicquel, L. Y., G. Staffelbach, and T. Poinsot** (2012). Large eddy simulations of gaseous flames in gas turbine combustion chambers. *Progress in Energy and Combustion Science*, **38**(6), 782–817.
90. **Glass, L.** (2001). Synchronization and rhythmic processes in physiology. *Nature*, **410**(6825), 277.
91. **Godavarthi, V., V. Unni, E. Gopalakrishnan, and R. Sujith** (2017). Recurrence networks to study dynamical transitions in a turbulent combustor. *Chaos: An Interdisciplinary Journal of Nonlinear Science*, **27**(6), 063113.
92. **Gonzalez-Miranda, J. M.** (2002). Amplitude envelope synchronization in coupled chaotic oscillators. *Physical Review E*, **65**(3), 036232.
93. **Gopalakrishnan, E., Y. Sharma, T. John, P. S. Dutta, and R. Sujith** (2016a). Early warning signals for critical transitions in a thermoacoustic system. *Scientific reports*, **6**, 35310.

94. **Gopalakrishnan, E. and R. Sujith** (2014). Influence of system parameters on the hysteresis characteristics of a horizontal rijke tube. *International Journal of Spray and Combustion Dynamics*, **6**(3), 293–316.
95. **Gopalakrishnan, E. and R. Sujith** (2015). Effect of external noise on the hysteresis characteristics of a thermoacoustic system. *Journal of Fluid Mechanics*, **776**, 334–353.
96. **Gopalakrishnan, E., J. Tony, E. Sreelekha, and R. Sujith** (2016b). Stochastic bifurcations in a prototypical thermoacoustic system. *Physical Review E*, **94**(2), 022203.
97. **Gotoda, H., M. Amano, T. Miyano, T. Ikawa, K. Maki, and S. Tachibana** (2012). Characterization of complexities in combustion instability in a lean premixed gas-turbine model combustor. *Chaos: An Interdisciplinary Journal of Nonlinear Science*, **22**(4), 043128.
98. **Gotoda, H., H. Kinugawa, R. Tsujimoto, S. Domen, and Y. Okuno** (2017). Characterization of combustion dynamics, detection, and prevention of an unstable combustion state based on a complex-network theory. *Physical Review Applied*, **7**(4), 044027.
99. **Gotoda, H., H. Nikimoto, T. Miyano, and S. Tachibana** (2011). Dynamic properties of combustion instability in a lean premixed gas-turbine combustor. *Chaos: An Interdisciplinary Journal of Nonlinear Science*, **21**(1), 013124.
100. **Gotoda, H., Y. Shinoda, M. Kobayashi, Y. Okuno, and S. Tachibana** (2014). Detection and control of combustion instability based on the concept of dynamical system theory. *Physical Review E*, **89**(2), 022910.
101. **Gottwald, G. A. and I. Melbourne**, A new test for chaos in deterministic systems. *In Proceedings of the Royal Society of London A: Mathematical, Physical and Engineering Sciences*, volume 460. The Royal Society, 2004.
102. **Green, S. I.** (1995). Fluid vortices: fluid mechanics and its applications, vol. 30.
103. **Griffin, O. M. and M. Hall** (1991). Vortex shedding lock-on and flow control in bluff body wakes. *Journal of fluids engineering*, **113**(4), 526–537.
104. **Griffin, O. M. and S. E. Ramberg** (1974). The vortex-street wakes of vibrating cylinders. *Journal of Fluid Mechanics*, **66**(3), 553–576.
105. **Griffin, O. M. and S. E. Ramberg** (1976). Vortex shedding from a cylinder vibrating in line with an incident uniform flow. *Journal of Fluid Mechanics*, **75**(2), 257–271.
106. **Griffith, T., D. Parthimos, J. Crombie, and D. H. Edwards** (1997). Critical scaling and type-iii intermittent chaos in isolated rabbit resistance arteries. *Physical Review E*, **56**(6), R6287.
107. **Grinsted, A., J. C. Moore, and S. Jevrejeva** (2004). Application of the cross wavelet transform and wavelet coherence to geophysical time series. *Nonlinear Processes in Geophysics*, **11**(5/6), 561–566.
108. **Gunnoo, H., N. Abcha, and A. Ezersky** (2016). Frequency lock-in and phase synchronization of vortex shedding behind circular cylinder due to surface waves. *Physics Letters A*, **380**(7), 863–868.

109. **Gutmark, E., T. Parr, D. Hanson-Parr, and K. Schadow** (1989). On the role of large and small-scale structures in combustion control. *Combustion Science and Technology*, **66**(1-3), 107–126.
110. **Gysling, D., G. Copeland, D. McCormick, and W. Proscia** (2000). Combustion system damping augmentation with helmholtz resonators. *Journal of Engineering for gas Turbines and Power*, **122**(2), 269–274.
111. **Hallberg, M. and P. Strykowski** (2008). Open-loop control of fully nonlinear self-excited oscillations. *Physics of Fluids*, **20**(4), 041703.
112. **Hammer, P. W., N. Platt, S. M. Hammel, J. F. Heagy, and B. D. Lee** (1994). Experimental observation of on-off intermittency. *Physical review letters*, **73**(8), 1095.
113. **Han, X., J. Li, and A. S. Morgans** (2015). Prediction of combustion instability limit cycle oscillations by combining flame describing function simulations with a thermoacoustic network model. *Combustion and Flame*, **162**(10), 3632–3647.
114. **Hasson, C. J., R. E. Van Emmerik, G. E. Caldwell, J. M. Haddad, J. L. Gagnon, and J. Hamill** (2008). Influence of embedding parameters and noise in center of pressure recurrence quantification analysis. *Gait & posture*, **27**(3), 416–422.
115. **Heagy, J., T. Carroll, and L. Pecora** (1994). Synchronous chaos in coupled oscillator systems. *Physical Review E*, **50**(3), 1874.
116. **Heckl, M. A.** (1988). Active control of the noise from a rijke tube. *Journal of Sound and Vibration*, **124**(1), 117–133.
117. **Hegde, U., D. Reuter, B. Zinn, and B. Daniel**, Fluid mechanically coupled combustion instabilities in ramjet combustors. *In 25th AIAA Aerospace Sciences Meeting*. 1987.
118. **Hermeth, S., G. Staffelbach, L. Y. Gicquel, and T. Poinsot** (2013). Les evaluation of the effects of equivalence ratio fluctuations on the dynamic flame response in a real gas turbine combustion chamber. *Proceedings of the Combustion Institute*, **34**(2), 3165–3173.
119. **Higgins, B.** (1802). cited by w. nicholson, on the sound produced by a current of hydrogen gas passing through a tube. with a letter from dr. higgins, respecting the time of its discovery. *J. Nat. Phil., Chem., and the Arts*, **1**, 129–131.
120. **Hilborn, R. C.**, *Chaos and nonlinear dynamics: an introduction for scientists and engineers*. Oxford University Press on Demand, 2000.
121. **Holyst, J., M. Żebrowska, and K. Urbanowicz** (2001). Observations of deterministic chaos in financial time series by recurrence plots, can one control chaotic economy? *The European Physical Journal B-Condensed Matter and Complex Systems*, **20**(4), 531–535.
122. **Huerre, P. and P. A. Monkewitz** (1990). Local and global instabilities in spatially developing flows. *Annual review of fluid mechanics*, **22**(1), 473–537.
123. **Huygens, C.** (1665). Letter to his father, dated 26 february 1665. *Oeuvres complets de Christian Huygens*, **5**, 243.

124. **Issartel, J., T. Bardainne, P. Gaillot, and L. Marin** (2015). The relevance of the cross-wavelet transform in the analysis of human interaction—a tutorial. *Frontiers in Psychology*, **5**, 1566.
125. **Jahnke, C. C. and F. E. Culick** (1994). Application of dynamical systems theory to nonlinear combustion instabilities. *Journal of Propulsion and Power*, **10**(4), 508–517.
126. **Jarosinski, J. and B. Veyssiere**, *Combustion phenomena: Selected mechanisms of flame formation, propagation and extinction*. CRC press, 2009.
127. **Jegadeesan, V. and R. Sujith** (2013). Experimental investigation of noise induced triggering in thermoacoustic systems. *Proceedings of the Combustion Institute*, **34**(2), 3175–3183.
128. **Juniper, M. P.** (2011). Triggering in the horizontal rijke tube: non-normality, transient growth and bypass transition. *Journal of Fluid Mechanics*, **667**, 272–308.
129. **Juniper, M. P. and R. Sujith** (2017). Sensitivity and nonlinearity of thermoacoustic oscillations. *Annual Review of Fluid Mechanics*, **50**(1).
130. **Juniper, M. P. and R. Sujith** (2018). Sensitivity and nonlinearity of thermoacoustic oscillations. *Annual Review of Fluid Mechanics*, **50**(1), 661–689.
131. **Kabiraj, L., A. Saurabh, P. Wahi, and R. Sujith** (2012a). Route to chaos for combustion instability in ducted laminar premixed flames. *Chaos: An Interdisciplinary Journal of Nonlinear Science*, **22**(2), 023129.
132. **Kabiraj, L. and R. Sujith** (2012). Nonlinear self-excited thermoacoustic oscillations: intermittency and flame blowout. *Journal of Fluid Mechanics*, **713**, 376–397.
133. **Kabiraj, L., R. Sujith, and P. Wahi** (2012b). Bifurcations of self-excited ducted laminar premixed flames. *Journal of Engineering for Gas Turbines and Power*, **134**(3), 031502.
134. **Kabiraj, L., R. Sujith, and P. Wahi** (2012c). Investigating the dynamics of combustion-driven oscillations leading to lean blowout. *Fluid Dynamics Research*, **44**(3), 031408.
135. **Kantz, H. and T. Schreiber**, *Nonlinear time series analysis*, volume 7. Cambridge university press, 2004.
136. **Kaplan, D. T. and L. Glass** (1992). Direct test for determinism in a time series. *Physical review letters*, **68**(4), 427.
137. **Kashinath, K., L. K. Li, and M. P. Juniper** (2018). Forced synchronization of periodic and aperiodic thermoacoustic oscillations: lock-in, bifurcations and open-loop control. *Journal of Fluid Mechanics*, **838**, 690–714.
138. **Kashinath, K., I. C. Waugh, and M. P. Juniper** (2014). Nonlinear self-excited thermoacoustic oscillations of a ducted premixed flame: bifurcations and routes to chaos. *Journal of Fluid Mechanics*, **761**, 399–430.
139. **Keller, J. ., L. Vaneveld, D. Korschelt, G. Hubbard, A. Ghoniem, J. Daily, and A. Oppenheim** (1982). Mechanism of instabilities in turbulent combustion leading to flashback. *Aiaa Journal*, **20**(2), 254–262.

140. **Keller, J. J.** (1995). Thermoacoustic oscillations in combustion chambers of gas turbines. *AIAA Journal*, **33**(12), 2280–2287.
141. **Kelley, A.** and **C. Law** (2009). Nonlinear effects in the extraction of laminar flame speeds from expanding spherical flames. *Combustion and Flame*, **156**(9), 1844–1851.
142. **Ken, H. Y., A. Trouvé,** and **J. W. Daily** (1991a). Low-frequency pressure oscillations in a model ramjet combustor. *Journal of Fluid Mechanics*, **232**, 47–72.
143. **Ken, H. Y., A. Trouve,** and **J. W. Daily** (1991b). Low-frequency pressure oscillations in a model ramjet combustor. *Journal of Fluid Mechanics*, **232**, 47–72.
144. **Kennel, M. B., R. Brown,** and **H. D. Abarbanel** (1992). Determining embedding dimension for phase-space reconstruction using a geometrical construction. *Physical review A*, **45**(6), 3403.
145. **Kheirkhah, S., J. M. Cirtwill, P. Saini, K. Venkatesan,** and **A. M. Steinberg** (2017). Dynamics and mechanisms of pressure, heat release rate, and fuel spray coupling during intermittent thermoacoustic oscillations in a model aeronautical combustor at elevated pressure. *Combustion and Flame*, **185**, 319–334.
146. **Kim, M.-Y., R. Roy, J. L. Aron, T. W. Carr,** and **I. B. Schwartz** (2005). Scaling behavior of laser population dynamics with time-delayed coupling: theory and experiment. *Physical review letters*, **94**(8), 088101.
147. **Klimaszewska, K.** and **J. J. Żebrowski** (2009). Detection of the type of intermittency using characteristic patterns in recurrence plots. *Physical review E*, **80**(2), 026214.
148. **Kocarev, L.** and **U. Parlitz** (1995). General approach for chaotic synchronization with applications to communication. *Physical review letters*, **74**(25), 5028.
149. **Koseska, A., E. Volkov,** and **J. Kurths** (2013). Oscillation quenching mechanisms: Amplitude vs. oscillation death. *Physics Reports*, **531**(4), 173–199.
150. **Kulkarni, R., K. Balasubramanian,** and **R. Sujith** (2011). Non-normality and its consequences in active control of thermoacoustic instabilities. *Journal of Fluid Mechanics*, **670**, 130–149.
151. **Külshammer, C.** and **H. Büchner** (2002). Combustion dynamics of turbulent swirling flames. *Combustion and flame*, **131**(1-2), 70–84.
152. **Kumagai, S.** and **H. Isoda**, Combustion of fuel droplets in a vibrating air field. *In Symposium (International) on Combustion*, volume 5. Elsevier, 1955.
153. **Kumar, P., A. Prasad,** and **R. Ghosh** (2008). Stable phase-locking of an external-cavity diode laser subjected to external optical injection. *Journal of Physics B: Atomic, Molecular and Optical Physics*, **41**(13), 135402.
154. **Kuramoto, Y.** (1984). Chemical oscillations, waves, and turbulence.
155. **Lakshmanan, M.** and **D. V. Senthilkumar**, *Dynamics of nonlinear time-delay systems*. Springer Science & Business Media, 2011.
156. **Lang, W., T. Poinsot,** and **S. Candel** (1987). Active control of combustion instability. *Combustion and Flame*, **70**(3), 281–289.

157. **Langhorne, P., A. Dowling, and N. Hooper** (1990). Practical active control system for combustion oscillations. *Journal of Propulsion and Power*, **6**(3), 324–333.
158. **Lee, J. G., K. Kim, and D. Santavicca** (2000). Measurement of equivalence ratio fluctuation and its effect on heat release during unstable combustion. *Proceedings of the Combustion Institute*, **28**(1), 415–421.
159. **Lei, S. and A. Turan** (2009). Nonlinear/chaotic behaviour in thermo-acoustic instability. *Combustion Theory and Modelling*, **13**(3), 541–557.
160. **Li, L. K. and M. P. Juniper** (2013a). Lock-in and quasiperiodicity in a forced hydrodynamically self-excited jet. *Journal of Fluid Mechanics*, **726**, 624–655.
161. **Li, L. K. and M. P. Juniper** (2013b). Lock-in and quasiperiodicity in hydrodynamically self-excited flames: Experiments and modelling. *Proceedings of the Combustion Institute*, **34**(1), 947–954.
162. **Li, L. K. and M. P. Juniper** (2013c). Lock-in and quasiperiodicity in hydrodynamically self-excited flames: Experiments and modelling. *Proceedings of the Combustion Institute*, **34**(1), 947–954.
163. **Li, L. K. and M. P. Juniper** (2013d). Phase trapping and slipping in a forced hydrodynamically self-excited jet. *Journal of Fluid Mechanics*, **735**.
164. **Li, X., D. Zhao, J. Li, and Y. Xu** (2013). Experimental evaluation of anti-sound approach in damping self-sustained thermoacoustics oscillations. *Journal of Applied Physics*, **114**(20), 204903.
165. **Li, X., D. Zhao, and X. Li** (2018). Effects of background noises on nonlinear dynamics of a modelled thermoacoustic combustor. *The Journal of the Acoustical Society of America*, **143**(1), 60–70.
166. **Lieuwen, T.** (2001). Phase drift characteristics of self-excited, combustion-driven oscillations. *Journal of sound and vibration*, **242**(5), 893–905.
167. **Lieuwen, T.** (2003a). Modeling premixed combustion-acoustic wave interactions: A review. *Journal of propulsion and power*, **19**(5), 765–781.
168. **Lieuwen, T.** (2005a). Nonlinear kinematic response of premixed flames to harmonic velocity disturbances. *Proceedings of the Combustion Institute*, **30**(2), 1725–1732.
169. **Lieuwen, T.** (2005b). Online combustor stability margin assessment using dynamic pressure data. *Transactions of the ASME-A-Engineering for Gas Turbines and Power*, **127**(3), 478–482.
170. **Lieuwen, T. and Y. Neumeier** (2002). Nonlinear pressure-heat release transfer function measurements in a premixed combustor. *Proceedings of the Combustion Institute*, **29**(1), 99–105.
171. **Lieuwen, T., Y. Neumeier, and B. Zinn** (1998). The role of unmixedness and chemical kinetics in driving combustion instabilities in lean premixed combustors. *Combustion Science and Technology*, **135**(1-6), 193–211.
172. **Lieuwen, T. C.** (2002). Experimental investigation of limit-cycle oscillations in an unstable gas turbine combustor. *Journal of Propulsion and Power*, **18**(1), 61–67.

173. **Lieuwen, T. C.** (2003b). Statistical characteristics of pressure oscillations in a premixed combustor. *Journal of Sound and Vibration*, **260**(1), 3–17.
174. **Lieuwen, T. C.**, *Unsteady combustor physics*. Cambridge University Press, 2012.
175. **Lieuwen, T. C.** and **A. Banaszuk** (2005). Background noise effects on combustor stability. *Journal of Propulsion and Power*, **21**(1), 25–31.
176. **Macquisten, M.** (1995). Combustion oscillations in a twin-stream afterburner. *Journal of sound and vibration*, **188**(4), 545–560.
177. **Mangesius, H.** and **W. Polifke** (2011). A discrete-time, state-space approach for the investigation of non-normal effects in thermoacoustic systems. *International Journal of spray and combustion dynamics*, **3**(4), 331–350.
178. **Manrubia, S. C.**, **A. S. Mikhailov**, *et al.*, *Emergence of dynamical order: synchronization phenomena in complex systems*. World Scientific, 2004.
179. **Mariappan, S.** and **R. Sujith** (2010). Thermoacoustic instability in a solid rocket motor: non-normality and nonlinear instabilities. *Journal of Fluid Mechanics*, **653**, 1–33.
180. **Mariappan, S.** and **R. Sujith** (2011). Modelling nonlinear thermoacoustic instability in an electrically heated rijke tube. *Journal of Fluid Mechanics*, **680**, 511–533.
181. **Marwan, N.** (2011). How to avoid potential pitfalls in recurrence plot based data analysis. *International Journal of Bifurcation and Chaos*, **21**(04), 1003–1017.
182. **Marwan, N.**, **J. F. Donges**, **Y. Zou**, **R. V. Donner**, and **J. Kurths** (2009). Complex network approach for recurrence analysis of time series. *Physics Letters A*, **373**(46), 4246–4254.
183. **Marwan, N.**, **M. C. Romano**, **M. Thiel**, and **J. Kurths** (2007). Recurrence plots for the analysis of complex systems. *Physics reports*, **438**(5), 237–329.
184. **Marwan, N.**, **N. Wessel**, **U. Meyerfeldt**, **A. Schirdewan**, and **J. Kurths** (2002). Recurrence-plot-based measures of complexity and their application to heart-rate-variability data. *Physical review E*, **66**(2), 026702.
185. **Masselin, M.** and **C.-M. Ho**, Lock-on and instability in a flat plate wake. *In Shear Flow Control Conference*. 1985.
186. **Matveev, K. I.** and **F. Culick** (2003). A model for combustion instability involving vortex shedding. *Combustion Science and Technology*, **175**(6), 1059–1083.
187. **McIntosh, A.** (1999). Deflagration fronts and compressibility. *Philosophical Transactions of the Royal Society of London A: Mathematical, Physical and Engineering Sciences*, **357**(1764), 3523–3538.
188. **McManus, K.**, **T. Poinot**, and **S. M. Candel** (1993). A review of active control of combustion instabilities. *Progress in energy and combustion science*, **19**(1), 1–29.
189. **McMurtry, P.**, **J. Riley**, and **R. Metcalfe** (1989). Effects of heat release on the large-scale structure in turbulent mixing layers. *Journal of Fluid Mechanics*, **199**, 297–332.

190. **Menon, S.** and **W.-H. Jou** (1991). Large-eddy simulations of combustion instability in an axisymmetric ramjet combustor. *Combustion Science and Technology*, **75**(1-3), 53–72.
191. **Minorsky, N.** (1967). Comments" on asynchronous quenching". *IEEE Transactions on Automatic Control*, **12**(2), 225–227.
192. **Mondal, S., S. A. Pawar,** and **R. I. Sujith** (2017a). Synchronous behaviour of two interacting oscillatory systems undergoing quasiperiodic route to chaos. *Chaos: An Interdisciplinary Journal of Nonlinear Science*, **27**(10), 103119.
193. **Mondal, S., V. R. Unni,** and **R. Sujith** (2017b). Onset of thermoacoustic instability in turbulent combustors: an emergence of synchronized periodicity through formation of chimera-like states. *Journal of Fluid Mechanics*, **811**, 659–681.
194. **Morgans, A. S.** and **I. Duran** (2016). Entropy noise: A review of theory, progress and challenges. *International Journal of Spray and Combustion Dynamics*, **8**(4), 285–298.
195. **Murugesan, M.** and **R. Sujith** (2015). Combustion noise is scale-free: transition from scale-free to order at the onset of thermoacoustic instability. *Journal of Fluid Mechanics*, **772**, 225–245.
196. **Murugesan, M.** and **R. Sujith** (2016). Detecting the onset of an impending thermoacoustic instability using complex networks. *Journal of Propulsion and Power*, **32**(1), 707–712.
197. **Murugesan, M.** and **R. Sujith** (2018). Physical mechanisms that cause intermittency that presages combustion instability and blowout in a turbulent lifted jet flame combustor. *Combustion Science and Technology*, **190**(2), 312–335.
198. **Nair, V.** and **R. Sujith** (2014). Multifractality in combustion noise: predicting an impending combustion instability. *Journal of Fluid Mechanics*, **747**, 635–655.
199. **Nair, V.** and **R. Sujith** (2015). A reduced-order model for the onset of combustion instability: physical mechanisms for intermittency and precursors. *Proceedings of the Combustion Institute*, **35**(3), 3193–3200.
200. **Nair, V., G. Thampi, S. Karuppusamy, S. Gopalan,** and **R. Sujith** (2013). Loss of chaos in combustion noise as a precursor of impending combustion instability. *International journal of spray and combustion dynamics*, **5**(4), 273–290.
201. **Nair, V., G. Thampi,** and **R. Sujith** (2014). Intermittency route to thermoacoustic instability in turbulent combustors. *Journal of Fluid Mechanics*, **756**, 470–487.
202. **Najm, H. N.** and **A. F. Ghoniem** (1994). Coupling between vorticity and pressure oscillations in combustion instability. *Journal of Propulsion and Power*, **10**(6), 769–776.
203. **Nayfeh, A. H.** and **B. Balachandran**, *Applied nonlinear dynamics: analytical, computational and experimental methods*. John Wiley & Sons, 2008.
204. **Neumeier, Y.** and **B. Zinn**, Active control of combustion instabilities with real time operation of unstable combustor modes. *In 34th Aerospace Sciences Meeting and Exhibit*. 1996.

205. **Newman, M.**, *Networks: an introduction*. Oxford university press, 2010.
206. **Noiray, N., D. Durox, T. Schuller, and S. Candel** (2007). Passive control of combustion instabilities involving premixed flames anchored on perforated plates. *Proceedings of the Combustion Institute*, **31**(1), 1283–1290.
207. **Noiray, N., D. Durox, T. Schuller, and S. Candel** (2008). A unified framework for nonlinear combustion instability analysis based on the flame describing function. *Journal of Fluid Mechanics*, **615**, 139–167.
208. **Noiray, N. and B. Schuermans** (2012). Theoretical and experimental investigations on damper performance for suppression of thermoacoustic oscillations. *Journal of sound and vibration*, **331**(12), 2753–2763.
209. **Noiray, N. and B. Schuermans** (2013). Deterministic quantities characterizing noise driven hopf bifurcations in gas turbine combustors. *International Journal of Non-Linear Mechanics*, **50**, 152–163.
210. **Oefelein, J. C. and V. Yang** (1993). Comprehensive review of liquid-propellant combustion instabilities in f-1 engines. *Journal of Propulsion and Power*, **9**(5), 657–677.
211. **Okai, K., O. Moriue, M. Araki, M. Tsue, M. Kono, J. Sato, D. Dietrich, and F. Williams** (2000). Combustion of single droplets and droplet pairs in a vibrating field under microgravity. *Proceedings of the Combustion Institute*, **28**(1), 977–983.
212. **Osipov, G. V., B. Hu, C. Zhou, M. V. Ivanchenko, and J. Kurths** (2003). Three types of transitions to phase synchronization in coupled chaotic oscillators. *Physical Review Letters*, **91**(2), 024101.
213. **Panaggio, M. J. and D. M. Abrams** (2015). Chimera states: coexistence of coherence and incoherence in networks of coupled oscillators. *Nonlinearity*, **28**(3), R67.
214. **Paschereit, C. O., E. Gutmark, and W. Weisenstein** (1998). Structure and control of thermoacoustic instabilities in a gas-turbine combustor. *Combustion Science and Technology*, **138**(1-6), 213–232.
215. **Paschereit, C. O., E. Gutmark, and W. Weisenstein** (1999). Coherent structures in swirling flows and their role in acoustic combustion control. *Physics of Fluids*, **11**(9), 2667–2678.
216. **Peracchio, A. and W. Proscia**, Nonlinear heat-release/acoustic model for thermoacoustic instability in lean premixed combustors. *In ASME 1998 International Gas Turbine and Aeroengine Congress and Exhibition*. American Society of Mechanical Engineers, 1998.
217. **Pikovsky, A., M. Rosenblum, and J. Kurths**, *Synchronization: a universal concept in nonlinear sciences*, volume 12. Cambridge university press, 2003.
218. **Poinsot, T., S. Candel, E. Esposito, W. Lang, and F. Bourienne** (1989). Suppression of combustion instabilities by active control. *Journal of Propulsion and Power*, **5**(1), 14–20.
219. **Poinsot, T. and S. M. Candel** (1988). A nonlinear model for ducted flame combustion instabilities. *Combustion science and technology*, **61**(4-6), 121–153.

220. **Poinsot, T. J., A. C. Trouve, D. P. Veynante, S. M. Candel, and E. J. Esposito** (1987). Vortex-driven acoustically coupled combustion instabilities. *Journal of fluid mechanics*, **177**, 265–292.
221. **Pomeau, Y. and P. Manneville** (1980). Intermittent transition to turbulence in dissipative dynamical systems. *Communications in Mathematical Physics*, **74**(2), 189–197.
222. **Putnam, A. A.**, *Combustion driven oscillations in industry*. Elsevier Publishing Company, 1971.
223. **Putnam, A. A. and W. R. Dennis** (1956). Survey of organ-pipe oscillations in combustion systems. *The Journal of the Acoustical Society of America*, **28**(2), 246–259.
224. **Pyragas, K.** (1998). Properties of generalized synchronization of chaos. *Nonlinear Analysis: Modelling and Control*, **3**, 1–29.
225. **Rajasekar, S. and M. A. Sanjuan**, *Nonlinear resonances*. Springer, 2016.
226. **Rayleigh, J.**, *The theory of sound*. Dover-New York, 1945.
227. **Rayleigh, J. W. S.** (1878). The explanation of certain acoustical phenomena. *Nature*, **18**(455), 319–321.
228. **Renard, P.-H., D. Thevenin, J.-C. Rolon, and S. Candel** (2000). Dynamics of flame/vortex interactions. *Progress in energy and combustion science*, **26**(3), 225–282.
229. **Richards, G. A. and M. C. Janus**, Characterization of oscillations during premix gas turbine combustion. In *ASME 1997 International Gas Turbine and Aeroengine Congress and Exhibition*. American Society of Mechanical Engineers, 1997.
230. **Richards, G. A., J. D. Thornton, E. H. Robey, and L. Arellano** (2007). Open-loop active control of combustion dynamics on a gas turbine engine. *Journal of engineering for gas turbines and power*, **129**(1), 38–48.
231. **Rijke, P. L.** (1859). Lxxi. notice of a new method of causing a vibration of the air contained in a tube open at both ends. *The London, Edinburgh, and Dublin Philosophical Magazine and Journal of Science*, **17**(116), 419–422.
232. **Ringuet, E., C. Rozé, and G. Gouesbet** (1993). Experimental observation of type-ii intermittency in a hydrodynamic system. *Physical Review E*, **47**(2), 1405.
233. **Rogers, D. E. and F. E. Marble** (1956). A mechanism for high frequency oscillations in ramjet combustors and afterburners. *Jet Propulsion*, **26**(1), 456–462.
234. **Romano, M. C., M. Thiel, J. Kurths, I. Z. Kiss, and J. Hudson** (2005). Detection of synchronization for non-phase-coherent and non-stationary data. *EPL (Europhysics Letters)*, **71**(3), 466.
235. **Rosenblum, M. G., A. S. Pikovsky, and J. Kurths** (1996). Phase synchronization of chaotic oscillators. *Physical review letters*, **76**(11), 1804.
236. **Rosenblum, M. G., A. S. Pikovsky, and J. Kurths** (1997). From phase to lag synchronization in coupled chaotic oscillators. *Physical Review Letters*, **78**(22), 4193.
237. **Roy, R. and K. S. Thornburg Jr** (1994). Experimental synchronization of chaotic lasers. *Physical Review Letters*, **72**(13), 2009.

238. **Rulkov, N. F., M. M. Sushchik, L. S. Tsimring, and H. D. Abarbanel** (1995). Generalized synchronization of chaos in directionally coupled chaotic systems. *Physical Review E*, **51**(2), 980.
239. **Sacher, J., W. Elsässer, and E. O. Göbel** (1989). Intermittency in the coherence collapse of a semiconductor laser with external feedback. *Physical review letters*, **63**(20), 2224.
240. **Saito, M., M. Hoshikawa, and M. Sato** (1996). Enhancement of evaporation/combustion rate coefficient of a single fuel droplet by acoustic oscillation. *Fuel*, **75**(6), 669–674.
241. **Sampath, R. and S. R. Chakravarthy** (2016). Investigation of intermittent oscillations in a premixed dump combustor using time-resolved particle image velocimetry. *Combustion and Flame*, **172**, 309–325.
242. **Sattinger, S. S., Y. Neumeier, A. Nabi, B. T. Zinn, D. J. Amos, and D. D. Darling**, Sub-scale demonstration of the active feedback control of gas-turbine combustion instabilities. *In ASME 1998 International Gas Turbine and Aeroengine Congress and Exhibition*. American Society of Mechanical Engineers, 1998.
243. **Saxena, G., A. Prasad, and R. Ramaswamy** (2012). Amplitude death: The emergence of stationarity in coupled nonlinear systems. *Physics Reports*, **521**(5), 205–228.
244. **Schadow, K. and E. Gutmark** (1992). Combustion instability related to vortex shedding in dump combustors and their passive control. *Progress in Energy and Combustion Science*, **18**(2), 117–132.
245. **Schadow, K., E. Gutmark, and K. Wilson** (1992). Active combustion control in a coaxial dump combustor. *Combustion Science and Technology*, **81**(4-6), 285–300.
246. **Schinkel, S., O. Dimigen, and N. Marwan** (2008). Selection of recurrence threshold for signal detection. *The European Physical Journal-Special Topics*, **164**(1), 45–53.
247. **Schmid, P. and D. Henningson**, *Stability and transition in shear flows*. Springer, 2001.
248. **Schmid, S. R., B. J. Hamrock, and B. O. Jacobson**, *Fundamentals of machine elements: SI version*. CRC Press, 2014.
249. **Schmitt, P., T. POINSOT, B. Schuermans, and K. Geigle** (2007). Large-eddy simulation and experimental study of heat transfer, nitric oxide emissions and combustion instability in a swirled turbulent high-pressure burner. *Journal of Fluid Mechanics*, **570**, 17–46.
250. **Schreiber, I. and M. Marek** (1982). Strange attractors in coupled reaction-diffusion cells. *Physica D: Nonlinear Phenomena*, **5**(2-3), 258–272.
251. **Schuller, T., S. Ducruix, D. Durox, and S. Candel** (2002). Modeling tools for the prediction of premixed flame transfer functions. *Proceedings of the Combustion Institute*, **29**(1), 107–113.
252. **Schuster, H. G. and W. Just**, *Deterministic chaos: an introduction*. John Wiley & Sons, 2006.

253. **Selimefendigil, F., R. Sujith, and W. Polifke** (2011). Identification of heat transfer dynamics for non-modal analysis of thermoacoustic stability. *Applied Mathematics and Computation*, **217**(11), 5134–5150.
254. **Selkoe, D. J.** (2000). Toward a comprehensive theory for alzheimer’s disease. hypothesis: Alzheimer’s disease is caused by the cerebral accumulation and cytotoxicity of amyloid  $\beta$ -protein. *Annals of the New York Academy of Sciences*, **924**(1), 17–25.
255. **Seshadri, A., V. Nair, and R. Sujith** (2016). A reduced-order deterministic model describing an intermittency route to combustion instability. *Combustion Theory and Modelling*, **20**(3), 441–456.
256. **Seshadri, A. and R. Sujith** (2016). A bifurcation giving birth to order in an impulsively driven complex system. *Chaos: An Interdisciplinary Journal of Nonlinear Science*, **26**(8), 083103.
257. **Shanbhogue, S., D. H. Shin, S. Hemchandra, D. Plaks, and T. Lieuwen** (2009a). Flame-sheet dynamics of bluff-body stabilized flames during longitudinal acoustic forcing. *Proceedings of the Combustion Institute*, **32**(2), 1787–1794.
258. **Shanbhogue, S. J., S. Husain, and T. Lieuwen** (2009b). Lean blowoff of bluff body stabilized flames: Scaling and dynamics. *Progress in Energy and Combustion Science*, **35**(1), 98–120.
259. **Sheridan, J., J. Carberry, J.-C. Lin, and D. Rockwell** (1998). On the near-wake topology of an oscillating cylinder. *Journal of fluids and structures*, **12**(2), 215–220.
260. **Shin, D. H., D. V. Plaks, T. Lieuwen, U. M. Mondragon, C. T. Brown, and V. G. McDonnell** (2011). Dynamics of a longitudinally forced, bluff body stabilized flame. *Journal of Propulsion and Power*, **27**(1), 105.
261. **Shreekrishna, S. Hemchandra, and T. Lieuwen** (2010). Premixed flame response to equivalence ratio perturbations. *Combustion Theory and Modelling*, **14**(5), 681–714.
262. **Singaravelu, B. and S. Mariappan**, Criterion for vortex acoustic lock-on in combustors with backward facing step. In *Journal of Physics: Conference Series*, volume 822. IOP Publishing, 2017.
263. **Smith, D. A. and E. E. Zukoski** (1985). Combustion instability sustained by unsteady vortex combustion.
264. **Sondhauss, C.** (1850). Über die schallschwingungen der luft in erhitzten gläseröhren und in gedeckten pfeifen von ungleicher weite. *Annalen der Physik*, **155**(1), 1–34.
265. **Staubli, T.** (1987). Entrainment of self-sustained flow oscillations: Phaselooking or asynchronous quenching? *Journal of applied mechanics*, **54**, 707.
266. **Steele, R. C., L. H. Cowell, S. M. Cannon, and C. E. Smith**, Passive control of combustion instability in lean premixed combustors. In *ASME 1999 International Gas Turbine and Aeroengine Congress and Exhibition*. American Society of Mechanical Engineers, 1999.
267. **Steinberg, A. M., I. Boxx, M. Stohr, W. Meier, and C. D. Carter** (2012). Effects of flow structure dynamics on thermoacoustic instabilities in swirl-stabilized combustion. *AIAA Journal*, **50**(4), 952–967.

268. **Sterling, J.** and **E. Zukoski** (1987). Longitudinal mode combustion instabilities in a dump combustor.
269. **Sterling, J. D.** (1993). Nonlinear analysis and modelling of combustion instabilities in a laboratory combustor. *Combustion Science and Technology*, **89**(1-4), 167–179.
270. **Stow, S. R.** and **A. P. Dowling**, Low-order modelling of thermoacoustic limit cycles. In *ASME turbo expo 2004: power for land, sea, and air*. American Society of Mechanical Engineers, 2004.
271. **Strahle, W. C.** (1978). Combustion noise. *Progress in Energy and Combustion Science*, **4**(3), 157–176.
272. **Strogatz, S.** and **A. W. Edwards** (2005). Sync-how order emerges from chaos in the universe, nature, and daily life. *The Mathematical Intelligencer*, **27**(1), 89–89.
273. **Strogatz, S. H.**, *Nonlinear dynamics and chaos: with applications to physics, biology, chemistry, and engineering*. CRC Press, 1994.
274. **Subramanian, P.** (2011). Dynamical systems approach to the investigation of thermoacoustic instabilities.
275. **Subramanian, P.**, **S. Mariappan**, **R. Sujith**, and **P. Wahi** (2010). Bifurcation analysis of thermoacoustic instability in a horizontal rijke tube. *International journal of spray and combustion dynamics*, **2**(4), 325–355.
276. **Subramanian, P.**, **R. Sujith**, and **P. Wahi** (2013). Subcritical bifurcation and bistability in thermoacoustic systems. *Journal of Fluid Mechanics*, **715**, 210–238.
277. **Sujith, R.** (2005). An experimental investigation of interaction of sprays with acoustic fields. *Experiments in Fluids*, **38**(5), 576–587.
278. **Sujith, R.**, **M. Juniper**, and **P. Schmid** (2016). Non-normality and nonlinearity in thermoacoustic instabilities. *International Journal of Spray and Combustion Dynamics*, **8**(2), 119–146.
279. **Sujith, R.**, **G. Waldherr**, **J. Jagoda**, and **B. Zinn** (1997). An experimental investigation of the behavior of droplets in axial acoustic fields. *Journal of Vibration and Acoustics*, **119**, 285–292.
280. **Sujith, R.**, **G. Waldherr**, **J. Jagoda**, and **B. Zinn** (2000). Experimental investigation of the evaporation of droplets in axial acoustic fields. *Journal of Propulsion and Power*, **16**(2), 278–285.
281. **Sun, C.** and **C. Law** (2000). On the nonlinear response of stretched premixed flames. *Combustion and flame*, **121**(1-2), 236–248.
282. **Suresh, S.**, *Fatigue of materials*. Cambridge university press, 1998.
283. **Suresha, S.**, **R. Sujith**, **B. Emerson**, and **T. Lieuwen** (2016). Nonlinear dynamics and intermittency in a turbulent reacting wake with density ratio as bifurcation parameter. *Physical Review E*, **94**(4), 042206.
284. **Takens, F.** *et al.* (1981). Detecting strange attractors in turbulence. *Lecture notes in mathematics*, **898**(1), 366–381.

285. **Tanabe, M., T. Morita, K. Aoki, K. Satoh, T. Fujimori, and J. Sato** (2000). Influence of standing sound waves on droplet combustion. *Proceedings of the Combustion Institute*, **28**(1), 1007–1013.
286. **Tanida, Y., A. Okajima, and Y. Watanabe** (1973). Stability of a circular cylinder oscillating in uniform flow or in a wake. *Journal of Fluid Mechanics*, **61**(4), 769–784.
287. **Theiler, J., S. Eubank, A. Longtin, B. Galdrikian, and J. D. Farmer** (1992). Testing for nonlinearity in time series: the method of surrogate data. *Physica D: Nonlinear Phenomena*, **58**(1-4), 77–94.
288. **Thévenin, J., M. Romanelli, M. Vallet, M. Brunel, and T. Erneux** (2011). Resonance assisted synchronization of coupled oscillators: frequency locking without phase locking. *Physical review letters*, **107**(10), 104101.
289. **Thomas, N., S. Mondal, S. A. Pawar, and R. Sujith** (2018). Effect of time-delay and dissipative coupling on amplitude death in coupled thermoacoustic oscillators. *Chaos: An Interdisciplinary Journal of Nonlinear Science*, **28**(3), 033119.
290. **Thumuluru, S. K. and T. Liewen** (2009). Characterization of acoustically forced swirl flame dynamics. *Proceedings of the Combustion Institute*, **32**(2), 2893–2900.
291. **Tony, J., E. Gopalakrishnan, E. Sreelekha, and R. Sujith** (2015). Detecting deterministic nature of pressure measurements from a turbulent combustor. *Physical Review E*, **92**(6), 062902.
292. **Torrence, C. and G. P. Compo** (1998). A practical guide to wavelet analysis. *Bulletin of the American Meteorological society*, **79**(1), 61–78.
293. **Trulla, L., A. Giuliani, J. Zbilut, and C. Webber** (1996). Recurrence quantification analysis of the logistic equation with transients. *Physics Letters A*, **223**(4), 255–260.
294. **Tulsyan, B., K. Balasubramanian, and R. Sujith** (2009). Revisiting a model for combustion instability involving vortex shedding. *Combustion Science and Technology*, **181**(3), 457–482.
295. **Unni, V. R., A. Mukhopadhyay, and R. Sujith** (2015). Online detection of impending instability in a combustion system using tools from symbolic time series analysis. *International Journal of Spray and Combustion Dynamics*, **7**(3), 243–255.
296. **Unni, V. R. and R. Sujith** (2015). Multifractal characteristics of combustor dynamics close to lean blowout. *Journal of Fluid Mechanics*, **784**, 30–50.
297. **Unni, V. R. and R. Sujith** (2017). Flame dynamics during intermittency in a turbulent combustor. *Proceedings of the Combustion Institute*, **36**(3), 3791–3798.
298. **Unni, V. R., V. N. Vinod, S. R. P. I. Nair, and A. Mukhopadhyay** (2016). System and method for controlling oscillatory instabilities in a device. US Patent App. 15/033,897.
299. **Vander Velde, W. E.**, *Multiple-input describing functions and nonlinear system design*. McGraw-Hill, New York, 1968.
300. **Vishnu, R., R. Sujith, and P. Aghalayam** (2015). Role of flame dynamics on the bifurcation characteristics of a ducted v-flame. *Combustion Science and Technology*, **187**(6), 894–905.

301. **Wang, W., I. Z. Kiss, and J. Hudson** (2000). Experiments on arrays of globally coupled chaotic electrochemical oscillators: Synchronization and clustering. *Chaos: An Interdisciplinary Journal of Nonlinear Science*, **10**(1), 248–256.
302. **Wang, W., I. Z. Kiss, and J. L. Hudson** (2001). Clustering of arrays of chaotic chemical oscillators by feedback and forcing. *Physical review letters*, **86**(21), 4954.
303. **Wagh, I., M. Geuß, and M. Juniper** (2011). Triggering, bypass transition and the effect of noise on a linearly stable thermoacoustic system. *Proceedings of the Combustion Institute*, **33**(2), 2945–2952.
304. **Webber, C. L. and J. P. Zbilut** (1994). Dynamical assessment of physiological systems and states using recurrence plot strategies. *Journal of applied physiology*, **76**(2), 965–973.
305. **Wicker, J. M., W. D. Greene, S.-I. Kim, and V. Yang** (1996). Triggering of longitudinal combustion instabilities in rocket motors-nonlinear combustion response. *Journal of Propulsion and Power*, **12**(6), 1148–1158.
306. **Wickramasinghe, M. and I. Z. Kiss** (2013). Spatially organized dynamical states in chemical oscillator networks: Synchronization, dynamical differentiation, and chimera patterns. *PloS one*, **8**(11), e80586.
307. **Wieczorek, K., C. Sensiau, W. Polifke, and F. Nicoud** (2011). Assessing non-normal effects in thermoacoustic systems with mean flow. *Physics of Fluids*, **23**(10), 107103.
308. **Wilhite, J. M., B. J. Dolan, L. Kabiraj, R. V. Gomez, E. J. Gutmark, and C. O. Paschereit**, Analysis of combustion oscillations in a staged mldi burner using decomposition methods and recurrence analysis. In *54th AIAA Aerospace Sciences Meeting, AIAA SciTech Forum, (AIAA 2016-1156)*. 2016.
309. **Williams, J. F.** (1984). Review lecture-anti-sound. *Proc. R. Soc. Lond. A*, **395**(1808), 63–88.
310. **Williamson, C. H. and A. Roshko** (1988). Vortex formation in the wake of an oscillating cylinder. *Journal of fluids and structures*, **2**(4), 355–381.
311. **Winfree, A. T.** (1967). Biological rhythms and the behavior of populations of coupled oscillators. *Journal of theoretical biology*, **16**(1), 15–42.
312. **Xiao, Y., Y. Wang, and Y.-C. Lai** (2009). Dependence of intermittency scaling on threshold in chaotic systems. *Physical Review E*, **80**(5), 057202.
313. **Yalçmkaya, T. and Y.-C. Lai** (1997). Phase characterization of chaos. *Physical Review Letters*, **79**(20), 3885.
314. **You, D., Y. Huang, and V. Yang** (2005). A generalized model of acoustic response of turbulent premixed flame and its application to gas-turbine combustion instability analysis. *Combustion Science and Technology*, **177**(5-6), 1109–1150.
315. **Young, V.**, *Liquid rocket engine combustion instability*, volume 169. Aiaa, 1995.
316. **Yu, K., T. Parr, K. Wilson, K. Schadow, and E. Gutmark**, Active control of liquid-fueled combustion using periodic vortex-droplet interaction. In *Symposium (International) on Combustion*, volume 26. Elsevier, 1996.

317. **Yu, M. H.** and **P. A. Monkewitz** (1990). The effect of nonuniform density on the absolute instability of two-dimensional inertial jets and wakes. *Physics of Fluids A: Fluid Dynamics*, **2**(7), 1175–1181.
318. **Zanette, D.** and **A. Mikhailov** (1998). Condensation in globally coupled populations of chaotic dynamical systems. *Physical Review E*, **57**(1), 276.
319. **Zdravkovich, M.** (1982). Modification of vortex shedding in the synchronization range. *Journal of Fluids Engineering*, **104**(4), 513–517.
320. **Zinn, B. T.** and **T. C. Lieuwen** (2005). Combustion instabilities: Basic concepts. *Combustion Instabilities in Gas Turbine Engines: Operational Experience, Fundamental Mechanisms, and Modeling*, **210**, 3–26.

## LIST OF PAPERS BASED ON THESIS

### REFEREED JOURNALS BASED ON THE THESIS

1. **Samadhan A. Pawar**, R. Vishnu, M. Vadivukkarasan, M. V. Panchagnula and R. I. Sujith (2016) Intermittency Route to Combustion Instability in a Laboratory Spray Combustor. *Journal of Engineering for Gas Turbines and Power*, **138(4)**, 041505: 1-8.
2. **Samadhan A. Pawar**, Akshay Seshadri, Vishnu R. Unni and R. I. Sujith (2017) Thermoacoustic instability as mutual synchronization between the acoustic field of the confinement and turbulent reactive flow. *Journal of Fluid Mechanics*, **827**, 664-693.
3. **Samadhan A. Pawar**, R. I. Sujith, Benjamin Emerson and Tim Lieuwen (2018) Characterization of forced response of density stratified reacting wake. *Chaos: An Interdisciplinary Journal of Nonlinear Science*, **28(2)**, 023108: 1-14.
4. **Samadhan A. Pawar** and R. I. Sujith (2018) Transition to thermoacoustic instability in a turbulent combustor. *Journal of the Combustion Society of Japan*, **60(192)**, 99-111.
5. **Samadhan A. Pawar**, M. V. Panchagnula and R. I. Sujith (2019) Phase synchronization and collective interaction of multiple flamelets in a laboratory scale spray combustor. *Proceedings of the Combustion Institute*.
6. **Samadhan A. Pawar**, Sirshendu Mondal, Nitin B. George and R. I. Sujith. Temporal and spatiotemporal analysis of synchronization transition in a swirl-stabilized combustor. *AIAA Journal*. (under review)
7. Sirshendu Mondal, **Samadhan A. Pawar** and R. I. Sujith. Forced synchronization and asynchronous quenching of periodic oscillations in a thermoacoustic system. *Journal of Fluid Mechanics*. (under review)

## REFEREED JOURNALS (Others)

1. Sirshendu Mondal, **Samadhan A. Pawar** and R. I. Sujith (2017) Synchronous behavior of two interacting oscillating systems undergoing quasiperiodic route to chaos. *Chaos: An Interdisciplinary Journal of Nonlinear Science*, **27**, 103119.
2. Nevin Thomas, Sirshendu Mondal, **Samadhan A. Pawar** and R. I. Sujith (2018) Effect of time-delay and dissipative coupling on amplitude death in coupled thermoacoustic oscillators. *Chaos: An Interdisciplinary Journal of Nonlinear Science*, **28**, 033119.
3. Krishna Manoj, **Samadhan A. Pawar** and R. I. Sujith (2018) Experimental Evidence of Amplitude Death and Phase-Flip Bifurcation between In-Phase and Anti-Phase Synchronization. *Scientific reports*, **8**, 11626.

## BOOK CHAPTERS

1. **Samadhan A. Pawar** and R. I. Sujith. Intermittency: a state that precedes thermoacoustic instability. Chapter 14 in the book titled 'Droplets and Sprays: Applications for Combustion and Propulsion', Editors: Saptarshi Basu, Avinash Kumar Agarwal, Achintya Mukhopadhyay and Chetankumar Patel *Springer*, 403-430, 2017.
2. Sirshendu Mondal, **Samadhan A. Pawar** and R. I. Sujith. Synchronization transition in a thermoacoustic system: Temporal and spatiotemporal analysis. Chapter in the book titled 'Energy for Propulsion - A Sustainable Technologies Approach', Editors: Akshai Runchal, Ashwani Gupta, Abhijit Kushari, Ashoke De and Suresh Aggarwal *Springer*, 2018.

## PRESENTATIONS IN CONFERENCES

1. **Samadhan A. Pawar**, R. Vishnu, M. Vadivukkarasan, M. V. Panchagnula and R. I. Sujith. Intermittency route to combustion instability in a laboratory spray combustor. *ASME Turbo Expo, (GT2015-42919)*, Montreal, Canada, June 15 - 19, 2015.
2. **Samadhan A. Pawar**, Akshay Seshadri, Vishnu R. Unni and R. I. Sujith. Mutual synchronization of coupled oscillators of a thermoacoustic system. *Conference on Nonlinear Systems and Dynamics, (CNSD-16)*, IISER, Kolkata, India, December 16 - 18, 2016.

3. **Samadhan Pawar**, Sirshendu Mondal, Nitin Babu George and R I Sujith. Synchronization behaviour during the dynamical transition in swirl-stabilized combustor: temporal and spatiotemporal analysis. *AIAA Aerospace Sciences Meeting, AIAA SciTech Forum, (AIAA 2018-0394)*, Kissimmee, Florida, USA, January 8 - 12, 2018.
4. **Samadhan A. Pawar**, M. V. Panchagnula and R. I. Sujith. Phase synchronization and collective interaction of multiple flamelets in a laboratory scale spray combustor. *37th International Symposium on Combustion, (PROCI-D-17-00694)*, Dublin, Ireland, July 29 - August 3, 2018.

# CURRICULUM VITAE

**1. NAME** : Pawar Samadhan Ananda

**2. DATE OF BIRTH** : 17 September, 1988

**3. EDUCATIONAL QUALIFICATION**

**2012 Bachelor of Engineering (B.E.)**

Institution : Aeronautical Society of India, New Delhi

Specialization : Aeronautical Engineering

**2018 Master of Science (M.S. by Research) - Integrated**

Institution : Indian Institute of Technology Madras, Chennai

Specialization : Aerospace Engineering

**2018 Doctor of Philosophy (Ph.D.)**

Institution : Indian Institute of Technology Madras, Chennai

Registration date : 16 July, 2012

## **DOCTORAL COMMITTEE**

- CHAIRPERSON:** Dr. P. Sriram  
Professor and Head  
Department of Aerospace Engineering
- GUIDE(S):** Dr. R. I. Sujith  
Professor  
Department of Aerospace Engineering
- Dr. M. V. Panchagnula  
Professor  
Department of Applied Mechanics
- MEMBERS:** Dr. Amit Kumar  
Professor  
Department of Aerospace Engineering
- Dr. Srikrishna Sahu  
Assistant Professor  
Department of Mechanical Engineering